

✓ VOLUME 81

MARCH 24, 1977

NUMBER 6

JPCHAx

THE JOURNAL OF

PHYSICAL

CHEMISTRY



PUBLISHED BIWEEKLY BY THE AMERICAN CHEMICAL SOCIETY

THE JOURNAL OF PHYSICAL CHEMISTRY

BRYCE CRAWFORD, Jr., Editor
STEPHEN PRAGER, Associate Editor
ROBERT W. CARR, Jr., C. ALDEN MEAD, Assistant Editors

EDITORIAL BOARD: C. A. ANGELL (1973-1977), F. C. ANSON (1974-1978), V. A. BLOOMFIELD (1974-1978), J. R. BOLTON (1976-1980), L. M. DORFMAN (1974-1978), W. FALCONER (1977-1978), H. L. FRIEDMAN (1975-1979), H. L. FRISCH (1976-1980), W. A. GODDARD (1976-1980), E. J. HART (1975-1979), W. J. KAUZMANN (1974-1978), R. L. KAY (1977-1981), D. W. McCLURE (1974-1978), K. MYSELS (1977-1981), R. M. NOYES (1973-1977), R. G. PARR (1977-1979), W. B. PERSON (1976-1980), J. C. POLANYI (1976-1980), S. A. RICE (1976-1980), F. S. ROWLAND (1973-1977), R. L. SCOTT (1973-1977), W. A. STEELE (1976-1980), J. B. STOTHERS (1974-1978), F. A. VAN-CATLEDGE (1977-1981), B. WEINSTOCK (1977)

Published by the
AMERICAN CHEMICAL SOCIETY
BOOKS AND JOURNALS DIVISION

D. H. Michael Bowen, Director
Marjorie Laflin, Assistant to the Director

Editorial Department: Charles R. Bertsch,
Head; Marianne C. Brogan, Associate
Head; Celia B. McFarland, Joseph E.
Yurvati, Assistant Editors

Magazine and Production Department:
Baecil Guiley, Head

Research and Development Department:
Seldon W. Terrant, Head

Advertising Office: Centcom, Ltd., 50 W.
State St., Westport, Conn. 06880.

Editorial Department at the ACS Easton
address.

Page charges of \$60.00 per page may be
paid for papers published in this journal.
Ability to pay does not affect acceptance or
scheduling of papers.

Bulk reprints or photocopies of indi-
vidual articles are available. For information
write to Business Operations, Books and
Journals Division at the ACS Washington
address.

Requests for **permission to reprint**
should be directed to Permissions, Books and
Journals Division at the ACS Washington
address. The American Chemical Society and
its Editors assume no responsibility for the
statements and opinions advanced by con-
tributors.

Subscription and Business Information

1977 Subscription rates—including surface
postage

	U.S.	PUAS	Canada, Foreign
Member	\$24.00	\$33.00	\$34.00
Nonmember	96.00	105.00	106.00
Supplementary material	15.00	19.00	20.00

Air mail and air freight rates are avail-
able from Membership & Subscription Ser-
vices, at the ACS Columbus address.

New and renewal subscriptions should
be sent with payment to the Office of the
Controller at the ACS Washington address.

Changes of address must include both old
and new addresses with ZIP code and a recent
mailing label. Send all address changes to the
ACS Columbus address. Please allow six
weeks for change to become effective. **Claims
for missing numbers** will not be allowed if
loss was due to failure of notice of change of
address to be received in the time specified:

if claim is dated (a) North America—more
than 90 days beyond issue date, (b) all other
foreign—more than 1 year beyond issue date;
or if the reason given is "missing from files".
Hard copy claims are handled at the ACS
Columbus address.

Microfiche subscriptions are available
at the same rates but are mailed first class to
U.S. subscribers, air mail to the rest of the
world. Direct all inquiries to Special Issues
Sales, at the ACS Washington address or call
(202) 872-4554. **Single issues** in hard copy
and/or microfiche are available from Special
Issues Sales at the ACS Washington address.
Current year \$4.75. Back issue rates available
from Special Issues Sales. **Back volumes** are
available in hard copy and/or microform.
Write to Special Issues Sales at the ACS
Washington address for further information.
Microfilm editions of ACS periodical pub-
lications are available from volume 1 to the
present. For further information, contact
Special Issues Sales at the ACS Washington
address. **Supplementary material** men-
tioned in the journal appears in the microfilm
edition. Single copies may be ordered directly
from Business Operations, Books and Jour-
nals Division, at the ACS Washington ad-
dress.

	U.S.	PUAS	Other Foreign
Microfiche	\$2.50	\$3.00	\$3.50
Photocopy			
1-7 pages	4.00	5.50	7.00
8-20 pages	5.00	6.50	8.00

Orders over 20 pages are available only on
microfiche, 4 × 6 in., 24X, negative, silver
halide. Orders must state photocopy or mi-
crofiche if both are available. Full biblio-
graphic citation including names of all au-
thors and prepayment are required. Prices
are subject to change.

© Copyright, 1977, by the American
Chemical Society. No part of this publication
may be reproduced in any form without
permission in writing from the American
Chemical Society.

Published biweekly by the American
Chemical Society at 20th and Northampton
Sts., Easton, Pennsylvania 18042. Second
class postage paid at Washington, D.C. and
at additional mailing offices.

Editorial Information

Instructions for authors are printed in
the first issue of each volume. Please conform
to these instructions when submitting man-
uscripts.

Manuscripts for publication should be
submitted to *The Journal of Physical
Chemistry*, Department of Chemistry, Uni-
versity of Minnesota, Minneapolis, Minn.
55455. Correspondence regarding **accepted
papers and proofs** should be directed to the

American Chemical Society
1155 16th Street, N.W.
Washington, D.C. 20036
(202) 872-4600

Member & Subscription Services
American Chemical Society
P.O. Box 3357
Columbus, Ohio 43210
(614) 421-7230

Editorial Department
American Chemical Society
20th and Northampton Sts.
Easton, Pennsylvania 18042
(215) 258-9111

Volume 81, Number 6 March 24, 1977

JPCHAx 81(6) 499-592 (1977)

ISSN 0022-3654

- Reaction Rates for $O_3 + HCl \rightarrow O + O_2 + HCl$, $Cl + O_3 \rightarrow ClO + O_2$, and $HCl + O \rightarrow OH + Cl$ at Elevated Temperatures **Chul Park** 499
- Oxidative Demethoxylation of Methoxylated Phenols and Hydroxybenzoic Acids by the OH Radical. An in Situ Electron Spin Resonance, Conductometric Pulse Radiolysis, and Product Analysis Study **Steen Steenken* and Peter O'Neill** 505
- Decomposition of Chloral Hydrate in Aqueous Solution by the Action of Ultrasound **Yoshiro Sakai,* Yoshihiko Sadaoka, and Yoshinori Takamaru** 509
- Warming-Induced Reactions in γ -Irradiated Naphthalene Solutions in Freon-Mixture Glass **Akira Kira,* Takashi Nakamura, and Masashi Imamura** 511
- Deuterium Isotope Effect on Hydrogen Atom Abstraction by Methyl Radicals in Acetonitrile at 77 K. Evidence for Tunneling **Estel D. Sprague** 516
- Ionic Vs. Molecular Nature of Monomeric Ammonium and Hydronium Nitrate. Infrared Spectra of $H_3O^+NO_3^-$ and $NH_4^+NO_3^-$ Solvated in Argon Matrices **G. Ritzhaupt and J. P. Devlin*** 521
- Thermodynamics of the Lithium-Lithium Deuteride System **Ewald Veleckis** 526 ■
- Thermometric Titration Studies of Ligand Binding to Macromolecules. Sodium Dodecyl Sulfate to β -Lactoglobulin **Gordon C. Kresheck,* Walter A. Hargraves, and David C. Mann** 532
- Photogalvanic Effect in the Thionine-Iron System **Tadayoshi Sakata, Yasuhiro Suda, Jiro Tanaka, and Hiroshi Tsubomura*** 537
- Thermal Variations of Rotatory Power. Conformational Equilibrium and Conformer Rotivities Determinations **Robert Lauricella, Josette Kechayan, and Hubert Bodot*** 542
- Determination of the Specific Heat Capacities of Aqueous Sodium Chloride Solutions at High Pressure with the Temperature Jump Technique **K. G. Liphard, A. Jost, and G. M. Schneider*** 547
- Study of Oxygen Isotopic Exchange over Ultraviolet Irradiated Anatase Samples and Comparison with the Photooxidation of Isobutane into Acetone **Henri Courbon, Marc Formenti, and Pierre Pichat*** 550
- Analysis of Torsional Spectra of Molecules with Two Internal C_{3v} Rotors. 3. Far-Infrared and Gas Phase Raman Spectra of Dimethylamine- d_0 , - d_3 , and - d_6 **J. R. Durig,* M. G. Griffin, and P. Groner** 554
- Selective Carbon-Hydrogen Bond Fission in Partially Deuterated 3-Methylpentane Glasses Irradiated at 77 K as Studied by Electron Spin Resonance **Takahisa Ichikawa* and Nobuaki Ohta** 560
- Utility of Pulse Nuclear Magnetic Resonance in Studying Protons in Coals **B. C. Gerstein,* C. Chow, R. G. Pembleton, and R. C. Wilson** 565
- Electron Spin Resonance Spectra of *tert*-Butyl Substituted Naphthalene Anion Radicals **Ira B. Goldberg* and Barrie M. Peake** 571
- Calculation of the Electronic Spectra of Chlorophyll *a*- and Bacteriochlorophyll *a*-Water Adducts **Lester L. Shipman* and Joseph J. Katz** 577
- The Compressibility and Electrical Conductivity of Concentrated Aqueous Calcium Nitrate Solutions to 6 kbar and 150 °C **L. Pickston, S. I. Smedley,* and G. Woodall** 581

COMMUNICATIONS TO THE EDITOR

Selective Capture of Migrating Holes by Pyrene and Naphthalene in γ -Irradiated Butyl Chloride Glasses at 77 K Akira Kira,* Takashi Nakamura, and Masashi Imamura 591

■ Supplementary and/or miniprint material for this paper is available separately (consult the masthead page for ordering information); it will also appear following the paper in the microfilm edition of this journal.

* In papers with more than one author, the asterisk indicates the name of the author to whom inquiries about the paper should be addressed.

AUTHOR INDEX

Bodot, H., 542	Hargraves, W. A., 532	Nakamura, T., 511, 591	Schaal, R., 587
Chow, C., 565	Ichikawa, T., 560	Ohta, N., 560	Schneider, G. M., 547
Courbon, H., 550	Imamura, M., 511, 591	O'Neill, P., 505	Shipman, L. L., 577
Devlin, J. P., 521	Jost, A., 547	Park, C., 499	Simonnin, M.-P., 587
Durig, J. R., 554	Katz, J. J., 577	Peake, B. M., 571	Smedley, S. I., 581
Formenti, M., 550	Kechayan, J., 542	Pembleton, R. G., 565	Sprague, E. D., 516
Gerstein, B. C., 565	Khan, T., 587	Pichat, P., 550	Steenken, S., 505
Goldberg, I. B., 571	Kira, A., 511, 591	Pickston, L., 581	Suda, Y., 537
Griffin, M. G., 554	Kresheck, G. C., 532	Ritzhaupt, G., 521	Takamaru, Y., 509
Groner, P., 554	Lauricella, R., 542	Sadaoka, Y., 509	Tanaka, J., 537
Halle, J.-C., 587	Liphard, K. G., 547	Sakai, Y., 509	Tsubomura, H., 537
	Mann, D. C., 532	Sakata, T., 537	Veleckis, E., 526
			Wilson, R. C., 565
			Woodall, G., 581

THE JOURNAL OF PHYSICAL CHEMISTRY

Registered in U. S. Patent Office © Copyright, 1977, by the American Chemical Society

VOLUME 81, NUMBER 6 MARCH 24, 1977

Reaction Rates for $O_3 + HCl \rightarrow O + O_2 + HCl$, $Cl + O_3 \rightarrow ClO + O_2$, and $HCl + O \rightarrow OH + Cl$ at Elevated Temperatures

Chul Park

Ames Research Center, National Aeronautics and Space Administration, Moffett Field, California 94035 (Received February 23, 1976; Revised Manuscript Received October 15, 1976)

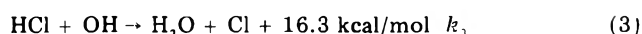
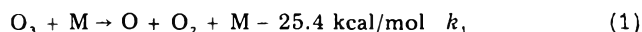
Publication costs assisted by Ames Research Center, National Aeronautics and Space Administration

A mixture of ozone and hydrogen chloride, diluted by oxygen and argon, was heated by a shock wave process in a shock tube to a temperature in the range 480–1300 K at pressures from 4 to 8 atm. From the variations in the concentration of O_3 , determined by the attenuation of 2537-Å radiation, the rate coefficient for the reaction $O_3 + HCl \rightarrow O + O_2 + HCl$ was determined to be $k_1 = (4.0 \pm 1.5) \times 10^{-10} \exp(-10,408/T) \text{ cm}^3/\text{s}$ for temperatures of 480–720 K. From the concentration of ClO remaining at the end of ozone decomposition, determined also by 2537-Å attenuation, the rate coefficients for the reactions $Cl + O_3 \rightarrow ClO + O_2$ and $HCl + O \rightarrow OH + Cl$ were deduced to be $k_4 = (1.35 \pm 0.40) \times 10^{-11}$ and $k_2 = (2.0 \pm 1.0) \times 10^{-14} \text{ cm}^3/\text{s}$, respectively, at $T \approx 1100$ K.

In an earlier work,¹ the author studied the process of ozone decomposition in O_3 - Cl_2 mixtures in a shock tube. The study yielded rates of two exchange reactions involving Cl, O, and ClO at temperatures in the range of 1000–1400 K. The present paper reports a sequel to that work and describes parallel experiments conducted with O_3 -HCl mixtures.

Kinetics of Ozone Decomposition in O_3 -HCl Mixtures

In the present work, the ozone decomposition process was studied with a mixture of ozone and hydrogen chloride. The concentration of HCl was kept always much greater than that of O_3 . The O_3 -HCl mixture was diluted by O_2 or O_2 -Ar mixture. In such a system, the concentration of HCl and O_2 can be considered unchanged during the reaction. Changes in temperature and pressure can also be neglected. As the mixture is compressed and suddenly heated behind a shock wave, ozone decomposes initially through thermal dissociation (process 1). The resulting oxygen atoms react with HCl, triggering a chain of reactions. From the known orders of magnitude of rate coefficients involved,² one expects the dominant ozone-removing reactions to be as follows:



where M is an unspecified third body. Although many other reactions can occur simultaneously with those of (1) through (5), there are several reasons why such additional reactions can be neglected in the present test conditions. For example, the reaction $O + O_3 \rightarrow O_2 + O_2$ can be neglected because the rate of O_3 removal by the process is much smaller than that by (1) and that of O removal is much smaller than that by (2).

When O_3 has disappeared completely, there remains a finite concentration of ClO. The residual ClO concentration can be related to the initial concentration of O_3 and HCl and the coefficients of the governing rates k_1 through k_5 by integrating the rate equations associated with the processes. Of the five resulting rate equations (for O_3 , O, OH, Cl, ClO), those expressing O atom and OH radical can be eliminated because, under the conditions of interest, most likely a steady state exists for these species; since the

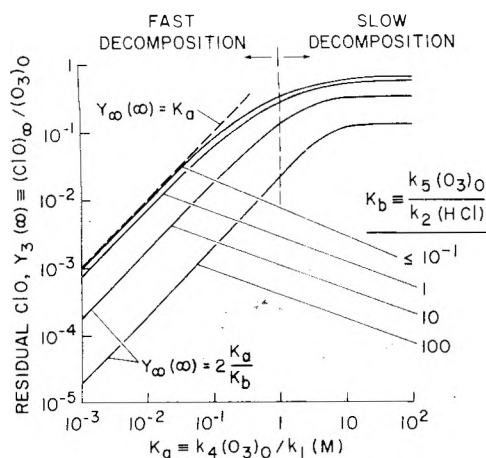


Figure 1. Residual concentration of ClO as function of K_a and K_b , obtained by numerical integration of eq 6–8.

HCl concentration is high, reactions 2 and 3 can take place so rapidly that the rates of production of O and OH can be considered balanced by their rates of removal. By expressing the remaining variables in the nondimensional form

$$Y_1 = (\text{O})/(\text{O}_3)_0, \quad Y_2 = (\text{Cl})/(\text{O}_3)_0$$

$$Y_3 = (\text{ClO})/(\text{O}_3)_0$$

$$K_a = k_4(\text{O}_3)_0/k_1(\text{M}), \quad K_b = k_5(\text{O}_3)_0/k_2(\text{HCl})$$

$$\tau = k_1(\text{M})t$$

where the subscript 0 refers to the initial condition $t = 0$, the rate equations become

$$dY_1/d\tau = -(1 + K_a Y_2)Y_1 \quad (6)$$

$$dY_2/d\tau = (1 - K_a Y_2)Y_1 + Y_1/(1 + K_b Y_3) \quad (7)$$

$$dY_3/d\tau = K_a Y_1 Y_2 - K_b Y_1 Y_3/(1 + K_b Y_3) \quad (8)$$

To obtain the residual concentration of ClO, the rate equations are integrated from $\tau = 0$ to $\tau = \infty$. The initial values are $Y_1(0) = 1$ and $Y_2(0) = Y_3(0) = 0$. Figure 1 shows the result of the numerical integration.

As Figure 1 shows, the residual ClO is a moderately strong function of K_a and K_b . Within the regime $K_a < 1$, which will be referred to hereafter as "fast decomposition", one can distinguish two different limiting regions depending on the magnitude of K_b . In the region $K_b < 1$, the solution of (6) and (8) approaches

$$Y_3(\infty) \rightarrow K_a \equiv k_4(\text{O}_3)_0/[k_1(\text{M})] \quad (9)$$

In the opposite regime, $K_b > 1$, the solution becomes

$$Y_3(\infty) \rightarrow 2K_a/K_b \equiv 2k_2k_4(\text{HCl})/[k_1k_5(\text{M})] \quad (10)$$

By measuring the concentrations of the residual ClO, therefore, information regarding the rate coefficients k_1 to k_5 can be obtained.

In the slow decomposition regime, $K_a > 1$, a different approach is necessary. Here, the Cl concentration, as well as the O and OH concentrations, is in quasi-steady state. This leads to the differential equations for O_3 and ClO of the form

$$dY_1/d\tau = -[2 + 1/(1 + K_b Y_3)]Y_1 \quad (11)$$

$$dY_3/d\tau = 2Y_1/(1 + K_b Y_3) \quad (12)$$

That is, there is an equivalent of quantum efficiency of ozone decomposition by the thermal process (1) which is initially 3 and decreases toward 2 as time progresses. By measuring the initial rate of decay of ozone, and dividing

the apparent rate coefficient by 3, one obtains k_1 . Equations 11 and 12 hold, however, only in the early portion of the decomposition process $\tau < 1$. In the later period, $\tau > 1$, processes neglected in the reaction scheme of eq 1–5 could become important. One example is a hypothetical reaction



This reaction has not yet been verified, but is energetically possible, especially at the relatively high temperatures prevailing in the present test conditions. By defining K_c by

$$K_c = k_6(\text{O}_3)_0/[k_1(\text{M})] \quad (14)$$

the differential equations become

$$dY_1/d\tau = -[2 + 1/(1 + K_b Y_3) + 2K_c Y_3]Y_1 \quad (15)$$

$$dY_3/d\tau = 2Y_1/(1 + K_b Y_3) \quad (16)$$

In the regime $\tau < 1$, Y_3 is small and hence (15) reduces to (11). When $\tau > 1$, Y_3 approaches 2/3 and (15) becomes

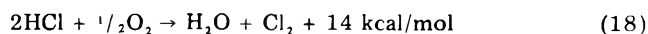
$$dY_1/d\tau \approx -(3 + 4/3 K_c)Y_1$$

That is, the equivalent quantum efficiency could become significantly larger than 3 depending on the magnitude of K_c .

The reactions discussed above are all initiated by decomposition of O_3 . In addition, O_2 could decompose via the reaction



The processes that ensue ultimately lead to combustion of HCl



accompanied by a substantial change in pressure and temperature. The rate-limiting step for this process is reaction 17, which requires reaction times much longer than are of interest here, i.e., over 1 s. Hence decomposition of O_2 and associated combustion of HCl are neglected in the present work.

In the present work, the thermal decomposition rate coefficient k_1 was determined from the initial slope of ozone decomposition. Then, through the measurement of $(\text{ClO})_\infty$, under the two different operating regimes described above, the coefficients k_4 and k_2 were deduced. The coefficients k_4 and k_2 were determined from the test data using a scheme involving a computer calculation rather than using Figure 1, although Figure 1 is conceptually correct and useful in showing in what regime a rate measurement should be conducted, it is numerically inaccurate, by up to about $\pm 20\%$ in the present work, because the reverse reactions are neglected. To derive more accurate relationships between the rate coefficient values and $(\text{ClO})_\infty$, a family of theoretical curves (of the same format as the test data) was generated with the computer by integrating the rate equations for O_3 , O, Cl, ClO, and OH with k_2 and k_4 as variable parameters, allowing for the reverse reactions and without invoking the quasi-steady-state assumption. In the calculation, internal modes are assumed to be fully excited but temperature and pressure relax toward the equilibrium values (see section of Test Results. Thermal Decomposition Rates). The theoretical curves were then compared with the experimental data; through a process of trial and error the curve that most closely matched the data was then selected.

Experimental Design

The basic experimental setup and test procedures are described in ref 1. The only significant difference between

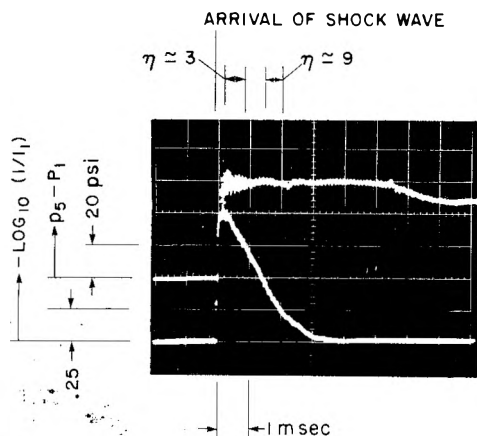


Figure 2. Typical oscillograph trace showing end-wall pressure p_5 and attenuation of 2537 Å in a slow decomposition: $p_1 = 507$ Torr; O₃:O₂:HCl = 0.07:2.93:97; $U_s = 490$ m/s; $p_5 = 4.43$ atm; $T_5 = 531$ K.

the present and the previous work concerns hydrogen chloride. The electronic grade (99.999%) hydrogen chloride was used as a test gas here. The test gases were charged into the driven section through a monel dispersing tube. The three gases, O₃ + O₂ mixture, HCl, and argon, were charged into the driven section in various different sequences. No difference was observed in the test results.

Test Results. Thermal Decomposition Rates

Figure 2 is a typical oscillograph record taken in a slow decomposition experiment. The upper trace in the picture shows the end-wall pressure and the lower trace is for the attenuation of 2537-Å radiation. As seen here, the end-wall pressure stays constant, at least over the duration of the decomposition process. The attenuation trace deflects abruptly in two steps: once when the primary shock wave crosses the optical path and again when the reflected shock crosses the optical path. The sudden increases in attenuation are due to shock compression of ozone. After the second compression, the level of attenuation stays nearly constant for a short while. This is believed to correspond to the incubation period in which electronic and vibrational excitations of ozone take place. Thermal decomposition occurs after the incubation period is passed. In the slow decomposition process, attenuation of radiation is at first principally due to ozone because ozone is the only species in large enough concentration here. However, toward the end (later than 2.5 ms after the shock arrival in the case shown) the ClO concentration reaches a level large enough to affect the net attenuation. Since the trace is a logarithm of attenuation, deflection is directly proportional to the concentration of the absorbing species.

The temperature and pressure indicated for Figure 2 are the "excited-frozen" values, i.e., the values reached after the internal degrees of freedom are fully excited but chemical compositions are the same as ahead of shock wave. These values are chosen in the present work, as well as in ref 1, as the prevailing parameters because, as mentioned earlier, all reactions of concern occur within an early period during which the two parameters remain virtually unchanged. Computer calculations involving 14 species (O, H, Cl, O₂, H₂, Cl₂, HCl, OH, ClO, O₃, OClO, ClOO, H₂O, and HO₂) reveal that the equilibrium state reached by the mixture is generally at a slightly (i.e., by 30 K) higher temperature and a lower (by 0.2 atm) pressure than indicated here, presumably because of the processes involving (17) and (18).

From the attenuation level observed prior to the shock arrival, the absolute ozone concentration in the test gas

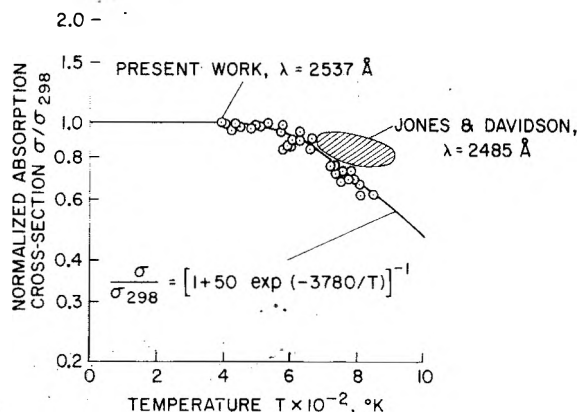


Figure 3. Absorption cross section of 2537 Å in ozone.

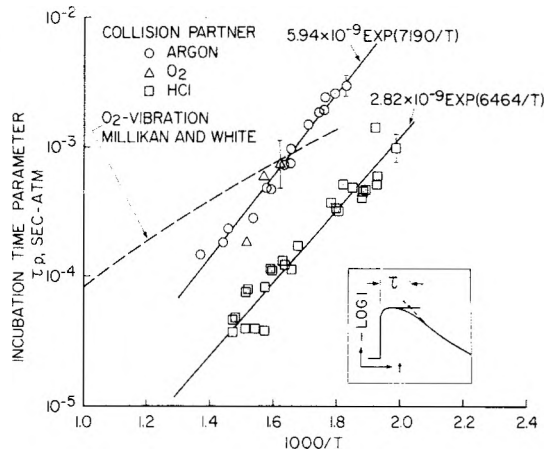


Figure 4. Time for incubation of O₃ preceding thermal decomposition as determined by 2537-Å attenuation.

was determined. The value of absorption cross section, at room temperature, was taken to be $\sigma_{298} = 1.148 \times 10^{-17}$ cm² for this purpose. From the deflection of the attenuation trace during the incubation period immediately after the shock arrival, one can deduce the absorption cross section of ozone at elevated temperature. The cross-section measurement is facilitated by operating at low pressures (e.g., reflected shock pressures of 1.5 to 3 atm in the present work) because the incubation period becomes longer at low pressures. Figure 3 shows the values of the absorption cross section determined by this method, normalized by the room temperature value. The present data are compared with those obtained by Jones and Davidson³ at 2485 Å. As seen here, two results are comparable. The present results can be approximated by

$$\sigma/\sigma_{298} = 1/[1 + 50 \exp(-3780/T)]$$

Figure 4 shows the lengths of incubation time τ preceding thermal decomposition, determined using 2537-Å attenuation, as a function of temperature with argon, O₂, and HCl as collision partners. The time τ is defined as shown in the inset. Vibrational relaxation times of O₂ given by Mullikan and White⁶ are shown also for comparison. As seen in the figure, HCl is 5 to 10 times more efficient as a collision partner compared with argon or O₂ in the range of temperatures tested. The present data values for O₂ and argon are of the same order of magnitude as for O₂ vibrational relaxation, leading one to speculate that the incubation mainly involves vibrational relaxation of O₃. For argon or O₂ as a collision partner, the test results can be represented approximately by

$$\tau p = (5.9 \pm 2.5) \times 10^{-9} \exp(7190/T) \text{ s atm (O}_2\text{-Ar)}$$

TABLE I: Experimental Results on Coefficients of Thermal Decomposition Rate of Ozone, $O_3 + M \rightarrow O + O_2 + M$

M	P_s , atm	T_s , K	$10^{-16} (O_3)_0$, cm^{-3}	$\log k_1$	M	P_s , atm	T_s , K	$10^{-16} (O_3)_0$, cm^{-3}	$\log k_1$
Ar	4.44	541	3.35	-18.51	HCl	3.64	478	3.86	-18.81
	4.55	566	3.78	-18.01		3.63	483	3.79	-18.73
	4.55	567	3.37	-17.99		3.78	498	3.86	-18.45
	4.39	570	4.16	-18.02		3.91	503	3.91	-18.23
	4.63	584	3.04	-17.82		4.14	511	2.73	-17.90
	4.56	603	3.24	-17.69		4.09	516	6.69	-18.15
	5.29	604	3.46	-17.57		1.97	521		-18.21
	6.64	630	3.80	-17.12		3.83	529	4.19	-17.74
	6.85	633	4.03	-17.07		4.43	531	4.18	-17.73
	6.70	634	3.62	-17.18		2.18	540	2.10	-18.00
	2.56	637	1.38	-17.03		3.60	544	4.73	-17.67
	6.58	651	4.34	-16.94		4.75	549	4.53	-17.67
	2.44	671	1.44	-16.77		4.10	554	4.55	-17.33
	6.58	694	4.05	-16.34		1.90	556	2.20	-17.73
	6.38	710	4.05	-16.36		3.77	561	4.36	-17.40
	5.29	712	4.17	-16.35		4.00	596	5.07	-17.11
	2.55	742	1.46	-16.06		3.74	605	4.45	-16.73
	5.13	596	5.84	-17.43		3.47	610	5.38	-16.81
	2.50	610	5.58	-17.19		3.68	614	4.67	-16.74
	5.49	617	4.60	-17.11		2.78	628	5.69	-16.47
5.37	634	4.22	-16.92	3.31	637	5.75	-16.51		
5.23	640	5.66	-16.96	1.99	658	3.46	-16.27		
4.93	641	4.82	-16.84	4.30	660	6.27	-16.46		
4.59	654	5.53	-16.58	3.78	663	4.26	-16.44		
4.69	655	4.81	-16.63	3.44	665	0.89	-15.94		
4.95	669	4.62	-16.52	3.57	677	1.93	-16.04		
4.36	696	6.10	-15.99	3.70	678	6.23	-16.22		
4.93	703	4.62	-16.05	3.54	679	5.99	-16.10		
4.53	734	5.03	-15.91	1.55	709	2.62	-15.68		
5.02	773	4.09	-15.45						
4.53	806	6.20	-15.27						

while for HCl, the best fit is

$$\tau p = (2.8 \pm 1) \times 10^{-9} \exp(6464/T) \text{ s atm (HCl)}$$

To test the accuracy of the present experimental procedure for determining k_1 , tests were conducted first with argon and oxygen as the main bath gas. The results of this series of tests are shown in Figure 5 and Table I. The rate coefficient values are shown in Figure 5 normalized by efficiency factors⁴ of 0.25 for argon and 0.44 for oxygen. The present results are in excellent agreement with those of Jones and Davidson³ and of Garvin,⁵ when their nitrogen data are normalized by the nitrogen efficiency factor⁴ of 0.39.

In the test run shown in Figure 2, the conditions were such that the reactions 2 and 3 drove O and OH concentrations into quasi-steady-state values within the first few microseconds. Hence the assumption that the equivalent quantum efficiency equals 3 would be valid from as early as the photograph can resolve. One notices, however, that the attenuation profile is not that of an exponential decay, in which slope should decrease monotonically with time. Instead, the slope becomes steeper as time passes and reaches a peak at about 1.5 ms at which point the apparent quantum efficiency is 9. One concludes, therefore, that there are reactions that are unaccounted for in the scheme 1-5, for example, that expressed by (13), in the later period. If the unidentified additional ozone removal mechanism is that expressed by (13), the rate coefficient k_6 for the reaction should be $k_6 = 1.2 \times 10^{-14} \text{ cm}^3/\text{s}$ to be consistent with the assumed mechanism. The k_6 value is within the range possible at the prevailing temperature.

The thermal decomposition rate k_1 for HCl was obtained by dividing the initial slope of ozone decay by the theoretical quantum efficiency value of 3. The results are shown in Figure 6 and Table I. There are no data in the literature with which to compare the present values. Since

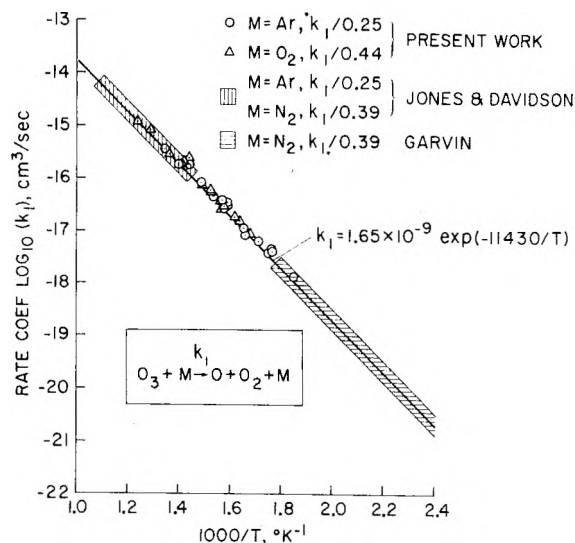


Figure 5. Rate coefficient for thermal decomposition of ozone with oxygen and argon as collision partners.

the standard deviation of the data from the mean is about 35%, the results in Figure 6 can be represented by

$$k_1 = (4.0 \pm 1.5) \times 10^{-10} \exp(-10408/T) \text{ cm}^3/\text{s} \text{ (M = HCl)}$$

Alternatively, an error limit can be assigned to the slope, in the form

$$k_1 = 4 \times 10^{-10} \exp(-10408/T) \exp[\pm 350(1/T - 1/550)] \text{ cm}^3/\text{s} \text{ (M = HCl)}$$

that is, with an uncertainty in activation energy of ± 700 cal/mol. The uncertainty can be attributed in this case mostly to that in reading the slope in the oscillograph; unlike argon-rich or oxygen-rich mixtures, an HCl-mixture

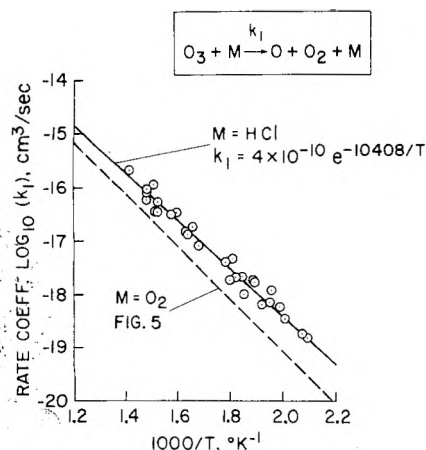


Figure 6. Rate coefficient for thermal decomposition of ozone with HCl as collision partner.

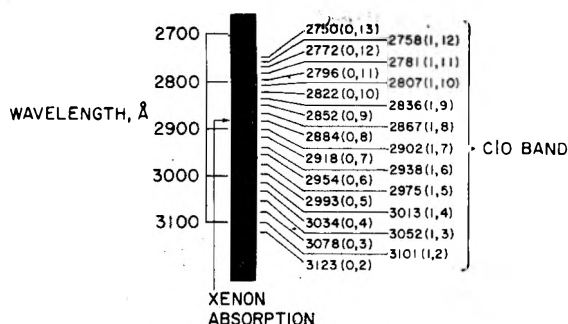


Figure 7. Absorption spectra of mixture of HCl, O₃, and O₂ behind reflected shock: $p_1 = 100$ Torr; O₃:O₂:HCl = 1:61:38; $U_s = 960$ m/s; $p_5 = 7.6$ atm; $T_5 = 1180$ K; O₃ and ClO in nonequilibrium.

produces a trace with a slope that varies nonmonotonically, as illustrated in Figure 2. The k_1 values for HCl are greater than those for oxygen, nitrogen, or argon. The activation energy for HCl is less than that for argon, oxygen, and nitrogen by approximately 2 ± 0.7 kcal/mol. The reason for these differences is presently unknown.

Test Results. Exchange Reactions

Before undertaking the quantitative measurements of exchange rates, the compositions of the gas samples behind the reflected shock wave were studied qualitatively by means of absorption spectroscopy.¹ Figure 7 shows the absorption spectra for the wavelength range of 2700–3100 Å taken under a condition qualitatively the same as that in the main tests; that is, a mixture of HCl, oxygen, and ozone undergoing reactions behind a reflected shock wave. For the test, the width of the entrance slit of the spectrograph was set at 25 μ m, which corresponds to an effective spectral bandwidth of 0.28 Å. The film was a Tri-X Panchromatic, and was developed by D-19 developer for 5 min at 30 °C. The flash tube discharge was initiated 10 μ s after the reflected shock passed the optical axis, and lasted approximately 2 μ s (see ref 1). The photograph shows a strong ClO band as expected.

In order to determine the concentration of ClO from the measured attenuation of 2537-Å radiation, one needs to know the absorption cross section of ClO at the prevailing temperature. The ClO absorption cross section values were obtained by the author in a previous work¹ for temperatures ranging up to 2200 K as

$$\sigma = (1 - e^{-1236/T}) \sum_{v=0}^7 \sigma_v e^{-1236v/T}$$

$$\sigma_v = (4.35 - 0.55v) \times 10^{-18} \text{ cm}^2$$

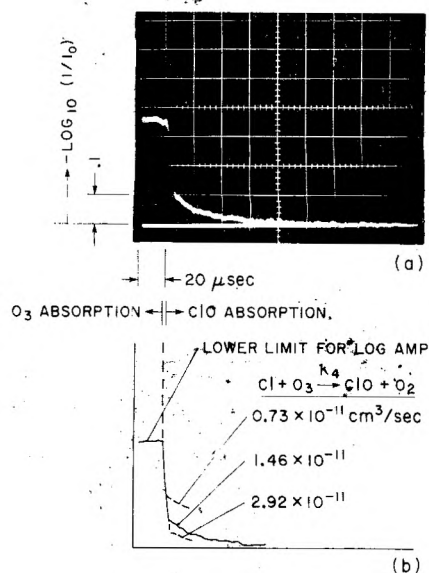


Figure 8. Typical oscillograph trace showing attenuation of 2537 Å in fast decomposition of ozone: $p_1 = 253$ Torr; O₃:O₂:HCl:Ar = 0.019:19.5:10:70.5; $U_s = 758$ m/s; $p_5 = 8.87$ atm; $T_5 = 1147$ K.

Figure 8a shows a typical oscillograph trace taken during a fast decomposition experiment. Figure 8b shows how the trace was interpreted. Sweep of the oscillograph trace was initiated at the instant of arrival of the primary shock wave at the end-wall.

Approximately 10 μ s after the initiation of the sweep, the reflected-shock crosses the optical axis, and the reactions under observation commence. The trace does not show the true variation in 2537-Å attenuation until at about $t \approx 20$ μ s because attenuation signal is out of the operation range of the logarithmic amplifier for the case shown. As shown in the photograph, attenuation of 2537-Å radiation is due almost entirely to ozone up to about $t \approx 28$ μ s; after that it is due to ClO. The level of attenuation attained at about $t \approx 28$ μ s thus indicates the ClO concentration, at the end of thermal decomposition, (ClO)_∞, that is plotted in the ordinate of Figure 1. At the conditions under which the test of Figure 8 was made, the parameters K_a and K_b were approximately 0.2 and 0.3, respectively, satisfying the conditions necessary for (ClO)_∞ to be inversely proportional to the rate coefficient k_4 (see Figure 1). ClO concentration decays in the region $\tau > 30$ μ s mainly by the reaction¹ ClO + ClO → Cl + ClO/Cl₂ + O₂.

The concentrations of ozone at $t = 0$ (immediately behind the reflected shock wave), which must also be known in order to determine the desired rate coefficient values, were calculated from the initial ozone concentration (prior to the arrival of the primary shock) using the Rankine-Hugoniot relation. The rate coefficient k_4 was then determined using a computer program through the trial and error procedure described earlier. The procedure yields the ratio $K_a = k_4(O_3)_0/k_1(M)$ where $k_1(M)$ represents, in this case, for the net thermal dissociation rate, that is, the sum of contributions from all species present. Since the third body M consists in this case mostly of argon, for which the rate coefficient is accurately known (see Figure 5), $k_1(M)$ can be considered as known. Therefore, the tests can be considered to yield the value of k_4 directly. Figure 8b illustrates how the (ClO)_∞ value is affected by k_4 . Figure 9 summarizes the k_4 values determined by the present procedure and compare them with the available data.⁷⁻¹⁰ The figure shows a scattering in data of about 15%. The scatter can be attributed mostly to the error in reading an absolute deflection of an

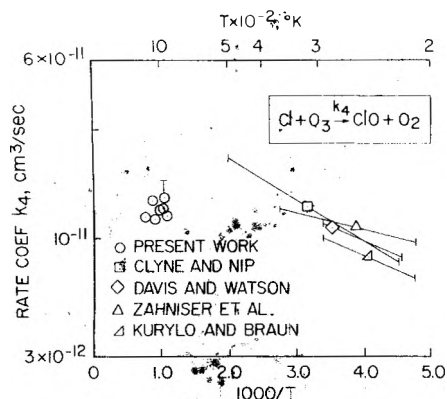


Figure 9. Experimental results on rate coefficients for $\text{Cl} + \text{O}_3 \rightarrow \text{ClO} + \text{O}_2$.

oscillograph trace. Allowing for the possible uncertainty of up to 15% in $k_1(M)$, the measured k_4 can be expressed as

$$k_4 = (1.35 \pm 0.40) \times 10^{-11} \text{ cm}^3/\text{s}$$

for temperatures of 930–1310 K. As seen in the figure, the present data cover a temperature range at least a factor of 2 larger than has been. The present results give generally lower rate coefficient values than would be obtained by straight-line extrapolation of the existing data. Exact cause of this phenomenon is presently unknown. One can speculate, however, that the rate coefficient is indeed constant at high temperatures, i.e., above around 500 K; a fast reaction such as the one under study can easily reach a collision limit at such a temperature.

The rate coefficient k_2 for the reaction $\text{HCl} + \text{O} \rightarrow \text{OH} + \text{Cl}$ was obtained similarly from the $(\text{ClO})_\infty$ value by conducting the experiment in the regime $K_b > 1$. As indicated by eq 10, the measurement should yield the ratio $(k_2/k_5)(k_4/k_1)$. Here the ratio k_4/k_1 is known from the previous experiment to within a reading error. Using the value of k_5 obtained by the author earlier,¹ k_2 values were deduced again through the use of a computer. The results are plotted in Figure 10.

As seen in the figure, the present results show the rate coefficient to be approximately $2 \times 10^{-14} \text{ cm}^3/\text{s}$ at $T \approx 1050 \text{ K}$. Considering that k_5 is uncertain, perhaps by as much as 25%, and the ratio k_4/k_1 by as much as 15%, the measured k_2 value should be expressed with an error limit as

$$k_2 = (2.0 \pm 1.0) \times 10^{-14} \text{ cm}^3/\text{s}$$

at $T = 1050 \pm 150 \text{ K}$. Shown also in the figure are the existing rate value data^{11,12} for lower temperature regimes. The present data seem to be in closer agreement with the data of Balakhnin et al. than with those of Wong and Belles, when one allows for a possibility that activation energy may change between temperatures of 400 and 1000

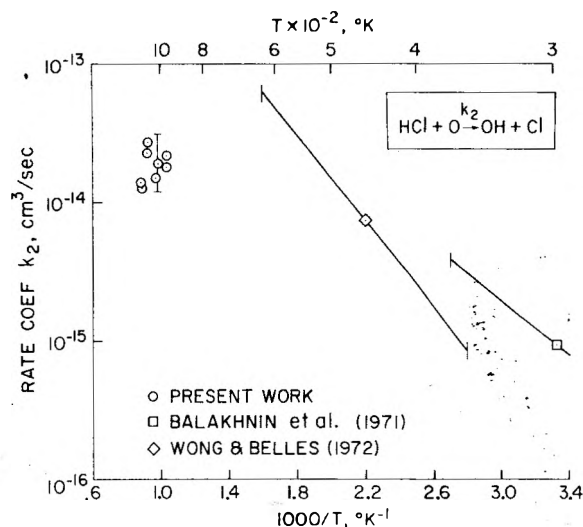


Figure 10. Experimental results on rate coefficients for $\text{HCl} + \text{O} \rightarrow \text{OH} + \text{Cl}$.

K. There is a significant discrepancy between the results of Wong and Belles and the other two sets of data. This discrepancy is yet unexplained although one could make various speculations; for example, the discrepancy could be attributed to an effect of excited atomic oxygen. In any event, the discrepancy needs to be resolved in a future study.

Conclusions

At pressures in the range of 4–8 atm and at temperatures between 480 and 1300 K the rate coefficients of the reaction $\text{O}_3 + \text{HCl} \rightarrow \text{O} + \text{O}_2 + \text{HCl}$ are determined as $k_1 = (4.0 \pm 1.5) \times 10^{-10} \exp(-10408/T) \text{ cm}^3/\text{s}$. In the same range of pressures, the rate coefficients of the reactions $\text{Cl} + \text{O}_3 \rightarrow \text{ClO} + \text{O}_2$ and $\text{HCl} + \text{O} \rightarrow \text{OH} + \text{Cl}$ are found to be $k_4 = (1.35 \pm 0.40) \times 10^{-11}$ and $k_2 = (2.0 \pm 1.0) \times 10^{-14} \text{ cm}^3/\text{s}$, respectively, at $T \approx 1100 \text{ K}$.

References and Notes

- (1) C. Park, *J. Phys. Chem.*, **80**, 565 (1976).
- (2) R. T. Watson, "Chemical Kinetics Data Survey, VIII, Rate Constants of ClO_2 of Atmospheric Interest", NBSIR 74-516, National Bureau of Standards, Washington, D. C.
- (3) W. M. Jones and N. Davidson, *J. Am. Chem. Soc.*, **68**, 2868 (1962).
- (4) H. S. Johnston, *Natl. Stand. Ref. Data Ser., Natl. Bur. Stand.*, **No. 20** (1968).
- (5) D. Garvin, *J. Am. Chem. Soc.*, **76**, 1523 (1954).
- (6) R. C. Millikan and D. R. White, *J. Chem. Phys.*, **39**, 3209 (1963).
- (7) D. D. Davis and R. T. Watson, Abstract of paper presented at 4th International Symposium on Gas Kinetics, Edinburgh, 1975.
- (8) M. S. Zahniser, F. Kaufman, and J. G. Anderson, *Chem. Phys. Lett.*, **37**, 226 (1976).
- (9) M. J. Kurylo and W. Braun, *Chem. Phys. Lett.*, **37**, 232 (1976).
- (10) M. A. A. Clyne and W. S. Nip, *J. Chem. Soc., Faraday Trans. 2*, **72**, 838 (1976).
- (11) V. P. Balakhnin, V. I. Egorov, and E. I. Intezarova, *Kinet. Catal.*, **12**, 258 (1971). Translation from *Kinet. Catal.*, **12**, 299 (1971).
- (12) E. L. Wong and F. E. Belles, *NASA Tech. Note*, **D-6495** (1972).

Oxidative Demethoxylation of Methoxylated Phenols and Hydroxybenzoic Acids by the OH Radical. An in Situ Electron Spin Resonance, Conductometric Pulse Radiolysis, and Product Analysis Study

Steen Steenken* and Peter O'Neill

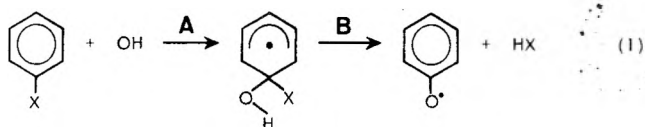
Institut für Strahlenchemie im Max-Planck-Institut für Kohlenforschung, Stiftstrasse 34-36, D-4330 Mulheim, West Germany (Received October 4, 1976)

Publication costs assisted by Institut für Strahlenchemie im Max-Planck-Institut für Kohlenforschung

OH radicals react with methoxylated phenols and methoxylated hydroxybenzoic acids by attachment to ring positions occupied by methoxyl groups (*ipso* attack) in addition to attachment to other positions. The OH radical adds preferentially to those ring positions which are activated by the electron-donating OH or OCH₃ groups. The radicals formed by addition of OH to ring carbons carrying methoxyl groups eliminate methanol to yield semiquinones ($k \approx 10^3\text{--}10^4 \text{ s}^{-1}$).

Introduction

With benzene derivatives, oxidative replacement of substituents X by the OH radical as shown in reaction 1.



has been observed for X = F,¹ NO₂,² and NH₂.³ The formation of chloride⁴ on irradiation of chlorobenzene in aqueous solution probably proceeds by this mechanism as well. Reaction 1 has also been discussed for X = OH⁵ or OCH₃,⁶ although it could not be unambiguously demonstrated to occur. Step 1B is of the 1,1-elimination type which has been observed also with radicals derived from halo,⁷⁻⁹ and nitrofurans,¹⁰ nitro- and bromofurans,¹¹ and chloroethylenes.¹²

From pulse radiolysis studies on radical cation¹³ and zwitterion¹⁴ formation by reaction of OH in acid solution with methoxylated benzenes and benzoic acids, respectively, evidence was obtained^{14,15} for the involvement of reaction 1 with X = OCH₃. The present investigation was performed in order to study this type of reaction in detail using methoxylated phenols and hydroxybenzoic acids.

Experimental Section

N₂O saturated aqueous solutions containing 5–10 mM substrate were irradiated with ⁶⁰Co γ-rays using doses from 4.8 × 10¹⁸ to 2.4 × 10¹⁹ eV mL⁻¹ at a dose rate of 8.1 × 10¹⁷ eV mL⁻¹ min⁻¹. Samples (10 μL) of the irradiated solutions were analyzed for methanol by gas chromatography using the double column technique with back-flushing¹⁶ (pre-column: length 1.5 m, packed with 10% Marlophen on Teflon; main column: length 3 m, packed with P 4000; both columns were operated at 85 °C). The detection limit corresponded to ~0.05 mM methanol.

The 3-MeV van de Graaff accelerator and the optical and conductivity detection systems have been described.^{17,18} Solutions were irradiated at 20 ± 2 °C with electron pulses of 1 μs duration. The pH of the solutions was adjusted using HClO₄ or NaOH. Dosimetry was performed using either 10 mM FeSO₄ in 0.8 N H₂SO₄ or C(NO₂)₄.¹⁹

The in situ radiolysis ESR experiments were carried out using the method described by Eiben and Fessenden.²⁰

The coupling constants and *g* factors were determined as described^{13,21} and are estimated to be accurate to 30 mG and 5 × 10⁻⁵, respectively.

The substrates were obtained from Fluka or Aldrich. They were of the highest purity available and were used as received with the exception of 2,6-dimethoxyphenol, which was zone refined prior to use.

Results and Discussion

Production of Methanol. On ⁶⁰Co γ-irradiation of N₂O saturated 5–10 mM solutions of 2-, 3-, or 4-methoxyphenol (MP), 2,3-, 2,6-, or 3,5-dimethoxyphenol (DMP), 2-hydroxy-5-methoxybenzoic acid (5-methoxysalicylic acid), 3-methoxy-4-hydroxybenzoic acid (vanillic acid), or 3,5-dimethoxy-4-hydroxybenzoic acid (syringa acid) at pH 3–7, methanol is formed as a reaction product. The concentration of methanol in irradiated substrate solutions is linearly dependent on dose in the range 4.8 × 10¹⁸–(1.2–2.4)10¹⁹ eV mL⁻¹. At the highest dose the removal of substrate corresponds to <25%. The yields of methanol determined from plots of concentration of methanol vs. dose are presented in Table I. It is evident from Table I that the yields of methanol are high when there is an ortho or para relation between a hydroxyl and a methoxyl group whereas the yields are low in cases where these groups are meta to one another.

ESR Studies. On in situ electron irradiation of N₂O saturated 1 mM solutions of 2- and 4-MP, of 2,3- and 2,6-DMP, and of the methoxylated hydroxybenzoic acids at pH 5–11, phenoxyl and semiquinone anion radicals were observed (Figure 1). The ESR parameters of a number of these radicals have been reported.^{3,22} The phenoxyls are formally derived from the substrates by loss of the phenolic H, whereas the semiquinones formed are characterized by exchange of one methoxyl group by -O· (Table II). With 2,3-DMP and 5-methoxysalicylic acid at low flow rates (~0.5 mL s⁻¹) relatively weak lines from additional semiquinone anions were detected. These radicals are possibly formed, as secondary products, by a mechanism analogous to that described³ for other phenols. With 3-MP and 3,5-DMP only phenoxyl radicals, derived from the substrates by removal of the phenolic H's, were observed. There was no indication of substitution of -O· for a methoxyl group. This is in agreement with the low yields of methanol obtained on γ irradiation from these compounds which are characterized by a meta relation between the

TABLE I: Yields^a of Methanol and Benzosemiquinones Produced on Irradiation of N₂O Saturated Solutions of Methoxylated Phenols and Hydroxybenzoic Acids at 20 ± 2 °C

Substrate	G(CH ₃ OH)/G(OH), ^b %		G(SQ)/G(OH), ^c %	G(SQ) ₀ /G(OH), ^d %
	pH 3	pH 7		
2-MP	18 ± 2.7	16 ± 2.4	8	19 ± 1.9
3-MP	<5	<5	3 ^e	6 ± 0.6
4-MP	25 ± 3.8	22 ± 3.3	13	27 ± 2.7
2,3-DMP	24 ± 3.6	22 ± 3.3	10	25 ± 2.5
2,6-DMP	27 ± 4.0	24 ± 3.6	6	25 ± 2.5
3,5-DMP	7 ± 1.0	8 ± 1.2	3 ^e	6 ± 0.6
5-Methoxysalicylic acid	22 ± 3.3	16 ± 2.4		
Vanillic acid	13 ± 2.0	18 ± 2.7		
Syringa acid	25 ± 3.8	27 ± 4.0		

^a The yields are expressed as ratios of G values. The G value defines the number of molecules produced per 100 eV of absorbed radiation. G(OH) = 5.5. ^b Obtained from ⁶⁰Co γ radiolysis. ^c Measured using ~600 rads/pulse at pH 5-6. ^d Obtained by extrapolating to zero dose rate using eq 3. ^e Measured at pH > 6 and corrected for 100% dissociation of *m*-hydroxyphenoxyl radical.

TABLE II: Coupling Constants (in Gauss) and g Factors of Semiquinone Radical Anions in Aqueous Solution at ~5 °C

SUBSTRATE					
2-MP; 2-Ethoxyphenol	4-MP; 4-Benzyloxyphenol; Thyronine	2,3-DMP; 2,6-DMP	Vanillic acid	5-Methoxysalicylic acid	Syringa acid
2.00454 ^{a)}	2.00457 ^{a)}	2.00464	2.00473 ^{a)}	2.00469 ^{a)}	2.00479
		2.00453 ^{b)}		2.00459 ^{c)}	

^a Nearly identical parameters are reported by ref 3. ^b Secondary radical, observed only in the case of 2,3-DMP. ^c Secondary radical.

hydroxyl and methoxyl groups(s).

2,3- and 2,6-DMP yield the same radical, the *o*-methoxy-*o*-semiquinone radical anion, with about the same yield, which demonstrates that in the reaction of OH with 2,3-DMP the methoxyl group at the 2 position is replaced preferentially. This position is doubly activated: by the OH group at C₁ and by the methoxyl group at C₃ (see below).

Three additional compounds were studied by ESR, using N₂O saturated 1 mM solutions at pH 6-10: On the situ irradiation of 2-ethoxyphenol strong lines from the *o*-semiquinone radical anion were observed and ethanol was isolated as a reaction product. On irradiation of 4-benzyloxyphenol and of thyronine (4-(4'-hydroxyphenoxy)phenylalanine) the *p*-semiquinone radical anion was produced.

Proposed Reaction Mechanism. The experimental results are explained in terms of two processes: (a) Addition of OH to ring carbons not carrying methoxyl groups leads to formation of phenoxyl radicals via²³ elimination of H₂O from the OH adducts. This reaction will be described in detail elsewhere.²⁴ (b) Addition of OH to ring

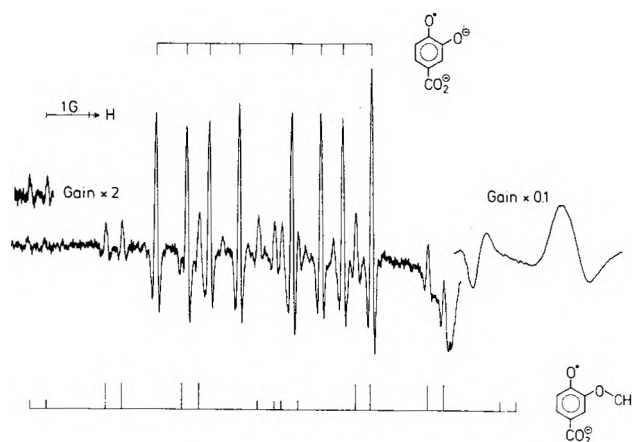
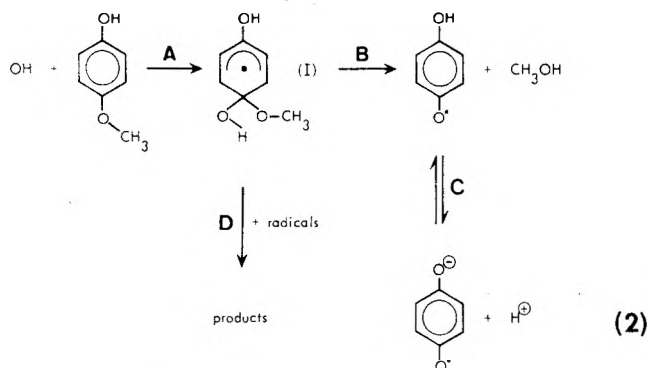


Figure 1. Second derivative ESR spectrum obtained on radiolysis of a N₂O saturated 1 mM solution of vanillic acid at pH 9.5 and ~5 °C.

positions occupied by methoxyl groups leads to OH adducts which may decay by elimination of methanol to yield semiquinone radicals, e.g.



Processes (a) and (b) account²⁴ for removal of >90% of the OH radicals.

Oxidative replacement reactions analogous to (2) have previously been reported^{1-3,7,12} or discussed.^{5,6,14} The difference in the degree of demethoxylation of substrates with methoxyl groups meta to the OH group on the one hand and those characterized by methoxyl groups ortho or para to the OH groups on the other is attributed to preferential addition of the electrophilic²⁵ OH radical to those ring positions which are activated by the ortho-para directing OH or methoxyl groups. With the former class of compounds (meta methoxylated phenols) none of the activated positions carry methoxyl substituents whereas with the latter group (ortho or para methoxylated phenols) the activated positions include those occupied by methoxyl groups. From the difference in the yields of methanol from 3-MP and 3,5-DMP on the one hand and those from 2- and 4-MP and 2,3- and 2,6-DMP on the other it may be estimated that the rate of OH attachment to activated positions exceeds that to nonactivated positions by a factor ~4. Similar conclusions have recently been drawn¹⁵ concerning the reactivity of OH with methoxylated benzenes and benzoic acids.

Conductivity Measurements. The semiquinones formed in reaction 2 should result in changes in conductivity of the methoxyphenol solutions after pulse irradiation. These conductivity changes should mainly be due to H⁺ produced by deprotonation of the semiquinone formed (steps B and C). No conducting species result from the formation of phenoxy radicals, produced²⁴ by H₂O elimination from those OH adducts where OH is attached to ring carbons not occupied by a methoxyl group. By conductivity it should therefore be possible to determine the yields of semiquinones formed in reaction 2 provided pK_a(substrate) > pH(solution) ≥ pK_a(semiquinone).

(a) 2- and 4-MP and 2,3- and 2,6-DMP. On pulse irradiation (~600 rads/pulse) of N₂O saturated 0.2 mM solutions of 2- or 4-MP or of 2,3- or 2,6-DMP at pH 5-6 changes in conductivity were observed after the pulse as shown in Figure 2. The initial conductivity change after the pulse is due to the neutralization reaction between H⁺ and OH⁻, produced during the pulse. The increase of conductivity observed after 50-100 μs is attributed to formation of H⁺ and semiquinone radical anion in steps B and C, eq 2.

The *G* values for formation of semiquinone were calculated from the maximum increase of conductivity at 50-100 μs after the pulse using μ(H⁺) = 3.62 × 10⁻³ V⁻¹ cm² s⁻¹ and μ(semiquinone) = 3.3 × 10⁻⁴ V⁻¹ cm² s⁻¹. The *G* values thus obtained (second column of Table I) are a factor ~2 smaller than the *G* values for production of methanol by γ radiolysis. A discrepancy of this kind is expected if step B is too slow to prevent bimolecular decay of OH adduct I (step D) from being important. Since step D is a bimolecular reaction, its rate depends on the

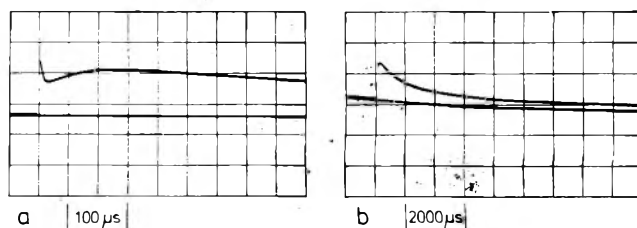


Figure 2. Changes observed in the conductivity of a N₂O saturated 2 mM solution of 2,3-DMP on irradiating with a pulse of ~600 rads: (a) sweep 50 μs/division; (b) sweep 1 ms/division.

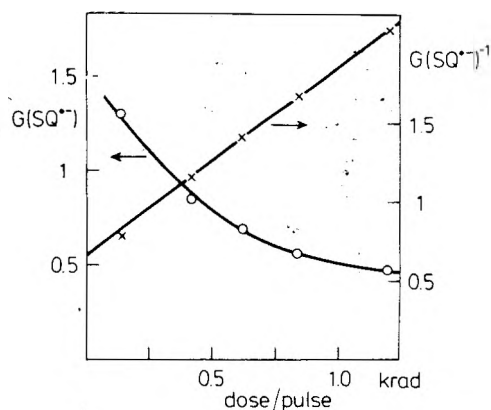


Figure 3. Dependence of maximum conductivity increase at 50-100 μs after the pulse on dose/pulse for N₂O saturated 2 mM 4-MP at pH 6 (O). Data plotted according to eq 3 (X).

concentrations of the reactants (i.e., dose rate), whereas the rate of step B, which is a unimolecular reaction, is independent of dose rate. Differences in dose rate therefore result in differences in the relative contributions of steps B and D to the reaction products. Under conditions of high initial radical concentrations as produced in pulse radiolysis, step D is of greater importance than in γ radiolysis, where dose rates are typically a factor of ~10⁶ lower.

From reaction 2, the following expression is obtained for the dependence of *G*(semiquinone) on dose rate, expressed in terms of krad/μs

$$\frac{1}{G(\text{SQ})} = \frac{1}{G(\text{SQ})_0} + \frac{k_D \times \text{dose rate}}{k_B} f \quad (3)$$

where *G*(SQ) and *G*(SQ)₀ are the yields of semiquinone for finite and zero dose rates, respectively, and *k_B* and *k_D* are the first- and second-order rate constants, respectively, for steps B and D. *f* = 1.04 × 10⁻⁶ *t_p* *G*(OH)/*G*(SQ)₀ where *t_p* is the pulse length in microseconds. *G*(SQ)₀ can be determined from the intercept of a plot of *G*(SQ)⁻¹ vs. dose/pulse (Figure 3). The *G*(SQ)₀ values thus obtained are presented in column 5 of Table I; within experimental error they are in agreement with the methanol yields from ⁶⁰Co γ irradiations for which step D is slow as compared to step B.

Due to overlap between the conductivity changes from the neutralization reaction H⁺ + OH⁻ and those from step 2B (Figure 2), it was not possible to accurately determine the rate of formation of semiquinones from OH adduct I (step B). However, from the time scale over which the conductivity changes occur, the rate constant for this process is estimated to be 10³-10⁴ s⁻¹ at pH 5-6. The same order of magnitude for *k_B* is obtained from the slope of plots similar to that shown in Figure 3 if a value of 2 × 10⁹ M⁻¹ s⁻¹ is used for *k_D*. From measurements at pH 4-5, there is qualitative evidence that the rate of step B in-

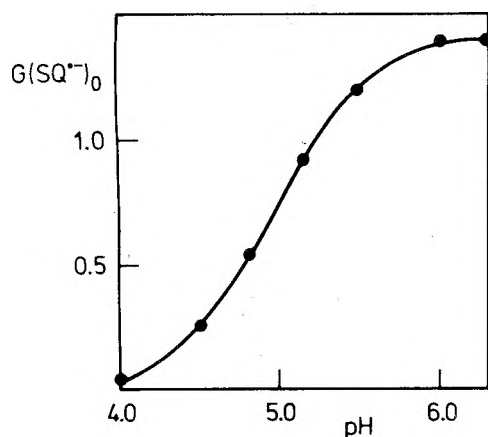


Figure 4. Dependence of $G(\text{SQ}^-)_0$ at 50–100 μs after the pulse on pH for N_2O saturated 2 mM solution of 2,3-DMP.

creases with decreasing pH indicating that methanol elimination from OH adduct I can be enhanced by H^+ . At the same pH, the rate constant for formation of the *p*-semiquinone from 4-MP is approximately 2–3 times larger than those for production of the *o*-semiquinones from 2-MP and 2,3- and 2,6-DMP.

Optical measurements to determine the rates of formation of the semiquinones do not yield quantitatively analyzable results due to overlap of the semiquinone spectra with those²⁴ of the phenoxyl radicals formed. The absorption maximum of the *o*-semiquinone radical anions from 2-MP and 2,3- and 2,6-DMP must be <400 nm since no optical absorptions after 50–100 μs were observed at $\lambda > 400$ nm in pulse irradiated solutions at pH 6. This is in agreement with the published spectra⁵ obtained on pulse irradiation of catechol solutions.

The increase in conductivity at 50–100 μs after the pulse is followed by a decrease of conductivity almost (>85%) to the original value prior to the pulse (Figure 2). The nonquantitative regeneration of conductivity after all radical species have disappeared may be rationalized in terms of the $\text{p}K_a$ values of the reaction products being slightly lower than those of the starting materials.

The $\text{p}K_a$ values of the semiquinones produced from 2- and 4-MP and from 2,3- and 2,6-DMP were determined by measuring as a function of pH the conductivity changes observed 50–100 μs after the pulse in N_2O saturated 0.2 mM solutions. A dose rate variation (0.2–1 krad/pulse) was performed for each pH value. Using eq 3, the $G(\text{SQ}^-)_0$ values were calculated and plotted vs. pH (Figure 4). A $\text{p}K_a$ of 5.0 ± 0.2 is obtained for *o*-semiquinone formed from 2-MP. The same value is determined for *o*-methoxy-*o*-semiquinone produced from both 2,3- and 2,6-DMP. For *p*-semiquinone produced from 4-MP the $\text{p}K_a$ obtained is 3.9 ± 0.2 , which is in good agreement with the reported values of 4.0⁵ and 4.1²⁶ measured optically.

(b) *Methoxylated Hydroxybenzoic Acids*. Conductivity changes at 50–100 μs after the pulse were also observed on pulse irradiation of solutions of the methoxylated hydroxybenzoic acids. However, these signals are not exclusively due to formation of semiquinones but reflect

in addition changes in the ionization state of the carboxyl group which occur on reaction of the substrates with OH. Without detailed information on the latter effect the yields of production of semiquinones can therefore not be determined quantitatively.

(c) *3-MP and 3,5-DMP*. With 3-MP and 3,5-DMP at pH 5–7 the conductivity changes at 50–100 μs after the pulse were found to be very small. This is expected on the basis of the low yields of methanol from γ irradiations (Table I). However, the conductivity signals cannot be analyzed in terms of yields unless the $\text{p}K_a$ value of the *m*-hydroxyphenoxyl radical is known. This $\text{p}K_a$ value was therefore determined using N_2O saturated solutions containing 2 mM Ti_2SO_4 and 0.2 mM resorcinol. In this system the rate of production of *m*-hydroxyphenoxyl radical by reaction of Ti(II) with resorcinol is independent of pH.²⁷ By measuring the changes as a function of pH in the optical absorption at λ 450 nm, where the ionized radical absorbs, the $\text{p}K_a$ value of the *m*-hydroxyphenoxyl radical was determined to be 7.1 ± 0.2 . The yields of *m*-hydroxyphenoxyl radical from 3-MP and 3,5-DMP (Table I) were calculated on the basis of conductivity signals measured at pH 6–7 using the dissociation curve of the *m*-hydroxyphenoxyl radical for appropriate corrections. The yields obtained are in good agreement with the methanol yields from γ irradiations which is further support for reaction 2.

Acknowledgment. We thank U. Haske, M. Lyda, and H. Selbach for technical assistance.

References and Notes

- (1) R. Koster and K.-D. Asmus, *J. Phys. Chem.*, **77**, 749 (1973).
- (2) K. Eiben, D. Schulte-Frohlinde, C. Suarez, and H. Zorn, *Int. J. Radiat. Phys. Chem.*, **3**, 409 (1971).
- (3) P. Neta and R. W. Fessenden, *J. Phys. Chem.*, **78**, 523 (1974).
- (4) G. R. A. Johnson, G. Stein, and J. Weiss, *J. Chem. Soc.*, 3275 (1951).
- (5) G. E. Adams and B. D. Michael, *Trans. Faraday Soc.*, **63**, 1171 (1967).
- (6) J. H. Fendler and G. L. Gasowski, *J. Org. Chem.*, **33**, 2755 (1968).
- (7) O. Volkert, W. Bors, and D. Schulte-Frohlinde, *Z. Naturforsch. B*, **22**, 480 (1967).
- (8) K. M. Bansal, L. K. Patterson, and R. H. Schuler, *J. Phys. Chem.*, **76**, 2386 (1972).
- (9) P. Neta, *J. Phys. Chem.*, **76**, 2399 (1972).
- (10) P. Neta and C. L. Greenstock, *Radiat. Res.*, **54**, 35 (1973).
- (11) C. L. Greenstock, I. Dunlop, and P. Neta, *J. Phys. Chem.*, **77**, 1187 (1973).
- (12) R. Koster and K.-D. Asmus, *Z. Naturforsch. B*, **26**, 1108 (1971).
- (13) P. O'Neill, S. Steenken, and D. Schulte-Frohlinde, *J. Phys. Chem.*, **79**, 2773 (1975).
- (14) P. O'Neill, S. Steenken, and D. Schulte-Frohlinde, *J. Phys. Chem.*, **81**, 31 (1977).
- (15) P. O'Neill, D. Schulte-Frohlinde, and S. Steenken, *J. Chem. Soc., Farad. Discuss.*, in press.
- (16) D. R. Deans, *Chromatographia*, **1**, 18 (1968).
- (17) N. Getoff and F. Schworer, *Radiat. Res.*, **41**, 1 (1970).
- (18) H. G. Klever, Ph.D. Thesis, Ruhr-Universität, Bochum, 1974.
- (19) K.-D. Asmus, *Int. J. Radiat. Phys. Chem.*, **4**, 417 (1972).
- (20) K. Eiben and R. W. Fessenden, *J. Phys. Chem.*, **75**, 1186 (1971).
- (21) S. Steenken, P. O'Neill, and D. Schulte-Frohlinde, *J. Phys. Chem.*, **81**, 26 (1977).
- (22) W. T. Dixon, M. Moghimi, and D. Murphy, *J. Chem. Soc., Faraday Trans. 2*, 1713 (1974).
- (23) E. J. Land and M. Ebert, *Trans. Faraday Soc.*, **63**, 1181 (1967).
- (24) P. O'Neill and S. Steenken, to be submitted for publication.
- (25) M. Anbar, D. Meyerstein, and P. Neta, *J. Phys. Chem.*, **70**, 2660 (1966).
- (26) R. L. Willson, *Trans. Faraday Soc.*, **67**, 3020 (1971).
- (27) P. O'Neill, to be submitted for publication.

Decomposition of Chloral Hydrate in Aqueous Solution by the Action of Ultrasound

Yoshiro Sakai,* Yoshihiko Sadaoka, and Yoshinori Takamaru

Department of Industrial Chemistry, Faculty of Engineering, Ehime University, Matsuyama, 790, Japan (Received July 12, 1976; Revised Manuscript Received December 28, 1976)

Publication costs assisted by Ehime University

The decomposition of chloral hydrate in aqueous solution induced by the action of ultrasound of 29 and 400 kHz was studied. The reaction rate is proportional to the intensity of ultrasound and to the square root of the chloral hydrate concentration. The rate is also proportional to the square root of the oxygen concentration dissolved in solutions at relatively low concentration, while at high oxygen concentration the rate is independent of the oxygen concentration. The proposed reaction scheme is as follows. $\text{H}_2\text{O} \rightarrow \dot{\text{R}}$ (radicals produced in cavitation), $\dot{\text{R}} + \text{chloral hydrate} \rightarrow \text{chloral hydrate radical}$. Chloral hydrate radical + activated oxygen produced in cavitation \rightarrow peroxy radical, peroxy radical \rightarrow hydrochloric acid + $\dot{\text{R}}$. The chain reaction was assumed to terminate bimolecularly. The reactions induced by ultrasound are different from those induced by γ rays in that an activation step of oxygen in cavitation bubbles is included in the former case.

Introduction

Intense ultrasonic waves cause chemical changes in aqueous solutions by a mechanism involving cavitation. Prasad and Sharma¹ reported that the major product in the decomposition of aqueous solution of chloral hydrate by ultrasonic waves is hydrochloric acid. Although they have studied the effect of additives and pH on the yield of hydrochloric acid, they have not elucidated the kinetics of this reaction. It has been found by several workers²⁻⁵ that the similar reaction takes place in the radiolysis of aqueous solution of chloral hydrate. Spinks and his co-workers^{3,4} found that the reaction rate is proportional to the concentration of chloral hydrate to the 0.39 power and to the intensity of γ rays to the 0.66 power. They proposed a mechanism in which both bimolecular and unimolecular termination reactions were assumed to occur. In contrast to the case of radiolysis, in the present study of ultrasonic decomposition it was found that the reaction rate is proportional to the intensity of ultrasound and to the square root of the concentration of chloral hydrate. In addition, the rate is also proportional to the half power of oxygen concentration dissolved in solution when the oxygen concentration is low, whereas the rate is independent of the oxygen concentration when oxygen is dissolved sufficiently. In the present paper a reaction mechanism including the activation of dissolved oxygen in the cavitation bubbles⁶ will be proposed. This mechanism agrees well with the observed results.

Experimental Section

Chloral hydrate (reagent grade) was dissolved in highly purified water which had been distilled twice and further purified with ion exchange resins. The solution (10 mL) in a test tube (3 cm diameter) was irradiated with ultrasonic waves in a thermostat at 30 °C. Before irradiation the solution was saturated with air or the mixture of oxygen and nitrogen in various composition and then the test tube was sealed. The test tube was fixed 1.5 cm above the transducer. The ultrasonic frequency was 29 and 400 kHz. The concentration of chloride ion produced in decomposition by ultrasound irradiation was determined by turbidimetry.⁷

The power output of ultrasound was determined by the following method. A cylindrical polyethylene block (83 mm diameter \times 55 mm high) was held 0.5 cm above the transducer. After the irradiation with ultrasound for a certain time, the amount of heat produced by ultrasound

in the polyethylene block was determined in a water calorimeter. The power output of the transducer was thus obtained on the basis of the assumption that the sonic energy is completely transformed to the heat energy inside the polyethylene block. The relative intensity of the ultrasound at the position of the sample was measured by use of a thermocouple sandwiched between two small plate of polyethylene (20 mm diameter \times 2 mm thickness). When the temperature indicated by the thermocouple was plotted against the irradiation time, the slope of the first linear part of the line is proportional to the intensity of the ultrasound. It was confirmed that the power input into the transducer is proportional to the ultrasonic intensity.

Results and Discussion

The yield of chloride ion by the action of ultrasound is shown in Figure 1. The reaction rate produced by irradiation with 400 kHz ultrasound is 1.8 times greater than that by 29 kHz ultrasound.

In order to study the effect of dissolved oxygen in aqueous solutions on the rate of decomposition of chloral hydrate, various mixtures of nitrogen and oxygen were bubbled into the solutions and the test tubes were sealed at 1 atm. The reaction rate was plotted against the partial pressure of oxygen in Figure 2. On the basis of the assumption that the oxygen concentration is proportional to the partial pressure of oxygen above the solution, it was found that the rate is proportional to the square root of oxygen concentration at low concentration, while at relatively high concentration the rate is independent of the oxygen concentration. When the solution was saturated with nitrogen gas after degassing by repeated freezing and melting, the yield of chloride ion is very small, indicating that nitrogen gas is inert in the present reactions.

Figures 3 and 4 show the effect of concentration of chloral hydrate and the intensity of ultrasound on the rate of decomposition of chloral hydrate in aqueous solution. It was determined by the least-squares method that the reaction rate is proportional to $[\text{Ch}]^{0.45}I^{0.96}$ for the solution which had been bubbled with the mixture of gases containing 20% oxygen, where $[\text{Ch}]$ represents the concentration of chloral hydrate and I is the intensity of the ultrasound. When the solution had been bubbled with the gas containing 2% of oxygen, the reaction rate was found to be proportional to $[\text{Ch}]^{0.51}I^{1.06}$. Consequently, the reaction rate is proportional to the square root of the concentration of chloral hydrate and to the intensity of

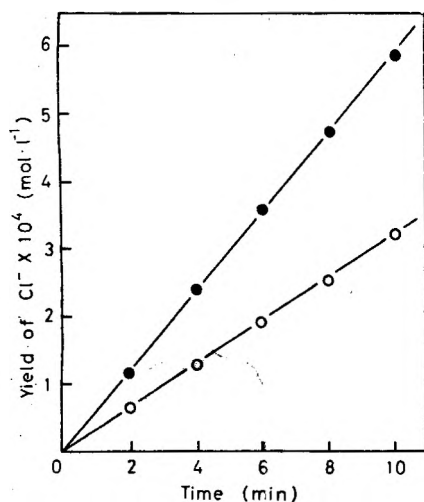


Figure 1. Yield of chloride ion with two different ultrasound frequencies: (●) 400 kHz, (○) 29 kHz ultrasound. Both saturated with air. The concentration of chloral hydrate was 0.1 M. The power output was 0.5 W cm^{-2} .

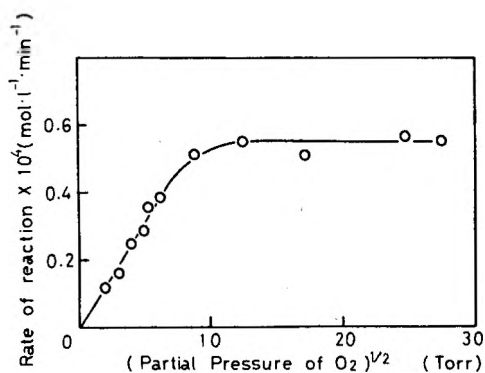


Figure 2. Relation between the reactor rate and the partial pressure of oxygen bubbled into the solution. The ultrasound frequency was 400 kHz and its power output 0.5 W cm^{-2} . The concentration of chloral hydrate was 0.1 M.

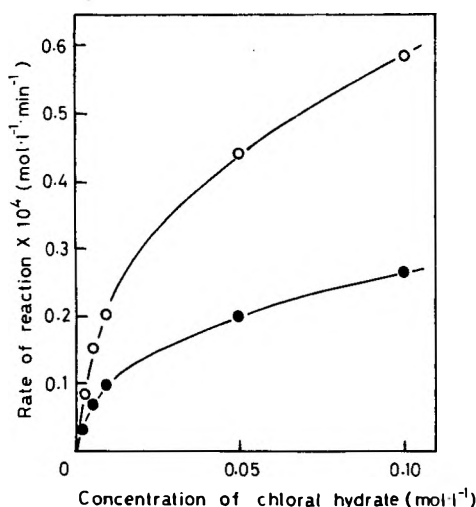


Figure 3. Concentration dependence of the rate of reaction. ○ represents the solution which had been saturated with the mixture of 20% O_2 gas and 80% N_2 gas. ● represents the solution saturated with the mixture of 2% O_2 and 98% N_2 . The ultrasound frequency was 400 kHz and its power output 0.5 W cm^{-2} .

ultrasound, regardless of the concentration of oxygen gas dissolved in the solutions. These results are different from those observed in radiolysis by McIntosh et al.⁴ They reported that in the case of radiation-induced decomposition of aqueous solution of chloral hydrate the rate is

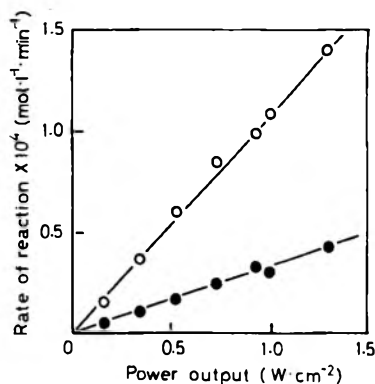


Figure 4. Effect of the intensity of ultrasound on the rate of reaction. ○ and ● represent the same as those in Figure 3. The ultrasound frequency was 400 kHz. The concentration of chloral hydrate was 0.1 M.

proportional to $[\text{Ch}]^{0.39} I^{0.66}$, where I is the intensity of γ rays.

In order to interpret the present results in sonolytic decomposition, the following reactions are assumed:



where R represents the initiating free radical, Ch, and $\dot{\text{C}}\text{h}$ is chloral hydrate molecule and radical, respectively. O_2^* represents an oxygen molecule activated in cavitation. Reaction 1 and 3 take place in cavitation bubbles. The rate of reaction 1 is proportional to the intensity of ultrasound. As will be discussed later the rate of reaction 3 is also proportional to the intensity I when the concentration of the dissolved oxygen is high, while the rate is proportional to the concentration of oxygen as well as to the intensity I when the dissolved oxygen concentration is relatively low. By applying the stationary state concept to R, Ch, and $\dot{\text{C}}\text{hO}_2$ radicals, one can derive the following equation:

$$k_2[\text{Ch}] - k_6k_7[\dot{\text{C}}\text{hO}_2]/k_5[\text{O}_2^*] - 2k_6^2k_7[\dot{\text{C}}\text{hO}_2]^2/k_1Ik_5[\text{O}_2^*] = 0 \quad (8)$$

Since $k_2[\dot{\text{R}}][\text{Ch}] \gg k_7[\dot{\text{R}}][\dot{\text{C}}\text{h}]$ and $k_5[\text{Ch}][\text{O}_2^*] = k_6[\dot{\text{C}}\text{hO}_2]$, $k_6k_7[\dot{\text{C}}\text{hO}_2]/k_5[\text{O}_2^*]$ can be neglected in comparison with $k_2[\text{Ch}]$. Then the following expression is obtained for the rate of production of hydrochloric acid:

$$\begin{aligned} d[\text{HCl}]/dt &= k_6[\dot{\text{C}}\text{hO}_2] \\ &= (k_1k_2k_5/2k_7)^{1/2}[\text{Ch}]^{1/2}I^{1/2}[\text{O}_2^*]^{1/2} \end{aligned} \quad (9)$$

As for the activation of oxygen in the cavities expressed by reaction 3, different mechanism must be considered below and above the transition at 80 Torr of oxygen as shown in Figure 2. It is assumed that all the cavities (cavitation bubbles) are nearly the same size and that the amount of ultrasonic energy available in each cavity is limited and only a certain amount of oxygen can be activated with this amount of energy. Consequently, when the concentration of the dissolved oxygen is high, the

amount of activated oxygen is independent of the oxygen concentration. In that case the intensity of the ultrasound I should become the limiting factor. The rate of activation of O_2 can be expressed proportional to the intensity I . Then

$$d[O_2^*]/dt = k_3'I - k_4[O_2^*] - k_5[Ch][O_2^*] \quad (10)$$

On the other hand, when the concentration of oxygen is low, the rate of reaction 3 also depends on O_2 . In this case eq 11 must be used instead of eq 10. If most of the ac-

$$d[O_2^*]/dt = k_3[O_2]I - k_4[O_2^*] - k_5[Ch][O_2^*] \quad (11)$$

tivated oxygen decay unimolecularly, one can assume that $k_4[O_2^*] \gg k_5[Ch][O_2^*]$. Taking in the stationary state concept to the activated oxygen, eq 12 and 13 are derived

$$[O_2^*] = (k_3'/k_4)I \quad (12)$$

$$[O_2^*] = (k_3/k_4)[O_2]I \quad (13)$$

for the high and low concentration of dissolved oxygen, respectively. Substituting eq 12 and 13 for $[O_2^*]$ in eq 9 yields the following: at high concentration of oxygen

$$\frac{d[HCl]}{dt} = \left(\frac{k_1 k_2 k_3' k_5}{2k_4 k_7} \right)^{1/2} [Ch]^{1/2} I \quad (14)$$

at low concentration of oxygen

$$\frac{d[HCl]}{dt} = \left(\frac{k_1 k_2 k_3 k_5}{2k_4 k_7} \right)^{1/2} [Ch]^{1/2} [O_2]^{1/2} I \quad (15)$$

Equation 14 or 15 agrees quite well with the experimental results which are shown in Figures 2-4, viz. the rate of decomposition is proportional to the square root of the concentration of chloral hydrate and to the intensity of ultrasound when sufficient oxygen is dissolved in the solution. On the other hand, when the concentration of dissolved oxygen is low, the rate is proportional to the square root of the concentration of oxygen as well as that of chloral hydrate, and to the intensity of ultrasound.

It is concluded that the decomposition of chloral hydrate in aqueous solution by the action of ultrasound proceeds by a different mechanism from that induced by ionizing radiation. In the former case, the activation of dissolved oxygen caused in the cavities must be taken into account in the study of kinetics. It was also concluded that all the cavities are nearly the same size and contain about the same amount of available energy for activating O_2 .

References and Notes

- (1) B. Prasad and P. K. Sharma, *Chim. Anal.*, **51**, 619 (1969).
- (2) H. L. Andrew and P. A. Shore, *J. Chem. Phys.*, **18**, 1165 (1959).
- (3) R. F. Platford and J. W. T. Spinks, *Can. J. Chem.*, **37**, 1022 (1959).
- (4) R. G. McIntosh, R. L. Eager, and J. W. T. Spinks, *Can. J. Chem.*, **42**, 2033 (1964); **43**, 3490 (1965).
- (5) A. Lutz and K. Schmidt, *Nature (London)*, **201**, 493 (1964).
- (6) I. E. El'piner, "Ultrasound—Physical, Chemical and Biological Effects", Consultants Bureau, New York, N.Y., 1964, p 58.
- (7) E. Hayon and O. Allen, *J. Phys. Chem.*, **65**, 2181 (1961).

Warming-Induced Reactions in γ -Irradiated Naphthalene Solutions in Freon-Mixture Glass

Akira Kira,* Takashi Nakamura, and Masashi Imamura

The Institute of Physical and Chemical Research, Wako, Saitama 351, Japan (Received August 2, 1976; Revised Manuscript Received December 30, 1976)

Publication costs assisted by The Institute of Physical and Chemical Research

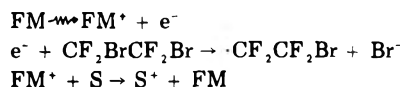
Naphthalene solutions in a Freon mixture consisting of $CFCl_3$ and CF_2BrCF_2Br were γ irradiated at 77 K and then warmed to 83.7 K. Warming produced an intermediate having a characteristic absorption band at 0.76 μm on the change of a naphthalene cation to a dimer cation. Analysis of the effects of both naphthalene concentration and dose led to a conclusion that the intermediate is a complex of the naphthalene cation with $\cdot CF_2CF_2Br$. Another new species absorbing strongly near 1.16 μm was formed from the dimer cation upon warming. This band was assigned to a tetramer dication, $S_4^{2+} \cdots 2Br^-$. Extinction coefficients of the new species as well as those of the naphthalene cation and dimer cation were determined.

Introduction

Either cations or anions¹ of organic compounds can be selectively prepared by γ irradiation of solutions in 77 K matrices of suitably chosen solvents.² Recent spectroscopic studies on cations and anions by Shida and Iwata³ demonstrate the usefulness of the selective preparation. Warming an irradiated solution allows diffusion, which induces chemical reactions such as charge neutralization,⁴ formation of dimer and tetramer cations,⁵⁻⁸ and formation of I_4^- .⁹ However, not much has been revealed about the details of warming-induced processes in irradiated rigid solutions.

The present paper deals with the warming-induced change of the absorption spectrum in γ -irradiated naphthalene solutions in Freon mixture glass. The Freon mixture, FM, is an equivolume mixture of $CFCl_3$ and

CF_2BrCF_2Br , which forms an optically transparent glass at 77 K.¹⁰ Irradiation of solutions in the FM matrix gives cations of solute molecules.¹¹ In our preliminary experiments, FM glass was found not to crack for the temperature change necessary for the present experiments. An established mechanism for primary processes in irradiated matrices of alkyl halides² enables us to write the following reactions for FM rigid solutions:



where FM^+ represents positive holes, which are trapped by naphthalene molecules, S, to give cations, S^+ . Radiation-induced S^+ , $\cdot CF_2CF_2Br$, and Br^- ¹² as well as solute and solvent molecules may participate in warming-induced

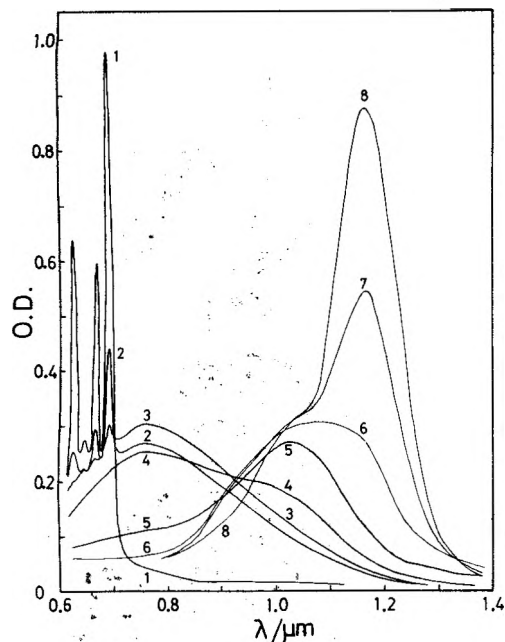


Figure 1. The warming-induced change of the absorption spectrum in a 4.9 mmol kg^{-1} naphthalene glassy solution in FM γ -irradiated with a dose $6.0 \times 10^{22} \text{ eV kg}^{-1}$ in a 0.48-mm thick cell. The 8 depicted curves are selected from 16 curves measured in a sequence. (1) Immediately after irradiation. Warming intervals between two successive measurements at 83.7 K: (1), 30 s (2), 30 s (3), 4 min (4), 25 min (5); at 90 K: (5), 10 s (6), 30 s (7), 18 min (8).

reactions. In this paper we present a scheme for warming-induced processes involving these species on the basis of the analysis of the concentration and dose effects. Warming at precisely controlled temperature made the analysis possible.

The absorption spectrum of the naphthalene dimer cation, S_2^+ , was first measured by Brocklehurst and co-workers,⁵ and their assignment was supported by quantitative pulse radiolysis studies.^{13,14} The previous assignment of the dimer cation was accepted in the present study without further argument.

Experimental Section

Daiflons 11 (99.9% CFCl_3) and 114B2 (99% $\text{CF}_2\text{BrCF}_2\text{Br}$) purchased from Daikin Industry Co. were used without further purification. Naphthalene was Tokyo Kasei's zone-refined reagent. Sample solutions were degassed, except for experiments with aerated solutions, and frozen to glass at 77 K in 0.6–1.6-mm thick cells made of Suprasil. A sample at 77 K was γ irradiated at a dose rate of $2.0 \times 10^{21} \text{ eV kg}^{-1} \text{ min}^{-1}$. After the measurement of the absorption spectrum on a Cary 14RI spectrophotometer, the sample was immersed in a mixture of liquid nitrogen and liquid oxygen which was kept at a temperature of $83.7 \pm 0.3 \text{ K}$. The sample thus warmed for a certain period was cooled to 77 K to measure the spectrum again. The procedure was repeated more than 10 times until the amount of naphthalene dimer cation reached its maximum. The warming temperature was raised to 90 K after completion of dimer-cation formation in order to accelerate a reaction.

Results

Figures 1 and 2 show the change of the absorption spectra induced by warming in γ -irradiated naphthalene solutions in FM matrices. In Figure 1 the 0.55–0.69- μm bands for the naphthalene monomer cation (M) seen at step 1 were replaced at step 3 by a broad band with a peak at $0.76 \mu\text{m}$, which characterizes a hitherto unknown

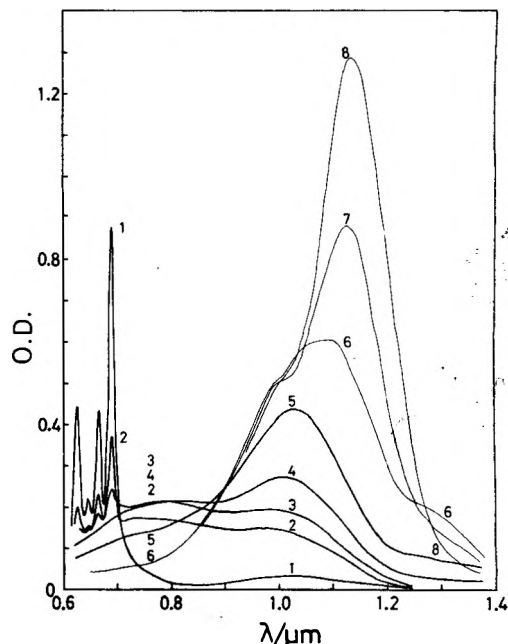


Figure 2. The warming-induced change of the absorption spectrum in a 15 mmol kg^{-1} naphthalene glassy solution in FM γ -irradiated with a dose $1.0 \times 10^{22} \text{ eV kg}^{-1}$ in a 1.5-mm thick cell. (1) Immediately after irradiation. Warming intervals at 83.7 K: (1), 70 s (2), 60 s (3), 4 min (4), 15 min (5); at 90 K: (5), 20 s (6), 30 s (7), 15 min (8).

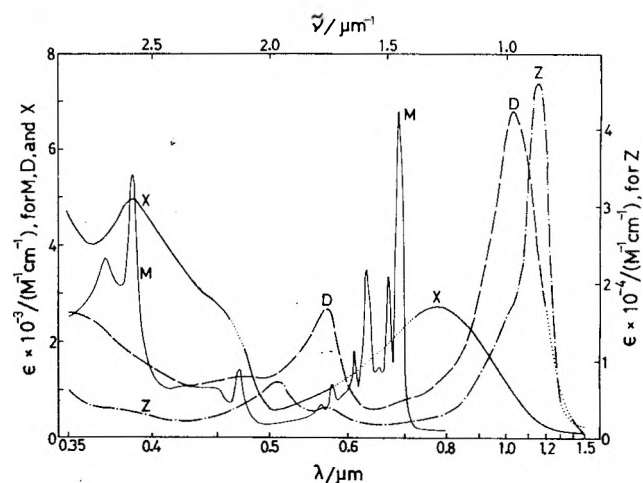


Figure 3. The absorption spectra of transients M, X, D, and Z. See Discussion as to the estimation of the extinction coefficients.

species, X. Prolonged warming changed X to the naphthalene dimer cation (D) having a characteristic band at $1.03 \mu\text{m}$.⁵ Thus, X is an intermediate in consecutive reactions, $M \rightarrow X \rightarrow D$. The growth of the dimer-cation band during steps 2–4 in Figure 2 is considered to be due to the enhancement of the conversion of X to the dimer cation by the increase in the naphthalene concentration. Exposure to tungsten light, under the same illumination conditions that caused trapped electrons in alcohols to be thoroughly removed, did not change appreciably either the monomer cation or X. Figure 3 shows the spectra of the monomer cation, dimer cation, and X in the region of 0.35–1.6 μm . The transient X was also found in glassy solutions of a 3-methylpentane (3MP)– $\text{CF}_2\text{BrCF}_2\text{Br}$ mixture, but not in those of 3MP– CFCl_3 , 3MP–BuCl, isopentane–BuCl, or 3MP. Thus, X formation seems to be peculiar to matrices containing $\text{CF}_2\text{BrCF}_2\text{Br}$. The formation of dimer cations did not depend on solvent.

Warming after completion of the dimer-cation formation replaced the $1.03\text{-}\mu\text{m}$ band by a strong band near $1.16 \mu\text{m}$, which appears so near to the $1.03\text{-}\mu\text{m}$ band that it has been

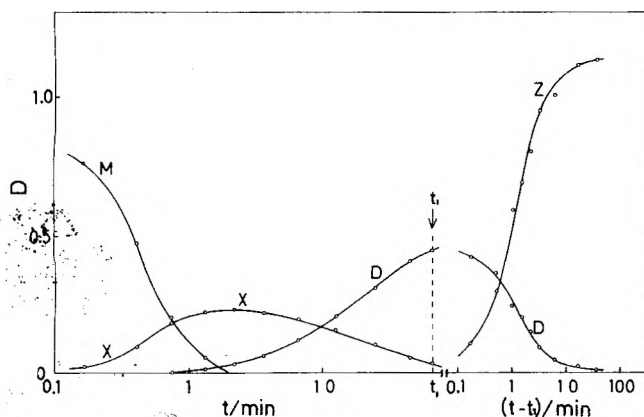


Figure 4. The change with time in the net optical densities for the transients at the characteristic wavelengths. A 4.9 mmol kg^{-1} solution was irradiated with a dose of $1.2 \times 10^{22} \text{ eV kg}^{-1}$ and warmed at 83.7 K until time t_1 , after which temperature was raised to 90 K .

assigned mistakenly to the dimer cation.^{3a} The species with the $1.16\text{-}\mu\text{m}$ band is denoted by Z. Its spectrum in the region of $0.35\text{--}1.6 \mu\text{m}$ is also shown in Figure 3. Z formation was not peculiar to FM solutions. As shown in Figure 2, another band near $1.3 \mu\text{m}$ rose temporarily in the course of Z formation. The yield of the intermediate (Y) with the $1.3\text{-}\mu\text{m}$ band increased with increase in the naphthalene concentration, but was not high enough to discuss its formation quantitatively.

The observed spectra were composites of the spectrum of each species except for the special cases in which only one species dominated. When two species coexist, the net optical density for one species is calculated from the optical densities observed at the peak wavelengths for the species concerned. The peak wavelengths, $0.69, 0.76, 1.03,$ and $1.16 \mu\text{m}$ for M, X, D, and Z, respectively, are denoted by $m, x, d,$ and z when used as a subscript for the extinction coefficient and optical density. For example, the net optical density for X at $0.76 \mu\text{m}$, D_x^X , is given by

$$D_x^X = \rho \epsilon_x^X(X) = \frac{OD_x - \beta OD_d}{1 - \alpha \beta}$$

where $\alpha = \epsilon_d^X/\epsilon_x^X$ and $\beta = \epsilon_x^D/\epsilon_d^D$, and OD_x and OD_d are the observed optical densities at 0.76 and $1.03 \mu\text{m}$, respectively. The ratios α and β were determined from the spectra of X and the dimer cation, respectively. The density of a solution, ρ , is involved because of the use of molality (mol kg^{-1}), represented by $\langle \rangle$ instead of the molar concentration (mol dm^{-3}) to avoid the intricacy caused by the change in volume with temperature.

An example of the change with time of the net optical density during warming is shown in Figure 4, which illustrates the successive formation of the species. A logarithmic time scale in Figure 4 is used merely to show the sequence clearly; it is not intended to suggest the tunneling mechanism for which a D vs. $\log t$ plot is linear.¹⁵ The warming-induced processes seem to result from diffusion, since the reactions occur between two molecules such as X and a naphthalene molecule. The inspection of many decay and growth curves revealed that the rate was not determined only by the naphthalene concentration, dose, and temperature. All the reactions were accelerated or retarded by unknown factors depending on each sample. This finding suggests that a subtle difference in the frozen state exists among solutions and affects the diffusion.¹⁶ This diffusion effect was observed regardless of concentration and dose, although the yields of the transients were found to depend on the naphthalene concentration and dose. The difference in the frozen state does not seem to

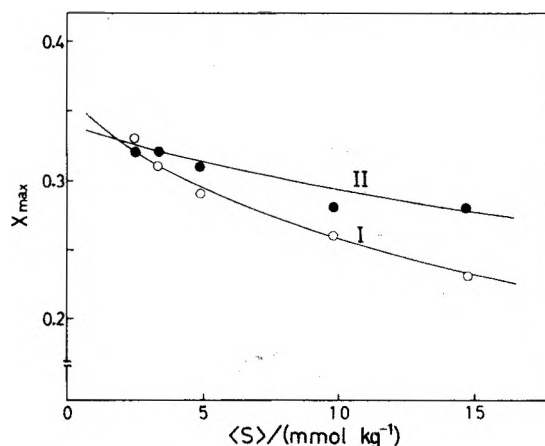


Figure 5. The concentration dependence of X_{max} at doses of 1.0×10^{22} and $6.0 \times 10^{22} \text{ eV kg}^{-1}$ (O and \bullet , respectively). The curves are calculated in terms of eq III and IV with parameters adjusted to fit best the data (see Discussion): (I) $1.0 \times 10^{22} \text{ eV kg}^{-1}$; (II) $6.0 \times 10^{22} \text{ eV kg}^{-1}$.

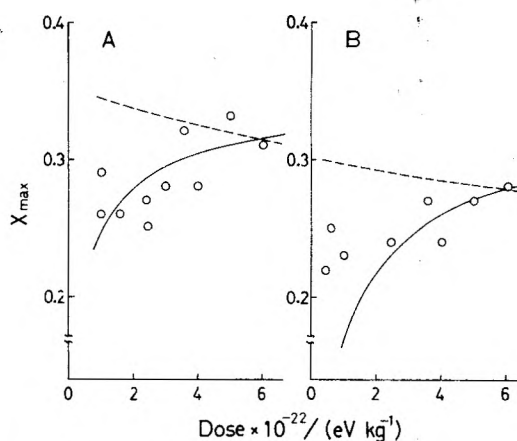


Figure 6. The dose dependence of X_{max} in 4.9 mmol kg^{-1} (A) and 15 mmol kg^{-1} (B) solutions. The curves are calculated in terms of eq IV with eq V (solid lines) and with eq VI (broken lines).

change ratios of reaction rates in one sample solution, but, seems to change every reaction rate by the same factor.

The kinetics of the warming-induced processes were analyzed on the basis of the yields of the transients with respect to concentration and dose. A maximum yield of X is defined by

$$X_{\text{max}} = \text{maximum } D_x^X / \text{initial } D_m^M$$

Figures 5 and 6 show plots of X_{max} vs. the naphthalene concentration and dose, respectively. Chemical kinetics tells us that in the consecutive reactions the maximum X concentration divided by the initial M concentration is a function of a ratio of a decay rate to a formation rate of X.¹⁷ Therefore, the observed dependence of X_{max} on both the naphthalene concentration and dose, as shown in Figures 5 and 6, indicates that naphthalene molecules and radiolysis products (dose-dependent species) are involved in the formation and decay of X.

A formation process of the dimer cation was not influenced by the much slower processes of its decay. In fact, D_d^D increased linearly with the increase in D_x^X except for the initial and final stages of dimer cation formation. Thus, the treatment based on consecutive reactions is unnecessary for dimer-cation formation, and a conversion factor for the change of X to the dimer cation is defined by

$$f(D/X) = \Delta D_d^D / (-\Delta D_x^X)$$

standard dose, $r_0 = 6.0 \times 10^{22}$ eV kg^{-1} . The solid curves in Figure 6 are based on eq IV and V with the appropriate parameter values calculated above. If R were not involved in process 1, the broken curves in Figure 6 based on the following equation would fit the data:

$$p = \frac{k_2}{k_1'} \left((S) + \frac{k_3(Q)_0 r}{k_2 r_0} \right) \quad (\text{VI})$$

where k_1' is a first-order rate constant whose magnitude is equal to $k_1(R)_0$. The agreement of the solid curves with the data is sufficient to affirm the participation of R, though the data scatter.

The suppression of X formation by oxygen can be attributed to the removal of R by oxygen. The finding that X formation is peculiar to $\text{CF}_2\text{BrCF}_2\text{Br}$ suggests that R also relates to this compound. Species formed by the irradiation of naphthalene solutions in a FM matrix include a naphthalene monomer cation, $\cdot\text{CF}_2\text{BrCF}_2$, and Br^- . Among these, a radical $\cdot\text{CF}_2\text{BrCF}_2$ can be removed by oxygen. Haloalkane radicals such as $\cdot\text{CCl}_3$ are believed to react efficiently with oxygen to form peroxy radicals.¹⁸ The monomer cation is not considered to be removed by oxygen, since in alkane-BuCl matrices the presence of oxygen assisted dimer-cation formation.¹⁹ The removal of aromatic cation radicals by oxygen has not been reported as far as the authors know. Therefore, R is identified with $\cdot\text{CF}_2\text{BrCF}_2$. This identification leads to the conclusion that X is a complex of the monomer cation with the radical, $\text{S}^+ \cdots \text{CF}_2\text{BrCF}_2$. Process 1 is accordingly represented as



The complex was removed by another radiation-induced species Q, which seems to be unreactive to oxygen, because $f(D/X)$ would increase on aeration if Q were removed by oxygen. The monomer cation cannot be Q, since the former has changed to X before process 2 becomes predominant. Therefore, Q is most likely a bromide ion, Br^- . Processes 2 and 3 are written as



When R is removed by oxygen, monomer cations are probably neutralized by Br^-



The efficient formation of the dimer cation via the complex suggests that reaction 4 is much slower than reaction 1. Radicals $\cdot\text{CF}_2\text{BrCF}_2$ cannot recombine with bromide ions in warmed FM matrices, since this recombination is the reverse process of a spontaneous reaction (the second reaction in the Introduction). Both the monomer cation and radical seem to be removed through the complex in reaction 3 where neutralization and radical recombination occur simultaneously to form stable molecules.

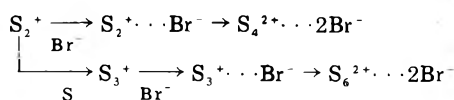
We cannot answer the question why only $\cdot\text{CF}_2\text{BrCF}_2$ can form a complex with the monomer cation. Not all the aromatic hydrocarbons ever tested gave similar complexes in FM matrices.²⁰ There might be other matrices that give similar complexes. The conditions for complex formation should be revealed before answering the above question. Experiments on various aromatic hydrocarbons in FM and other solvents are in progress. The present results show that reaction 1 proceeds faster than the direct formation of the dimer cation



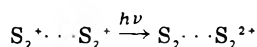
though the radical concentrations, which are estimated at about 0.5 and 3 mmol kg^{-1} for doses 1.0×10^{22} and 6.0×10^{22} eV kg^{-1} ,²¹ respectively, are comparable to or lower than

naphthalene concentrations of 2.5–15 mmol kg^{-1} . Although R might be intrinsically more reactive to the monomer cation than naphthalene molecules are, the fast diffusion of the radical can account for the preference of reaction 1 to reaction 5. For example, in an isopentane-*n*-butyl chloride glass, benzene forms its dimer cation at 77 K, but naphthalene requires warming to form its dimer cation.⁵ Thus, small R radicals probably diffuse faster than naphthalene molecules do. The appearance of a small amount of the dimer cation immediately after irradiation in a 15 mmol kg^{-1} solution (Figure 2) suggests that the direct dimer cation formation could compete with process 1 if the naphthalene concentration could be increased.

On the Species Z. In this section, the near-IR band of Z will be called a Z band. The concentration dependence of $f(Z/D)$ and concurrent shift of the Z band shown in Figure 8 can be accounted for if it is assumed that the band is composed of bands for two species; one denoted by Z-1 has an absorption peak at 1.16 μm and the other, Z-2, has a peak at 1.13 μm whose intensity is smaller than that of the Z-1 band. It is also assumed that the Z-1 band is so strong that the observed change in the Z-band intensity reflects the behavior of Z-1. The decrease of $f(Z/D)$ with increasing naphthalene concentration indicates that Z-1 formation is inhibited by naphthalene molecules, suggesting that Z-1 cannot be an aggregate naphthalene monocation such as a trimer cation, S_3^+ . The increase of $f(Z/D)$ with increase in dose suggests that a radiation-induced species is involved in the Z-1 formation. Furthermore the absence of oxygen effects suggests that the radiation-induced species is a bromide ion. Therefore, the results shown in Figure 8 are explained qualitatively by the scheme:



We believe that Z-1 is a tetramer dication, $\text{S}_4^{2+} \cdots 2\text{Br}^-$. From the kinetic point of view an ion pair, $\text{S}_2^+ \cdots \text{Br}^-$, could also be Z-1. However, it is doubtful whether ion-pair formation can increase the intensity of the charge-resonance band (at 1.03 μm)⁵ of the dimer cation as markedly as shown in Figures 1 and 2. The proposed tetramer dication is analogous to already known cation dimers (dimer dications).²² In the tetramer dication, a charge transfer



might be responsible for the strong Z-1 band.

A hexamer dication, $\text{S}_6^{2+} \cdots 2\text{Br}^-$, formed via a trimer cation, might be Z-2. The transient Y whose 1.3- μm band was intensified by the increase in the naphthalene concentration may be assigned to the trimer cation.

Estimation of the Extinction Coefficients. The ratios, $\epsilon_x^X/\epsilon_m^M$ and $\epsilon_d^D/\epsilon_x^X$, were evaluated in the above analysis. A value of $6.8 \times 10^3 \text{ M}^{-1} \text{ cm}^{-1}$ for ϵ_m^M was calculated from a G value of 2.1/(100 eV) for the cation formation in an FM solution measured by Shida.²³ The combination of this value with the above ratios gives values of 2.7×10^3 and $6.8 \times 10^3 \text{ M}^{-1} \text{ cm}^{-1}$ for ϵ_x^X and ϵ_d^D , respectively. It should be noted that in FM glass the vibrational structure of the monomer-cation band appears so sharply³ that the value for ϵ_m^M must be higher in FM solution than in other solutions where bands become broad. A value for ϵ_z^Z was obtained by setting it equal to the maximum $f(Z/D)$ multiplied by $2\epsilon_d^D$, where the factor, 2, comes from the fact that the tetramer dication is formed from the dimer cation. The value thus determined is not as precise as those given

above, because the Z band consists of two components which were not resolved experimentally and because the scheme was not tested quantitatively. We consider ϵ_z^Z as a crude value for the extinction coefficient for Z-1. The calculated extinction coefficients are given in Figure 3.

Concluding Remarks

An intermediate of dimer-cation formation from the monomer cation was first found in the present study and assigned to a complex between a naphthalene monomer cation and a radical, $\cdot\text{CF}_2\text{CF}_2\text{Br}$. The formation of similar complexes has not been found in matrices other than the FM matrix; accordingly, the complex formation does not always precede the dimer cation formation. However, a scheme involving the reaction of monomer cations with solvent fragment radicals prior to reactions of monomer cations with solute molecules or anionic species seems applicable to warming-induced processes in other solvents. It has been conjectured that neutralization is the main process removing monomer cations. According to the above scheme, however, solvent radicals can remove solute monomer cations by positive-charge transfer if the ionization potential of the radical is lower than that of a solute molecule. Conditions for the complex formation are not known yet, but the ionization potential might be one factor. The participation of neutral radicals in the removal of charged species has been reported for γ -irradiated hydrocarbon glasses where radicals capture phototrapped electrons.²⁴

Acknowledgment. We thank Dr. Tadamasu Shida for permitting us to cite a *G* value for cations in FM matrices from his paper before its publication.

References and Notes

- (1) Cation and anion radicals will be called cations and anions, respectively.
- (2) W. H. Hamill, "Radical Ions", E. T. Kaiser and L. Kevan, Ed., Interscience, New York, N.Y., 1968, p 321.
- (3) (a) T. Shida and S. Iwata, *J. Am. Chem. Soc.*, **95**, 3473 (1973); (b) *J. Phys. Chem.*, **75**, 2591 (1971).
- (4) (a) B. Brocklehurst, *Int. J. Radiat. Phys. Chem.*, **6**, 483 (1974); (b) F. Kieffer and M. Magat, "Actions Chimiques et Biologiques des Radiations", M. Haissinsky, Ed., Vol. 14, Masson, Paris, 1969, p 135.
- (5) B. Badger, B. Brocklehurst, and R. D. Russel, *Chem. Phys. Lett.*, **1**, 122 (1967).
- (6) (a) B. Badger and B. Brocklehurst, *Trans. Faraday Soc.*, **65**, 2576 (1969); (b) *ibid.*, **65**, 2582 (1969); (c) *ibid.*, **65**, 2588 (1969).
- (7) R. E. Buhler and W. Funk, *J. Phys. Chem.*, **79**, 2098 (1975).
- (8) A. Kira, M. Imamura, and T. Shida, *J. Phys. Chem.*, **80**, 1445 (1976).
- (9) T. Shida, Y. Takahashi, H. Hatano, and M. Imamura, *Chem. Phys. Lett.*, **33**, 491 (1975).
- (10) C. Sandorfy, *Can. Spectrosc.*, **10**, 85 (1965).
- (11) A. Grimison and G. A. Simpson, *J. Phys. Chem.*, **72**, 3776 (1968).
- (12) Consideration based on both the carbon-halogen bond energy and electron affinity indicates that the dissociative electron attachment occurs more easily on $\text{CF}_2\text{BrCF}_2\text{Br}$ than on CFCl_3 .
- (13) M. A. J. Rodgers, *J. Chem. Soc., Faraday Trans. 1*, **68**, 1278 (1972).
- (14) A. Kira, S. Arai, and M. Imamura, *J. Phys. Chem.*, **76**, 1119 (1972).
- (15) J. R. Miller, *J. Phys. Chem.*, **79**, 1070 (1975).
- (16) Several phases may be concerned with freezing near the glass-transition temperature. For example, see M. Sugisaki, K. Adachi, H. Suga, and S. Seki, *Bull. Chem. Soc. Jpn.*, **41**, 593 (1968); K. Adachi, H. Suga, and S. Seki, *ibid.*, **41**, 1073 (1968).
- (17) For example, A. A. Frost and R. G. Pearson, "Kinetics and Mechanism", 2nd ed, Wiley, New York, N.Y., 1961, Chapter 8.
- (18) Z. Spurny, *Int. J. Appl. Radiat. Isotopes*, **14**, 337 (1963).
- (19) Our unpublished results.
- (20) Our unpublished results. About 20 aromatic hydrocarbons were examined in solutions of various solvents.
- (21) A *G* value for radical formation was assumed to be the same as that for cation formation in FM glass, which is given in the section on the estimation of extinction coefficients. An actual *G* value may be higher, because the radical may be produced from excited states.
- (22) K. H. Hausser and J. N. Murrell, *J. Chem. Phys.*, **27**, 500 (1957).
- (23) T. Shida, private communication.
- (24) J. E. Willard, *Int. J. Radiat. Phys. Chem.*, **6**, 325 (1974).

Deuterium Isotope Effect on Hydrogen Atom Abstraction by Methyl Radicals in Acetonitrile at 77 K. Evidence for Tunneling

Estel D. Sprague

Department of Chemistry, University of Cincinnati, Cincinnati, Ohio 45221 (Received September 7, 1976)

By ESR techniques, the rate of disappearance of methyl radicals at 77 K in a crystalline matrix composed largely of acetonitrile- d_3 was determined. Although hydrogen atom abstraction proceeds readily under such conditions, deuterium atom abstraction was not observed. The methyl radical population decayed extremely slowly at 77 K by some alternative mechanism. It was nevertheless established from these measurements that the deuterium isotope effect on abstraction is at least 28000. Since this is almost 20 times greater than the *maximum* effect in the absence of tunneling, it is strongly indicated that tunneling is important in hydrogen atom abstraction at 77 K.

Introduction

Recent studies of the reactivity of methyl radicals at low temperatures in crystalline or glassy matrices of organic compounds have demonstrated the occurrence of hydrogen atom abstraction.¹⁻⁵ This was contrary to expectation, since such reactions, characterized by activation energies in excess of 5 kcal/mol at ordinary temperatures, were assumed to have negligibly small reaction rates at temperatures as low as 77 K.⁶ It has been found that the experimental activation energies at low temperatures are greatly reduced from the values found at ordinary temperatures in the gas phase. Typical values around 77 K are 1-2 kcal/mol, with substantial positive curvature in Arrhenius plots of the abstraction rate constant.^{2,7} In

acetonitrile, for example, the gas-phase, high-temperature (373-573 K) activation energy of 10.0 ± 0.5 kcal/mol⁸ was decreased to 1.4 kcal/mol, measured between 77 and 87 K.¹

The most attractive explanation for these observations is the hypothesis of a large degree of quantum mechanical tunneling in hydrogen atom abstraction at low temperature. It was shown, in fact, using exact one-dimensional tunneling calculations, that all of the data for abstraction from acetonitrile, in the gas phase and the solid phase, are consistent with this hypothesis.⁹ It remains possible, however, that some unknown factor is responsible for these low activation energies and curved Arrhenius plots. Thus, it is often suggested, although such effects would be at

present essentially impossible to predict, that the potential energy surface for the reaction might be drastically modified upon going to the solid state.

This study was undertaken to obtain definitive evidence for tunneling in the acetonitrile system at 77 K. The approach was to determine the primary deuterium isotope effect on the rate of the abstraction reaction, since the occurrence of tunneling will result in a marked enhancement of this isotope effect.¹⁰ While previous measurements have indicated that a very large isotope effect is indeed present,^{1,11} the reliability of the results from these difficult experiments was not adequately established. Significant improvement in experimental design has provided a firm base for the present study, in which a lower limit for the primary isotope effect has been determined which is more than an order of magnitude higher than the earlier estimates. The new value greatly exceeds the maximum value predicted in the absence of tunneling, so strong support for the tunneling hypothesis is obtained.

Experimental Section

Acetonitrile (Fisher Certified ACS grade; >99%) and acetonitrile-*d*₃ (Merck Sharp and Dohme; >99 atom % deuterium) were dried in vacuo over anhydrous magnesium sulfate (Matheson Coleman and Bell; reagent grade). Samples were prepared by standard high vacuum techniques in Suprasil tubes of 2–3 mm i.d. Mixtures containing approximately 10 mol % CH₃CN in CD₃CN were prepared by condensing the materials to measured heights in the sample tubes. Irradiation of the samples was carried out at 77 K in a Gammacell-200 source of cobalt-60 at a dose rate of 0.30 Mrad h⁻¹ to a total dose of 1.0 Mrad.

ESR measurements were made at X-band on a Varian E-4 spectrometer, with the samples under liquid nitrogen in a standard quartz dewar. Unfiltered light from the tungsten filament of a microscope illuminator (American Optical Model 653) was focused on the ESR cavity grid to provide sample illumination. All measurements were made with a nominal microwave power of 0.5 mW, at which level power saturation of the radical signals of interest is negligible. All other spectrometer variables were adjusted to avoid signal distortion and maximize the precision with which features of interest in the spectra could be measured.

A most important aspect of these measurements was the use of a reference signal to correct for day-to-day fluctuations in spectrometer conditions. A small ruby crystal was attached with epoxy adhesive to the outside of the quartz dewar, so that it was vertically centered in the ESR cavity. By rotating the dewar about its axis, an orientation was found for which none of the several resonance lines appeared in the vicinity of *g* = 2. Since the ruby signal is highly anisotropic, this orientation was easily reproduced by positioning one of the resonance lines at a particular magnetic field value, 3800 ± 2 G in this case. Since moving this line as much as 50 G to either side of 3800 G resulted in a decrease in its intensity of only about 1%, it was chosen to serve as the intensity standard to which all sample signals were subsequently referenced. As a test of this system, the intensity of the signal from a Varian strong pitch sample was determined at 77 K numerous times during the course of the kinetic studies described below. Each measurement was referenced to the corresponding ruby signal, and it was found that the standard deviation of the corrected measurements was about 0.6% of the mean value.

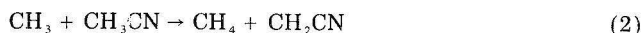
During the kinetic studies, long-term visible illumination of the samples at 77 K was necessary. A dewar (ca. 10 cm o.d.) was constructed from Pyrex tubing, with a small

window in the silvering near the bottom. In use, this end of the dewar was immersed in a large beaker of water, which filtered out the infrared radiation from the light source. A 15-W tungsten filament bulb provided an intensity of light on the samples sufficient to cause the bleaching of the radical anions in acetonitrile (see below) with a pseudo-first-order rate constant of 0.24 min⁻¹.

Results

Acetonitrile has two crystalline phases, with a solid–solid transition temperature of 216.9 K, approximately 12 K below the fusion temperature of 229.3 K.¹² When a sample of liquid acetonitrile is cooled suddenly to 77 K by immersion in liquid nitrogen, a polycrystalline matrix of the high-temperature crystalline phase results, which remains stable indefinitely at 77 K. All the information reported here refer to this crystalline phase of acetonitrile (crystal I). The identity of the free radical species generated in crystal I by γ radiation and their subsequent behavior at low temperature have been the subject of considerable study.¹³ Results of importance to this work are outlined briefly here.

When crystal I of acetonitrile, CH₃CN, or any of its isotopic variations, is exposed to γ radiation in the dark at 77 K, the main species observed are CH₂CN and the dimer radical anion, (CH₃CN)₂⁻, or the corresponding isotopic species. Illumination with visible light dissociates the dimer radical anions, yielding methyl radicals. When photobleached samples are maintained at low temperature in the dark, the methyl radicals experience a simple, parallel first-order competition between regeneration of the dimer radical anions, reaction 1, and hydrogen atom



abstraction from neighboring acetonitrile molecules, reaction 2. The reverse of reaction 1 is the photobleaching reaction. The kinetic parameters are such that, at 77 K, recovery of the dimer radical anions in CD₃CN is effectively complete, while abstraction dominates almost totally in CH₃CN, although partial recovery of the anions is found at higher temperatures. If reaction 1 is reversed by continuous illumination, the methyl radicals can only disappear via hydrogen atom abstraction. This fact can be exploited to isolate reaction 2 for study.

The experiments described in this work were performed on samples of crystal I of CH₃CN, CD₃CN, and mixtures containing approximately 10% CH₃CN in CD₃CN. All samples were maintained at 77 K during and after γ irradiation. Photobleaching and ESR measurements were begun after the irradiated samples had stood in the dark for periods ranging from a few days to a few weeks. This ensured the absence of minor contributions from species produced during irradiation, but not stable indefinitely at 77 K in the dark. Typical ESR spectra are shown in Figure 1 for samples during illumination. Figure 1a is from CH₃CN after the CH₃ radicals had completely reacted. Only CH₂CN is observed. The seven-line spectrum of CD₃ radicals is obvious in Figure 1b, with weak outer lines from CD₂CN also visible. A mixture of CD₃ and CH₃ radicals, about 20–25% CH₃ in each case, was evident in the 10% CH₃CN samples, as indicated in Figure 1c. The stick plots show which lines belong to each of the species. The lettered arrows designate the features whose intensities in these first-derivative spectra were taken to be proportional to the concentrations of the various free radicals. Spectrometer conditions were chosen for each such that 10–

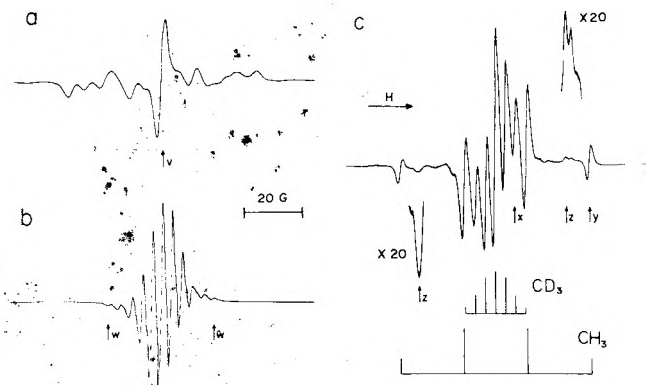


Figure 1. ESR spectra during photobleaching at 77 K of irradiated samples of crystal I of acetonitrile: (a) CH_3CN after complete CH_3 decay; (b) CD_3CN ; (c) 10% CH_3CN -90% CD_3CN . See text for explanation.

20-cm deflections on the chart paper resulted, thereby allowing precise measurement, and each determination was adjusted according to the signal from the ruby crystal, as described in the Experimental Section. The features labeled v, w, x, y, and z belong to CH_2CN , CD_2CN , CD_3 , CH_3 , and CH_2CN , respectively.

Mixtures of CH_3CN and CD_3CN were used in order to obtain CH_3 radicals in a matrix consisting predominantly of CD_3CN molecules. This was desirable for two reasons. First, since one line in the four-line ESR spectrum of CH_3 radicals was essentially free of overlap with other spectra in this case, its intensity provided an unambiguous measure of the relative concentration of the CH_3 radicals, thus permitting small changes to be measured with confidence. Second, it is the *primary* isotope effect in reaction 2 which is of interest. If the analogue of reaction 2 is studied in pure CD_3CN , there are five deuterium atoms which might contribute secondary effects. Three of these are eliminated if CH_3 is allowed to react with CD_3CN .

The presence of the CH_3CN molecules in the mixed samples resulted in a division of the methyl radicals into three relatively distinct groups, distinguished by the time intervals during which they decayed. These were a few hours, a few weeks, and a few months or longer, respectively. Since, as is shown below, the methyl radicals are unable to actually diffuse through the acetonitrile matrix at 77 K, their decay behavior is determined by the isotopic makeup of the molecules surrounding them. Some decay of both CH_3 and CD_3 was seen immediately upon photobleaching. Analysis of features x, y, and z in Figure 1c revealed that, within experimental error, the first-order rate constants calculated from the decay of CH_3 , the decay of CD_3 , and the growth of CH_2CN were the same for this portion of the reaction. This rate constant was the same as that for CH_3 disappearance by abstraction in CH_3CN , so this decay is ascribed to the reaction of those methyl radicals which happened to be adjacent to CH_3CN molecules in the crystal. Since the half-life for this reaction is about 25–30 min at 77 K, decay had essentially ceased after a few hours. These results also yielded the relationship between the magnitudes of the increase in the CH_2CN signal and the decrease in the CH_3 and CD_3 signals. This is of importance in consideration of further decay of the methyl radicals at 77 K.

The second time period extended from a few hours to roughly 3 weeks. Additional, but much slower, decay of CH_3 and CD_3 took place, accompanied by further growth in CH_2CN . Since ESR measurements were made only about once a week after the first day, the rate constant for this portion of the decay was not accurately determined. A value of $1 \times 10^{-4} \text{ min}^{-1}$ for the first-order rate constant

is estimated. Using the intensity relationship determined in the first interval, it was nevertheless found that hydrogen atom abstraction from CH_3CN again accounted for the decay which had occurred.

The fraction of methyl radicals disappearing during these first two stages of reaction depended somewhat on the exact composition of the mixture, which varied to a certain extent as a result of the method of preparation employed here. The approximate behavior is illustrated by the data for a single sample, for which it was found that about 20% of the CH_3 radicals and 30% of the CD_3 radicals reacted during the first two time intervals, about twice as much reaction occurring in the second interval as in the first. The lesser extent of reaction for CH_3 is a reflection of the smaller likelihood of finding a CH_3CN molecule to have been adjacent in the original matrix, and this is statistically unlikely in a matrix consisting predominantly of CD_3CN .

Since the acetonitrile samples were polycrystalline, the microscopic environment is expected to be the same for each methyl radical, except with regard to the isotopic composition of the acetonitrile molecules around it. It should be possible to predict the actual arrangement of surrounding molecules, but, unfortunately, the structure of neither crystalline phase of acetonitrile has been determined. The probable explanation for the fact that hydrogen atom abstraction occurred at two greatly differing rates in the same system is that a given methyl radical could have more than one matrix molecule near it with which it might react. If one is less accessible than the other, reaction with it will be slower. Decay in the first interval is thus presumed to be the loss of those methyl radicals which had an easily accessible CH_3CN molecule, while that in the second interval is the reaction of methyl radicals for which the available CH_3CN molecule was less accessible.

Since the chief interest in this study was in the rate of deuterium atom abstraction from CD_3CN , the first two intervals were simply a necessary delay imposed by the presence of CH_3CN in the matrix. The methyl radicals remaining at the beginning of the third interval were those completely surrounded by CD_3CN molecules, so it is the behavior of these radicals which must be compared with that of CH_3 in CH_3CN in order to determine the kinetic isotope effect.

Measurements were continued over a period of 1.5×10^5 min (3.5 months) on five samples of 10% CH_3CN in CD_3CN and one each of pure CH_3CN and pure CD_3CN . At the beginning of these measurements, each sample had been photobleached at 77 K for a minimum of 3×10^4 min (3 weeks). At the conclusion of the study, the samples were allowed to stand in the dark at 77 K until recovery of the dimer radical anions was complete. ESR spectra were then recorded before and after photobleaching in the ESR cavity, so that the effect of the background signal on features x and y in Figure 1c could be determined. The dimer radical anion signal contributed little to the background, since it was strongly saturated at the microwave power level used. The magnitude of the background correction was referred to the intensity of features z in Figure 1c, and this relationship was used to correct all other spectra in the series. The corrections usually amounted to only 5–10%, so their effect on the kinetic measurements was small. Omitting this correction affected the final results only slightly.

It was found that further decay of the methyl radicals did take place during this series of measurements. This

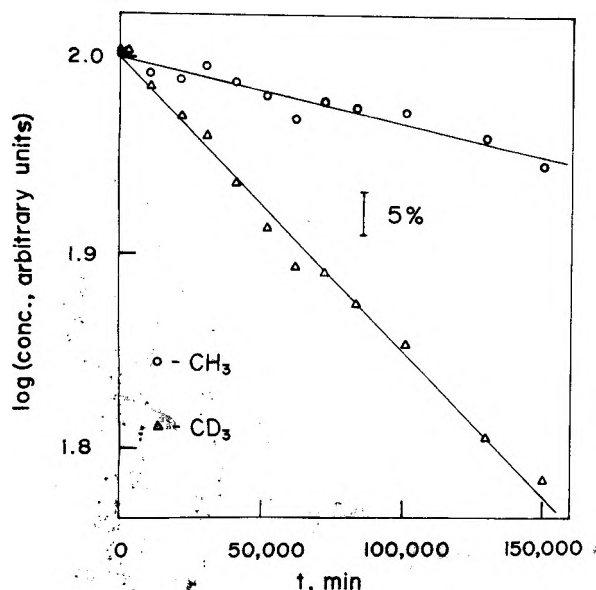


Figure 2. Decay of methyl radicals during photobleaching at 77 K in 10% CH_3CN -90% CD_3CN beginning after 3×10^4 min of photobleaching.

TABLE I: First-Order Rate Constants for Methyl Radical Decay in Crystal I of Acetonitrile during Illumination at 77K^a

Matrix	Radical	k , min^{-1}
10% CH_3CN -90% CD_3CN	CH_3	$9.0 (\pm 1.5) \times 10^{-7}{}^b$
10% CH_3CN -90% CD_3CN	CD_3	$3.6 (\pm 0.2) \times 10^{-6}{}^b$
CD_3CN	CD_3	$2.1 (\pm 0.1) \times 10^{-6}$
CH_3CN	CH_3	$2.5 (\pm 0.3) \times 10^{-2}$

^a All values except for CH_3 in CH_3CN refer to samples previously illuminated for at least 3×10^4 min. ^b Average of five determinations.

is illustrated for a representative sample in Figure 2, where a striking result is immediately apparent. The CD_3 radicals decayed at a considerably greater rate than the CH_3 radicals, and, therefore, to a much greater extent in 1.5×10^5 min. Assuming first-order behavior, least-squares techniques¹⁴ were employed to determine rate constants for CD_3 and CH_3 disappearance. Least-squares lines were drawn in Figure 2, and the rate constants are summarized in Table I. The values listed for the mixed matrix are mean values for the five samples. The stated uncertainties are standard deviations calculated from the five values for each quantity. The least-squares calculations also provided an estimate of the standard deviation for k for each sample, and these were usually about half those in Table I. The larger standard deviations for the mean values reflect the additional uncertainty due to background corrections. The uncertainty for k in CD_3CN is the least-squares estimate of the standard deviation in one determination, and is probably too small. The uncertainty listed for k in CH_3CN was chosen both on the basis of the standard deviation associated with its measurement and to include previous determinations.^{1,15} The reported values fall within the quoted range.

Interpretation of these results depends upon the nature of the reaction being observed. If it were further hydrogen atom abstraction, the CH_2CN concentration should have continued to increase in parallel with CD_3 and CH_3 decay, as it did in the first two phases of the measurements. Analysis of features z in Figure 1c showed that this did not happen. Only a very slight increase in CH_2CN was observed, sufficient to account for about 10% of the methyl radical decay at most. The uncertainties in the CH_2CN measurements are a little larger than for the methyl

radicals, since higher spectrometer sensitivities, and consequently greater noise, were necessary for the weaker CH_2CN signals. To learn whether CH_2CN production might have been obscured by concurrent CH_2CN decay, the long-term stability of the CH_2CN radicals at 77 K was checked in the CH_3CN sample where no methyl radicals were present. The intensity of the strong single line in the CH_2CN spectrum, prominent in Figure 1a, was determined along with the other measurements. No trend was found in the data. They were simply scattered with a standard deviation equal to 1.4% of the mean value. The CH_2CN radicals, and CD_2CN radicals as well, are not expected to be any less stable in the isotopically mixed matrix than in pure CH_3CN .

Deuterium atom abstraction would not be detected directly in the mixed samples, because the CH_3 and CD_3 spectra seriously overlap and distort that of CD_2CN . In pure CD_3CN , however, weak lines in the CD_2CN spectrum lie sufficiently far outside the seven-line CD_3 spectrum for accurate measurement, as may be seen in Figure 1b. The intensity of the outermost features was determined under high sensitivity conditions during the course of these measurements, but no change was observed. The data were scattered with a standard deviation equal to 0.9% of the mean value. The CD_3 signal, on the other hand, decreased by 27%. Since double integration of the ESR signal in the dark and during illumination showed the concentrations of CD_3 and CD_2CN to be roughly equal, deuterium atom abstraction would have been easily detected if it had occurred.

The nature of the decay of methyl radicals in the third reaction interval will be considered further in the Discussion. An experiment was performed on one of the mixed samples which may be of some interest there. An approximate determination of the rates of the recovery reaction of the methyl radicals in the dark at 77 K yielded first-order rate constants of about $3.2 \times 10^{-4} \text{ min}^{-1}$ for CH_3 and $1.9 \times 10^{-3} \text{ min}^{-1}$ for CD_3 . Thus the CD_3 recovery reaction proceeds about 6 times as fast as that for CH_3 .

Since deuterium atom abstraction was not actually observed, the deuterium isotope effect on abstraction cannot be determined. It may be safely concluded, though, that deuterium atom abstraction is definitely slower than the observed decay rate. Therefore, a lower limit for the isotope effect may be calculated from the data in Table I. For CH_3 , $(2.5 \times 10^{-2} \text{ min}^{-1}) / (9.0 \times 10^{-7} \text{ min}^{-1}) = 2.8 \times 10^4$. From the standard deviations in Table I, the standard deviation associated with this value is 0.6×10^4 .

Discussion

Before comparisons with theoretical predictions of the deuterium isotope effect are made, it must be ascertained whether the lower limit established in this work refers to a primary effect only, or whether secondary effects from nonreacting deuterium atoms might be present. Such effects could, in principle, be important at temperatures as low as 77 K. Experimental evidence shows, however, that secondary isotope effects are, in fact, negligible in this reaction. It was found in this work that the initial decay rates of CD_3 and CH_3 in the mixed samples, by hydrogen atom abstraction from CH_3CN , were the same. The methyl deuterium atoms, therefore, contribute no significant secondary effects. In addition, previous measurements by optical methods at 87 K, on crystal I of CD_3CN , CD_2HCN , CDH_2CN , and CH_3CN , showed a linear variation of the hydrogen atom abstraction rate constant with the number of hydrogen atoms in the acetonitrile molecule.¹ This is a clear indication of an extremely large primary isotope effect and negligible secondary effects

from the acetonitrile deuterium atoms. It is concluded, therefore, that the lower limit of 2.8×10^4 established in this work refers to the *primary* deuterium isotope effect alone.

The magnitude of the isotope effect to be expected in the absence of tunneling must be determined before it can be seen whether a large enhancement is indeed present. If the potential energy surface for the reaction were known in detail, the isotope effect could be formulated in terms of activated complex theory,¹⁶ but sufficient information is not available. As an alternative approach, a good estimate of the *maximum* primary isotope effect in the absence of tunneling is obtained from eq 3, where k_H and

$$k_H/k_D = \sqrt{2} \exp(\Delta E_0/RT) \quad (3)$$

k_D are the rate constants for hydrogen and deuterium atom abstraction, respectively, and ΔE_0 is the difference in zero-point energy between the C-H and C-D bonds being broken.¹⁷ From measured values of the asymmetric stretching frequencies in solid CH_3CN and CD_3CN ,¹⁸ ΔE_0 is found to be about 375 cm^{-1} (1.07 kcal/mol), yielding a maximum primary isotope effect at 77 K in the absence of tunneling of 1.5×10^3 .

The experimental lower limit found here exceeds this maximum by nearly a factor of 20, providing strong support for the hypothesis that quantum mechanical tunneling is important in this reaction. Indeed, the existence of such an extremely large effect would be difficult to rationalize in any other way. The exact, one-dimensional tunneling calculations referred to above predict a value of about 10^5 for this isotope effect at 77 K.⁹ The present results are entirely consistent with this prediction.

The mechanism whereby the methyl radicals remaining after extended photobleaching at 77 K are able to slowly decay is not known. It has been shown in this work that it is neither hydrogen nor deuterium atom abstraction from acetonitrile, and that CD_3 radicals react about four times as fast as CH_3 radicals (see Table I). The fact that the recovery reaction is faster for CD_3 radicals by a similar factor suggests a possible connection between the two. During continuous illumination, the methyl radicals occasionally undergo reaction 1 to regenerate dimer radical anions, which are immediately photobleached again. This cycling occurs more rapidly for CD_3 radicals since their recovery reaction rate is greater. It is possible that some occurrence connected with such cycling could lead to methyl radical loss. For example, the photobleaching reaction might not always go as written in eq 1. If the excess electron were simply ejected from the anion, it could move to a new location in the matrix to form a new anion. Or the recovery reaction might proceed in such a manner that the neutral molecule involved were not from the

original dimer radical anion, depending, of course, on appropriate three-dimensional lattice structure. Either of the above phenomena would confer a certain artificial "mobility" on the radical species. Subsequent decay, however, would most likely be by hydrogen atom abstraction in the new location, and this was not observed. Real mobility of the radicals via diffusion through the crystal lattice also seems to be ruled out. Thus, the substituted methyl radical, CH_2CN , did not decay at 77 K in CH_3CN . In addition the CD_2CN radicals in CD_3CN did not decay while the CD_3 radicals were doing so. Diffusion of either should have led to a decrease in both through radical-radical combination reactions. Although the actual mechanism remains unknown for the present, it should be emphasized that conclusions reached in this work are independent of it. The intervention of a decay reaction other than deuterium atom abstraction simply forced the determination of a lower limit to, rather than the value of, the primary isotope effect. The difference in CD_3 and CH_3 behavior in the mixed samples is not related to the abstraction reaction, so it is appropriate to determine the isotope effect from the more slowly reacting of the two.

Acknowledgment. The author is indebted to Professor J. E. Willard for the gift of the ruby crystal and to Professor F. Williams for use of the γ radiation source and for valuable discussions. Financial support from the Research Corporation is gratefully acknowledged.

References and Notes

- (1) E. D. Sprague and F. Williams, *J. Am. Chem. Soc.*, **93**, 787 (1971).
- (2) J.-T. Wang and F. Williams, *J. Am. Chem. Soc.*, **94**, 2930 (1972).
- (3) A. Campion and F. Williams, *J. Am. Chem. Soc.*, **94**, 7633 (1972).
- (4) E. D. Sprague, *J. Phys. Chem.*, **77**, 2066 (1973).
- (5) M. A. Neiss, E. D. Sprague, and J. E. Willard, *J. Chem. Phys.*, **63**, 1118 (1975).
- (6) For a review, see J. E. Willard in "Fundamental Processes in Radiation Chemistry", P. Ausloos, Ed., Wiley-Interscience, New York, N.Y., 1968, p 599.
- (7) J.-T. Wang, Ph.D. Thesis, The University of Tennessee, 1972.
- (8) M. H. J. Wijnen, *J. Chem. Phys.*, **22**, 1074 (1954).
- (9) R. J. LeRoy, E. D. Sprague, and F. Williams, *J. Phys. Chem.*, **76**, 546 (1972).
- (10) See, for example, E. F. Caldin, *Chem. Rev.*, **69**, 135 (1969).
- (11) E. D. Sprague, Ph.D. Thesis, The University of Tennessee, 1971.
- (12) W. E. Putnam, D. M. McEachern, and J. E. Kilpatrick, *J. Chem. Phys.*, **42**, 749 (1965).
- (13) See E. D. Sprague, K. Takeda, J.-T. Wang, and F. Williams, *Can. J. Chem.*, **52**, 2840 (1974), and references therein.
- (14) P. R. Bevington, "Data Reduction and Error Analysis for the Physical Sciences", McGraw-Hill, New York, N.Y., 1969.
- (15) F. P. Sargent, M. G. Bailey, and E. M. Gardy, *Can. J. Chem.*, **52**, 2171 (1974).
- (16) See, for example, R. E. Weston and H. A. Schwarz, "Chemical Kinetics", Prentice-Hall, Englewood Cliffs, N.J., 1972, p 109.
- (17) See, for example, R. P. Bell, "The Proton in Chemistry", 2nd ed, Cornell University Press, Ithaca, N.Y., 1973, Chapter 12.
- (18) (a) D. E. Milligan and M. E. Jacox, *J. Mol. Spectrosc.*, **8**, 126 (1962); (b) E. L. Pace and L. J. Noe, *J. Chem. Phys.*, **49**, 5317 (1968).

Ionic Vs. Molecular Nature of Monomeric Ammonium and Hydronium Nitrate. Infrared Spectra of $\text{H}_3\text{O}^+\text{NO}_3^-$ and $\text{NH}_4^+\text{NO}_3^-$ Solvated in Argon Matrices

G. Ritzhaupt and J. P. Devlin*

Department of Chemistry, Oklahoma State University, Stillwater, Oklahoma 74074 (Received July 28, 1976)

Publication costs assisted by the National Science Foundation

Nitric acid was allowed to react with NH_3 and H_2O in an argon matrix environment to permit study of the proton transfer process leading to the ion pairs $\text{H}_3\text{O}^+\text{NO}_3^-$ and $\text{NH}_4^+\text{NO}_3^-$. For concentrations of HNO_3 that yield primarily the monomer spectrum in a pure argon matrix (i.e., matrix gas to HNO_3 mole ratios of ~ 1000), only $\text{NH}_4^+\text{NO}_3^-$ forms upon reaction with NH_3 . However, reaction with H_2O under similar conditions yields primarily the $\text{H}_2\text{O}\cdot\text{HNO}_3$ complex; the ion pair, $\text{H}_3\text{O}^+\text{NO}_3^-$, is not stabilized until sufficient water of hydration is present in the matrix ($\sim 6\text{--}10\%$). Since ion pairs, $\text{NH}_4^+\text{NO}_3^-$ and $\text{H}_3\text{O}^+\text{NO}_3^-$, are stable for an extensive range of NH_3 or H_2O matrix concentrations, it has been possible to observe the effect of variable extents of solvation of these cations on the distortion of the NO_3^- ion by monitoring the $\nu_3(\text{e})$ splitting as a function of matrix composition. Regardless of the degree of solvation the cation and anion are apparently contact paired since the ions are formed in direct contact and it has been shown that, for analogous systems, M^+NO_3^- ions are paired in direct contact. The magnitude of the $\nu_3(\text{e})$ splitting ranges from 20 cm^{-1} for completely ammoniated $\text{NH}_4^+\text{NO}_3^-$ and 65 cm^{-1} for completely hydrated $\text{H}_3\text{O}^+\text{NO}_3^-$ to $\sim 173\text{ cm}^{-1}$ for the former in a 3% NH_3 -argon matrix and $\sim 150\text{ cm}^{-1}$ for the latter in a 6% H_2O -argon matrix. These data emphasize the severe distortion produced by a bare NH_4^+ or H_3O^+ ion in contact with an oxyanion, a distortion believed to represent a composite of charge polarization and hydrogen bonding. Finally, work with concentrated $\text{H}_3\text{O}^+\text{NO}_3^-$ -in-glassy- H_2O deposits show conclusively that $\Delta\nu_3$ increases, in such primarily ionic media, as the solvent concentration becomes insufficient for complete hydration of the cations. This observation is compared with differences noted previously between M^+NO_3^- ion pairs at high dilution in glassy matrices and the same ion pairs in highly concentrated liquid solutions. Insights to the behavior of concentrated liquid solutions and molten salts follow.

Introduction

In a recent series of papers^{1,3} it has been shown that (a) the molten alkali metal nitrates volatilize smoothly in the form of ion pairs M^+NO_3^- ; (b) the nitrate anion is severely distorted in such ion pairs in a manner gauged by the splitting of the $\nu_3(\text{e})$ degeneracy, $\Delta\nu_3$, which ranges from 171 cm^{-1} for K^+NO_3^- to 260 cm^{-1} for Li^+NO_3^- in argon matrices; (c) the variation in extent of solvation of these contact ion pairs, by H_2O or NH_3 in argon matrices, is clearly observable by the stepwise collapse of $\Delta\nu_3$; and (d) the solvated M^+ ions in contact with the NO_3^- ion have lost 80–90% of their ability to distort the NO_3^- ion. Such data are useful in the interpretation of liquid solution spectra^{3,4} so the adaptation of this approach to other familiar ion pairs such as $\text{NH}_4^+\text{NO}_3^-$ and $\text{H}_3\text{O}^+\text{NO}_3^-$ is desirable.

It is general knowledge that ammonium salts NH_4X , such as NH_4Cl and NH_4NO_3 , vaporize as the molecular species NH_3 and HX ; thus any attempt to observe the vibrational spectra of the NH_4^+X^- ion pairs isolated in various matrices might appear to be doomed to failure. However, when it is recognized that it is the ion pairs solvated to varying degrees that are of greatest interest, the difficulty can be sidestepped by preparation of the $\text{NH}_4^+\text{NO}_3^-$ or $\text{H}_3\text{O}^+\text{NO}_3^-$ ion pairs within matrices by codeposition of HNO_3 with an excess of NH_3 or H_2O . The variably solvated $\text{NH}_4^+\text{NO}_3^-$ or $\text{H}_3\text{O}^+\text{NO}_3^-$ pairs are then obtained by introduction of appropriate quantities of argon as a third component.

Such an approach to the study of these variably solvated ion pairs must be predicated on the formation of ionic $\text{NH}_4^+\text{NO}_3^-$ or $\text{H}_3\text{O}^+\text{NO}_3^-$ from HNO_3 in contact with NH_3 or H_2O in a matrix. This cannot be safely presumed since Ault and Pimentel have shown that HCl and NH_3 (or H_2O)

in dilute N_2 matrices do not engage in a proton transfer reaction but rather associate through strong hydrogen bonds.^{5,6} They conclude that for NH_3 and HCl , but most likely not NH_3 and HI , long-range ionic lattice forces are necessary to stabilize the ionized form in the pure crystal. Presumably, since the ionized forms are also stable in H_2O and NH_3 liquid solutions, the stabilization energy can be derived from the solvation of the ions and/or the contact ion pairs.

Thus, this study was designed to determine initially whether or not HNO_3 engages in proton transfer with NH_3 and H_2O when in contact within nonionic matrices such as solid argon, NH_3 -argon, and H_2O -argon mixtures, and pure glassy NH_3 or H_2O . Once it had been established that the ionic forms, $\text{NH}_4^+\text{NO}_3^-$ and $\text{H}_3\text{O}^+\text{NO}_3^-$, are present in matrices containing 3% or more H_2O or NH_3 , most interest was centered on the effect of varying the degree of solvation of the ion pairs within an argon matrix. As in the previous matrix studies of alkali metal nitrate ion pairs, the principal indicator of the solvation effect is the progressively reduced splitting of the "degenerate" nitrate ion antisymmetric stretching mode. The reasonably extensive vibrational data obtained include values for the hydrogen-bonded $\text{H}_2\text{O}\cdot\text{HNO}_3$ complex, which is the dominant species in matrices dilute in HNO_3 and H_2O , but principal emphasis will be placed on the magnitude of $\Delta\nu_3$ and its variation with solvation.

Experimental Section

The sampling consisted essentially in imbedding HNO_3 molecules in a variety of solid matrices at $\sim 10\text{ K}$. In a few experiments this was effected by volatilizing HNO_3 from concentrated aqueous nitric acid. However, in the usual case the HNO_3 was obtained by vaporizing NH_4NO_3

TABLE I: Infrared Frequencies for Matrix-Isolated Nitric Acid in N₂^a and Argon Matrices (cm⁻¹)

Assignments	H ¹⁴ NO ₃		D ¹⁴ NO ₃	
	N ₂ ^a	Argon	N ₂ ^a	Argon
OH stretch	3490	3505	2574	2586
NO ₂ antisymmetrical stretch	1697	1695	1669	1673
NOH bend	1343	1318	1031	1010
NO ₂ symmetrical stretch	1311	1305	1311	1307
NO'	902	893	905	892
Nitrogen out-of-plane	767	762	767	760
NO ₂ valence bend	660		660	
ONO' bend	597		559	
OH torsion	479		361	

^a From ref 7.

at ~50 °C. Of course this implied simultaneous deposition of NH₃ but, in over half of the experiments, much more NH₃ was deliberately added to the matrix-forming gas. In any case, since the HNO₃ was usually present in the matrix as a trace impurity, the same quantity of NH₃ introduced from the salt vaporization could not influence the spectroscopic measurements. This was guaranteed by employing sampling conditions which had been shown to give complete isolation for HNO₃ in pure argon. Such isolation is indicative of matrix gas-to-HNO₃ mole ratios of the order of 1000.

A predetermined percentage of NH₃, ND₃, or H₂O was premixed with dry argon to form the gas for matrix co-deposition with the vapors of either NH₄NO₃ or ND₄NO₃. Typical sample deposition times were 3 h with condensation at 10 K on an infrared substrate within a standard low-temperature cell fitted to an Air Products CS-202 closed-cycle helium refrigerator. Spectra were recorded in the 600–4000-cm⁻¹ range with a Beckman IR-7 infrared spectrometer. Deuterated samples were employed in many instances to eliminate ambiguity in the interpretation of the ν₃ nitrate-band complex, introduced by the NH₄⁺ bending mode near 1480 cm⁻¹ and the N–O–H bending mode of HNO₃ near 1320 cm⁻¹.

Results and Interpretation

A. Pure Argon Matrices. Spectra for both NH₄NO₃ and ND₄NO₃ isolated in pure argon have been obtained for a considerable range of matrix-to-sample ratios. As expected, for the highly dilute matrices the infrared spectra were composites of the HNO₃ (DNO₃) monomer spectra, as reported by Guillory and Bernstein,⁷ and the NH₃ (ND₃) monomer spectra of Pimentel et al.,^{5,8} with only minor dimer concentrations and small matrix shifts. For slightly greater concentrations, for which the nitric acid dimer bands were more intense, extremely weak absorption bands could be identified as due to NH₄⁺NO₃⁻. The pure-argon matrix spectra indicate that, even at low temperatures (50 °C), NH₄NO₃ vapor is composed of molecular NH₃ and HNO₃ only, with no evidence found for either NH₃·HNO₃ or NH₄⁺NO₃⁻.

At much lower argon-to-sample ratios (~10:1) the monomer and dimer HNO₃ bands, for which frequencies are shown in Table I, were replaced by broad shifted bands undoubtedly indicative of aggregation of the HNO₃ and NH₃. Moreover, bands produced by the ν₁, ν₂, and ν₃(e) vibrations of the NO₃⁻ ion became apparent. Complete elimination of the argon matrix, i.e., direct deposition of NH₄NO₃ vapor, had little further effect except to noticeably increase the fraction of ionized species.

Since the ionized form of NH₄⁺NO₃⁻ (or ND₄⁺NO₃⁻) was not observed in the most dilute argon matrix samples, it might appear impossible to assign frequencies to the ν₃ doublet for the ion pair isolated in argon. However, as for

TABLE II: Infrared Frequencies for the Nitric Acid Monomer, Dimer, and Molecular Complex, H₂O·HNO₃, in an Argon Matrix (cm⁻¹)

Assignment	Monomer	Dimer ^a	Complex
NO ₂ antisymmetrical stretch	1695	1692	1673
NO ₂ symmetrical stretch	1305	1302	1303
NO' stretch	893	927	947
NOH bend	1318	1407	1432

^a Dimer values for N₂ matrix from ref 7 are 1689, 1318, 939, and 1398 cm⁻¹.

TABLE III: Frequencies, in cm⁻¹, for the Dominant ν₃ Band Components for H₂O·NO₃⁻ Ion Pairs Isolated in Mixed H₂O–Argon and NH₃–Argon Matrices, Respectively

	H ₃ O ⁺ NO ₃ ⁻				100% H ₂ O	
	6% H ₂ O	12%	25%	50%		
ν _{3a}	~1290	1335	1335	1335	1335	
ν _{3b}	1440	1415	1410	1405	1400	
Δν ₃	150	80	75	70	65	
n ^a	NH ₄ ⁺ NO ₃ ⁻					100% NH ₃
	3% NH ₃	6%	12%	25%	50%	
	0	1	2	-	-	m - 1
ν _{3a}	1282	1290	1313	1336	1337	1348
ν _{3b}	1455	1440	1395	1386	1372	1368
Δν ₃	173	150	82	50	35	20

^a n refers to the number of NH₃ molecules solvating the NH₄⁺, and m is the maximum inner shell solvation number for the cation (It is reduced by one for the 100% NH₃ matrix because of the contacting NO₃⁻ ion).

the earlier results for M⁺NO₃⁻ ion pairs, this study has yielded a direct measure of the ultimate distortion of a nitrate ion by the NH₄⁺ cation. Such a measure, in terms of Δν₃, can be made from the mixed matrix data presented in the following sections.

B. Mixed H₂O–Argon Matrices. It might seem more natural first to consider the effect of excess NH₃ rather than H₂O on the state of HNO₃ within a matrix, and this was the chronology of the experimental study. However, it develops that the H₂O·HNO₃ complex is significantly more stable, relative to the ion pair state, than the NH₃·HNO₃ complex, at least in the presence of solvating molecules, and it is advantageous to discuss first the system in which the complex is sufficiently stable that the transition from a molecular complex to an ion pair can be spectrally traced as additional solvating molecules are added.

The influence of H₂O of solvation on the HNO₃ spectrum in the 1250–1500-cm⁻¹ range is clear from Figure 1. This figure shows the most dramatic effect of the solvation sequence. The addition of water up to concentrations of ~3% in the matrix eliminates the N–O–H bending mode band at 1318 cm⁻¹ and slightly broadens the NO₂ stretching mode band at 1303 cm⁻¹. Simultaneously, two broad bands, one at 1435 cm⁻¹ and the second underlying the NO₂ stretch band (~1290 cm⁻¹), begin to appear. (The 1290-cm⁻¹ band appears most clearly in a 6% H₂O sample not represented in Figure 1.) As Guillory and Bernstein point out, the NOH mode, which they observe to shift by 45 cm⁻¹ upon dimerization, should be ultrasensitive to H bonding involving the OH group of HNO₃, so the disappearance of the 1318-cm⁻¹ band, which occurs simultaneously with a shift of the monomer symmetric stretch fundamental from 893 to ~950 cm⁻¹, is attributed to formation of the H₂O·HNO₃ complex. The high-frequency N–O antisymmetric stretching mode, which is somewhat masked by the H₂O ν₂ bending mode, appears to shift from

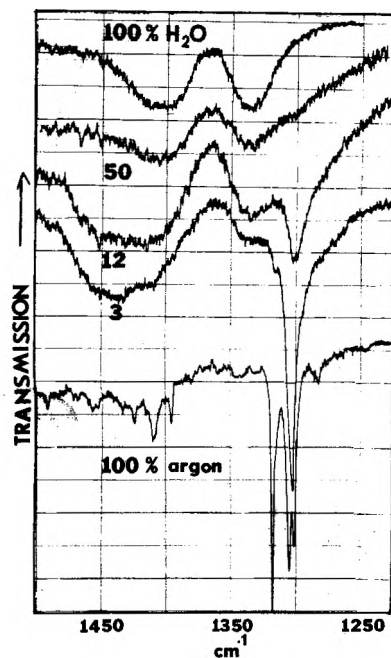


Figure 1. Infrared bands in the ν_3 nitrate ion mode region for HNO_3 isolated in matrices with composition varying from pure argon to pure H_2O . The numbers indicate the percent water for the mixed water-argon matrices.

1695 to $\sim 1670\text{ cm}^{-1}$ upon complexation of HNO_3 with H_2O . The frequencies assigned to the H-bonded complex of HNO_3 are summarized in Table II, where they are also compared with the monomer and dimer values. A new weak sharp band at 1432 cm^{-1} in a 1.5% H_2O sample (not shown) has been assigned to the shifted NOH frequency.

When the H_2O concentration is increased to 12% the bands assigned to the complex rapidly fade away while the broad doublet in the $1300\text{--}1450\text{-cm}^{-1}$ region gains intensity and, aside from the intense water bands, dominates the spectrum. The effect of further hydration, as depicted by the top two curves of Figure 1, is continued reduction of the spacing of the two bands until for a pure glassy H_2O matrix the splitting is reduced to 65 cm^{-1} and the band system is very reminiscent of that obtained for the ν_3 nitrate ion mode of various M^+NO_3^- ion pairs in glassy water matrices.³ Thus this doublet is assigned to the ν_3 mode of $\text{H}_3\text{O}^+\text{NO}_3^-$ existing as the completely hydrated, but contacting, ion pair. The increase in the doublet spacing, to a maximum of $\sim 150\text{ cm}^{-1}$ for the 3% H_2O sample, reflects the effect of decreasing hydration, particularly of the H_3O^+ ion, an effect very similar to that reported for Li^+NO_3^- and K^+NO_3^- .³ In fact, the top three curves of Figure 1 are remarkably similar to the corresponding published Li^+NO_3^- curves.

This interpretation requires that the H_3O^+ ion exist in all HNO_3 samples having a water content of 3% or greater. Apparently the infrared bands of this species, expected at 2800 , 1750 , and 1200 cm^{-1} ,⁹ are relatively weak compared to the notoriously intense nitrate ν_3 band, since no evidence of these features was found in the matrix samples prepared by codeposition of the dilute NH_4NO_3 vapors. However, extremely broad bands are observed in these spectral regions for concentrated HNO_3 in H_2O samples prepared by direct deposition of concentrated nitric acid vapors.

C. *Mixed $\text{NH}_3(\text{ND}_3)$ -Argon Matrices.* In contrast to the H_3O^+ case, the NH_4^+ modes have been observed in these matrices, with interference from the ν_2 bending mode in the $1400\text{--}1500\text{-cm}^{-1}$ range necessitating the use of deuterated ammonium nitrate and ammonia. Thus the discussion here will refer to Figure 2, which contains both

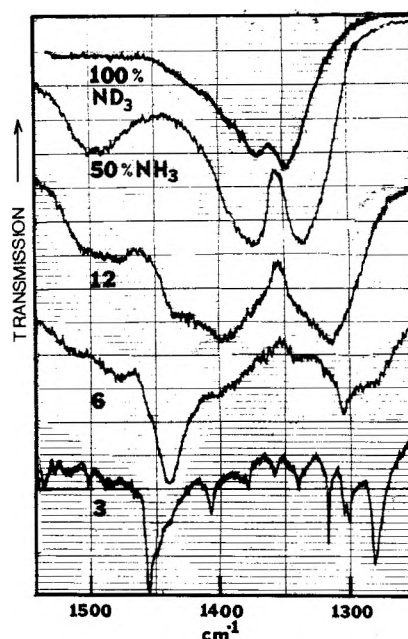


Figure 2. Infrared bands in the ν_3 nitrate ion mode region for HNO_3 (DNO_3) isolated in matrices containing a varying percentage of NH_3 (ND_3) in argon. The numbers indicate the percent ammonia in the mixed matrix.

normal and deuterated sample spectra, and to Figure 1 for the HNO_3 -in-pure-argon curve, since it has not been duplicated in Figure 2.

A comparison of the 3% NH_3 matrix spectrum of Figure 2 with the pure argon matrix spectrum of Figure 1 shows a dramatic reduction in the intensity of the HNO_3 monomer bands at 1305 and 1318 cm^{-1} and a strong increase in the intensity of the previously very weak features at 1282 and 1455 cm^{-1} . Since no new bands assignable to the $\text{NH}_3\text{-HNO}_3$ complex appear, simultaneously, in either the N-O antisymmetric (1680 cm^{-1}) or symmetric (950 cm^{-1}) stretching regions, and since the 1282 - and 1455-cm^{-1} bands behave, on further ammoniation, as expected for the $\nu_3(e)$ doublet of a nitrate ion in the $\text{NH}_4^+\text{NO}_3^-$ ion pair, this strong doublet in the 3% NH_3 matrix has been assigned to this contact ion pair isolated in an argon matrix. Further, in considering the 6% NH_3 curve of Figure 2, it is likely, in view of the previous discussion, that little of either isolated HNO_3 or molecularly complexed nitric acid remains at this ammonia concentration. Again, an examination of the symmetric and antisymmetric nitric acid N-O stretching regions shows very weak features for the isolated HNO_3 monomer but nothing assignable to the molecular complex. Since the ν_3 nitrate ion mode doublet (1290 and 1440 cm^{-1}) is strong and dominant in this matrix the conclusion is forced that the molecular complex $\text{NH}_3\text{-HNO}_3$ is not sufficiently stable to contribute to the spectrum for HNO_3 in a dilute argon matrix, whether enriched with NH_3 or not. It is particularly clear that the $\text{NH}_3\text{-HNO}_3$ complex is less stable than the $\text{H}_2\text{O-HNO}_3$ complex, relative to the ionized form, and it appears that NH_4NO_3 behaves in the manner predicted for NH_4I ,⁵ i.e., the ionic crystal does not depend on a long-range Coulomb field for stability.

As for other cations,³ it is clear that increasing ammoniation of the NH_4^+ ion, which occurs with increasing NH_3 matrix concentration (Figure 2), diminishes distortion of the contact-paired NO_3^- anion and thus reduces $\Delta\nu_3$ from the 173-cm^{-1} value for a 3% NH_3 sample to only 20 cm^{-1} in a pure glassy NH_3 matrix. This reduction is more impressive than that described for $\text{H}_3\text{O}^+\text{NO}_3^-$ but, when the residual water matrix distortion of $\sim 55\text{ cm}^{-1}$ is

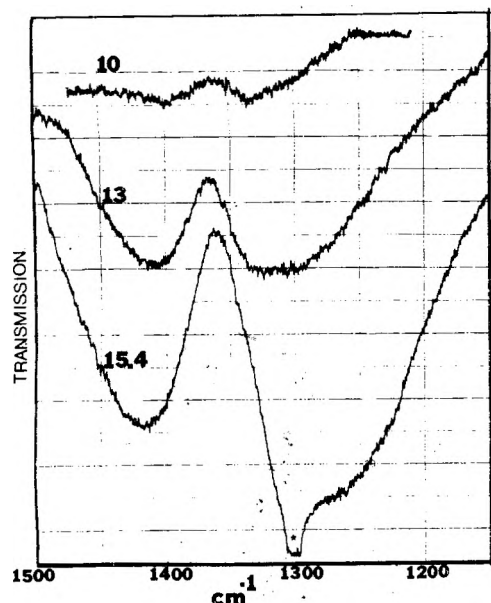


Figure 3. Infrared bands in the ν_3 nitrate ion mode region for HNO_3 -in- H_2O glasses. The numbers refer to the HNO_3 molarities for the aqueous solutions that served as vapor sources for the glassy deposits. The asterisk marks the $\text{H}_2\text{O}\cdot\text{HNO}_3$ feature most apparent in the 3% H_2O curve of Figure 1.

considered^{3,10} (from H bonding of H_2O with NO_3^-), the behaviors are quite comparable.

As mentioned, bands assignable to the NH_4^+ ion appear in all the mixed NH_3 -argon matrix spectra. Thus, the feature at 1495 cm^{-1} in the 50% NH_3 curve (Figure 2), which is missing in the corresponding deuterated sample spectrum, has been assigned to the ν_2 band of NH_4^+ . Similarly NH_4^+ is the likely source of a broad band at $\sim 2850\text{ cm}^{-1}$ that shifts to $\sim 2150\text{ cm}^{-1}$ in the deuterated samples.

D. HNO_3 in Pure Glassy H_2O . The top curve of Figure 1 is for HNO_3 at extremely low concentration in an otherwise pure glassy H_2O matrix. As noted, the spectrum for such a sample is that for pure H_2O plus hydrated, but well-isolated, $\text{H}_3\text{O}^+\text{NO}_3^-$ contact ion pairs. By direct deposition of the vapors from aqueous nitric acid solutions, ranging in concentration from 10 to 15.4 M, a considerable range of HNO_3 concentrations in H_2O matrices was obtained. For a 10 M solution the deposit spectrum, Figure 3, was similar to that of Figure 1 (top curve), but the ratio of HNO_3 to H_2O in the vapor phase increases rapidly and the deposit spectra are changed greatly for the 13 and 15.4 M HNO_3 solutions. The complete spectrum for the 13 M case shows definite bands for the $\text{NO}_3^- \nu_2$ and ν_1 modes (825 and 1037 cm^{-1}) in addition to the ν_3 doublet (~ 1325 and 1410 cm^{-1}) of Figure 3, as well as very weak $\text{H}_2\text{O}\cdot\text{HNO}_3$ bands near 950 and 1300 cm^{-1} . The 15.4 M deposit, on the other hand, shows strong complex ($\text{H}_2\text{O}\cdot\text{HNO}_3$) bands (945 , 1303 , and 1670 cm^{-1}) in addition to intense NO_3^- absorptions including the ν_3 components seen at ~ 1280 and 1418 cm^{-1} in Figure 3.

These data raise two basic questions: (1) why does the complex gain some stability, relative to the ion pair, as the HNO_3 concentration in the H_2O matrix increases, and (2) why does the ν_3 splitting, i.e., $\Delta\nu_3$, increase from 65 cm^{-1} in the dilute H_2O matrix to $\sim 138\text{ cm}^{-1}$ for the concentrated case? The latter question is particularly interesting as a similar behavior is familiar for other cation systems in liquid aqueous and ammonia solutions.^{11,13} It seems that answering the first question may help with the answer to the second. Although the concentrations in the matrices are not known, the measured spectra indicate that the

$\text{H}_2\text{O}:\text{HNO}_3$ ratio is small for the 13 M deposit and very small for the 15.4 M case. For example, for the same samples which yielded the curves in Figure 3, the torsional (800 cm^{-1}) H_2O band was detectable in the 13 M case but missing for the 15.4 M sample. This suggests that there is insufficient H_2O to hydrate every $\text{H}_3\text{O}^+\text{NO}_3^-$ ion pair so, in the absence of solvent stabilization energy, the $\text{H}_2\text{O}\cdot\text{HNO}_3$ species gains stability, as was also noted for the argon matrices. This also requires that the long-range Coulomb ionic stabilization energy does not dominate as it does in the crystal phase, a situation apparently assured by the disordered character of the glassy deposits.

If this is an acceptable view of the origin of the stability of the complex in the deposits formed from concentrated HNO_3 in H_2O , then it follows that the H_3O^+ ions that do form are relatively bare and will have a much greater, anion-distorting ability than the fully hydrated H_3O^+ ions that adjoin the NO_3^- ion in the dilute pure- H_2O matrices. In essence, this approach leads to the conclusion that the increased $\Delta\nu_3$ value results from the increased ability of a given cation, H_3O^+ in this case, to polarize a given anion. This is another way of saying that the ions are paired in rather specific configurations. The general validity of the $\text{H}_3\text{O}^+\text{NO}_3^-$ data under consideration here is strengthened by the related observation that, for glassy $\text{NH}_4^+\text{NO}_3^-$ prepared by direct deposition of NH_4NO_3 vapors and, therefore, having a definite 1:1 ratio, the $\Delta\nu_3$ value is 82 cm^{-1} ($\nu_{3a} = 1333\text{ cm}^{-1}$ and $\nu_{3b} = 1415\text{ cm}^{-1}$), the ν_3 values being similar to those reported for the molten salt (1315 and 1415 cm^{-1}).¹⁴ The molten NH_4NO_3 salt ν_3 splitting was interpreted as a reflection of a specific cation-anion interaction involving some hydrogen bonding, and we have reached a similar conclusion for the glassy $\text{H}_3\text{O}^+\text{NO}_3^-$ salt.

Discussion

The data for dilute solid solutions of HNO_3 in mixtures of argon with H_2O and argon with NH_3 are consistent with results from similar previous studies. The observation that the complex $\text{H}_2\text{O}\cdot\text{HNO}_3$ is considerably more stable, relative to $\text{H}_3\text{O}^+\text{NO}_3^-$, than is $\text{NH}_3\cdot\text{HNO}_3$, relative to $\text{NH}_4^+\text{NO}_3^-$, is consistent with the conclusion of Ault and Pimentel that NH_3 is a better proton acceptor (forms a stronger hydrogen bond) with HCl than is H_2O .^{5,6} On the other hand, the stabilization of the contact ion pair, $\text{H}_3\text{O}^+\text{NO}_3^-$, in a molecular environment via the hydration energy, though predictable, has not been previously demonstrated for a matrix environment. It is interesting, however, that, in spite of the hydration energy, there is evidence for small amounts of $\text{H}_2\text{O}\cdot\text{HNO}_3$ even in a 50% H_2O -argon matrix. It is equally noteworthy that, because solvent stabilization is required for the $\text{H}_3\text{O}^+\text{NO}_3^-$ pair, it is impossible to observe the simple (unsolvated) ion pair imbedded in the argon matrix, while the corresponding $\text{NH}_4^+\text{NO}_3^-$ ion pair, with no solvation, forms upon NH_3 contact with HNO_3 in the dilute matrices and, consequently, produces sharp bands at 1282 and 1455 cm^{-1} as appear in Figure 2 for the 3% NH_3 matrix.

If one ignores spectral features of the $\text{H}_2\text{O}\cdot\text{HNO}_3$ complex, the results for varying degrees of solvation of the $\text{H}_3\text{O}^+\text{NO}_3^-$ ion pairs are analogous to previous ones for M^+NO_3^- contact ion pairs, where M^+ is an alkali metal cation.³ In fact, considering the greater size and much lower polarizing power of the NH_4^+ and H_3O^+ ions relative to the M^+ ions, it is surprising how closely the distorting ability of these cations mirrors that of the M^+ cations. For a given percentage of H_2O or NH_3 in the matrix the $\Delta\nu_3$ value is very similar to the corresponding $\Delta\nu_3$ value of Li^+NO_3^- . However, it should be remembered that, in the present case, the first H_2O or NH_3 to contact an HNO_3

molecule acts not to solvate the cation but rather to form the complex, which subsequently ionizes. With this in mind one expects one unit of solvation less, for a given solvent percentage, than in the M^+ case and it follows that the anion distortion, though large, is less than for a comparably solvated Li^+ ion and more closely resembles the K^+ case, which indeed is closer to NH_4^+ in ionic radius. Nevertheless, an explanation of the large $\Delta\nu_3$ values, other than polarization of the anion by the cation, is required so it is suggested that the H_3O^+ and NH_4^+ ions engage in hydrogen bonding with the NO_3^- ion. This is not a revolutionary thought, since H bonding of such species with the nitrate ion has been suggested previously.^{10,14}

The results for the concentrated HNO_3 -in- H_2O glasses at 10 K are also consistent with previous liquid solution data which show that the $\Delta\nu_3$ nitrate value increases rapidly with decreasing solvent (H_2O or NH_3)-nitrate ratios.^{12,13} There are several extant rationalizations of this phenomenon: (1) one observes the contact ion pair spectrum only at high concentrations and, when that spectrum becomes dominant, $\Delta\nu_3$ becomes large; (2) $\Delta\nu_3$ is not necessarily large for contact ion pairs, but, at concentrations where such ion pairs are dominant species, dipole-dipole coupling, possible because of the large dipole oscillation associated with ν_3 , gives rise to an increased splitting of the two ν_3 components; and (3) $\Delta\nu_3$ is moderate in size for completely solvated contact ion pairs, but, at high concentrations, the less highly solvated cations can more severely distort the contacting anion.

The published glassy water- and ammonia-isolated contact-ion-pair data together with results presented in this paper show conclusively that $\Delta\nu_3$, for completely hydrated or ammoniated ion pairs in direct contact, is not large, ranging from 20 cm^{-1} for $K^+NO_3^-$ in NH_3 to 65 cm^{-1} for $Li^+NO_3^-$ in H_2O .³ Thus, interpretation (1), taken literally, is ruled out. However, if it is recognized that the cations are incompletely solvated at high salt concentrations, then the data for mixed dilute solvent-argon matrices imply that the cation-distorting ability may increase and greater values of $\Delta\nu_3$ are to be expected. This is basically the third explanation presented above, and is essentially the one reached in this analysis, though some significant contribution to the ultimate splitting from dipole-dipole coupling is possible, judging from molten salt dilution results.¹⁵ Since dipole-dipole coupling effects are sensitive to nitrate ion densities, such coupling effects alone cannot explain a $\Delta\nu_3$ value (138 cm^{-1}) for glassy $H_3O^+NO_3^-$ considerably greater than that (110 cm^{-1}) for molten $Li^+NO_3^-$.

The interpretation presented above is in effect a specific interaction, or ion pair, model for concentrated solutions and molten salts. The remarkable and disturbing element in this viewpoint is that the anions that replace the solvent in the inner coordination sphere of the given cation do not always have a comparable neutralizing effect on the distorting ability of the cation. In the case for $Li^+NO_3^-$, with decreasing amounts of H_2O , this neutralization does occur; the value of $\Delta\nu_3$ increases only 5 cm^{-1} in going from a $Li^+NO_3^-$ contact pair isolated in H_2O (65 cm^{-1})³ to

$Li^+NO_3^-$ isolated in anhydrous molten $Li^+ClO_3^-$ (70 cm^{-1}).¹⁵ However, as the data of Figure 3 show, replacing H_2O in the coordination shell of H_3O^+ with NO_3^- results in a dramatic increase in $\Delta\nu_3$ from 65 to 138 cm^{-1} . The evidence is, therefore, that the H_3O^+ interacts much more specifically with one NO_3^- than does Li^+ in the solvent-free glassy ionic (or molten salt) systems. That is, some molten and glassy salts, such as $Li^+NO_3^-$, may continue to be conveniently viewed as anions in somewhat asymmetric cation cages whereas others, such as $NH_4^+NO_3^-$ and $H_3O^+NO_3^-$, involve considerably stronger interaction of the anion with one cation than with other near-neighbor cations. In fact, the evidence is that, since $\Delta\nu_3$ is similar for $H_3O^+NO_3^-$ whether imbedded in argon or in a nearly pure $H_3O^+NO_3^-$ glassy salt, this specific ion pair interaction is not even much influenced by other near-neighbor anions. Perhaps all we are saying is that H bonds are directional and specific whereas Coulombic forces are not.

A final comment is in order regarding the relative magnitude of $\Delta\nu_3$ for various $M^+NO_3^-$ ion pairs isolated in glassy NH_3 compared to the corresponding $\Delta\nu_3$ values for concentrated solutions in liquid NH_3 . We have measured $\Delta\nu_3$ to be 20 cm^{-1} for the cases where M^+ is NH_4^+ , Na^+ , and K^+ and 47 cm^{-1} for Li^+ while liquid NH_3 values for quite concentrated solutions of MNO_3 are 39, 33, 36, and 43 cm^{-1} for these four cations. At this stage, it appears that the greater values for the solvent-deficient liquid solutions reflect some composite of (1) dipole-dipole coupling effects, (2) reduced solvation of the cation with some increase in anion-distorting ability despite compensating NO_3^- coordination, and (3) errors in curve resolution. The latter point refers to the fact that, whereas the two ν_3 components are clearly observed in all cases for the glassy matrix samples, the solution values are usually determined by resolving a single broad feature into two components.^{4,11,13}

Acknowledgment. This research has been supported by the National Science Foundation.

References and Notes

- (1) D. Smith, D. W. James, and J. P. Devlin, *J. Chem. Phys.*, **54**, 4437 (1971).
- (2) N. Smyrl and J. P. Devlin, *J. Phys. Chem.*, **77**, 3067 (1973).
- (3) G. Ritzhaupt and J. P. Devlin, *J. Phys. Chem.*, **79**, 2265 (1975).
- (4) J. W. Lundeen and R. S. Tobias, *J. Chem. Phys.*, **63**, 924 (1975).
- (5) B. S. Ault and G. C. Pimentel, *J. Phys. Chem.*, **77**, 1649 (1973).
- (6) B. S. Ault and G. C. Pimentel, *J. Phys. Chem.*, **77**, 57 (1973).
- (7) W. A. Guillory and M. L. Bernstein, *J. Chem. Phys.*, **62**, 1058 (1975).
- (8) R. C. Pimentel, M. P. Bulanin, and M. Van Thiel, *J. Chem. Phys.*, **36**, 500 (1962).
- (9) S. Turrell, C. Martel, and P. A. Giguere, Paper $\Sigma M31$, Thirty-First Symposium on Molecular Spectroscopy, The Ohio State University, June 1976.
- (10) (a) D. E. Irish and A. R. Davis, *Can. J. Chem.*, **46**, 943 (1968); (b) T. J. V. Findlay and M. C. R. Symons, *J. Chem. Soc., Faraday Trans. 2*, No 1-6, 820 (1976).
- (11) A. T. Lemley and J. J. Lagowski, *J. Phys. Chem.*, **78**, 708 (1974).
- (12) D. Irish, D. L. Nelson, and M. H. Brooker, *J. Chem. Phys.*, **54**, 654 (1971).
- (13) D. J. Gardiner, R. C. Hester, and W. E. L. Grossman, *J. Chem. Phys.*, **59**, 175 (1973).
- (14) J. P. Devlin, P. C. Li, and G. Pollard, *J. Chem. Phys.*, **52**, 2267 (1970).
- (15) J. P. Devlin, G. Ritzhaupt, and T. Hudson, *J. Chem. Phys.*, **58**, 817 (1973).

Thermodynamics of the Lithium–Lithium Deuteride System

Ewald Veleckis

Chemical Engineering Division, Argonne National Laboratory, Argonne, Illinois 60439 (Received July 1, 1976; Revised Manuscript Received January 10, 1977)

Publication costs assisted by Argonne National Laboratory

Pressure–composition–temperature data were collected for the Li–LiD system in the ranges 0–750 Torr, 1–99 mol % LiD, and 705–871 °C by measuring equilibrium deuterium pressures over encapsulated Li–LiD mixtures. The data yielded a family of five $P_{D_2}^{1/2}$ vs. N_{LiD} isotherms whose shapes indicate the existence of two homogeneous terminal solutions that are separated by a wide miscibility gap. Beginning at the consolute point (1000 ± 10 °C, 61 ± 3 mol % LiD), the gap widens to a range of 21.3–99.0 mol % LiD at the monotectic temperature (689 °C). The mole-fraction solubility at the Li-rich gap boundary and plateau pressures above and below the monotectic temperature may be represented by $N'_{LiD}(\text{satd}) = \exp(2.604 - 3992T^{-1})$, $P_{P_{LiD}}(\text{Torr}) = \exp(21.21 - 16940T^{-1})$, and $P_{P_{LiD}}(\text{Torr}) = \exp(28.04 - 23510T^{-1})$, respectively. The data yielded the equilibrium constant [$K(\text{atm}^{-1/2}) = \exp(-6.630 + 7995T^{-1})$] for the reaction $\text{Li}(\text{soln}) + \frac{1}{2}\text{D}_2(\text{g}) \rightleftharpoons \text{LiD}(\text{soln})$ and expressions for the chemical potentials and activity coefficients of each species as functions of temperature and composition. Activity coefficients, evaluated at $N_{LiD} \rightarrow 0$ and $N_{Li} \rightarrow 0$, were combined with the equilibrium constant to generate temperature-dependence equations for various constants associated with dilute solutions. For the Li-rich limit, the Sieverts' constant [$K' = N_{LiD}/(P_{D_2})^{1/2}$] is given by $K'(\text{mol fraction LiD}/\text{atm}^{1/2}) = \exp(-6.138 + 5599T^{-1})$. Advantages of the Ostwald coefficient in describing the distribution of the dissolved species between liquid and gas phase are discussed.

Introduction

The interaction of gaseous hydrogen isotopes with alkali metals produces ionic monohydrides that, in many respects, are similar to the corresponding halides.¹ Their solutions in the parent metals are usually characterized by the formation of wide miscibility gaps that separate homogeneous terminal solutions. The hydrides of lithium (LiH, LiD, and LiT) are of particular interest since, owing to their simple electronic configurations, they are amenable to theoretical studies.¹ They also have great practical significance, especially in D–T–fueled fusion reactor concepts that employ lithium as a tritium-breeding blanket material.²

Comprehensive studies of solution thermodynamics and phase relations in the lithium–hydrogen isotope systems have been under way in this laboratory for several years. Studies of the Li–LiH system have been reported previously.³ Work on the Li–LiT system is near completion and will be described in a subsequent paper. The results obtained for the Li–LiD system are presented here.

Literature information on the Li–LiD system is sparse. Heumann and Salmon⁴ measured deuterium dissociation pressures over Li–LiD alloys at 700, 750, and 800 °C and deduced approximate decomposition pressures in the two-phase region (plateau pressures) and miscibility gap limits. More recently, Smith et al.⁵ reported plateau pressures and Sieverts' law constants at four temperatures between 700 and 1000 °C. Goodall and McCracken⁶ used a mass-spectrometric technique to measure deuterium dissociation pressures at 700 °C at very low deuterium concentrations ($10^{-5} < N_{LiD} < 0.05$).

All of the above studies were made with lithium sealed in metal capsules whose walls were sufficiently thin to permit rapid permeation by deuterium. Ihle and Wu,⁷ on the other hand, made mass-spectrometric measurements on the vapor phase above dilute solutions ($5 \times 10^{-7} < N_{LiD} < 3 \times 10^{-5}$) contained in Knudsen cells having 0.8-mm-diameter orifices. They found that, in addition to Li and Li₂, the effusing beam contained LiD, Li₂D, and D₂

molecules; at 700 °C and $N_{LiD} = 10^{-5}$ these were in approximate partial pressure ratios of 80:30:1.

Experimental Section

Apparatus and Procedure. The measurements were made using the same experimental approach as that employed for the Li–LiH system.³ The procedure used was as follows. Approximately 1.8 g of pure lithium was sealed in vacuo in a thin-walled (0.38 mm) Armco iron capsule (5.7-cm long, 1.27-cm diameter). The capsule was placed in a double-walled, fused-silica tube which was connected to the apparatus and evacuated.

Double-walled construction of the reaction tube is important for avoiding losses of deuterium owing to its appreciable permeability through fused silica. [$\Phi(700 \text{ °C}) = 1.7 \times 10^{-10} \text{ cm}^3(\text{STP}) \text{ mm/s cm}^2 \text{ Torr}^8$] To minimize deuterium losses, a deuterium atmosphere was maintained in the annular space within the reaction tube at a pressure which was automatically varied (via a differential capacitance manometer) to match the pressure in the inner tube.³

Next, the encapsulated lithium was degassed by heating it in vacuo to just below the α – γ transformation point of iron (910 °C) for ~ 10 days. The volume of the inner reaction tube surrounding the capsule (residual volume) was then determined manometrically at temperature, with helium used as the calibrating gas. Deuterium was introduced in 20–30 measured portions (2–20 mmol). Additions were continued until the pressure reached 1 atm. After each addition, the sample was equilibrated for at least 8 h. This period was found to be adequate for achieving complete equilibration between deuterium and lithium across the capsule walls. The concentration of deuteride in lithium was calculated by subtracting, from the amount of total deuterium added, the amounts remaining in the residual volume, in the vapor space inside the capsule, and dissolved in iron.

Materials. Lithium (99.9+%) was purchased from the Lithium Corporation of America. The metal was purified

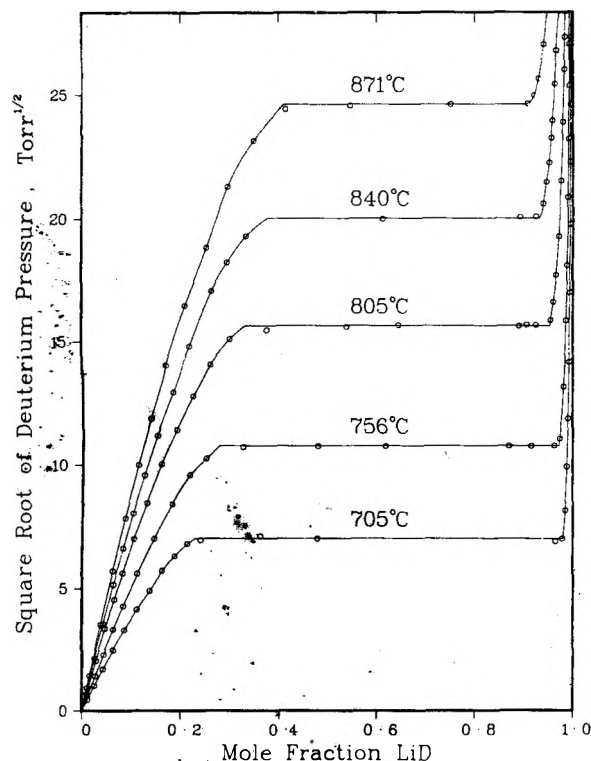


Figure 1. Projections of isothermal data on the square root of deuterium pressure vs. composition plane for the system Li-LiD.

during the capsule-filling step which consisted of immersing the filter end of the capsule (5- μ m porosity filter) in a pot of molten lithium at 400 °C and applying gentle suction through the top end. The purpose of the filter was the removal of solid lithium oxide which has a solubility under these conditions of <0.04 mol %.⁹

Deuterium (<99.99%) was supplied by Air Products and Chemicals, Inc. Prior to use, the gas was absorbed in a titanium-sponge bed. Required amounts of pure deuterium were evolved by heating the bed. The HD content of the gas was found to be $1.1 \pm 0.2\%$ by a mass-spectrometric assay of several gas samples from the residual volume during experiments.

Results

The data obtained for the Li-LiD system consisted of five sets of nearly isothermal pressure-composition values (115 data points), collected within ~ 3 °C of 705, 756, 805, 840, and 871 °C. Four types of corrections were applied to the raw data. (1) For each data set, the individual pressure readings were corrected to the average temperature for the set. (2) All pressure readings were corrected for 1.1% HD in the gas phase, assuming that the decomposition pressure of a hypothetical solution of pure HD in lithium would fall halfway between those of H₂ and D₂. (3) For the solutions dilute in deuterium, a correction was applied for the residual deuterium (or hydrogen) retained in the encapsulated lithium at the start of the experiments. The corrections were determined by extrapolation of the $P_{D_2}^{1/2}$ vs. N_{LiD} plots to zero pressure. For three of the isothermal data sets, the plots crossed the abscissa at $N_{LiD}^0 = 0.004$ (705 °C), 0.004 (756 °C), and 0.001 (871 °C). Therefore, for these isotherms, the calculated concentration at each datum point was incremented by the corresponding value of N_{LiD}^0 . The corrections are somewhat smaller than those of the Li-LiH system,³ probably because of the more rigorous initial degassing in the present work. (4) In the LiD-rich region, a similar extrapolation of the data points to $1/P_{D_2} = 0$ produced

TABLE I: Plateau Pressures for the System Li-LiD

$T, ^\circ\text{C}$	Deuterium pressure, Torr	Concn, mole fraction LiD ^a
Below Monotectic		
631.4	7.72	0.69
641.6	10.67	0.69
642.4	10.38	0.69
651.6	13.90	0.69
652.5	14.21	0.69
661.8	17.92	0.69
671.7	23.42	0.69
682.0	30.95	0.69
Above Monotectic		
692.2	38.92	0.68
702.3	46.64	0.68
722.8	66.86	0.68
743.3	94.72	0.67
763.8	131.5	0.66
784.2	180.3	0.65
805.2	246.3	0.69
826.3	331.4	0.67
836.7	384.3	0.66
857.5	507.9	0.63
879.2	669.0	0.59

^a Fluctuations in deuterium concentrations are due to changes in the amount of deuterium retained in the residual volume of the apparatus at different temperatures. All compositions are within the miscibility gap.

lines that crossed the composition axis at $N_{Li}^0 = -0.002$ (705 °C), -0.004 (756 °C), -0.012 (805 °C), -0.013 (840 °C), and -0.012 (871 °C) instead of at $N_{Li}^0 = 0$. These deviations were attributed to errors accumulated during the numerous additions of deuterium to lithium and, therefore, all N_{LiD} 's were multiplied by their respective normalization factor, $1/(1 - N_{Li}^0)$. Since the same bias in the deviations was also observed in the Li-LiH system,³ another possibility suggests itself; namely, that hyperstoichiometric hydrides may exist in both of these systems, although recent attempts¹⁰ to prepare LiH_{1+x} by exposing normal LiH to very high hydrogen pressures (1-4 MPa) have been unsuccessful.

Listings of corrected pressure-composition values for the Li-LiD system are available in ref 11 and as supplementary material (see paragraph at the end of text regarding supplementary material). The data are also represented in Figure 1 as projections on a plane representing square root of deuterium pressure vs. composition. Computer-generated smooth curves in Figure 1 represent arbitrary fits through the points of each isothermal set of measurements and have no other significance. Each of the curves comprises two rising portions that are separated by a plateau portion. The composition ranges within the first and second rising portions correspond to homogeneous phases; the constant-pressure plateau defines a two-phase coexistence region.

Plateau Dissociation Pressure. A separate series of experiments was made to measure the deuterium plateau pressure as a function of temperature both below and above the monotectic. For these experiments, the deuteride concentration in the sample was brought to the middle range of the plateau region and the deuterium pressure was measured at 19 different temperatures after the sample had been equilibrated for >24 h at each temperature. The results are shown in Table I.

When the logarithm of the plateau pressure is plotted against $1/T$, two distinct linear segments are obtained which correspond to the following least-squares equations:

above monotectic

$$\ln P_{P1,1}(\text{Torr}) = 21.21 - 16940T^{-1} \quad (1)$$

($r = 0.999994$)

below monotectic

$$\ln P_{P1,2}(\text{Torr}) = 28.07 - 23540T^{-1} \quad (2)$$

($r = 0.9994$)

where the "goodness" of fit of the regression lines is expressed in terms of the correlation coefficient, r .¹² The crossing point of eq 1 and 2 occurs at 689 °C and 36.7 Torr and corresponds to the monotectic temperature and plateau dissociation pressure at that temperature, respectively.

Plateau-pressure measurements of Heumann and Salmon⁴ (44, 99, and 250 Torr at 700, 750, and 800 °C) and of Smith and Land⁵ (46, 309, and >750 Torr at 700, 800, and 900 °C) are consistent with eq 1. Literature data are not available for the Li-LiD system at temperatures below the monotectic.

Miscibility Gap Boundaries. These boundaries are defined as points of intersection of the rising portions of the isotherms with the plateau portion. The first boundary, $N'_{\text{LiD}}(\text{satd})$, represents the solubility of LiD in liquid lithium; the second boundary, $N''_{\text{LiD}}(\text{satd})$, that of lithium in liquid LiD. The prime and double prime refer to the first (Li-rich) and the second (LiD-rich) homogeneous terminal solutions.

The miscibility gap boundaries (Table II) were determined graphically from Figure 1, with estimated errors of ± 0.01 for $N'_{\text{LiD}}(\text{satd})$ and ± 0.005 for $N''_{\text{LiD}}(\text{satd})$. The large uncertainty in $N'_{\text{LiD}}(\text{satd})$ resulted from graphical difficulties in establishing correct curvatures for the isotherms near the first boundaries. In the range 705–871 °C, the variation of $N'_{\text{LiD}}(\text{satd})$ with temperature may be adequately represented by the linear equation:

$$\ln N'_{\text{LiD}}(\text{satd}) = 2.604 - 3992T^{-1} \quad (3)$$

($r = 0.9998$)

Extrapolation of eq 3 to the monotectic temperature gives $N'_{\text{LiD}}(\text{satd}, 689 \text{ °C}) = 0.213$ for the solubility of LiD at that temperature.

No attempt was made to fit $N''_{\text{LiD}}(\text{satd})$ to an analytical form because there were too few data points for a curvilinear regression analysis. However, their graphical extrapolation to the monotectic temperature yielded $N''_{\text{LiD}}(\text{satd}, 689 \text{ °C}) = 0.010$ for the monotectic concentration. The corresponding freezing-point lowering, calculated from the heat of fusion of LiD¹³ and assuming ideal solution behavior, was found to be 3.4 °C. This gives a value of 692.4 °C for the melting point of LiD.

Miscibility gap boundaries reported for the Li-LiD system by Heumann and Salmon⁴ [$N_{\text{LiD}}(\text{satd}) = 0.28\text{--}0.94$ at 700 °C, 0.32–0.92 at 750 °C, and 0.38–0.90 at 800 °C] result in much narrower gaps than ours and are probably in error. [Possible sources of errors in the earlier work have been discussed previously.³]

Analysis of Data

The equilibrium constant for the reaction $\text{Li}(\text{soln}) + \frac{1}{2}\text{D}_2(\text{g}) \rightleftharpoons \text{LiD}(\text{soln})$ is given by

$$K = N_2\gamma_2/[N_1\gamma_1(P_{D_2})^{1/2}] \quad (4)$$

where the subscripts 1 and 2 refer to Li and LiD, respectively; N is the mole fraction; γ , the activity coefficient; and P_{D_2} , the equilibrium deuterium pressure.

It is customary to express γ as a power series of N according to Margules' equations.¹⁴ For the present system, two-term series expansions were deemed to be adequate. Thus

$$\ln \gamma_1 = \alpha N_2^2 + \beta N_2^3 \quad (5)$$

and

$$\ln \gamma_2 = (\alpha + \frac{3}{2}\beta)N_1^2 - \beta N_1^3 \quad (6)$$

Substitution of eq 5 and 6 into eq 4 and rearrangement yield a second-order power series in N_2 , i.e.

$$\ln [(P_{D_2})^{1/2}N_1/N_2] = -\ln K + \alpha(1 - 2N_2) + \frac{1}{2}\beta(1 - 3N_2^2) \quad (7)$$

in which experimentally measured quantities occur on the left-hand side, and the unknown temperature-dependent constants (K , α , and β) are on the right-hand side.

Because of the width and asymmetry of the miscibility gap, the data for each terminal solution were separately fitted to eq 7, subject to the following constraints: (1) activity of both components must remain constant across the miscibility gap, (2) the same equilibrium constant must govern both terminal solutions, and (3) $\ln K$, α , and β are linear functions of $1/T$. The data were subjected to an iterative least-squares procedure by which an improved value of K was generated in each iteration cycle. The final $\ln K$ vs. $1/T$ values obtained at the five experimental temperatures could be adequately represented by

$$\ln K(\text{atm}^{-1/2}) = -6.630 + 7995T^{-1} \quad (8)$$

($r = 0.999998$)

The corresponding standard free energy of formation of liquid LiD is

$$\Delta G_f^\circ(\text{kcal/mol}) = 13.17 \times 10^{-3}T - 15.87 \quad (9)$$

The iteration procedure also produced expressions for α 's and β 's as functions of temperature: $\alpha' = -0.9258 + 1746T^{-1}$, $\beta' = -0.8673 + 1301T^{-1}$, $\alpha'' = 20.861 - 28492T^{-1}$, and $\beta'' = 23.534 + 35204T^{-1}$. Substitution of these expressions and eq 8 into eq 7 gives equations relating deuterium pressure to the temperature and the alloy composition. Thus, for the first terminal solution

$$\ln (P_{D_2})^{1/2} = \ln (N_2/N_1) + 6.138 + 1.8516N_2 - 1.3010N_2^2 - (1/T)(5599 + 3492N_2 + 1951N_2^2) \quad (10)$$

and, for the second terminal solution

$$\ln (P_{D_2})^{1/2} = \ln (N_2/N_1) + 9.303 - 28.880N_1 + 35.301N_1^2 - (1/T)(14707 - 48628N_1 + 52806N_1^2) \quad (11)$$

where P_{D_2} is in atmospheres.

When combined with the data on miscibility gap boundaries and plateau pressures, eq 10 and 11 can be used to construct isotherms similar to those shown in Figure 1. The calculated isotherms for the temperatures used in this study were in excellent agreement with those derived experimentally.

The isotherms calculated from eq 10 can be extrapolated into the very dilute solution regions that were beyond the measuring capability of the apparatus used in this study. Reliability of such extrapolation was tested by comparisons with the data that had been obtained at 700 °C by Smith et al.,⁵ by Goodall and McCracken,⁶ and by Ihle and Wu.⁷ As is shown in Figure 2, in spite of long extrapolation, the

TABLE II: Miscibility Gap Data for the System Li-LiD

T, °C	Plateau pressure, ^a Torr	Miscibility gap boundaries ^b		Activity coefficients ^c			
		N _{LiD} (satd)	N _{Li} (satd)	γ _{Li} (satd)	γ _{LiD} (satd)	γ _{Li} ^{''} (satd)	γ _{LiD} ^{''} (satd)
705	49.0	0.228	0.020	1.073	4.33	46.6	1.003
756	115.6	0.280	0.028	1.112	3.54	28.6	1.007
805	244.2	0.332	0.047	1.166	2.94	17.5	1.016
840	400.2	0.377	0.069	1.217	2.58	11.3	1.033
871	604.4	0.411	0.095	1.276	2.31	7.31	1.064

^a Calculated from eq 1. ^b Observed data. ^c Calculated from eq 12-15.

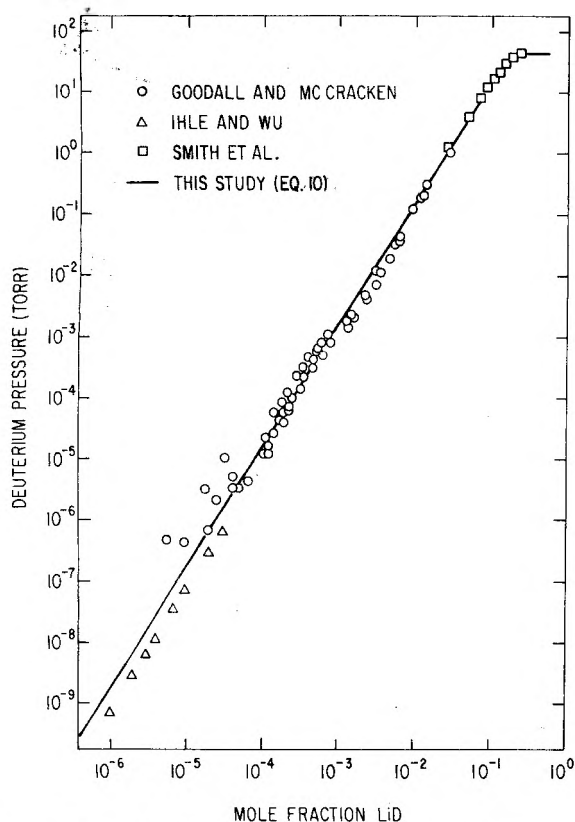


Figure 2. Comparison of the calculated P_{D_2} vs. N_{LiD} isotherm with the literature data at 700 °C.

agreement among the four studies is very good, thus verifying the accuracy of eq 10. Reliable extrapolations into dilute solution regions of hydrogen isotope-lithium systems are important in assessing lithium as a potential blanket material in fusion reactors.

The consolute point of the Li-LiD system was approximated by equating to zero the first and second derivatives with respect to N of eq 10 and 11. It was found to be at 1000 ± 10 °C and 61 ± 3 mol % LiD, value that are essentially the same as those for the Li-LiH system.³

Numerical expressions for the activity coefficients for the first (γ'_1, γ'_2) and the second (γ''_1, γ''_2) terminal solutions may be obtained by substituting the expressions for α and β into eq 5 and 6. Thus

$$(\ln \gamma'_1)/N_2^2 = -0.9258 + 0.8673N_2 + (1/T)(1746 + 1301N_2) \quad (12)$$

$$(\ln \gamma'_2)/N_1^2 = 0.3752 - 0.8673N_1 + (1/T)(3697 - 1301N_1) \quad (13)$$

$$(\ln \gamma''_1)/N_2^2 = 20.861 - 23.534N_2 - (1/T)(28492 - 35204N_2) \quad (14)$$

$$(\ln \gamma''_2)/N_1^2 = -14.440 + 23.534N_1 + (1/T)(24314 - 35204N_1) \quad (15)$$

where the standard states of Li and LiD are taken to be the pure liquid phases.

Activity coefficients calculated from eq 12-15 at the miscibility gap boundaries are listed in Table II. Their values indicate that the deviations from ideality are positive, as would be expected for solutions forming miscibility gaps, and are much larger for the LiD-rich solutions than for the Li-rich solutions.

Discussion

Important thermodynamic information bearing on the fundamental solution interactions between Li and LiD may be obtained by considering limiting cases at the extreme ends of the composition range: $N_{LiD} \rightarrow 0$ and $N_{Li} \rightarrow 0$. Activity coefficients evaluated at these limits can be combined with the equilibrium constant to generate expressions for a number of well-known constants associated with dilute solutions. Thirteen such expressions are presented in Table III, together with the corresponding changes in the standard chemical potentials and references to methods of their derivation. A brief description of the constants, represented by lines iii to xiii of Table III, is given below. For clarity, they are represented in three groups, each group belonging to one of the following equilibria.

1. $Li(soln) + \frac{1}{2}D_2(g) \rightleftharpoons LiD(soln) (K)$. For the condition $N_{LiD} \rightarrow 0$, it follows that $N_{Li}\gamma_{Li} \rightarrow 1$, $\gamma_{LiD} \rightarrow \gamma_{LiD}^*$, and the equilibrium constant in eq 4 is reduced to

$$\lim_{N_{LiD} \rightarrow 0} K = K' \gamma_{LiD}^* \quad (16)$$

where γ_{LiD}^* is the activity coefficient of LiD at infinite dilution as evaluated from eq 13 at $N_{Li} = 1$, and $K' = N_{LiD}/(P_{D_2})^{1/2}$ is essentially a constant for the concentrations $N_{LiD} < 0.01$ (cf. Figure 2). In this concentration range, K' can be taken to be equal to the more familiar Sieverts' law constant, $K_s = N_{D_2}/(P_{D_2})^{1/2}$. Knowledge of K' is of particular importance in fusion-reactor applications since hydrogen isotopes are expected to be present in liquid-lithium blankets at very low concentrations.

Similarly, for the limiting condition $N_{Li} \rightarrow 0$, we have $N_{LiD}\gamma_{LiD} \rightarrow 1$, $\gamma_{Li} \rightarrow \gamma_{Li}^*$, and eq 4 becomes

$$\lim_{N_{Li} \rightarrow 0} K = K''/\gamma_{Li}^* \quad (17)$$

where γ_{Li}^* is the activity coefficient of Li at infinite dilution as evaluated from eq 14 at $N_{LiD} = 1$, and $K'' = 1/[N_{Li}(P_{D_2})^{1/2}]$ is a constant analogous to K' .

2. $LiD(g) \rightleftharpoons LiD(soln) (K_1)$. This equilibrium gained a greater practical significance since the publication of a mass-spectrometric study by Ihle and Wu,⁷ who reported that, at low concentrations of deuterium in lithium, the LiD molecule becomes the predominant vapor species. Since the chemical potential of LiD must be the same in solution as in the vapor phase, $N_{LiD}\gamma_{LiD} = P_{LiD}/P_{LiD}^0$, and the equilibrium constant of the above reaction may be expressed as $K_1 = \gamma_{LiD}N_{LiD}/P_{LiD} = 1/P_{LiD}^0$. For the

TABLE III: Analytical Expressions for the Solution Constants Derived for the Limits $N_{\text{LiD}} \rightarrow 0$ and $N_{\text{Li}} \rightarrow 0$ Including the Values at 700 °C, References to the Methods of Derivation, and the Corresponding Changes in the Standard States

	Change in the standard states, $\Delta\mu^{oa}$	Expression for the corresponding constant, $\Delta\mu/R,T^b$	$\exp(\Delta\mu^0/RT)$ at 700 °C	Method of derivation ^b
(i)	$\mu_{\text{LiD}}^*(T,P) - \mu_{\text{LiD}}^0(l,T,P)$	$\ln \gamma_{\text{LiD}}^* = -0.4921 + 2396T^{-1}$	7.17	γ_{LiD}^* (eq 13 at $N_1 = 1$)
(ii)	$\mu_{\text{Li}}^*(T,P) - \mu_{\text{Li}}^0(l,T,P)$	$\ln \gamma_{\text{Li}}^* = -2.673 + 5712T^{-1}$	6.83×10^1	γ_{Li}^* (eq 14 at $N_2 = 1$)
(iii)	$[\mu_{\text{LiD}}^0(l,T,P) + 1/2\mu_{\text{D}_2}^0(g,T,1 \text{ atm})] - \mu_{\text{LiD}}^0(l,T,P)$	$\ln K(\text{atm}^{-1/2}) = -6.630 + 7995T^{-1}$	4.88	K (from eq 8)
(iv)	$[\mu_{\text{LiD}}^0(l,T,P) + 1/2\mu_{\text{D}_2}^0(g,T,1 \text{ atm})] - \mu_{\text{LiD}}^*(T,P)$	$\ln K'(\text{atm}^{-1/2}) = -6.138 + 5599T^{-1c}$	6.81×10^{-1}	$K' = K/\gamma_{\text{LiD}}^*$
(v)	$[\mu_{\text{Li}}^*(T,P) + 1/2\mu_{\text{D}_2}^0(g,T,1 \text{ atm})] - \mu_{\text{LiD}}^0(l,T,P)$	$\ln K''(\text{atm}^{-1/2}) = -9.303 + 14707T^{-1}$	3.33×10^2	$K'' = K\gamma_{\text{Li}}^*$
(vi)	$\mu_{\text{LiD}}^0(l,T,P) - \mu_{\text{LiD}}^0(g,T,1 \text{ atm})$	$\ln P^0_{\text{LiD}}(\text{atm}) = 15.296 - 26082T^{-1}$	1.01×10^{-5}	$P^0_{\text{LiD}} = 1/(K'_{\text{LiD}}\gamma_{\text{LiD}}^*)$
(vii)	$\mu_{\text{LiD}}^0(g,T,1 \text{ atm}) - \mu_{\text{LiD}}^*(T,P)$	$\ln K'_{\text{LiD}}(\text{atm}^{-1}) = -14.804 + 23686T^{-1}$	1.38×10^4	K'_{LiD} (ref 7)
(viii)	$\mu_{\text{LiD}}^0(g,T,P) - \mu_{\text{LiD}}^0(g,T,1 \text{ atm})$	$\ln P'(\text{atm}) = \ln(d_{\text{Li}}T) + 2.470$	5.35×10^3	$P' = R'Td_{\text{Li}}/M_{\text{Li}}$
(ix)	$\mu_{\text{LiD}}^0(g,T,P) - \mu_{\text{LiD}}^*(T,P)$	$\ln \lambda'_{\text{LiD}} = \ln(d_{\text{Li}}T) - 12.334 + 23686T^{-1}$	7.40×10^7	$\lambda'_{\text{LiD}} = K'_{\text{LiD}}P'$
(x)	$\mu_{\text{Li}}^0(l,T,P) - \mu_{\text{Li}}^0(g,T,1 \text{ atm})$	$\ln P^0_{\text{Li}}(\text{atm}) = 11.536 - 18572T^{-1}$	5.27×10^{-4}	P^0_{Li} (ref 16)
(xi)	$\mu_{\text{Li}}^0(g,T,1 \text{ atm}) - \mu_{\text{Li}}^*(T,P)$	$\ln K'_{\text{Li}}(\text{atm}^{-1}) = -8.863 + 11860T^{-1}$	2.78×10^1	$K'_{\text{Li}} = 1/(P^0_{\text{Li}}\gamma_{\text{Li}}^*)$
(xii)	$\mu_{\text{Li}}^0(g,T,P) - \mu_{\text{Li}}^0(g,T,1 \text{ atm})$	$\ln P''(\text{atm}) = \ln(d_{\text{LiD}}T) + 2.215$	4.91×10^3	$P'' = R'Td_{\text{LiD}}/M_{\text{LiD}}$
(xiii)	$\mu_{\text{Li}}^0(g,T,P) - \mu_{\text{Li}}^*(T,P)$	$\ln \lambda''_{\text{Li}} = \ln(d_{\text{LiD}}T) + 6.648 + 11860T^{-1}$	1.36×10^5	$\lambda''_{\text{Li}} = K''_{\text{Li}}P''$

^a $\mu_i^*(T,P)$, $\mu_i^0(l,T,P)$, and $\mu_i^0(g,T,P)$ are the standard chemical potentials of component i , defined (at T and P stated) in terms of an infinitely dilute solution, a pure liquid, and pure ideal gas, respectively. ^b For definitions of symbols, see the text. ^c The expression for K' is in good agreement with $\ln K'(\text{atm}^{-1/2}) = -6.198 + 5644T^{-1}$ reported by Smith et al.,⁵ but does not agree with $\ln K'(\text{atm}^{-1/2}) = -6.516 + 6381T^{-1}$ reported by Ihle and Wu.⁷

conditions $N_{\text{LiD}} \rightarrow 0$ and $\gamma_{\text{LiD}} = \gamma_{\text{LiD}}^*$ one can write

$$\lim_{N_{\text{LiD}} \rightarrow 0} (1/P^0_{\text{LiD}}) = K'_{\text{LiD}}\gamma_{\text{LiD}}^* \quad (18)$$

where the vapor phase is assumed to be ideal, P_{LiD} is the partial pressure of LiD over Li-LiD solutions, P^0_{LiD} is the vapor pressure of pure liquid LiD (line vi of Table III), and $K'_{\text{LiD}} = N_{\text{LiD}}/P_{\text{LiD}}$ is the Henry's law constant for very dilute solutions of LiD in liquid lithium, which was experimentally determined by Ihle and Wu (line vii of Table III).

The observed predominance of LiD molecules in the vapor phase at the very low deutride concentrations is apparently related to the crossing of the P_{D_2} vs. N_{LiD} and P_{LiD} vs. N_{LiD} lines, owing to the second-power relationship of the former line. From the values given in Table III one can calculate that, at 700 °C, the intersection would occur at $N_{\text{LiD}} = (K')^2/K'_{\text{LiD}} \approx 3 \times 10^{-5}$.

Equilibrium 2 may also be represented in terms of the Ostwald coefficient, γ'_{LiD} , which is defined as the ratio of concentration (in mol/cm³) of the solute (LiD) in the solution phase, $C_{\text{LiD}}(l)$, to the concentration of the solute in the gas phase, $C_{\text{LiD}}(g)$, and thus may be regarded as a distribution coefficient of the solute between liquid and gas phases. The Ostwald coefficient is related to K'_{LiD} by

$$\lambda'_{\text{LiD}} = C_{\text{LiD}}(l)/C_{\text{LiD}}(g) = K'_{\text{LiD}}R'Td_{\text{Li}}/M_{\text{Li}} = K'_{\text{LiD}}P' \quad (19)$$

where d_{Li} is the density of liquid Li given¹⁵ by $d_{\text{Li}}(\text{g/cm}^3) = 0.5364 - 1.0427 \times 10^{-4}t + 3.825 \times 10^{-9}t^2 - 5.2856 \times 10^{-12}t^3$, M_{Li} is its atomic weight, $R' = 82.06 \text{ cm}^3 \text{ atm/deg mol}$ is the gas constant, $P' = R'Td_{\text{Li}}/M_{\text{Li}}$ is the pressure of 1 mol of an ideal gas (in this case LiD), compressed to the molar volume of lithium (cf. line viii of Table III), and t is the temperature in degrees Celsius.

The quantity RT in λ'_{LiD} may be defined as the standard free energy of vaporization when 1 mol of the solute LiD is taken from an infinitely dilute solution phase into the same volume of the gas phase (cf. line ix of Table III). It differs from $RT \ln K'_{\text{LiD}}$ in that it eliminates the large (but physically unimportant) contribution due to expansion of gas from P' to 1 atm, which is inherent in the Henry's law constant. Thus, $RT \ln \gamma'_{\text{LiD}}$ provides a more direct measure of the interactions between LiD molecules and lithium. The large value of λ'_{LiD} , shown in Table III, suggests that the distribution of LiD is strongly in favor of the solution phase.

3. $\text{Li}(g) \rightleftharpoons \text{Li}(\text{soln}) (K_2)$. This equilibrium is analogous to that of the preceding section, except that it refers to the LiD-rich terminal solution regions and the solute-solvent relationship is reversed. The equilibrium constant for equilibrium 3 is given by $K_2 = \gamma_{\text{Li}}N_{\text{Li}}/P_{\text{Li}} = 1/P^0_{\text{Li}}$ and, for the limiting conditions $N_{\text{Li}} \rightarrow 0$ and $\gamma_{\text{Li}} \rightarrow \gamma_{\text{Li}}^*$, one may write

$$\lim_{N_{\text{Li}} \rightarrow 0} (1/P^0_{\text{Li}}) = K''_{\text{Li}}\gamma_{\text{Li}}^* \quad (20)$$

where P_{Li} is the partial pressure of Li over the Li-LiD solutions, P^0_{Li} is the vapor pressure of pure liquid lithium given¹⁶ by $\ln P^0_{\text{Li}}(\text{atm}) = 11.536 - 18572T^{-1}$, and $K''_{\text{Li}} = N_{\text{Li}}/P_{\text{Li}}$ is the Henry's law constant for dilute solutions of Li in liquid LiD.

The Ostwald coefficient for equilibrium 3 is similarly given by

$$\lambda''_{\text{Li}} = K''_{\text{Li}}R'Td_{\text{LiD}}/M_{\text{LiD}} = K''_{\text{Li}}P'' \quad (21)$$

where d_{LiD} is the density¹⁷ of liquid LiD, M_{LiD} is the molecular weight, and P'' is the pressure of 1 mol of ideal Li

gas compressed to the molar volume of LiD (cf. line xii of Table III).

The relationship of the Ostwald coefficient to the commonly known standard states and its advantages over the Henry's law constant in describing certain solute-solvent interactions were pointed out before. Another important utilization of the Ostwald coefficient can be found in certain distribution problems, as is indicated by the following example.

For dilute solutions of LiD in liquid lithium ($N_{\text{LiD}} < 10^{-5}$) there is considerable interest in evaluating the distribution of the dissolved species between liquid and gas phases, with possible applications to the tritium extraction problems in fusion-reactor blankets. In the liquid phase there is only one D-bearing species, namely, LiD. In the gas phase, on the other hand, there are three such species (LiD, Li₂D, and D₂), as reported by Ihle and Wu.⁷ These authors experimentally determined temperature-dependence expressions for the corresponding solution constants [$K'_{\text{LiD}} = N_{\text{LiD}}/P_{\text{LiD}}$ (line vii of Table III), $K'_{\text{Li}_2\text{D}} = N_{\text{LiD}}/P_{\text{Li}_2\text{D}} = -20.059 + 29584T^{-1}$, and $K' = N_{\text{LiD}}/(P_{\text{D}_2})^{1/2}$ (analogous to our line iv of Table III)] and formulated an equation for the distribution coefficient, κ , according to the Nernst distribution law. Thus, using the symbols of this study

$$\kappa = \frac{N_{\text{LiD}}(\text{l})}{N_{\text{D}}(\text{g})} = \left[\frac{1}{K'_{\text{LiD}}} + \frac{1}{K'_{\text{Li}_2\text{D}}} + \frac{2N_{\text{LiD}}(\text{l})}{K'^2} \right]^{-1} P_{\text{tot}} \quad (22)$$

where $N_{\text{D}}(\text{g}) = N_{\text{LiD}}(\text{g}) + N_{\text{Li}_2\text{D}}(\text{g}) + 2N_{\text{D}_2}(\text{g})$ is the atom fraction of total deuterium in the gas phase, $N_{\text{LiD}}(\text{l}) \simeq N_{\text{D}}(\text{l})$ is the mole fraction of LiD in the liquid phase, and $P_{\text{tot}} \simeq P_{\text{Li}} + P_{\text{Li}_2}$ is the total pressure of the gas phase.

The value of κ in eq 22 was found to decrease rapidly with temperature, reaching unity at ~ 1240 K, thereby showing a substantial enrichment of deuterium in the gas phase. These findings were later verified by Rayleigh distillation experiments.¹⁸

Because of large differences in the phase densities, the mole fraction-based Nernst coefficient may not be the best choice in describing the above distribution equilibrium. The volume-based Ostwald coefficient, λ , appears to be more realistically suited for this purpose. Thus, the above distribution may be alternatively represented by

$$\lambda = \frac{C_{\text{LiD}}(\text{l})}{C_{\text{D}}(\text{g})} = \left[\frac{1}{K'_{\text{LiD}}} + \frac{1}{K'_{\text{Li}_2\text{D}}} + \frac{2N_{\text{LiD}}(\text{l})}{K'^2} \right]^{-1} P' \quad (23)$$

where $C_{\text{D}}(\text{g}) = C_{\text{LiD}}(\text{g}) + C_{\text{Li}_2\text{D}}(\text{g}) + 2C_{\text{D}_2}(\text{g})$ is the concentration (in mol/cm³) of all D-bearing species in the gas phase, $C_{\text{LiD}}(\text{l}) \simeq C_{\text{D}}(\text{l})$ is the concentration of LiD in the liquid phase, and P' is defined in eq 19.

At 1240 K, where $\kappa = 1$, the Ostwald coefficient is quite large ($\lambda \simeq 1.6 \times 10^5$ from eq 23), indicating that the concentration of deuterium still remains high in the liquid phase. For a temperature increase from the monotectic to 1240 K, there is a 100-fold decrease in λ ; however, a temperature much higher than the boiling point of lithium would be required to reach the condition $\lambda = 1$.

Comparison of data for the Li-LiH³ and Li-LiD system allows one to make estimates of the D/H isotope effects. Within the temperature ranges investigated, both phase diagrams are essentially identical. A small isotope effect is seen in the solubility values at the Li-rich boundaries

of the miscibility gaps. The effect is largest at the monotectic temperatures (694 °C for H, 689 °C for D) where the solubilities are 23.2 mol % LiH and 21.3 mol % LiD.

A more pronounced D/H isotope effect was observed in the dissociation pressures. For example, in the plateau regions, the $P_{\text{D}_2}/P_{\text{H}_2}$ ratios range from 1.40 at 705 °C to 1.35 at 871 °C, i.e., slightly less than the square root of the D/H mass ratio. The variation with temperature may be due to differences in the temperature coefficients of the partition functions for hydrogen and deuterium.

Acknowledgment. I wish to thank D. H. J. Goodall and M. G. McCracken of the Culham Laboratory for permission to use their unpublished data; M. Blander, H. M. Feder, V. A. Maroni, J. Royal, and S. E. Wood for valuable discussions; and A. Engelkemeir for mass-spectrometric gas analyses. The work was supported by the Division of Physical Research of the U.S. Energy Research and Development Administration.

Supplementary Material Available: A listing of the data used to prepare Figure 1 (1 page). Ordering information is available on any current masthead page.

References and Notes

- (1) C. B. Magee in "Metal Hydrides", W. M. Mueller, J. P. Blackledge, and G. G. Libowitz, Ed., Academic Press, New York, N.Y., 1968, Chapter 6.
- (2) D. J. Rcse, "On the Feasibility of Power by Nuclear Fusion", Report ORNL-TM-2204, Oak Ridge National Laboratory, Oak Ridge, Tenn., 1968, p 93.
- (3) E. Veleckis, E. H. Van Deventer, and M. Blander, *J. Phys. Chem.*, **78**, 1933 (1974).
- (4) F. K. Heumann and O. N. Salmon, "The Lithium Hydride, Deuteride and Tritide Systems", USAEC Report No. KAPL-1667, Knolls Atomic Power Laboratory, Schenectady, N.Y., 1956.
- (5) (a) F. J. Smith, J. D. Redman, R. A. Strehlow, and J. T. Bell, "Current Tritium Chemical Studies at Oak Ridge National Laboratory", in Proceedings of the Symposium on Tritium Technology related to Fusion Reactor Systems, Report ERDA-50, June 1975. (b) F. J. Smith, J. F. Land, G. M. Begun, and J. T. Bell, "Equilibria in Hydrogen-Isotope-CTR-Blanket Systems", Chemistry Division Annual Progress Report No. ORNL-5111, Oak Ridge National Laboratory, Oak Ridge, Tenn., 1976, p 26.
- (6) (a) G. M. McCracken, D. H. J. Goodall, and G. Long, "The Extraction of Tritium from Liquid Lithium", IAEA Workshop on Fusion Reactor Design Problems, Culham, United Kingdom, February 1974; (b) Additional deuterium pressure vs. composition data were supplied by D. H. J. Goodall through a personal communication.
- (7) H. R. Ihle and C. H. Wu, "Experimental Determination of the Partial Pressures of D₂, LiD and Li₂D in Equilibrium with Dilute Solutions of Deuterium in Liquid Lithium", Proceedings of the 8th Symposium on Fusion Technology, Noordwijkerhout, The Netherlands, 1974.
- (8) F. J. Norton, *J. Am. Ceram. Soc.*, **36**, 90 (1953).
- (9) J. H. DeVan and R. L. Klueh, *Nucl. Technol.*, **24**, 64 (1974).
- (10) H. R. Leider and J. F. Lakner, "Lithium 'Super Hydride'", Report No. UCID-16834, Lawrence Radiation Laboratory, Lawrence, Calif., 1975.
- (11) Chemical Engineering Division, Liquid Metals Chemistry and Tritium Control Technology Annual Report, July 1974-June 1975, Argonne National Laboratory, Report ANL-75-50, p 11.
- (12) See, e.g., T. D. Sterling and S. V. Pollack, "Introduction to Statistical Data Processing", Prentice-Hall, Englewood Cliffs, N.J., 1968, p 398.
- (13) The heat of fusion of LiD was assumed to be the same as that of LiH ($\Delta H_f = 5.31 \pm 0.08$ kcal/mol), taken from E. E. Shpilrayn, K. A. Yakimovich, D. N. Kagan, and V. G. Shvalb, *Fluid Mech.-Sov. Res.*, **3**(4), 3 (1974).
- (14) J. H. Hildebrand and R. L. Scott, "The Solubility of Nonelectrolytes", 3rd ed. Reinhold, New York, N.Y., 1959, p 34.
- (15) I. I. Novikov, V. A. Gruzdev, O. A. Kraev, A. A. Odintsov, and V. V. Roshchupkin, *High Temp. (USSR)*, **7**, 65 (1969).
- (16) H. W. Davison, "Compilation of Thermophysical Properties of Liquid Lithium", NASA Report No. TND-4650, Lewis Research Center, Cleveland, Ohio, 1968.
- (17) The density of LiD was taken to be equal to that of LiH, which has been derived from unstated sources at six temperatures (700-950 °C) in F. H. Welsh, "Properties of LiH. III. Summary of GE-ANPD Data", Report No. XDC-61-5-67, 1961. We fitted these data to the equation $d_{\text{LiD}}(\text{g/cm}^3) = 5.572 - 14.547 \times 10^{-3}T + 14.116 \times 10^{-6}T^2 - 4.593 \times 10^{-9}T^3$, where T is the Kelvin temperature.
- (18) H. R. Ihle and C. H. Wu, *J. Phys. Chem.*, **79**, 2386 (1975).

Thermometric Titration Studies of Ligand Binding to Macromolecules. Sodium Dodecyl Sulfate to β -Lactoglobulin^{1a}

Gordon C. Kresheck,^a Walter A. Hargraves,^{1b} and David C. Mann

Department of Chemistry, Northern Illinois University, DeKalb, Illinois 60115 (Received March 15, 1976; Revised Manuscript Received January 3, 1977)

The changes in enthalpy which accompany the binding of sodium dodecyl sulfate to the bovine β -lactoglobulin strong and weak binding sites were studied by thermometric titrations. The temperature and pH dependence of the enthalpy of binding to both types of sites is described, and the observed changes are interpreted using micelle formation of surfactants as a model system. It is concluded that surfactant binding to the strong binding sites resembles salt formation in a hydrophobic pocket, whereas the surfactant which is bound to the weak binding sites is in nearly the same environment as when in the micellar state. Thermometric titrations also gave rise to stoichiometries for strong and weak binding which are consistent with previous analytical results.

Introduction

Many of the interesting biological properties of macromolecules are related to their interactions with small ions and molecules. One way to describe such interactions is by means of a thermodynamic analysis. The latter may provide mechanistic insights when similar data exist for an appropriate model system. We have selected micelle formation of surfactants as a model system which we hope will help understand several thermodynamic changes which accompany the binding of various surfactants and eventually other molecules to proteins.

The changes in enthalpy, entropy, and heat capacity which accompany micelle formation for eight surfactants with different head groups and chain lengths have been reported.^{2a} The main features of this process are as follows: (a) the change in heat capacity for micelle formation is negative and proportional to the size of the hydrophobic portion of the surfactant molecule, and (b) the enthalpy and entropy changes correlate giving rise to a compensation temperature of about 300 °C.^{2b}

The purpose of this presentation is to describe the enthalpy and heat capacity changes which accompany the binding of sodium dodecyl sulfate (SDS) to bovine β -lactoglobulin. Thermometric titrations have been found to be a useful way to obtain the required data as in the previous study of micellization.

Experimental Section

Materials. The method of Fox et al.³ was used to isolate β -lactoglobulin from bovine milk supplied by the J. Faivre Dairy Farm, DeKalb, Ill. The type B protein was used for most of our studies although the AB variety was used in some cases without any significant difference in behavior from the B type. The variant character of the milk was determined by polyacrylamide gel electrophoresis. The method of Fox et al.³ involving ammonium sulfate precipitation was modified by the use of positive pressure filtration rather than negative pressure dialysis for concentration of the protein solutions. The protein was lyophilized and stored in a stoppered brown bottle at 2 °C until used. The protein concentration in solution was determined on the basis of the absorbance at 278 nm using the extinction coefficient reported by Townsend et al.⁴ A sample of sodium dodecyl sulfate at 95% purity was purchased from Matheson Coleman and Bell. For future studies, it is recommended that attempts be made to obtain a sample of higher purity, although results consistent with the literature were recently found from a study of the micellization of this sample.^{2a} Deionized distilled

water was prepared from laboratory distilled water using a Barnstead mixed-bed ion exchange column. The pH of the solutions was adjusted with freshly boiled 0.05 M NaOH or 0.05 M perchloric acid using reagent grade chemicals (Baker). Solutions of known molarity were prepared by weighing the solid surfactant with a Mettler B6 semimicro analytical balance, followed by dilution to volume.

Methods. pH. The pH of all solutions was measured at room temperature (22 ± 2 °C) on a Corning Model 7 pH meter using commercial buffer standards for calibration.

Positive Pressure Filtration. An Amicon Model 401 ultrafiltration system with a RF-25 liquid reservoir was used for concentration of the protein solutions. The protein was retained in the cell with the use of UM-10 diaflo ultrafilter membranes and a positive nitrogen pressure of 75 psi at 2 °C.

Electrophoresis. The homozygous character of selected cows and purity of the isolated β -lactoglobulin was determined by polyacrylamide gel electrophoresis using an E-C vertical gel apparatus. A 5% gel in 0.02 M barbital buffer pH 8.6 was used with a 250 V potential for approximately 2.5 h. The protein was stained with Schwarz amido black dye.

Optical Activity. Optical rotatory dispersion and circular dichroism spectra were obtained using a JASCO Model 5 optical rotatory dispersion spectrophotometer. The samples were examined in 1 cm cells under ambient conditions. The Lorentz factor $3/(n^2 + 2)$ was used for the calculation of the specific rotation.

Ultracentrifugation. The sedimentation velocity and molecular weight were determined at 22.00 ± 0.05 °C with a Beckman Model E analytical ultracentrifuge equipped with a schlieren optical system. The film plates were measured with a Nikon Model 6C microcomparator equipped with an Elms Systems digital readout attachment.

Thermometric Titrations. The thermometric titration instrument used in these studies has been previously described.^{2a} A 25-mL solution containing about 1% β -lactoglobulin was generally titrated at the rate of 0.6 mL/min with 3.3 mL of 0.4 M sodium dodecyl sulfate. The temperature change was measured with a thermistor, and the heat change calculated from the known heat capacity of the calorimeter cell and its contents. Since the temperature changes and heat leak^{2a} were fairly small, the calorimeter was treated as an adiabatic system for purposes of calculations. A few titrations were performed with a

prototype instrument,⁵ and also with an instrument with a sample size of 7.0 mL and titrant volume of about 1.0 mL added at the rate of about 0.2 mL/min. The results obtained from all three calorimeters showed internal consistency within the limits of experimental error.

Adiabatic Calorimeter. A few heat of mixing experiments were performed with an adiabatic solution calorimeter⁶ which was constructed following the design of Benjamin.⁷

Theory

The interpretation of the titration curves for this study is based upon the earlier work of Keily and Hume.⁸ Equations were presented for the dilution of solute into a pure solvent or into another solution. In our studies, we need to consider dilution of a concentrated surfactant solution above the critical micelle concentration (cmc) into either solvent or protein solution. A comparison between the enthalpy changes for the two processes will be given.

1. *Solution Added to Pure Solvent.* The change in heat which results from the dilution of the solute, $d\Delta H$, is given as the product of the heat capacity, C_p , and temperature change, dT , as

$$d\Delta H = C_p dT \quad (1)$$

$$= \left[\left(\frac{\partial \Delta H}{\partial n_1} \right)^f - \left(\frac{\partial \Delta H}{\partial n_1} \right)^i \right] dn_1 + \left[\left(\frac{\partial \Delta H}{\partial n_2} \right)^f - \left(\frac{\partial \Delta H}{\partial n_2} \right)^i \right] dn_2 \quad (2)$$

where the subscripts 1 and 2 refer to the solvent and solute, the superscripts f and i correspond to final and initial states, and n is equal to the number of moles. If M_2 is the molarity of the titrant and dV equals the volume change for addition of the titrant, $dn_2 = M_2 dV$. Also, the relative partial molal heat content may be defined for any component as $\bar{L} = \partial \Delta H / \partial n$. Therefore

$$\frac{dT}{dV} = - \left[\frac{(\bar{L}_1^f - \bar{L}_1^i)M_1 + (\bar{L}_2^f - \bar{L}_2^i)M_2}{C_p} \right] \quad (3)$$

If $\bar{L}_1^f \approx \bar{L}_1^i$

$$\frac{dT}{dV} = - \frac{(\bar{L}_2^f - \bar{L}_2^i)M_2}{C_p} \quad (4)$$

or, in terms of the partial molal heat content, \bar{H} ,

$$\frac{dT}{dV} = \frac{(\bar{H}_2^i - \bar{H}_2^f)M_2}{C_p} \quad (5)$$

2. *Solution Added to Solution.* The situation is similar for the dilution of surfactant into a protein solution, except the third component is the protein, so that

$$\frac{dT}{dV} = - \left[\frac{(\bar{L}_1^f - \bar{L}_1^i)M_1 + (\bar{L}_2^f - \bar{L}_2^i)M_2 + (\bar{L}_3^f - \bar{L}_3^i)M_3}{C_p} \right] \quad (6)$$

If $\bar{L}_1^f \approx \bar{L}_1^i$ and $\bar{L}_3^f \approx \bar{L}_3^i$

$$\frac{dT}{dV} = \frac{(\bar{H}_2^i - \bar{H}_2^f)M_2}{C_p} \quad (7)$$

In general, the difference between the slope of the titration curve at any two points will give the difference between the partial molal heat content at those points according to either (5) or (7). This has been the basis for

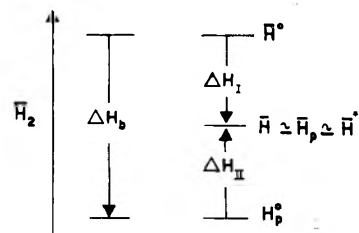


Figure 1. Partial molal enthalpy level diagram which describes the dilution of a surfactant molecule in water, $-\Delta H_I$, or protein solution, $-\Delta H_{II}$. The other symbols are defined in the text.

previous determinations of the heat of micellization,^{2a} but it may also be used to define the heat of binding ligands to macromolecules, ΔH_b . If the partial molal heat content of the surfactant in dilute aqueous or protein solution is \bar{H}^0 and \bar{H}_p^0 , respectively, and the partial molal heat content of the undiluted surfactant in the buret is \bar{H}^* , which is approximately equal to the heat content of the surfactant in water above the cmc, \bar{H} , and above the concentration of surfactant necessary to saturate the weak protein binding sites, \bar{H}_p , it is possible to define ΔH_I and ΔH_{II} shown in Figure 1 as

$$\Delta H_I = \bar{H} - \bar{H}^0 = \frac{C_p}{M_2} \left[\left(\frac{dT}{dV} \right)^i - \left(\frac{dT}{dV} \right)^f \right] \quad (8)$$

and

$$\Delta H_{II} = \bar{H}_p - \bar{H}_p^0 = \frac{C_p}{M_2} \left[\left(\frac{dT}{dV} \right)^i - \left(\frac{dT}{dV} \right)^f \right] \quad (9)$$

so that

$$\Delta H_b = \Delta H_I - \Delta H_{II} = \bar{H}_p^0 - \bar{H}^0 \quad (10)$$

The heat of binding was also calculated as an integral heat for the strong binding sites as

$$\Delta H_b = \frac{\text{heat change (cal)}}{\text{protein concentration (mol)}} \quad (11)$$

Finally, the change in heat capacity, ΔC_p , was calculated from the temperature dependence of the enthalpy change as

$$\Delta C_p = d\Delta H_b/dT \quad (12)$$

Results

Characterization of β -Lactoglobulin. The purified protein was free from major impurities according to gel electrophoresis at pH 2.8 and 8.6, and by sedimentation velocity at pH 2.8. A summary of the results for the characterization of β -lactoglobulin is given in Table I. All of the measured properties were found to be within experimental error of literature values. A value of 35 500 g/mol was used for the molecular weight of β -lactoglobulin and one-half that value for the monomer.

Heat of Mixing Experiments. The heat of dilution was observed for sodium dodecyl sulfate at 25 °C with the adiabatic solution calorimeter, and the results are illustrated in Figure 2 for the dilution into water or a 0.13% protein solution. Both processes are rapid compared with the thermal mixing process in the calorimeter. The apparent heat of binding, which is the difference between the two heat changes given in Figure 2, is 410 mcal. If it is

TABLE I: Physical Properties of Purified β -Lactoglobulin at 22 °C

Property	Conditions	Observed	Literature
$[\alpha]_{365}$	pH 2.8	$-80 \pm 10^{\circ}$	$-90^{\circ a}$
Mol wt	pH 5.5	$36\,600 \pm$	$35\,500^b$
	10 589 rpm	1 580 g/mol	g/mol
$s_{20,w}$	0.05 M succinate		
	pH 2.8	2.1 ± 0.2	2.3^c
CD_{min}	pH 2.8	215 ± 2 nm	216 nm ^d

^a From ref 9. ^b From ref 10. ^c From ref 11. ^d From ref 12.

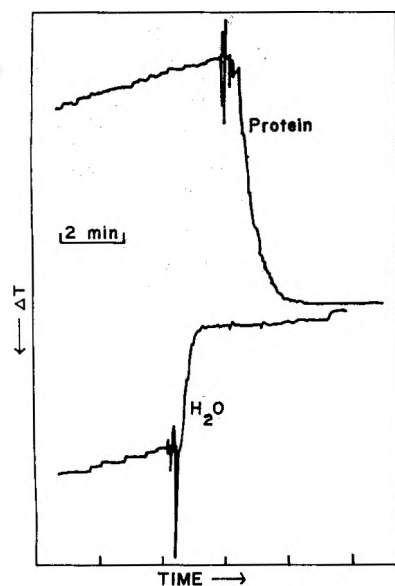


Figure 2. Reproductions of the recorder tracing for heat of mixing experiments at 25 °C which involved mixing 0.5 mL of 0.6 M sodium dodecyl sulfate with 29 mL of water or 0.13% β -lactoglobulin at pH 5.6 in the adiabatic solution calorimeter.

assumed that 0.9 g of sodium dodecyl sulfate binds to 1.0 g of β -lactoglobulin,¹³ the integral heat of binding would be -3.7 kcal/mol of surfactant.

Thermometric Titrations. The results for the thermometric titration of 0.4 M sodium dodecyl sulfate into water and β -lactoglobulin solution at pH 5.5 and 35 °C is given in Figure 3a and 3b, respectively. The dilution into water is endothermic, and exhibits a break in the curve at the critical micelle concentration as previously reported.^{2a,14} The heat of dilution of the micelle above the cmc is also endothermic, and is probably mainly due to counterion dissociations.¹⁴ Since the heat of dilution is endothermic, the heat of micelle formation would be exothermic, about -1.7 kcal/mol at 35 °C.^{2a} However, the heat change for dilution into the β -lactoglobulin solution may be seen from Figure 3b to be initially exothermic followed by a first endothermic, then exothermic, and finally endothermic region. The initial exothermic spike has been previously reported⁵ and it corresponds to the strong exothermic (about -10 kcal/mol of surfactant) stoichiometric binding of 1 mol of dodecyl sulfate to each of the subunits of the β -lactoglobulin dimer. This binding has been studied by noncalorimetric means by many workers¹⁵ and by batch calorimetry.¹⁶ The results of the two different calorimetric approaches have been found to yield equivalent enthalpy changes.⁵

The minimum which is observed in the titration curve following the initial exothermic spike approximates the critical micelle concentration. This is also seen from the titration in water. The final maximum corresponds to the end point for the binding of surfactant to the weak binding sites for this protein. The integral heat change for the

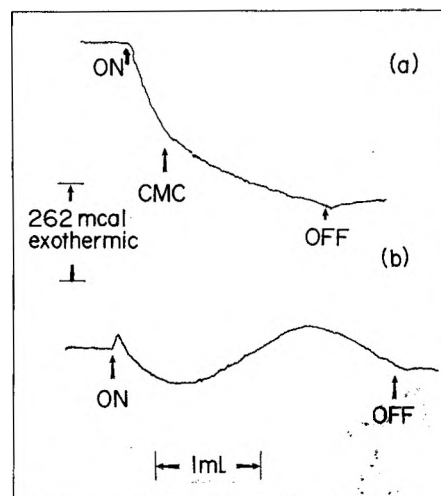


Figure 3. (a) Tracing of a thermometric titration curve for addition of 0.389 M sodium dodecyl sulfate into 25 mL of water at 35 °C. (b) Tracing of a thermometric titration curve for the addition of 0.389 M sodium dodecyl sulfate to 25 mL of 0.76% β -lactoglobulin at 35 °C and pH 5.5.

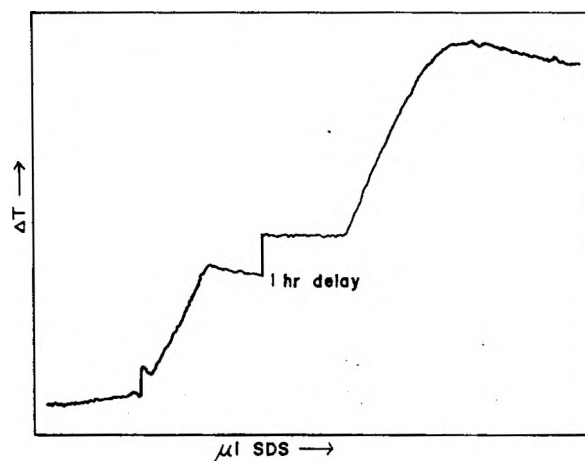


Figure 4. Tracing of a thermometric titration curve for the addition of 0.6 M sodium dodecyl sulfate to 0.96% β -lactoglobulin at 25 °C and pH 5.6. The titration was interrupted for about 1 h at the point indicated in the figure.

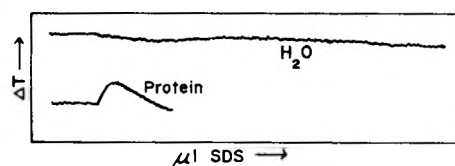


Figure 5. Tracing of a thermometric titration curve for the addition 0.1 M sodium dodecyl sulfate to water and to 0.7% β -lactoglobulin at pH 5.6 at 25 °C.

complete titration was in agreement with the integral heat of mixing for a comparable experiment in the adiabatic calorimeter.

A titration of the protein was also performed which was interrupted for 1.0 h about half way through the titration to determine if binding was rapid and there were any slow heat changes compared with the rate of titrant addition, and these results are given in Figure 4. It may be seen that the weak binding end point is the same with respect to position and slope change as found for titrations which were not interrupted (Figure 3b). This indicates that both the stoichiometry and the enthalpy of binding to the weak sites can be studied by thermometric titrations.

Titration of the protein with a more dilute surfactant solution, as shown in Figure 5, allows the strong binding

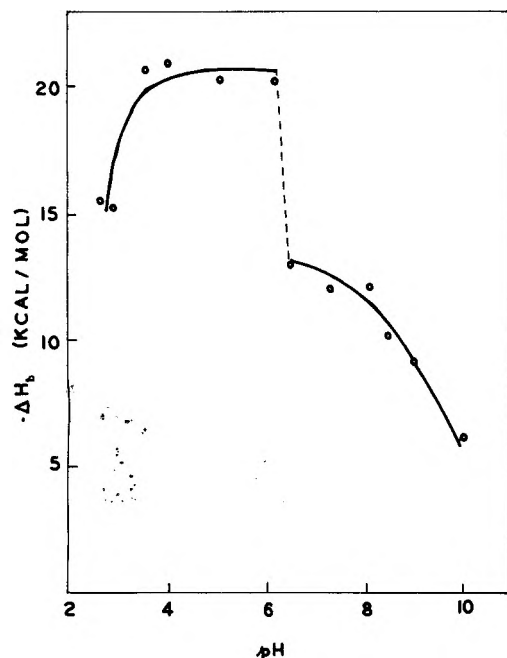


Figure 6. The influence of pH on ΔH_b for binding sodium dodecyl sulfate to the β -lactoglobulin strong binding site under ambient ($22 \pm 2^\circ\text{C}$) conditions. The enthalpy change corresponds to the binding of 2 mol of surfactant to 1 mol of protein dimer (the same as binding 2 mol of surfactant 2 mol of protein monomer).

site to be studied in the absence of the other thermal processes and in greater detail. The negative slope of the excess reagent line beyond the end point for the protein titration reflects slight differences in temperature between the sample and the titrant, and correction for this effect is made by simply extrapolating back to the origin of the titration to obtain the heat change for the binding process. The enthalpy change for the binding of SDS to the strong binding sites was calculated as an integral heat of binding according to eq 11.

The influence of pH on the strong binding sites was investigated since protein ionic side chains may be involved in the process,¹⁵ and the results obtained with the prototype calorimeter are shown in Figure 6. The apparent heat of binding shows a strong variation with pH, which may reflect changes in the state of aggregation or conformation of the protein. Changes in the state of ionization of the protein are not considered to contribute to ΔH_b since the pH of the protein solution did not change (± 0.05 pH units) from the addition of small quantities of dilute SDS solutions. The temperature dependence of the interaction of SDS with the β -lactoglobulin strong binding sites was studied at pH 5.6 and 8.6, and the results are shown in Figure 7. The decrease in heat capacity of about 0.1 kcal/mol deg per surfactant monomer at pH 8.6 is similar to that observed for micellization. However, ΔC_p for binding at pH 5.6 increases about 0.3 kcal/mol deg per surfactant monomer, which suggests that the temperature dependence of the enthalpy of SDS binding at pH 5.6 may be dominated by something other than simple hydrophobic binding. Finally, preliminary binding experiments with sodium dodecyl sulfate and β -lactoglobulin show that salts in general such as 0.5 M NaCl and Na_2SO_4 do not block the strong binding site, but they have a significant effect on ΔH_b . Additional work must be performed in order to completely describe the nature of the salt effects.

The variation of the enthalpy of SDS binding to the β -lactoglobulin weak sites with temperature was also studied at pH 5.6 and 8.6. The enthalpy change, ΔH_{II} , was calculated from eq 9 using the slopes before and after the

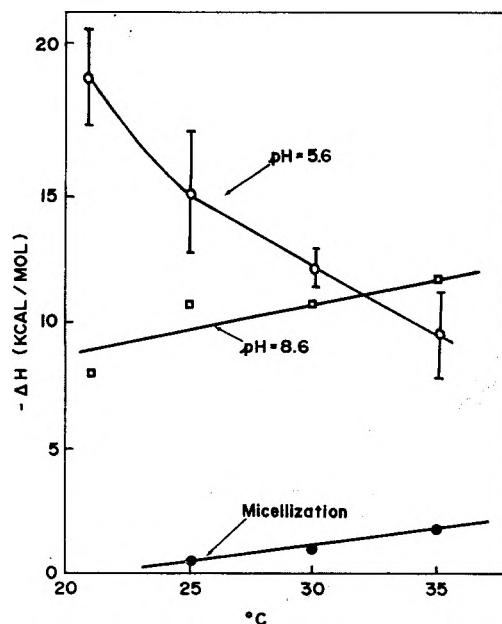


Figure 7. The influence of temperature on ΔH_b for binding sodium dodecyl sulfate to the β -lactoglobulin strong binding site at pH 5.6 and pH 8.6. The enthalpy change corresponds to the binding of 2 mol of surfactant to 1 mol of protein dimer (the same as binding 2 mol of surfactant to 2 mol of protein monomer).

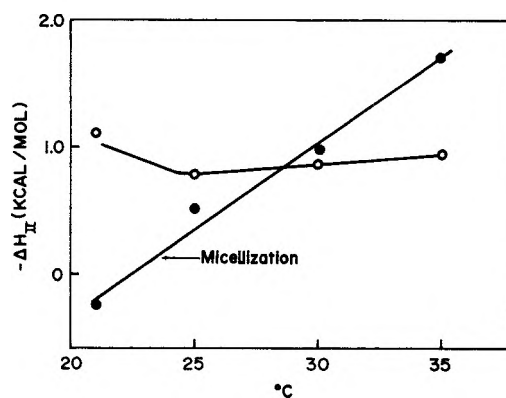


Figure 8. The influence of temperature on ΔH_{II} for binding sodium dodecyl sulfate to the β -lactoglobulin weak binding site (open circles) or ΔH_{II} for micellization (filled circles). The enthalpy change is expressed as per mole of surfactant bound.

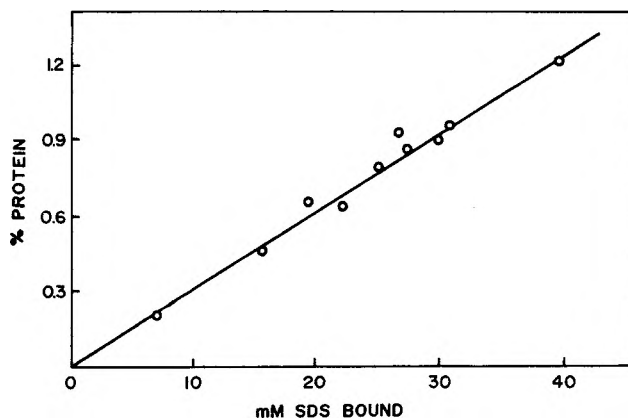


Figure 9. Variation of the amount of sodium dodecyl sulfate bound to β -lactoglobulin with the amount of protein titrated at 25°C .

end point for weak binding. There did not appear to be a significant pH effect, and the combined results are given in Figure 8. The standard deviation for duplicate trials performed for these experiments approximately corresponds to the size of the circles in the figure. The relative

TABLE II: Summary of the Thermometric Titration Data for Binding Sodium Dodecyl Sulfate to the Weak β -Lactoglobulin Binding Sites at Various Temperatures^a

Temp, °C	No. of titrations	End point, mM	ΔH_{II} , kcal/mol	<i>n</i>
21	1	32	1.09	132
25	2	30	0.77 \pm 0.07	127
30	2	29	0.86 \pm 0.05	123
35	4	24	0.92 \pm 0.06	88

^a The protein concentration was about 0.7% and the pH 5.5 \pm 0.1 (except for duplicates at 25 and 30 °C which were at pH 8.4) for these experiments using about 0.4 M SDS as the titrant.

TABLE III: Variation of ΔH_b for the β -Lactoglobulin Weak Binding Sites with Temperature

Temp, °C	ΔH_{II} , kcal/mol	ΔH_b , kcal/mol	ΔH_b , kcal/mol	$\Delta H_b'$, kcal/mol	Minimum, mM
21	1.09	0.26	-0.83	-1.50	3.7
25	0.77	-0.51	-1.28	-1.38	3.6
30	0.86	-0.96	-1.82	-1.81	4.7
35	0.92	-1.69	-2.61	-1.83	5.4

^a Evaluated from the change in slope at the minimum in the titration curve given in the last column in this table.

insensitivity of ΔH_{II} to temperature suggests that the SDS molecules which bind to the weak binding site are in the same state of solvation as in the micelle. The influence of protein concentration on the binding of sodium dodecyl sulfate to the weak sites of β -lactoglobulin was investigated at 25 °C using 0.6 M surfactant as a titrant and the 7.0 mL calorimeter cell for protein solutions ranging from 2 to 12 mg/mL. The value of ΔH_{II} was independent of protein concentration, 1.0 \pm 0.2 kcal/mol of surfactant. The end point was a linear function of concentration (Figure 8) and the data yielded an average value of 0.9 \pm 0.1 g of surfactant bound per gram of protein in agreement with previous analytical results from equilibrium dialysis studies.¹³ The amount of free SDS at the end point was assumed equal to the cmc.

A summary of the results from several titrations of the β -lactoglobulin weak binding sites at 21, 25, 30, and 35 °C is given in Table II. The end point in the titration, which corresponds to the final maximum shown in Figure 3a, may be seen to decrease with an increase in temperature. This gives rise to a decrease in the number of moles of SDS bound per mole of protein, *n*, with temperature. A cmc of 3.8 mM, which is an average value previously observed in the absence of protein,^{2a} was again taken as the amount of free SDS at the end point. The value of ΔH_{II} , calculated from eq 9 and identified in Figure 1, shows slight irregular temperature fluctuations. However, when ΔH_b was calculated according to eq 10 using the data for ΔH_I from ref 2a, a regular change with temperature is observed as presented in Table III. The heat of binding, $\Delta H_2'$, was also calculated directly from the minimum in the titration curve which approximates the cmc (Figure 3b) using eq 9 by identifying $\Delta H_{II}'$ with $\Delta H_b'$ due to the fact that the difference in slope at the cmc approximates the difference in partial molal heat contents of the bound and free surfactant. These results may be compared with the ones given in the preceding column in Table III, and it may be noted that good agreement is found for the values of ΔH_b calculated by the two different methods at 25 and 30 °C, whereas poor agreement exists at 21 and 35 °C. The poor agreement probably indicates that competition be-

tween micelles and protein for the surfactant monomer exists in dilute solution, and that the simplistic view used to evaluate the data from the apparent cmc in the presence of β -lactoglobulin is not justified. Denaturation of the protein may also be a factor in this region. The rather large temperature dependence of the apparent cmc when compared with the relative temperature insensitivity of the actual cmc in the absence of protein supports the notion that the process is complex in this region of the titration.

Discussion

Although it is recognized that proton binding to proteins may be studied by calorimetry,¹⁷ recent studies have shown that relatively weak surfactant binding may also be observed.^{18,19} The enthalpy changes which result from titrating β -lactoglobulin with SDS can be identified as due to binding to either strong or weak binding sites based upon previous analytical studies.^{13;15,16,20,21} The stoichiometry of binding SDS to both types of sites does not depend on the method which is used. It was not possible in this study to resolve the intermediate binding sites reported by Ray and Chatterjee.²¹

The pH dependence of binding SDS to the strong binding sites is interesting, and one may describe the probable basis for the observed behavior. The dissociation of β -lactoglobulin dimers below pH 3.0 has been reported,²² and this could be the basis for the change in ΔH_b below pH 5.5. The abrupt decrease in enthalpy of binding between pH 6 and 7 is most likely related to the known conformational change reported to occur between pH 7 and 8.^{23,24} The transition is apparently shifted to a lower pH in the case of SDS binding than for binding nonpolar gases.²⁴ The decrease in ΔH_b above pH 7 may also be related to dissociation of the dimeric form of the protein by the SDS binding, although this does not occur in the absence of surfactant with protein concentrations greater than about 1 mg/mL.²⁵ Those pH dependent structural changes which β -lactoglobulin undergoes have been summarized.²⁶

The difference between the temperature dependence of SDS binding to β -lactoglobulin at pH 5.6 and 8.6 is also consistent with the view that a conformational change occurs between pH 6 and 7 with a positive enthalpy change (about 7 kcal/mol for each β -lactoglobulin dimer) in that at low temperatures the binding of SDS is more exothermic at pH 5.6 than at pH 8.6, but at higher temperatures the enthalpy of binding becomes equal within the limits of experimental error. The temperature dependence of ΔH_b at pH 8.6 is similar to that for micelle formation, which suggests that the binding process may be described as a salt formation between the surfactant head group and histidine¹⁵ in a hydrophobic pocket.²⁴ The temperature dependence of the reaction would be dominated by hydrophobic rather than electrostatic forces.^{2a}

In contrast with binding to the strong sites, the magnitude of the enthalpy of binding SDS to the weak β -lactoglobulin binding sites is quite small, e.g., $\Delta H_{II} \approx 1.0$ kcal/mol. The temperature dependence of ΔH_b given in Table III gives rise to a change in heat capacity of about -130 cal/mol deg per surfactant, which is similar in sign and magnitude to that of -134 cal/mol deg reported for micellization.^{2a} This together with the lower enthalpy change provides evidence in support of the primarily hydrophobic nature of the weak binding process. It is interesting that an enthalpy change of about -1.0 kcal/mol accompanies the binding of SDS to ovalbumin,¹⁹ which was also ascribed to hydrophobic forces based upon the large positive entropy change which accompanies binding. The

small change in pH which occurs during the dilution of 0.4 and 0.6 M SDS in unbuffered solutions was followed in the presence and absence of protein, and it was found that the rate of pH change was the greatest during the first 10% of the titration, and that the pH remained nearly constant during the region of the titration which coincides with the titration of the weak binding sites. Therefore, it is considered that changes in the degree of ionization of the protein do not make a significant contribution to ΔH_{II} for the titration of the weak binding sites in agreement with the views of Brewer.¹⁹ The unfolding of β -lactoglobulin by SDS occurs before the onset of weak binding according to the data given by Tanford.²⁷ This unfolding may be a minor component of the endothermic curve which follows the exothermic strong binding spike as previously observed for other systems.¹⁸

It is by now clear that thermometric titrations provide much more information with respect to ligand binding from a single experiment than does a simple heat of mixing. For example, the heat of binding calculated from the data given in Figure 2 for a heat of mixing experiment represents an average of the heat change due to strong and weak binding and micelle dissociation as revealed by the analysis of the enthalpy titration curves. Integral heat of mixing experiments, when used, must be performed over a broad concentration range in the case of binding SDS to β -lactoglobulin, and probably most other proteins, in order to resolve the binding sites and to obtain partial molal enthalpies to be used for finding standard entropy changes.

Acknowledgment. This research was supported in part by a grant from the National Science Foundation, BS 75-14425.

References and Notes

- (1) (a) Taken in part from a thesis submitted by W. A. Hargraves for the Ph.D. Degree, Northern Illinois University, 1972. Presented in

- part at the First Chemical Congress of the North American Continent, Mexico City, Mexico, 1975. (b) Graduate Research Assistant of Northern Illinois University. Present address: St. Vincent Hospital, Worcester, Mass.
- (2) (a) G. C. Krescheck and W. A. Hargraves, *J. Colloid Interface Sci.*, **48**, 481 (1974); (b) G. C. Krescheck, *Water. Compr. Treat.*, **4**, 95 (1975).
- (3) K. K. Fox, V. H. Holsinger, L. P. Posati, and M. J. Pallansch, *J. Dairy Sci.*, **50**, 1363 (1967).
- (4) R. Townend, R. J. Winterbotton, and S. N. Timasheff, *J. Am. Chem. Soc.*, **82**, 3161 (1960).
- (5) G. C. Krescheck and W. A. Hargraves in "Structure and Function of Oxidation Reduction Enzymes", A. A. Keson and A. Ehrenberg, Ed., Pergamon Press, New York, N.Y., 1972, p 549.
- (6) G. C. Krescheck and I. N. Klotz, *Biochemistry*, **8**, 8 (1969).
- (7) L. Benjamin, *Can. J. Chem.*, **41**, 2210 (1963).
- (8) H. J. Kelly and D. N. Hume, *Anal. Chem.*, **28**, 1294 (1956).
- (9) N. C. Pace and C. Tanford, *Biochemistry*, **7**, 198 (1968).
- (10) K. Bell and H. A. McKenzie, *Nature (London)*, **204**, 1275 (1964).
- (11) S. N. Timasheff and R. Townend, *J. Am. Chem. Soc.*, **83**, 470 (1961).
- (12) R. Townend, T. F. Kurmosinski, and S. N. Timasheff, *J. Biol. Chem.*, **242**, 4538 (1967).
- (13) R. Pitt-Rivers and F. S. A. Impiombato, *Biochem. J.*, **109**, 825 (1968).
- (14) D. J. Eatough and S. J. Rehfeld, *Thermochim. Acta*, **2**, 443 (1971).
- (15) S. Selbles, *Biochemistry*, **8**, 2949 (1969).
- (16) R. Lovrien and W. Anderson, *Arch. Biochem. Biophys.*, **131**, 139 (1969).
- (17) J. Steinhardt and J. A. Reynolds, "Multiple Equilibria in Proteins", Academic Press, New York, N.Y., 1967, pp 60, 300.
- (18) E. Tipping, M. N. Jones, and H. A. Skinner, *J. Chem. Soc., Faraday Trans. 1*, **70**, 1306 (1974).
- (19) J. M. Brewer, *Arch. Biochem. Biophys.*, **165**, 213 (1974).
- (20) T. McMeekin, B. Polls, E. Monica, and J. Custer, *J. Am. Chem. Soc.*, **71**, 3606 (1949).
- (21) A. Ray and R. Chatterjee in "Conformation of Biopolymers", Vol. 1, G. N. Ramachandran, Ed., Academic Press, New York, N.Y., 1967, p 235.
- (22) S. N. Timasheff and R. Townend, *J. Am. Chem. Soc.*, **83**, 470 (1961).
- (23) C. Tanford, L. Bunville, and Y. Nozaki, *J. Am. Chem. Soc.*, **81**, 4032 (1959).
- (24) D. B. Wetlaufer and R. Lovrien, *J. Biol. Chem.*, **239**, 596 (1964).
- (25) J. K. Zimmerman, G. H. Barlow, and I. M. Klotz, *Arch. Biochem. Biophys.*, **138**, 101 (1970).
- (26) R. Townend, T. T. Herskovits, and S. N. Timasheff, *Arch. Biochem. Biophys.*, **129**, 567 (1969).
- (27) C. Tanford, *Adv. Protein Chem.*, **23**, 2112 (1968).

Photogalvanic Effect in the Thionine-Iron System

Tadayoshi Sakata,[†] Yasuhiro Suda, Jiro Tanaka, and Hiroshi Tsubomura*

Department of Chemistry, Faculty of Engineering Science, Osaka University, Toyonaka, Osaka 560, Japan (Received July 23, 1976; Revised Manuscript Received November 19, 1976)

The photogalvanic effect for the thionine-Fe²⁺ system has been investigated. From thermodynamic data and the dependence of the photocurrent on the light intensity, semithionine is concluded to be the main electrochemically active species. The results for electrodes of different metals show that the photocurrent has two components: a slow-response, positive and a fast-response, negative. These components, and hence the steady state photocurrent, are found to depend on the electrode metal and show a good correlation with the electrode potential in the dark, i.e., the Fermi level of the electrode. These results are explained in terms of the different electron transfer rates between the metals and the electrochemically active species in solution. The influence of agitation and oxygen on both the photocurrent and photovoltage have also been studied.

Introduction

The photogalvanic effect, a special case of the Becquerel effect,¹ is a build up of electrode potential by a photochemical reaction in an electrolyte solution. To clarify the mechanism of this effect is not only of scientific interest

but may also lead to a new method of solar energy utilization.^{2,3}

The thionine-iron aqueous system is one of the systems whose photogalvanic effect is the most extensively studied, since the earliest but excellent work of Rabinowitch,^{4,5} and the photochemical aspect of the system has also been fairly well understood. However, in spite of increasing numbers of papers concerning the electrochemical aspect of the

[†] Present address: Institute for Molecular Science, Okazaki, Aichi 444, Japan.

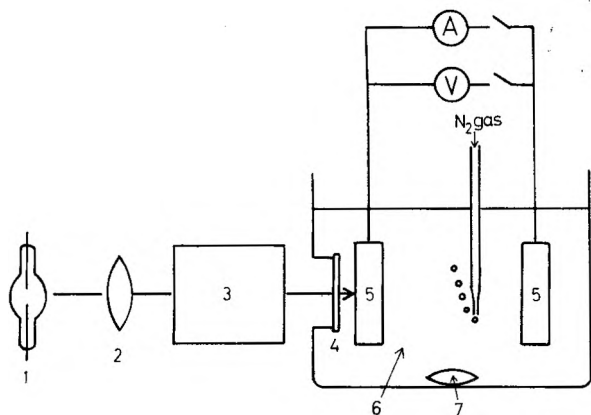


Figure 1. The experimental photogalvanic cell: (1) 500-W xenon lamp; (2) quartz lens; (3) monochromator; (4) quartz window; (5) electrode; (6) aqueous solution of thionine and ferrous sulfate, $[\text{Th}] = 5.0 \times 10^{-5}$ M, $[\text{FeSO}_4] = 1.0 \times 10^{-2}$ M, $[\text{K}_2\text{SO}_4] = 1.0 \times 10^{-1}$ M; (7) a magnetic stirrer.

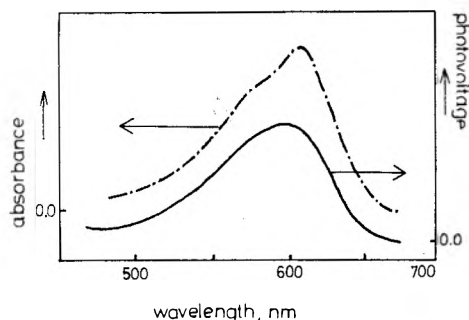


Figure 2. The action spectrum of the photovoltage for the Pt electrode (—), and the absorption spectrum of the Th- Fe^{2+} system (---).

system, the basic mechanism of the effect has not been elucidated. In this paper, we therefore present the results of our studies on the fundamental processes of the thionine-iron aqueous system.

Experimental Section

The apparatus used in our work is shown in Figure 1. Commercial thionine (chloride) and ferrous sulfate ($\text{FeSO}_4 \cdot 7\text{H}_2\text{O}$) were used without further purification. Platinum electrodes were used in most cases, but other metals such as Ti, W, Mo, Cu, Ag, Ni, Sn, Fe, Zn, and Pb and carbon were used to investigate the influence of electrode materials. All metal electrodes were polished with alumina abrasives. Before measurement, nitrogen gas was bubbled into the cell for at least 10 min to remove oxygen. Deionized water was used throughout the experiments. A 500-W xenon lamp was used as a light source. The current-voltage measurement was performed under potentiostatic conditions. A saturated calomel electrode (SCE) was used as a reference electrode.

Results

Figure 2 shows the photovoltage action spectrum arising between the illuminated and the dark Pt electrodes in a thionine- Fe^{2+} system together with its optical absorption spectrum. The similarity of the two spectra shows that the electrode reaction is initiated by the absorption of light by the thionine dye. When platinum electrodes are used, the polarity of the illuminated electrode is always negative and independent of the ratio of the initial concentrations, $[\text{Th}]_0/[\text{Fe}^{2+}]_0$. The photovoltage becomes $-50 \sim -150$ mV at the open circuit. Figure 3 shows the dependence of the photocurrent (i_p) on the light intensity (I) at pH 5.0 for the same system. The value of the slope is 1.0 showing that i_p is proportional to the light intensity.

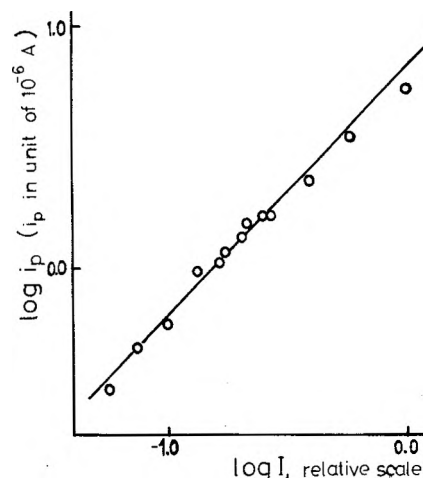


Figure 3. The dependence of the photocurrent, i_p , on the light intensity, I , at pH 5. Circles give the experimental results and the solid line is drawn to fit them with a gradient of 1.0.

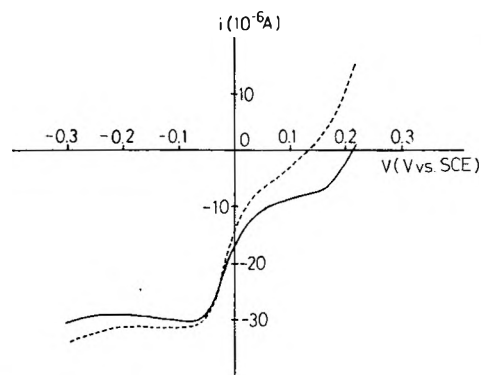


Figure 4. The current-voltage relations obtained potentiostatically between two platinum electrodes. The area of the illuminated electrode is 1.3 cm^2 . Curve a (—) is for the case where the two electrodes are kept in the dark. Curve b (---) is for the case where one of the electrodes is illuminated. The abscissa is the potential of the electrode to be illuminated vs. SCE. The negative sign for the current in the figure indicates cathodic currents for the illuminated electrode.

Figure 4 shows the current flowing between two Pt electrodes, with voltages applied by a potentiostat between them, vs. potential of the electrode to be illuminated. The photocurrent, i_p , defined here as the difference between the currents for the dark and illuminated electrodes, shows remarkable dependence on the electrode potential. It is to be noted that the i_p changes its direction at -0.03 V vs. SCE.

In order to observe the influence of the electrode material on the photovoltage and photocurrent, cell systems having the same metal as both dark and lighted electrode were investigated, using more than 10 different metals. Figure 5 shows the change of i_p with time for some typical cases. As seen in this figure, the photocurrent is strongly influenced by the electrode material. (Similar behavior was observed for the photovoltage.) In the case of Pt, the lighted (L) electrode becomes anodic (-) at the steady state, while for some other electrodes it becomes cathodic (+). The photocurrent behavior as shown in Figure 5 can be explained as a superposition of two components, i.e., a fast-response negative one (i_-) and a slow-response positive one (i_+) as schematically shown in Figure 6. Approximate ratios, i_-/i_+ , were obtained from the photocurrent curves. These values, together with the photocurrents i_p and photovoltages V_p at the steady state for various electrodes are given in Table I.

The dark electrode potentials (U) vs. SCE are found to correlate well with the sign of V_p and i_p as seen in Table

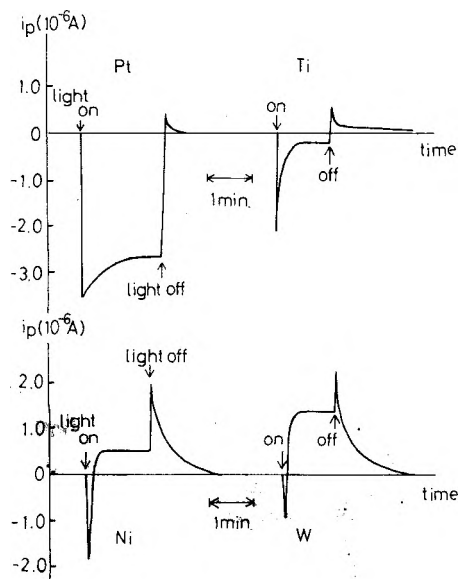


Figure 5. The change of the photocurrent, i_p , between directly connected two electrodes with time for four kinds of metal electrodes, Pt (1.3 cm²), Ti (2.8 cm²), Ni (1.7 cm²), and W (2.0 cm²). The number in parentheses is the area of each of the illuminated electrodes.

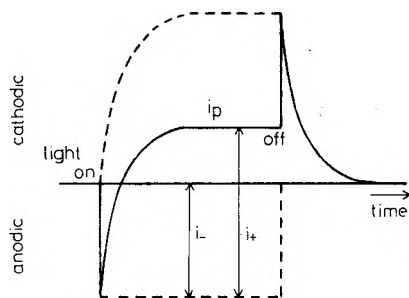


Figure 6. A typical photocurrent behavior, and its separation into two components, i_- and i_+ .

TABLE I: Photocurrent Densities (i_p) and Photovoltages (V_p) at Steady State for Various Electrodes, together with Electrode Potentials U and Fermi Levels E_F in the Dark

Electrode	V_p , mV	i_p , $\mu\text{A}/\text{cm}^2$	U , V vs. SCE	i_-/i_+	E_F , eV
Pt	-145	-3.1	+0.22	5.0~2.4	-4.97
C	-10	-1.0	+0.18	3.6~1.0	-4.93
Au	-77	-1.5	+0.15	2.1~1.9	-4.90
Ti	-30	-0.1	+0.01	~1.1	-4.76
Cu	-3 ^a	-0.3 ^a	+0.01	1.7~1.5	-4.76
Ag	-19	-0.8	-0.04	1.7~1.4	-4.71
W	+47	+0.5	-0.05	0.8~0.4	-4.70
Mo	+14	+2.2	-0.06	0.9~0.2	-4.69
Ni	+43	+0.6	-0.07	0.4~0.1	-4.68
Cr	+13	+1.5	-0.07	0.4~0.1	-4.68
Sn	+1.5	+0.2	-0.50	0.1~0.01	-4.25
Pb	+0.07	+0.3	-0.53		-4.22
Fe	^b	^b	-0.69		-4.06
Al	+27 ^c	+1.6	-0.85	~0.2	-3.90
Zn	+2.8	+10	-1.10	0.05	-3.65

^a In this case, an anodic current was observed by ultraviolet irradiation ($\lambda < 400$ nm). The value given here is obtained with a filter to remove UV light. ^b No distinct photoresponse was observed due to high noise levels. ^c A glass filter, transparent for wavelengths longer than 470 nm, was used to remove the ultraviolet light which causes a cathodic current in this case.

I. The V_p and i_p become negative when U is more positive than -0.05 V vs. SCE, while they become positive with more negative potentials. Furthermore, the ratio i_-/i_+ has a definite tendency to increase as U becomes more positive.

TABLE II: Photocurrent Densities (i_p) and Photovoltages (V_p) in the Case of Platinum Electrodes at Various Concentrations of Thionine and Fe²⁺ Ion

Thionine, M	FeSO ₄ , M	V_p , mV	i_p , $\mu\text{A}/\text{cm}^2$	U , V vs. SCE
5.0×10^{-5}	9.7×10^{-2}	-60	-3.2	+0.220
7.1×10^{-5}	5.4×10^{-5}	-65	-0.16	+0.280
7.1×10^{-5}	5.4×10^{-8}	-40	-0.11	+0.390

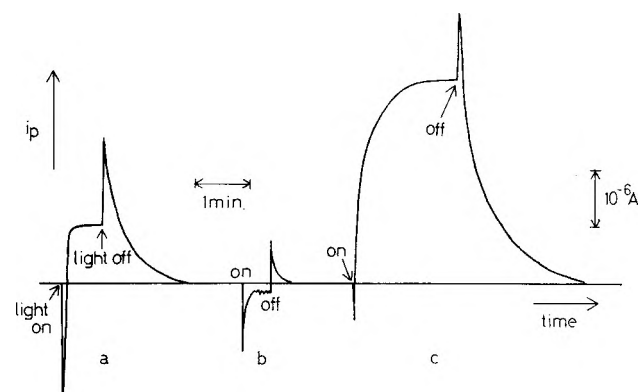


Figure 7. The influence of stirring and aeration on the photocurrent in the case of a Ni electrode. (a) A typical photocurrent curve measured after N₂ bubbling for more than 10 min. The potential of Ni electrode at dark was -0.098 vs. SCE. (b) The photocurrent curve measured while the solution was being stirred. (c) The photocurrent curve measured after introducing air. The electrode potential at dark changed to -0.240 V vs. SCE by introducing air.

The table also gives the Fermi levels (E_F) of the electrodes in contact with the solution, with the energy of the electron in vacuo taken as the reference point ($E = 0$). They have been calculated from the electrode potentials observed vs. SCE by assuming the electron energy for the normal hydrogen electrode (NHE) to be -4.50 eV.¹¹ Then, the Fermi level of an electrode is expressed by the relation $E_F = -eU - 4.50$

Table II gives the values of V_p and i_p for Pt electrodes in various concentrations of Th and Fe²⁺. They remain negative irrespective of the ratio of $[\text{Th}]_0/[\text{Fe}^{2+}]_0$ as it varied from 5.2×10^{-4} to 1.3×10^3 . Figure 7 shows the influence of agitation with a magnetic stirrer on the photocurrent in the case of the Ni electrode, for example. It shows that the positive component decreases while the influence on the negative one is relatively small, the i_p at the stationary state remaining negative. Figure 7 also shows that, when oxygen or air was introduced, the positive component increased, while the negative one decreased. The electrode potential in the dark shifted remarkably especially in the case of the Ni electrode, where the change was about -0.1 V. The effect was nearly reversible. In the case of Pt electrodes, both the V_p and i_p decreased remarkably upon introducing oxygen. In the case of the Ag electrode, the sign of V_p and i_p changed to positive. A similar remarkable influence of air (or oxygen) and agitation was observed for electrodes of other metals.

The exchange current densities i_0 for both the Th|Sem and the Fe³⁺|Fe²⁺ systems were determined from the so called Tafel plots. The Tafel equation is expressed as $\log i = \log i_0 + c\eta$

where i is the current, η is the overpotential, that is, the difference between the potential applied and the rest potential, and c is a constant. The plot of $\log i$ against η gave a straight line at small η values and the exchange current i_0 was obtained from the intercept of $\log i$ with $\eta = 0$. The results are shown in Table III. The rate

TABLE III: Exchange Current Densities for the Th|Sem and Fe³⁺|Fe²⁺ Systems Obtained from Their Tafel Coefficients in the Case of Pt Electrodes^a

Redox system	$i_0, \mu\text{A cm}^{-2}$	U, V		
		vs. SCE	k^a, s^{-1}	k^c, s^{-1}
Th Sem	2.58	0.23	2.0×10^{11}	1.8×10^4
Fe ³⁺ Fe ²⁺	4.95	0.225	1.56×10^2	1.82×10^7

^a The rate constants for each of the electron transfer reactions were evaluated by assuming the electron transition distance to be about 3 Å.

constants for each of the electron transfer reactions between the Pt electrode and the solute molecules were evaluated from the exchange current densities as follows: In the equilibrium



the exchange current density i_0 is expressed by the relation $i_0 = k_c dF[\text{Th}] = k_a dF[\text{Sem}]$ (2)

where k_c is the rate constant for the cathodic reaction, k_a is that of the anodic reaction, d is the electron transition distance, and F is the Faraday constant.^{6,7} Since the standard electrode potential of the Th|Sem system is estimated to be ~ 0.06 V at pH 5 (see Discussion), the concentration ratio $[\text{Th}]/[\text{Sem}]$ is evaluated to be $10^{7.05}$ from the observed electrode potential. As the initial concentration of thionine, $[\text{Th}]_0$, is 5×10^{-8} mol/cm³, $k_a d$ is found to be 6.0×10^3 cm/s. When d is assumed to be about 3 Å,⁶ k_a is found to be 2.0×10^{11} s⁻¹. In the same way, the rate of electron transfer from the Pt electrode to the ferric ion is obtained as 1.8×10^7 s⁻¹. Since the electrode potential of Pt in the thionine-iron solution is 0.22 V vs. SCE at pH 5.0, the rate constants obtained from the exchange current are appropriate for the thionine-iron system.

Discussion

The main scheme for the photochemical reactions of the thionine-iron system can be represented as^{4,5,8}



together with the back reactions



Here Th, Sem, and Leu represent thionine, semithionine, and leucothionine, respectively. Because of protonation reactions (not included in the above equations) these reactions are influenced by pH. The standard redox potentials are estimated to be 0.32 \sim 0.34 and 0.43 \sim 0.44 V at pH 2 for the redox couple Th|Sem and Sem|Leu, respectively.^{4,9} From the pH dependence of the redox potentials,⁴ they are estimated to take the values 0.05 \sim 0.07 and 0.16 \sim 0.17 V at pH 5 where most of our experiments were carried out. Since the redox potential for the Fe³⁺|Fe²⁺ system is known to be 0.77 V, independent of pH, the changes of the standard Gibbs' free energies for the reaction 6 and 7 are evaluated to be $-0.72 \sim -0.70$ and $-0.61 \sim -0.60$ eV at pH 5, respectively. From these values, it is concluded that the reverse of reactions 6 and 7 do not proceed thermally. The reduction of thionine is caused only by the absorption of photon energy, and leucothionine is produced thermally by dismutation reaction 5 from

semithionine. The photogalvanic effect essentially originates from the free energy change involved in (6) or (7).

Figure 3 shows that the photocurrent i_p is proportional to the light intensity (I): $i_p \propto I^{1.0}$. It is therefore concluded that, among the possible two anodic reactions, Sem \rightarrow Th + e (electrode), Leu \rightarrow Sem + e (electrode), only the former is actually important, since the concentration of Sem, [Sem], is proportional to I , and [Leu] is thought to be proportional to I^2 .

Consequently, the main electrode reactions are thought to be the following:



and the corresponding reverse reactions at both lighted (L) and dark (D) electrode.

As shown in Table I the electrode potentials of various metals dipped in thionine-Fe²⁺ aqueous solution, U , depend on the electrode material, becoming increasingly positive as the metal becomes more noble. If the electrode material is chemically inert to the solution (i.e., for Pt, Au, and C), the electrode potential is governed by the redox potential of the thionine-Fe²⁺ system, regardless of the electrode material, and is nearly equal to the value expected from the concentrations of thionine and Fe²⁺. For other metals, it is not equal to the expected value. We measured the current-voltage curve for the Zn electrode in an aqueous solution of 0.01 M FeSO₄ under the potentiostatic condition. At potentials more positive than -1.15 V vs. SCE, a current due to the dissolution of Zn was observed. The rest potential, -1.15 V, scarcely changed even when thionine (5×10^{-5} M) was added to this system. This fact shows that the electrode potential of Zn is a mixed potential, determined mainly by the dissolution of Zn and the production of H₂. Actually the value of -1.10 V vs. SCE for Zn electrodes in Table I is very close to the standard redox potential of -1.00 V vs. SCE for the reaction, Zn²⁺ + 2e⁻ \rightarrow Zn. Thus the electrode potentials given in Table I are generally interpreted to represent mixed potentials except for the Pt, Au, and C electrodes.

Table I also shows that the V_p and i_p change with the electrode material, and their signs and the i_-/i_+ values have a good correlation with the electrode potential, U . These results suggest that the photogalvanic effect in these systems is governed by the electron transfer rate across the interfaces, which, in turn, is influenced by U . As shown in Figure 6, the photocurrent is explained by a superposition of a fast-response negative component and a slow-response positive one. Most probably the former is attributable to electron transfer from Sem in the electrolyte to the L electrode and the latter to that from the L electrode to Fe³⁺ in the electrolyte. We can derive the same conclusion from the following reasoning: The cathodic currents at L and D electrodes, I_L^c and I_D^c , are expressed generally as

$$I_L^c/F \equiv i_p/F = {}^1k_L[\text{Fe}^{3+}]_L - {}^2k_L[\text{Sem}]_L - {}^3k_L[\text{Leu}]_L + {}^4k_L[\text{Th}]_L - {}^5k_L[\text{Fe}^{2+}]_L \quad (10)$$

$$I_D^c/F = {}^1k_D[\text{Fe}^{3+}]_D - {}^2k_D[\text{Sem}]_D - {}^3k_D[\text{Leu}]_D + {}^4k_D[\text{Th}]_D - {}^5k_D[\text{Fe}^{2+}]_D \quad (11)$$

Here ${}^n k$ ($n = 1, \dots, 5$) denotes the rate constant of electron transfer between the electrode and the respective species in solution. The subscript L or D shows that the value is for the L or D electrode. In these equations, the third term can be omitted because the effect of the leucothionine can be neglected as discussed earlier. Under the condition of a closed circuit, the equation

$${}^n k_D = {}^n k_L = {}^n k \quad (n = 1, \dots, 5) \quad (12)$$

holds because of the almost same electrode potential at both electrodes. At steady state, the following relationship also holds:

$$I_L^c = -I_D^c \quad (13)$$

From these equations, the photocurrent i_p is expressed as

$$i_p/F = I_L^c/F = (I_L^c - I_D^c)/2F = {}^1 k \Delta[\text{Fe}^{3+}] - {}^2 k \Delta[\text{Sem}] + {}^4 k \Delta[\text{Th}] - {}^5 k \Delta[\text{Fe}^{2+}] \quad (14)$$

where $\Delta[\text{Fe}^{3+}] = 1/2 \{[\text{Fe}^{3+}]_L - [\text{Fe}^{3+}]_D\}$, etc.

Before the illumination, $[\text{Fe}^{3+}]$ and $[\text{Sem}]$ are very small in solution. On illumination at the L electrode, these species are formed around the L electrode from Fe^{2+} and Th, therefore, $\Delta[\text{Fe}^{3+}]$, $\Delta[\text{Sem}]$, $\Delta[\text{Th}]$, and $\Delta[\text{Fe}^{2+}]$ are approximately equal to each other in their absolute values and, from Table III, ${}^1 k$ and ${}^2 k$ are thought to be much larger than ${}^4 k$ and ${}^5 k$ in the potential range of our experiments. Consequently, the last two terms can be omitted and i_p can be approximately expressed as follows:

$$i_p/F = {}^1 k \Delta[\text{Fe}^{3+}] - {}^2 k \Delta[\text{Sem}] \quad (15)$$

Here $\Delta[\text{Fe}^{3+}]$ and $\Delta[\text{Sem}]$ are positive and nearly independent of the kind of the electrode material, because they are determined mainly by the photochemical reaction and the diffusion processes in the bulk solution. Therefore, the polarity of the photocurrent is affected by the competition between two electrochemical rate constants ${}^1 k$ and ${}^2 k$. The good correlation between i_p or i_-/i_+ and U , as demonstrated in Table I, shows that the rate constants, ${}^1 k$ and ${}^2 k$, depend strongly on the electrode potential, U .

The dependence of the rate constants on U can be explained by the following theoretical expression:¹⁰

$$k \sim \int \nu(E) W_-(E) W_+(E) dE \quad (16)$$

Here E represent the electron energy, and $\nu(E)$ is the transfer frequency as a function of E . $W_-(E)$ gives the energy distribution function for the occupied electron states with energy E of the electrode (or the solution) and $W_+(E)$ that for the unoccupied electron states of the solution (or the electrode). This equation shows that the overlap between the state density of the donor and that of the acceptor is important for electron transfer. The distribution functions for the species in solution are expressed as follows, under a harmonic approximation for the thermal motions of solvent molecules:

$$W_{\text{sol}+}(E) \propto \exp[-(E - \epsilon_F^\circ - \lambda)^2/4\lambda kT] \quad (17)$$

$$W_{\text{sol}-}(E) \propto \exp[-(E - \epsilon_F^\circ + \lambda)^2/4\lambda kT] \quad (18)$$

Here λ designates the reorganization energy, and ϵ_F° the standard Fermi level of the redox system. The product of the distribution function and the concentration of an acceptor or a donor represents the state density.

Figure 8 shows the schematic representation of the Fermi levels of the various metal electrodes, the donor state energy distribution function of semithionine, and the acceptor state energy distribution function of ferric ion. They have maxima at $E = \epsilon^\circ(\text{Th}|\text{Sem}) + \lambda_1$ and $E = \epsilon^\circ(\text{Fe}^{3+}|\text{Fe}^{2+}) - \lambda_2$, respectively. The standard Fermi level of the Th|Sem redox system, $\epsilon^\circ(\text{Th}|\text{Sem})$, is obtained as about -4.56 eV by using the standard redox potential ($E^\circ(\text{Th}|\text{Sem}) = 0.06$ at pH 5.0) together with the potential of normal hydrogen electrode from vacuum (4.50 V).¹¹ Though the reorganization energy has not yet been obtained for the Th|Sem system, it is considered to be about 0.5 eV.¹² Therefore the state density of Sem has its maximum at about -5.06 eV.¹³ In the same way, as ϵ_F°

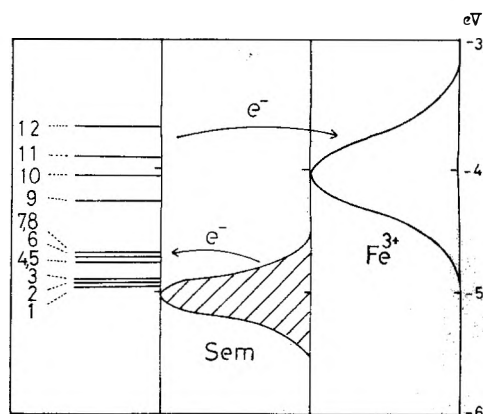


Figure 8. The Fermi levels of various electrodes immersed in Th-Fe²⁺ aqueous solution in the dark (left), the donor state distribution function of semithionine (middle), and the acceptor state distribution function of Fe³⁺ ion in vacuo is taken as the reference point, $E = 0.0$ eV: (1) Pt, (2) C, (3) Au, (4) Ti, (5) Cu, (6) Ag, (7) Ni, (8) Cr, (9) Sn, (10) Fe, (11) Al, (12) Zn.

($\text{Fe}^{3+}|\text{Fe}^{2+}$) = $-(0.77 + 4.5)$ eV, the acceptor level of Fe³⁺ is estimated to be located at about -4.02 eV by using 1.25 eV as the reorganization energy obtained experimentally for this system.¹⁴ As seen from Figure 8, an electron can transfer easily from Sem to the electrode, but hardly from the electrode to Fe³⁺ in other words, ${}^1 k \ll {}^2 k$, in the case where the Fermi level of the electrode lies in the region of the energy of Sem (Pt to Cr). It can easily be understood that the second term on the right-hand side of eq 15 is overwhelmingly larger than the first one and i_p/F becomes negative. The situation is reversed if the Fermi level is higher (for Sn, Fe, Al, Zn). Taking account of this dependence of the rate of electron transfer on the electrode potential, it is well understood that the polarity of the L electrode becomes negative in the case of an electrode with a low Fermi level such as Pt and Au, and that it becomes positive for an electrode with a high Fermi level such as Ni and Zn. These considerations agree well with the experimentally obtained polarity of V_p and i_p .

As seen in Figure 4, the photocurrent, i_p , the difference between the current under illumination and that at dark, changes its polarity at about -0.03 V vs. SCE. This result is also explained by the shift of the Fermi level of the Pt electrode: With the voltage moving toward the positive direction, the Fermi level is brought down, making electron transfer from Sem to the Pt electrode easier. With the voltage getting more negative, this electron injection is depressed and the electron transfer from Pt to Fe³⁺ in the solution gets stronger, owing to the upward shift of the Fermi level of the Pt electrode. It is interesting to note that the above-mentioned crossing point between the two current curves, about -0.03 V, is quite close to $-0.04 \sim -0.05$ V vs. SCE in Table I where the polarity of i_p and V_p changes. These facts are well explained by the present model.

As shown in eq 15, the i_p is governed by the competition between the two components, i.e., the electron injection from Sem to the electrode and the electron extraction by Fe³⁺ from the electrode. The strong influence of agitation on the positive components but not on the negative one as shown in Figure 7 suggests that the rate of electron extraction by Fe³⁺ from the electrode is slow enough to be influenced by stirring, while that of the electron donation from Sem to the electrode is too fast to be influenced by stirring.

The remarkable influence of oxygen for the nickel electrode on the photocurrent as shown in Figure 7 probably arises from two reasons. One is the oxidation of

Sem to Th by oxygen. The standard redox potential for the couple $O_2 + 4H^+ + 4e^- | 2H_2O$ at pH 5 is 0.94 V and that for Th|Sem couple is 0.06 V at pH 5. Secondly, the electrode potential shift by oxygen to the negative direction as described in the Results section suppresses the anodic current and enhances the cathodic current. The reason for the potential shift is not well established at present, though it may be probable that the adsorption of oxygen on the electrode surface causes a double layer.

Conclusion

The electron transfer rates between an electrode and active species in solution play an important role for the photogalvanic effect. Especially, the position of the Fermi level of the electrode dipped in the electrolyte solution relative to those of the donor or acceptor states the dissolved species is one of the most important factors that determine the polarity of the photocurrent and photovoltage of a photogalvanic cell.

References and Notes

- (1) E. Becquerel, *C. R. Acad. Sci., Paris*, **9**, 561 (1839).
- (2) A. E. Potter, Jr., and L. H. Thaller, *Solar Energy*, **4**, 1 (1959).
- (3) W. D. K. Clark and J. A. Eckert, *Solar Energy*, **17**, 147 (1975).
- (4) E. Rabinowitch, *J. Chem. Phys.*, **8**, 551 (1940).
- (5) E. Rabinowitch, *J. Chem. Phys.*, **8**, 560 (1940).
- (6) R. Gomer, *Electrochim. Acta*, **20**, 13 (1975).
- (7) T. N. Andersen and H. Eyring, "Physical Chemistry—An Advanced Treatise", Vol. 9A, Academic Press, New York, N.Y., 1970, p 247.
- (8) C. G. Hatchard and C. A. Parker, *Trans. Faraday Soc.*, **57**, 1041 (1961).
- (9) The calculation by Rabinowitch includes a simple error. The values given here are the corrected ones.
- (10) H. Gerischer, *Photochem. Photobiol.*, **16**, 243 (1972); H. Gerischer, "Advances in Electrochemistry and Electrochemical Engineering", Vol. 1, P. Delahay, Ed., Interscience, New York, N.Y., 1961.
- (11) F. Lohmann, *Z. Naturforsch. A*, **22**, 843 (1967).
- (12) R. Memming and F. Mollers, *Ber. Bunsenges. Phys. Chem.*, **76**, 609 (1972).
- (13) By taking into consideration the difference of the standard redox potentials of Th|Sem and Sem|Leu, the donor level of leucothionine is considered to be lower than that of semithionine by 0.1 eV.
- (14) R. Memming and F. Mollers, *Ber. Bunsenges. Phys. Chem.*, **76**, 475 (1972).

Thermal Variations of Rotatory Power. Conformational Equilibrium and Conformer Rotivities Determinations

Robert Lauricella, Josette Kechayan, and Hubert Bodot*

Laboratoire de Chimie Organique Structurale, Université de Provence, Centre de Saint Jérôme, 13397 Marseille Cedex 4, France
(Received December 6, 1976)

Publication costs assisted by the Université de Provence

Very accurate data on the rotatory power of α -pinene and of (3*R*)-3-methylmethylenecyclohexane at different temperatures in different apolar solvents have been obtained and used to calculate the rotivities, Ω_0 , under vacuum. These rotivities do not vary with temperature for a locked molecule (α -pinene). For the second molecule, a least-squares analysis of $\langle \Omega_0 \rangle = f(T)$ leads to values of the conformational enthalpy difference ($\Delta H^\circ = 1.1$ kcal mol⁻¹) and of the conformer rotivities Ω_0^i (-28.8 and +11.1) for the equatorial and axial methyl conformers respectively. These values are obtained for the hypothesis $\Delta S^\circ = 0$ eu. A different hypothesis ($\Delta S^\circ = \pm 1.37$ eu) results in little change of ΔH° (less than 0.2 kcal mol⁻¹) and Ω_0^{equat} (± 0.5). The validity of this kind of mean squares analysis is discussed.

Introduction

Several measurable physical parameters (dipole moments, NMR coupling constants, chemical shifts, etc.) depend on the conformational equilibrium of the molecule considered. In the simplest case of a two conformer equilibrium:

$$A \rightleftharpoons B \quad (1)$$

$$\omega \quad 1 - \omega$$

the average parameter is expressed as a function of the specific parameters D^A and D^B .

$$\langle D \rangle = (D^A - D^B)\omega + D^B \quad (2)$$

The mole fraction ω of the conformation A is a function of the temperature.

$$\omega = \frac{\exp(-\Delta S^\circ/R)}{\exp(-\Delta S^\circ/R) + \exp(-\Delta H^\circ/RT)}$$

If D^A , D^B , ΔH° , and ΔS° are temperature independent, their determination will theoretically be possible by

studying the experimental curve $\langle D \rangle = f(T)$ by a least-squares analysis.

This method has been used previously in NMR,^{1,2} rotatory power, and circular dichroism³ experiments. Critical studies of the method have been carried out and anomalies in the results have been explained.⁴⁻⁶

The first difficulty which has been revealed concerns the validity of the least-squares analysis when the experimental data are not precise enough. Govil and Bernstein⁴ showed that even when the value of ΔS° is assumed, the determination of ΔH° , D^A , and D^B is only possible when there is available a precision superior to 0.025 Hz in the coupling constant data. Garbish et al.⁵ made a more optimistic critical study of the method. They consider that within some limits of the ΔH° and ΔS° values, the probable errors obtained on these two parameters are acceptable if

$$\sigma \leq 4 |D^A - D^B| 10^{-4}$$

σ being the standard deviation of the observed parameters.

The second difficulty is related to the possible variations of ΔH° and ΔS° , and mainly those of D^A and D^B with the temperature.

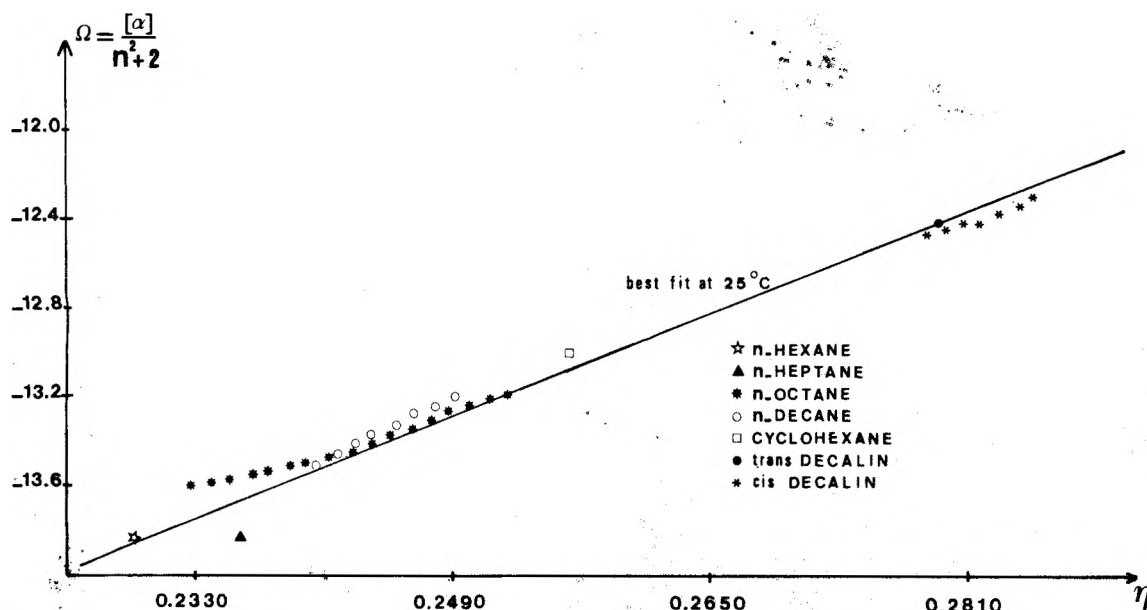


Figure 1. Solvent and temperature effects on the rotivity of α -pinene.

The study of the thermal variation of rotatory power can a priori lead to much more precise experimental determinations than those of NMR, because of recent technological improvements in these measurements. (cf. Experimental Section).

Rotatory Power and Rotivity

According to Rosenfeld's theory,⁷ the expression for molecular rotation is

$$[M] = \frac{96\pi N n^2 + 2}{hc} \sum \omega_i \beta_i \quad (3)$$

with

$$\beta_i = \sum_j \frac{R_{ij} \nu^2}{\nu_{ji}^2 - \nu^2} \quad (4)$$

n^2 is the dielectric constant of the surrounding medium; N is the number of molecules per volume unit; ω_i is the mole fraction of the i conformer; and R_{ij} the rotatory strength of the $i \rightarrow j$ transition between ground state and excited electronic levels.

From this expression, it is obvious that the rotivity⁸

$$\Omega = \frac{[\alpha]}{n^2 + 2} = \frac{[M]100}{M(n^2 + 2)} \quad (5)$$

where M is the molecular weight, is strongly dependent on the conformational equilibrium of the molecule according to eq 3 and 5:

$$\Omega = C^{te} \sum \omega_i \beta_i \quad (6)$$

Other numerous theoretical and semiempirical works^{9,10} have shown that β values can vary considerably from one conformer to the other.

A study of the solvent effect on rotatory power has been carried out by Beckmann and Cohen¹¹ and also by Eyring.¹² They show that the rotivity depends on the dielectric constant of the surroundings.

$$\Omega = \Omega_0 + P \left(\frac{\epsilon - 1}{\epsilon + 2} \right) = \Omega_0 + P\eta \quad (7)$$

P being a constant for a homogeneous family of solvents (for example, saturated hydrocarbons) at a given tem-

Chart I

	a	b	c	d	e
Ω_0	-20.55	-19.3	-22.2	-18.7	-19.9
P	29.2	24.6	36.1	21.9	26.7

perature. In nonpolar solvents, we can let $\epsilon = n^2$ and $\eta = (n^2 - 1)/(n^2 + 2)$.

Rotivity of a Locked Molecule

The rotivity in vacuo, Ω_0 , is the characteristic experimental property of a conformer a priori temperature independent. In order to check this, we have studied the thermal variation of the rotivity Ω of α -pinene, a locked molecule unable to undergo conformational equilibrium, in a series of nonpolar solvents.

In Figure 1, eq 7 is shown to be a good approximation; the observed discrepancies may correspond to specific effects of the solvents. From the experimental data (cf. Experimental Section, Table IV), the rotivity Ω_0 is calculated for the following groups of values (Chart I): (a) seven solvents at 25 °C; (b) seven temperatures in *cis*-decalin; (c) eight temperatures in *n*-decane; (d) 17 temperatures in *n*-octane; (e) on all the data.

The agreement between the different Ω_0 values being good, it is obvious that the change of Ω with temperature is only related to the variation of the solution refractive index; thus, Ω_0 and P are constants. All this suggests that for other molecules the variations of these last two parameters with temperature is only due to variations in conformer populations. So, for equilibrium 1:

$$\langle P \rangle = (P^A - P^B)\omega + P^B \quad (8)$$

$$\langle \Omega_0 \rangle = (\Omega_0^A - \Omega_0^B)\omega + \Omega_0^B \quad (9)$$

These two equations give

$$\langle \Omega_0 \rangle = K \langle P \rangle + L \quad (10)$$

with $K = (\Omega_0^A - \Omega_0^B)/(P^A - P^B)$ and $L = \Omega_0^B - KP^B$. The experimental results are in agreement with eq 10 (Table I).

Rotivity of Molecules in Conformational Equilibrium

A comparison between Figures 1 and 2 shows that *d*-limonene (1) is not in a locked structure. In fact, Figure 2 shows that the solvent effect (represented by lines at 25

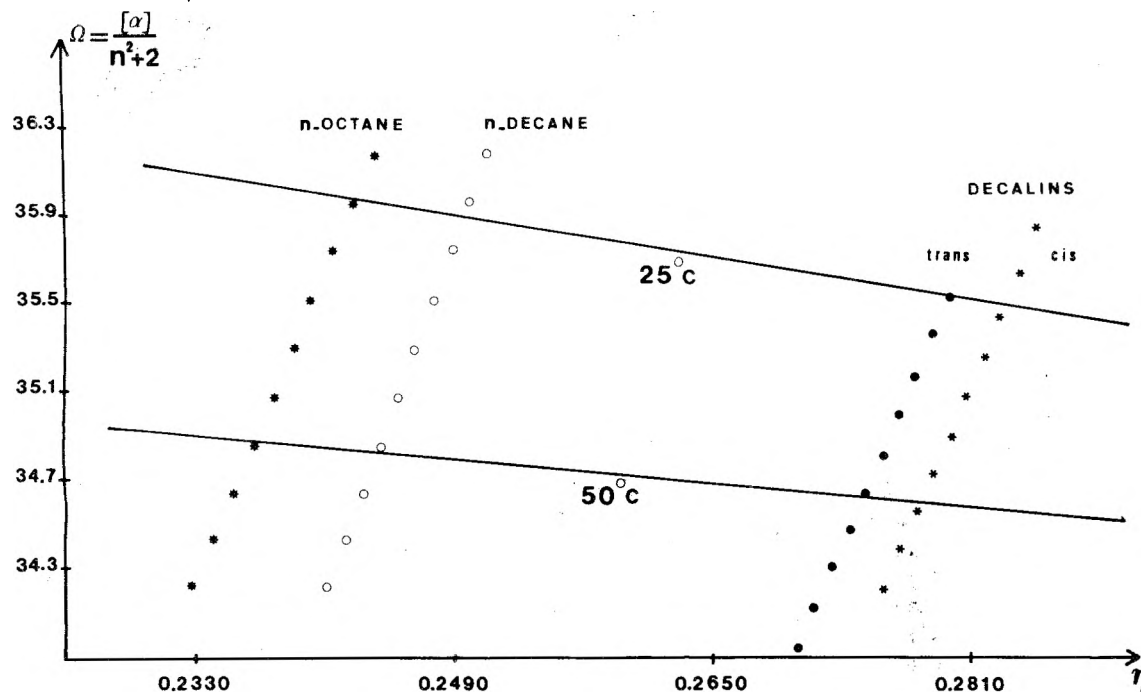


Figure 2. Solvent and temperature effects on the rotivity of *d*-limonene.

TABLE I: Parameters Associated with the Solvent Effect on the Rotivity (Eq 10) and Corresponding Standard Deviations^a

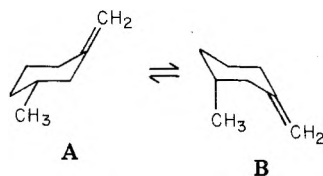
	1	2	3	4	5
<i>b</i>	4	3	4	4	6
<i>T</i> , K	{298	{258	{258	{258	{288
range	{338	{338	{338	{338	{338
<i>K</i>	-0.451	-0.397	-0.364	-0.617	-0.407
σ_K	0.005	0.008	0.003	0.029	0.007
<i>L</i>	33.46	-8.2	24.67	29.26	38.7
σ_L	0.05	0.28	0.04	0.75	0.4

^a 1, *d*-limonene; 2, (3*R*)-3-methylmethylenecyclohexane;¹³ 3, (3*R*)-3-methylcyclohexene;¹⁴ 4, (4*R*)-4-methylcyclohexene;¹⁴ 5, buten-3-ol.¹⁵ ^b Number of solvents.

and 50 °C) is superposed to a more important effect which is the variation of the conformational population with temperature.

The experimental results concerning limonene could not be used for the conformational determination because the exocyclic rotation of the isopropylidene group increases the number of conformers with different rotativities, as shown by a priori calculations done in connection with this work.^{16,17} However, this study was interesting for the solvent effect, and we report (Experimental Section, Table V) Ω_0 values at different temperatures; these results may be used later with the calculated rotivities of the different conformers.

The (3*R*)-3-methylmethylenecyclohexane (compound 2) shows a more simple conformational equilibrium:



The experimental results (Experimental Section, Table VI) lead to the same graph as in Figure 2, typical of the change in conformer populations with temperature.

For each temperature *T*, the rotivity $\langle \Omega_0 \rangle_T$ and the constant $\langle P \rangle_T$ are obtained through a least-squares analysis

TABLE II: Rotivity in Vacuo of (3*R*)-3-Methylmethylenecyclohexane Vs. Temperature

<i>t</i> , °C	$\langle \Omega_0 \rangle^a$	$\langle \Omega_0 \rangle^b$	$\langle \Omega_0 \rangle^c$
-15.0	-23.885	-24.082	-23.423
-10.0	-23.669	-23.929	-23.276
-5.0	-23.439	-23.769	-23.133
0.0	-23.223	-23.615	-22.988
+5.0	-23.006	-23.454	-22.839
+10.0	-22.882	-23.314	-22.690
+15.0	-22.736	-23.173	-22.553
+20.0	-22.643	-23.040	-22.426
+25.0	-22.514	-22.901	-22.300
+30.0	-22.361	-22.755	-22.160
+35.0	-22.240	-22.611	-22.036
+40.0	-22.121	-22.473	-21.908
+45.0	-22.028	-22.341	-21.784
+50.0	-21.912	-22.206	-21.643
+55.0	-21.803	-22.064	-21.505
+60.0	-21.701	-21.923	-21.364
+65.0	-21.654	-21.793	-21.232

^a From eq 7. ^b From eq 11 with values of $\langle \Omega \rangle_T$ in the solvent *n*-decane. ^c From eq 11 with values of $\langle \Omega \rangle_T$ in the solvent *n*-octane.

of the variation $\langle \Omega \rangle_T = f(\eta)_T$ (eq 7) which is obtained by a solvent change. The parameters *K* and *L* are then calculated from the variation $\langle \Omega_0 \rangle = f(P)$ (eq 10) which is obtained thanks to a change of temperature. The standard deviations in the values of *K* and *L* being particularly weak (Table I), those values are used in eq 11 (from eq 7 and 10) to obtain more precise values of the rotivity $\langle \Omega_0 \rangle_T$ (Table II). The experimental values of $\langle \Omega \rangle_T$ used are

$$\langle \Omega_0 \rangle_T = (\langle \Omega \rangle_T K + \eta_T L) / (K + \eta_T) \quad (11)$$

those determined in the solvent which gives the most important variation with temperature, that is to say a solvent corresponding to the lowest value of η (for example, solvent decane for 2). The whole process seems complex but, in fact, it is equivalent to a solvent effect parametrization applied as a correction to the most accurate measurements of rotivity.

To find ΔH° , ΔS° , Ω_0^A , and Ω_0^B from these values of $\langle \Omega_0 \rangle = f(T)$, we used a least-squares analysis program which is similar to the one described by Garbisch.⁵ The discussion

TABLE III: Enthalpy Differences and Specific Rotivities of Conformers for 2

$S_B^\circ - S_A^\circ, \text{eu}^a$	-1.37	0	+1.37
$H_B^\circ - H_A^\circ, \text{kcal mol}^{-1}$	0.98 ± 0.04	1.10 ± 0.04	1.28 ± 0.04
Ω_0^A	-28.5 ± 0.5	-28.2 ± 0.5	-27.7 ± 0.4
Ω_0^B	$+36.1 \pm 1.2$	$+11.1 \pm 0.7$	-1.86 ± 0.5
$\langle \Omega_0 \rangle_T^b$	0.0085	0.0087	0.0091

^a Hypothesis. ^b $\langle \Omega_0 \rangle_T$ standard deviation calculated from column b or c of Table II.

will show that experimental precision is not sufficient to obtain the four parameters simultaneously, so we have assumed $\Delta S^\circ = 0$ and minimized the errors to obtain ΔH° , Ω_0^A , and Ω_0^B (Table III). The same results are obtained if we use $\langle \Omega_0 \rangle_T$ of column b or those of column c. On the contrary, we cannot minimize the errors if we take $\langle \Omega_0 \rangle_T$ in column a.

It is important to notice the calculated values of ΔH° depend very little on the assumed ΔS° value (even when changing the ΔS° to improbable values, see Table III). The same is true for the Ω_0^A value of the conformer with the equatorial methyl group. On the contrary, Ω_0^B cannot be accurately determined since it strongly depends on the value of ΔS° .

If we admit that the most stable conformer A is the one which has the equatorial methyl group, we can compare the value thus obtained $\Delta H^\circ = 1.10 \pm 0.04 \text{ kcal mol}^{-1}$ to the free energy difference ($1.2 \text{ kcal mol}^{-1}$)¹⁸ calculated for the conformational equilibrium of 3-methylcyclohexanone, the structure of which is at first sight, very similar to that of 2.

Moreover, Lambert and Clikeman¹⁹ have recently measured for 2, $\Delta H^\circ = 0.8 \pm 0.1 \text{ kcal mol}^{-1}$, which is in reasonable agreement with our result considering the wide disparity in the physical conditions of the measurement.

Discussion

First, we must examine the limits of the least-squares analysis. The simplest way is to make a simulation: by calculation of the exact $\langle \Omega_0 \rangle_T$ values corresponding to the parameters of Table III (hypothesis $\Delta S^\circ = 0 \text{ eu}$); by comparison of the standard deviation of experimental $\langle \Omega_0 \rangle_T$'s (column b or c of Table II) to those obtained when the minimization is done on exact $\langle \Omega_0 \rangle_T$ and involve: (a) Ω_0^A and Ω_0^B for $\Delta S^\circ = 0 \text{ eu}$ and different values of ΔH° (Figure 3, graph I); (b) ΔH° , Ω_0^A , and Ω_0^B for different values of ΔS° (Figure 3, graph II).

In the first case, the standard deviation (Table III) is reached for $\Delta \Delta H^\circ \approx 150 \text{ cal}$; but the minimization with four parameters reveals a very large uncertainty. Only greater accuracy ($\times 30$) of the experimental values would enable the four parameters to be obtained simultaneously. However, our rotivity measurements appear far more satisfactory than the most accurate NMR measurements; so, if we do the same kind of simulation with experimental values of $\langle J \rangle = f(T)$ of Hawkins²⁰ related to 3-methylcyclohexene, we obtain Figure 4 which exhibits a larger uncertainty than Garbisch's.⁵

Finally, the necessity to take into account the solvent effect must be demonstrated since this factor has been neglected in a work⁶ which is interesting in another way for its view on the limits of the least-squares analysis. If this analysis is done in a straightforward way on $\langle \Omega \rangle_T$ values of the Table VI for *n*-decane and *n*-octane solvents, the error minimization leads respectively to $\Delta H^\circ = 2.40$ and $3.60 \text{ kcal mol}^{-1}$ (hypothesis $\Delta S^\circ = 0 \text{ eu}$). Obviously, these values are very different from the results of analysis

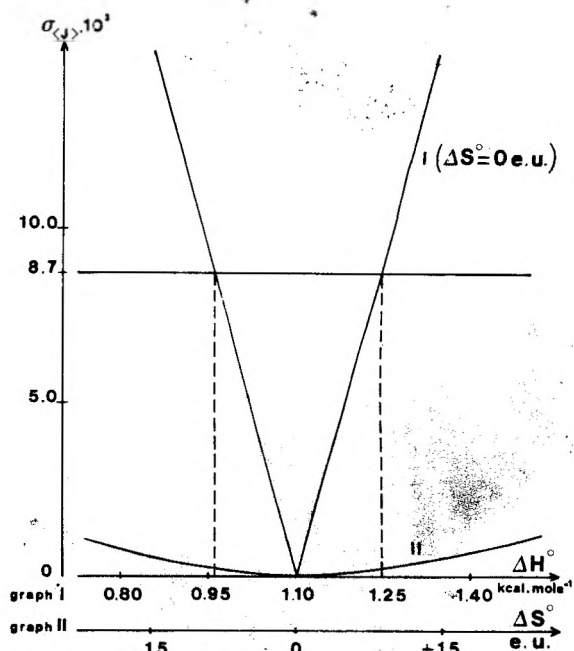


Figure 3. Standard deviations of three- (I) or four- (II) parameter least-squares analysis for calculated rotivities of (3R)-3-methylmethylene cyclohexane (Table III).

TABLE IV: Rotivities (Ω) of α -Pinene in Different Solvents and at Different Temperatures

<i>a</i>	<i>t</i> , °C	$10^2 C$	<i>n</i>	$\langle \Omega \rangle$	η
A	25	0.800	1.37751	-13.832	0.22920
B	25	0.800	1.38760	-13.812	0.23575
C	25	5.203	1.40051	-13.440	0.24269
D	25	1.604	1.41248	-13.191	0.24908
E	25	0.800	1.42584	-13.000	0.25614
F	25	0.800	1.46993	-12.397	0.27897
G	25	0.800	1.48167	-12.285	0.28492
G	30	0.794	1.47961	-12.328	0.28388
G	35	0.790	1.47741	-12.358	0.28277
G	40	0.791	1.47543	-12.394	0.28176
G	45	0.787	1.47311	-12.400	0.28058
G	50	0.784	1.47096	-12.430	0.27949
G	55	0.780	1.46874	-12.455	0.27836
D	25	1.604	1.41248	-13.191	0.24908
D	30	1.596	1.41019	-13.235	0.24787
D	35	1.587	1.40792	-13.274	0.24660
D	40	1.579	1.40564	-13.318	0.24540
D	45	1.570	1.40336	-13.362	0.24420
D	50	1.562	1.40108	-13.401	0.24300
D	55	1.554	1.39881	-13.451	0.24180
D	60	1.545	1.39653	-13.503	0.24056
C	-15	5.429	1.41899	-13.180	0.25253
C	-10	5.401	1.41668	-13.204	0.25130
C	-5	5.373	1.41436	-13.226	0.25008
C	0	5.344	1.41205	-13.255	0.24885
C	5	5.316	1.40974	-13.289	0.24762
C	10	5.288	1.40743	-13.331	0.24639
C	15	5.259	1.40512	-13.363	0.24516
C	20	5.231	1.40281	-13.402	0.24393
C	25	5.203	1.40051	-13.437	0.24269
C	30	5.174	1.39820	-13.464	0.24146
C	35	5.146	1.39590	-13.486	0.24022
C	40	5.118	1.39360	-13.500	0.23899
C	45	5.089	1.39130	-13.520	0.23775
C	50	5.061	1.38899	-13.539	0.23651
C	55	5.033	1.38670	-13.556	0.23527
C	60	5.005	1.38440	-13.573	0.23402
C	65	4.976	1.38210	-13.590	0.23278

^a For solvents, see Experimental Section.

starting with $\langle \Omega_0 \rangle_T$ and they are not in agreement with our structural knowledge (see the comparison with 3-methylcyclohexanone); also the apparent solvent effect on ΔH° cannot be justified when 2 and the two solvents are

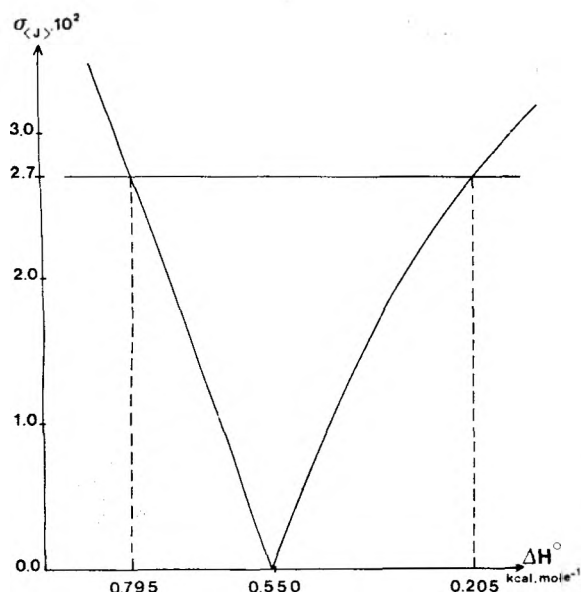


Figure 4. Standard deviations of three-parameter least-squares analysis ($\Delta S^\circ = 0$ eu) for calculated NMR coupling constants of 3-methylcyclohexene.¹⁹

TABLE V: Rotivities (Ω_0) of *d*-Limonene

$t, ^\circ\text{C}$	$\langle\Omega_0\rangle^a$	$\langle\Omega_0\rangle^b$
20	39.319	39.602
25	38.906	39.073
30	38.473	38.543
35	37.959	38.021
40	37.448	37.507
45	36.940	36.999
50	36.422	36.504
55	35.935	36.021
60	35.462	35.555
65	35.051	35.091

^a Experimental $\langle\Omega_0\rangle_T$. ^b $\langle\Omega_0\rangle$ calculated from values of $\langle\Omega\rangle$ in *n*-decane solvent.

nonpolar or very slightly polar.

Conclusion

The thermal variations of rotivity is thus an interesting experimental technique to determine the enthalpy differences between conformers, especially for nonpolar molecules; that is to say for molecules which are difficult to study by other methods. Eventually, we plan to extend

this technique to polar molecules.

Finally, conformer rotivity determinations give an important input to test the validity of these a priori calculations obtained through empirical or semiempirical calculations.^{16,17} When the validity is established, we shall have a useful tool for absolute configuration determinations.

Experimental Section

A. Rotatory Power. Apparatus. The equipment used is an electronic polarimeter Bendix NPL Type 143 fitted with a digital exit (voltmeter Schlumberger Type LM 1420 2F). A thermostated cell equipped with a platinum resistance thermometer was built allowing a satisfactory control of the temperature (with a precision of better than 0.1 °C). Moreover, the residual angle of the cell (and its variation according to the temperature) have been reduced: (a) by a decrease of the mechanical strains on the cell windows; and (b) by a linear variation with a weak temperature gradient.

Solvents. *cis*- and *trans*-decalin were separated during two distillations at reduced pressure (a 30 theoretical plates column). All the solvents used were dust free: (A) *n*-hexane; (B) *n*-heptane; (C) *n*-octane; (D) *n*-decane; (E) cyclohexane; (F) *cis*-decalin; (G) *trans*-decalin.

B. Refractive Indexes. The refractive index concerning any of the solutions for a wavelength equal to 5461 Å and at a temperature of 25 °C is measured with a Pulfrich refractometer (Bellingham & Stanley).

The refractive indexes at other temperatures are deduced from the density measurements thanks to the Eckman empirical formula²¹

$$\frac{n_2 - 1}{n + 0.4d} = C$$

The indexes are thus obtained with a precision of about 10⁻⁴.

C. Densities. The densities are measured with a digital microdensimeter Anton Paar DM A 10 with a precision of about 2.5 × 10⁻⁴.

These densities are used to estimate the concentrations *C* at different temperatures.

D. Experimental Data. Experimental data are reported in Tables IV–VI.

TABLE VI: Rotivities of 2

$t, ^\circ\text{C}$	<i>C</i> ^a		<i>D</i> ^a		<i>F</i> ^a	
	$\langle\Omega\rangle$	η	$\langle\Omega\rangle$	η	$\langle\Omega\rangle$	η
-15	-13.660	0.25498	-13.697	0.25990	-12.321	0.29102
-10	-13.655	0.25372	-13.691	0.25877	-12.331	0.28993
-5	-13.650	0.25246	-13.680	0.25761	-12.343	0.28883
0	-13.645	0.25121	-13.671	0.25645	-12.353	0.28774
+5	-13.636	0.24995	-13.659	0.25529	-12.360	0.28664
+10	-13.627	0.24869	-13.653	0.25413	-12.357	0.28554
+15	-13.621	0.24743	-13.645	0.25297	-12.359	0.28445
+20	-13.619	0.24617	-13.640	0.25180	-12.357	0.28335
+25	-13.616	0.24491	-13.634	0.25064	-12.359	0.28224
+30	-13.606	0.24360	-13.622	0.24947	-12.358	0.28114
+35	-13.602	0.24238	-13.611	0.24831	-12.357	0.28004
+40	-13.596	0.24111	-13.601	0.24714	-12.355	0.27893
+45	-13.591	0.23984	-13.594	0.24597	-12.350	0.27783
+50	-13.578	0.23857	-13.583	0.24480	-12.342	0.27672
+55	-13.566	0.23730	-13.570	0.24362	-12.333	0.27560
+60	-13.551	0.23603	-13.556	0.24245	-12.321	0.27450
+65	-13.540	0.23475	-13.545	0.24127	-12.304	0.27340

^a For solvents, see Experimental Section.

References and Notes

- (1) H. S. Gutowsky, G. G. Bedford, and P. E. Mac Mahon, *J. Chem. Phys.*, **36**, 3353 (1962).
- (2) R. J. Abraham and H. J. Bernstein, *Can. J. Chem.*, **39**, 39 (1961).
- (3) (a) H. J. Bernstein and E. Pedersen, *J. Chem. Phys.*, **17**, 885 (1949); (b) W. W. Wood, W. Fickett, and J. G. Kirkwood, *J. Chem. Phys.*, **20**, 561 (1952); (c) A. Moscovitz, K. Wellman, and C. Djerassi, *J. Am. Chem. Soc.*, **85**, 3515 (1963).
- (4) G. Govil and H. J. Bernstein, *J. Chem. Phys.*, **47**, 2818 (1967).
- (5) E. W. Garbisch, B. L. Hawkins, and K. D. Mackay in "Conformational Analysis", G. Chiurdoglu, Ed., Academic Press, London, 1971.
- (6) H. Joshua, R. Gans, and K. Misiow, *J. Am. Chem. Soc.*, **90**, 4884 (1968).
- (7) (a) L. Rosenfeld, *Z. Phys.*, **52**, 161 (1928); (b) M. Born and P. Jordan, "Elementare Quantenmechanik", Verlag Julius Springer, Berlin, 1930, p 250; (c) J. G. Kirkwood, *J. Chem. Phys.*, **5**, 479 (1937).
- (8) J. P. Mathieu, "Les Theories moleculaires du pouvoir rotatoire naturel", CNRS, Paris, 1946.
- (9) E. L. Eliel, "Stereochemistry of Carbon Compounds", McGraw-Hill, New York, N.Y., 1962.
- (10) R. R. Gould and R. Hoffmann, *J. Am. Chem. Soc.*, **92**, 1813 (1970).
- (11) C. O. Beckmann and K. Cohen, *J. Chem. Phys.*, **4**, 784 (1936).
- (12) W. J. Kauzmann, J. E. Walter, and H. Eyring, *Chem. Rev.*, **26**, 339 (1940).
- (13) Starting from commercial (3R)-3-methylcyclohexanone, the synthesis of this compound has been made by I. Douine, These de Specialite (Chimie Organique), Universite de Provence, Marseille, 1974.
- (14) The experimental data for this compound will be published later.
- (15) From experimental data of N. M. Baghenov and M. V. Volkenshtein, *Zh. Fiz. Khim.*, **28**, 1299 (1954).
- (16) A. Francois, These de Specialite (Chimie Organique), Universite de Provence, Marseille, 1975.
- (17) A. Francois, G. Pouzard, F. Vila, and L. Pujol, *C. R. Acad. Sci. Paris, Ser. C*, **278**, 1369 (1974).
- (18) E. L. Eliel, N. L. Allinger, S. J. Angyal, and G. A. Morrison, "Conformational Analysis", Interscience, New York N.Y., 1965.
- (19) J. B. Lambert and R. R. Clikeman, *J. Am. Chem. Soc.*, **98**, 4203 (1976).
- (20) B. L. Hawkins, Ph.D. Thesis, University Microfilms, Ann Arbor, Mich. No. 70-15738.
- (21) S. S. Kurtz, J. Senta Amon, and A. Sankin, *Ind. Eng. Chem.*, **42**, 174 (1950).

Determination of the Specific Heat Capacities of Aqueous Sodium Chloride Solutions at High Pressure with the Temperature Jump Technique

K. G. Liphard, A. Jost, and G. M. Schneider*

Institute of Physical Chemistry, University of Bochum, Bochum, German Federal Republic (Received November 9, 1976)

In this work specific heat capacities have been measured by the temperature jump technique. Electrical energy stored in a high voltage capacitor is discharged through the electrically conducting solution; this causes a rise in temperature which is measured indirectly by the optical absorbance change of a buffered indicator system. c_V data are reported for aqueous sodium chloride solutions in the concentration range from 0.1 to 2.0 mol kg⁻¹ at 293 K at 1 and 2 kbars. All c_V values decrease with increasing pressure. At 1 bar and 1 kbar c_V decreases monotonously with increasing salt concentration whereas at 2 kbars a maximum appears. Using data for compressibility and cubic expansion coefficients c_V was converted to c_p ; its dependence on pressure and salt concentration, respectively, is similar to the behavior of c_V . The data obtained are discussed with respect to structural effects. From the volume dependence of c_V and the pressure dependence of c_p , the temperature dependence of $(\partial p/\partial T)_V$ and of $(\partial V/\partial T)_p$, respectively, is calculated; with increasing salt concentration the temperature dependence of both decreases.

I. Introduction

Among the thermodynamic properties of electrolyte solutions the heat capacity is of primary importance. Several heat capacity studies on aqueous solutions of NaCl, a most important electrolyte in nature, have already been made during recent years¹⁻⁵ but there are no measurements at high pressure up to now. Such high pressure heat capacity data on NaCl and other electrolytes, however, would be of considerable interest not only for practical applications, e.g., for oceanography such as for the storage of heat in the deep sea; for mineralogy especially for geysers, hydrothermal syntheses etc.; for salt industry etc., but also for theoretical research, e.g., for the thermodynamics of electrolyte solutions, for the investigation of structural changes, etc.

In the laboratory heat capacities are mostly measured calorimetrically. The usual calorimetric methods, however, show some disadvantages for high pressure measurements: The mass of the autoclave is usually much more than a factor of 10 larger than that of the species investigated so that precision measurements are very difficult; heat losses through pressure connections also have to be considered.

These effects can be avoided using the temperature jump technique because here the measuring time is on the order of 1 ms. In the temperature jump technique a high

voltage capacitor is discharged through an electrically conducting solution. The electrical energy W_{el} absorbed causes a temperature increase ΔT according to

$$W_{el} = cm\Delta T \quad (1)$$

$$^{1/2}CU^2 = c\rho V\Delta T \quad (2a)$$

where c is the specific heat capacity in J K⁻¹ g⁻¹, m the mass in g, ΔT the temperature difference in K, C the capacity in F, U the loading voltage of the capacitor in V, ρ the density in g cm⁻³, and V the effective volume in cm³.

For the present investigations the change of temperature (temperature jump) ΔT is measured indirectly by means of the light absorption change of a colored pH indicator (here phenol red) dissolved in very low concentration in the buffered solution under test.

II. Experimental Section

A. *Temperature Jump.* The measurements of the heat capacities were carried out in a temperature jump apparatus that has been developed for the investigation of fast reactions in solutions under high pressure. The measuring cell with optical windows for spectroscopic measurements was mounted in a high pressure autoclave. Details of the experimental device have been described

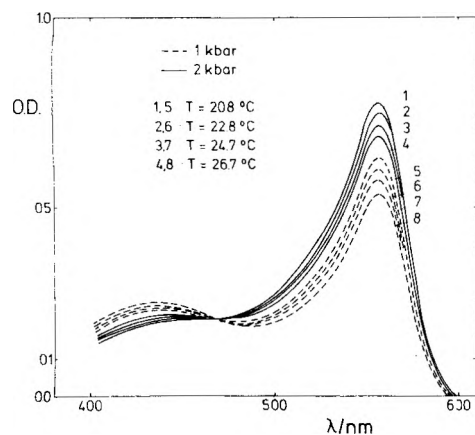


Figure 1. Spectrum of phenol red at different temperatures and pressures: 2×10^{-5} *m* phenol red, 9×10^{-4} *m* Tris buffer, 0.1 *m* NaCl, pH 7.4 at 20 °C, OD = $\log I_0/I$ = optical density.

elsewhere.⁶ With only slight modifications this apparatus was used for the measurements presented in this paper. In order to prevent dissolution of the pressure transmitting medium, nitrogen, in the solution under test a small flexible tube filled with solution was attached to the top of the cell and the pressure was transmitted to the solution from the pressurizing medium through the elastic walls of the tube.

The temperature in the cell was measured by a steel-sheathed thermocouple introduced into the cell through a capillary tube. The pressure was measured with Heise gauges.

B. *Spectrophotometry.* The relation between the optical absorption change and the rise in temperature was measured separately by a static method described in detail elsewhere.⁷ Here the pressure transmitting medium was also nitrogen. It was excluded from the cuvet to be dissolved by an open-ended tube filled with solution avoiding a quick mixing by a long diffusion path.

C. *Substances.* Sodium chloride was purchased from Baker Chemicals, Deventer (Holland), as "Analysed Reagent", and phenol red and tris(hydroxymethyl)aminomethane (Tris) by Merck AG, Darmstadt (Germany). These substances were used without further purification. The water used was triply distilled. All solutions were carefully degassed before measurement.

III. Results

Measurements have been carried out for solutions of NaCl in water in the concentration range from 0.1 to 2 mol kg^{-1} at 1 and 2 kbars. The temperature before the temperature jump was $T = 293.2$ K for all measurements. The concentration of the indicator phenol red was always 2×10^{-5} mol kg^{-1} in a solution of 9×10^{-4} mol kg^{-1} Tris buffer. Thus the concentration of both indicator and buffer was more than two orders of magnitude lower than that of the smallest salt concentration measured; thus any influence on the heat capacity could be neglected.

A. *Results of Spectrophotometric Measurements.* Absorption spectra of aqueous phenol red solutions were measured at different salt concentrations and pressures. One series of spectra is shown in Figure 1. The salt concentration is 0.1 mol kg^{-1} , the pressures are 1 and 2 kbars. The absorption maxima at λ 557 and 432 nm belong to the deprotonated and protonated form, respectively, of the indicator. The spectra were recorded at four different temperatures. It can easily be seen that the equilibrium is shifted toward the protonated form of the indicator with increasing temperature. From these spectra the temperature dependence of absorption (at constant wave-

TABLE I: Specific Heat Capacities of Aqueous Sodium Chloride^a

m_{NaCl} , mol kg^{-1}	c_V , J g^{-1} K ⁻¹		c_p , J g^{-1} K ⁻¹	
	1 kbar	2 kbars	1 kbar	2 kbars
0.1	3.84	3.59	3.92	3.78
0.5	3.80	3.63	3.89	3.83
1.0	3.72	3.56	3.82	3.77
2.0	3.59	3.46	3.75	3.71

^a c_V and c_p . Data taken at different pressures and molalities. The digits have been given beyond significant figures to avoid accumulation of roundout errors.

length) can be calculated for each pressure and salt concentration.

B. *Results of Temperature Jump Measurements.* The heat capacity can be calculated according to

$$c = \frac{CU^2}{V2\rho\Delta T} \quad (2b)$$

Here the effective volume V is most difficult to measure because of the complicated geometry of the measuring cell. Thus the ratio C/V was determined by calibration of the cell with solutions of different salt concentrations at normal pressure.¹⁻⁵ All density data were taken from the literature.^{2,8}

For the determination of specific heat capacities several temperature jumps were made starting from the initial temperature $T = 293.2$ K, the temperature jumps being in the range from 0.5 to 5 K. The resulting temperature differences ΔT (calculated from the optical absorption changes) were plotted vs. U^2 . The slope of the resulting lines were extrapolated to zero temperature jump and the heat capacity values were obtained from these limiting slopes. The error of this extrapolation is small since within the accuracy of the present measurements essentially straight lines were found.

The accuracy of the specific heat capacity data obtained is estimated to be $\pm 1\%$.

C. *Heat Capacity Data.* Another advantage of the temperature jump technique for heat capacity measurements is the alternative determination of specific heat capacity at constant volume or constant pressure, c_V and c_p , respectively. When the solution is heated normally thermal expansion occurs. For very short heating times (e.g., on the order of 1 μs) the heating takes place under essentially isochoric conditions, i.e., $dV = 0$, producing a shock wave which runs through the solution. For much slower heating times the pressure is balanced at each time. Thus at short heating times c_V values and at longer heating times c_p values can be measured. The heating times can easily be changed by the appropriate choice of the discharge unit, mainly by changing the capacity of the high voltage capacitor.

In this paper only measurements of c_V data are presented. The resulting c_V values are listed in Table I. The dependence on the molality m of the salt at 1 bar, 1 kbar, and 2 kbars is shown in Figure 2; here the data at normal pressure were taken from the literature.² The c_V values of pure water were calculated from c_p values taken from ref 9 using data for compressibilities and cubic expansion coefficients taken from ref 10.

Table I and Figure 2 show that the c_V values decrease with increasing pressure. At 1 bar and 1 kbar the c_V values decrease monotonously with concentration but at 2 kbars a maximum appears. The dependence on the square root of the molality of the salt is approximately linear above about 0.5 mol kg^{-1} for all pressures measured. The measured c_V values can be converted to c_p values using

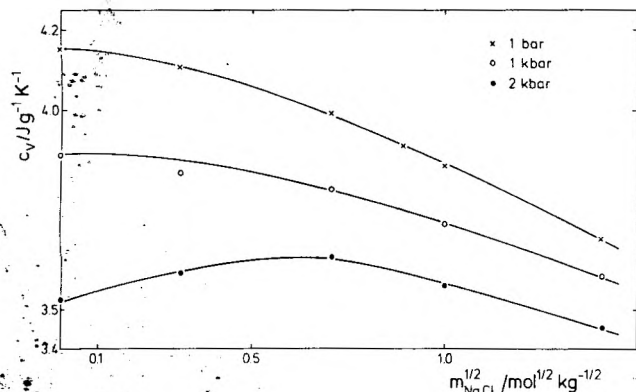


Figure 2. Specific heat capacity at constant volume c_v as a function of the square root of the molality m of NaCl: $T = 293.2$ K, $p = 1$ bar, 1 kbar, and 2 kbars.

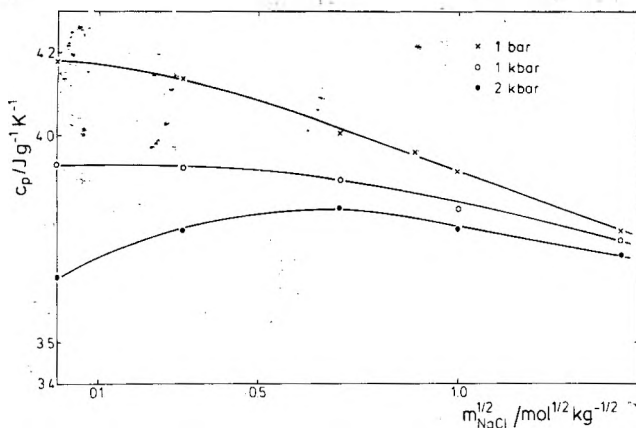


Figure 3. Specific heat capacity at constant pressure c_p as a function of the square root of the molality m of NaCl: $T = 293.2$ K, $p = 1$ bar, 1 kbar, and 2 kbars.

data for isothermal compressibilities and cubic expansion coefficients taken from the literature.⁸ The resulting c_p values are additionally listed in Table I; the concentration dependence is shown in Figure 3. The data at 1 bar were taken from the literature.^{1-6,9} The concentration dependence of the c_p values is very similar to that of the c_v values: the specific heat capacity at constant pressure c_p decreases monotonously with increasing molality of the salt at 1 bar and 1 kbar, whereas at 2 kbars a maximum appears.

IV. Conclusion

For discussion it is often useful to distinguish between solutes that are "structure breaking" or "structure making" with respect to pure water. As the unusual high specific heat capacity of pure water can be explained by assuming a highly ordered structure, changes of specific heat capacity can be attributed to "structure breaking" or "structure making" effects.

According to Figures 2 and 3 the specific heat capacity decreases with increasing salt concentration at 1 bar and 1 kbar; here the effect of NaCl on water can be explained by structure breaking. However at 2 kbars initially the specific heat capacity increases with increasing salt content, then it reaches a maximum, and finally decreases with further increasing salt concentration. Thus at higher pressures the effect of NaCl on water seems to be structure making at low concentrations and structure breaking at higher concentrations. A quantitative explanation of this behavior cannot be given at the moment.

Very often specific heat capacity data at high pressure are calculated from specific heat capacity values at normal pressure and from very precise pVT data. Caloric and

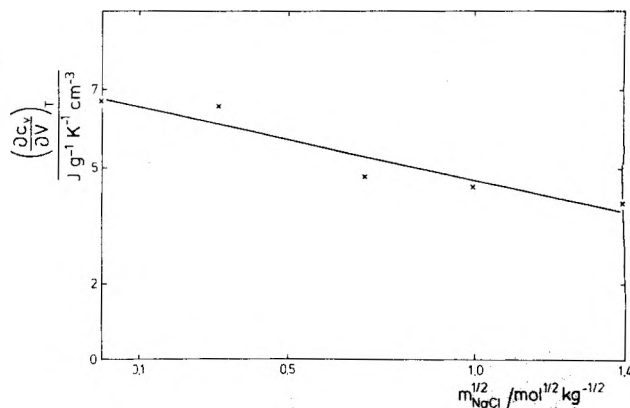


Figure 4. Plot of $(\partial c_v/\partial V)_T$ vs. the square root of the molality m of NaCl: $T = 293.2$ K.

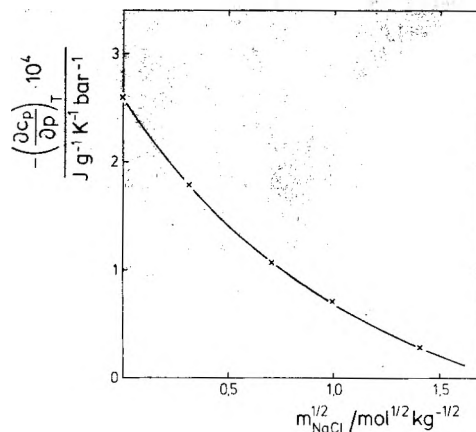


Figure 5. Plot of $(\partial c_p/\partial p)_T$ vs. the square root of the molality m of NaCl: $T = 293.2$ K.

pVT values are connected by the following thermodynamic relations

$$(\partial c_v/\partial V)_T = T(\partial^2 p/\partial T^2)_V \quad (3)$$

$$(\partial c_p/\partial p)_T = -T(\partial^2 V/\partial T^2)_p \quad (4)$$

where $(\partial^2 p/\partial T^2)_V$ represents the temperature dependence of the pressure coefficient $\beta \equiv (\partial p/\partial T)_V$ and $(\partial^2 V/\partial T^2)_p$ is related to the temperature dependence of the cubic expansion coefficient $\alpha \equiv (1/V)(\partial V/\partial T)_p$. By measuring the volume and pressure dependence of c_v and c_p , respectively, such as effectuated in this work both second derivatives can be obtained. The results could be useful, e.g., for testing the accuracy of pVT data or equations of state or for structural considerations.

In Figures 4 and 5 preliminary results for $(\partial c_v/\partial V)_T$ and $(\partial c_p/\partial p)_T$, respectively, are plotted vs. the square root of the salt concentration. The derivatives in the ordinate were obtained from plots of c_v vs. V (with the use of literature data for the specific volume⁸) and c_p vs. p , respectively, assuming the relations to be linear in the range of the present measurements.

Figure 4 shows that $(\partial c_v/\partial V)_T$ decreases with increasing salt concentration. The plot of $(\partial c_v/\partial V)_T$ vs. $m^{1/2}$ can be regarded as linear in a first approximation for the concentration range measured. This means that with increasing salt concentration the dependence of c_v on the specific volume decreases. According to eq 3 the temperature dependence of the pressure coefficient β decreases with increasing salt concentration, too.

Figure 5 demonstrates that with increasing salt concentration the effect of pressure on c_p decreases. The plot of $(\partial c_p/\partial p)_T$ vs. $m^{1/2}$ has a curved shape in the concentration range measured. According to eq 4 the temperature

dependence of $(\partial V/\partial T)_p$ also decreases with increasing salt concentration.

In order to obtain some more detailed information about the influence of a salt on the specific heat capacity and on the structure of water at high pressure, measurements are in preparation with salts showing strong structure-breaking effects such as CsI and with salts exhibiting strong structure-making effects such as LiF. In addition to these investigations measurements with sea water are planned.

Acknowledgment. Financial support of the Deutsche Forschungsgemeinschaft and of the Fonds der Chemischen

Industrie is gratefully acknowledged.

References and Notes

- (1) M. Randall and F. D. Rossini, *J. Am. Chem. Soc.*, **51**, 323 (1929).
- (2) E. B. Freyer, *J. Am. Chem. Soc.*, **53**, 1313 (1931).
- (3) M. Eigen and E. Wicke, *Z. Elektrochem., Ber. Bunsenges. Phys. Chem.*, **55**, 354 (1951).
- (4) V. B. Parker, *Natl. Stand. Ref. Data Ser., Natl. Bur. Stand.*, No. 2 (1965).
- (5) Yu. A. Epikhin and M. S. Stachanova, *Zh. Fiz. Khim.*, **41**, 2148 (1967); *Russ. J. Phys. Chem.*, **41**, 1157 (1967).
- (6) A. Jost, *Ber. Bunsenges. Phys. Chem.*, **78**, 300 (1974).
- (7) A. Jost, *Ber. Bunsenges. Phys. Chem.*, **79**, 850 (1975).
- (8) E. A. Polyakov, *Prikl. Geofiz.*, **41**, 163 (1965).
- (9) A. M. Sirota and P. E. Beljakov, *Teploenergetika*, **6**, 67 (1959).
- (10) R. A. Fine and F. J. Millero, *J. Chem. Phys.*, **59**, 5529 (1973).

Study of Oxygen Isotopic Exchange over Ultraviolet Irradiated Anatase Samples and Comparison with the Photooxidation of Isobutane into Acetone

Henri Courbon, Marc Formenti,[†] and Pierre Pichat*

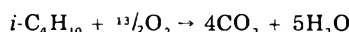
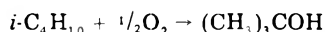
Institut de Recherches sur la Catalyse, CNRS, 79, boulevard du 11 Novembre 1918, 69626, Villeurbanne, Cedex, France (Received July 26, 1976)

Publication costs assisted by the Centre National de la Recherche Scientifique

Oxygen isotopic exchange (OIE) measurements have been carried out over UV irradiated anatase samples. At room temperature, simultaneous action of TiO₂ and UV light is needed for OIE which proceeds via a mechanism involving one oxygen surface atom at a time. For various anatase samples, the photocatalytic activities per unit of catalyst area for OIE and for isobutane oxidation (IOX) into acetone correlate. UV irradiation of a mixture of *i*-C₄H₁₀ and of an excess of ¹⁸O₂ shows that OIE occurs only after IOX. It is inferred that the same dissociated surface oxygen species participate in both reactions.

Introduction

It has been shown that anatase, irradiated by UV light at room temperature, can selectively oxidize various alkanes into ketones and aldehydes.¹ This photocatalytic oxidation has been studied in detail for isobutane.²⁻⁵ In this case, the main products are acetone, carbon dioxide, and water; small amounts of isobutanol and *tert*-butyl alcohol are also formed. The following equations account for these transformations:



Depending upon the fraction of isobutane in the reactants, the first equation may account for up to 95% of the isobutane molecules.² Partial oxidation is much more extensive than total oxidation.

Concerning the mechanism of this photocatalytic reaction, it has been found that isobutane does not interact strongly with the anatase surface under UV irradiation at room temperature.^{2,3a} In particular, no electronic interaction has been evidenced by photoconductivity measurements.⁴ Accordingly, the origin of the photocatalytic activity for alkane oxidation arises from the system O₂-TiO₂-UV radiations. This system has already been investigated by several techniques. The existence of O₂⁻ species was observed by ESR,⁵ whereas it was inferred from

measurements of thermoelectronic work function that a dissociated oxygen species, carrying approximately one negative charge, also occurs.^{3b} More recently, photoconductivity experiments showed the existence of both O₂⁻ and O⁻ species.⁴

Oxygen isotopic exchange has been employed to study the lability of surface oxygen for various solid oxides in connection with their catalytic activity in thermally activated oxidation reactions.⁶⁻⁸ However, two problems arise: (i) the isotopic exchange concerns only one of the reactants (O₂), (ii) the exchange and oxidation reactions do not occur at the same temperature. In the present case, the former problem is not important, since, as emphasized above, isobutane does not interact electronically with the surface and therefore the study of the system O₂-TiO₂-UV radiations is essential with respect to the oxidation mechanism. The second objection does not hold either, since, as indicated in this paper, oxygen isotopic exchange, as well as isobutane oxidation, takes place at room temperature over UV irradiated anatase.

Consequently, it seemed of interest (i) to study the mechanism of oxygen isotopic exchange (OIE) over UV-irradiated TiO₂; (ii) to compare the catalytic activity of various anatase samples for this reaction and for the formation of acetone by isobutane oxidation (IOX); (iii) finally, to determine how these reactions compete for the surface oxygen species which arise from the interaction between oxygen molecules and the electron hole pairs created by UV light.

The isotopic exchange reaction of ¹⁸O₂-¹⁶O₂ mixtures on rutile⁹ and ZnO¹⁰ under UV irradiation has been briefly depicted by Tanaka who suggested an O₃⁻ species, formed

[†] Present address: L.A. au CNRS de Catalyse Appliquée et Cinétique Hétérogène, Université Lyon I, France.

TABLE I: Anatase Samples

Sample	Surface area, m ² g ⁻¹	Morphology
1	41	Polyhedra + spheres
2	16	Spheres
3	24	Spheres
4	152	Polyhedra

from O⁻ and O₂, as the most plausible intermediate.

Experimental Section

1. *Apparatus.* For OIE experiments, the quartz cell which contained the powdered anatase had the shape of a cylinder box 1 cm high closed by two parallel optical windows of 6 cm diameter. After introduction of a solid sample, this cell was glass blown to the vacuum system. The sample could be irradiated through one of the optical windows using the UV light from a Philips HPK 125 mercury lamp. A water containing cuvette and convenient optical filters enabled one to use the 300–420 nm part of the spectrum with a maximum around 345 nm. In order to obtain a constant intensity for the solid, the intensity of the UV beam was controlled by using a microcalorimeter¹¹ so that variations may be compensated by adjusting the sample–lamp distance. For pretreatment of the solid samples, the cell was surrounded by a furnace whose cover was removed when illuminating.

The different parts of the vacuum line were separated by Granville-Phillips metallic valves. The vacuum, free of grease and mercury vapors, was obtained by traps filled with 13X molecular sieves and maintained at liquid nitrogen temperature. An ionization gauge was used to measure the residual pressure. A very sensitive Pirani-type gauge¹² allowed the measurements of the oxygen or isobutane pressures in the 10⁻⁶ to 5 Torr range.

The mass spectra were scanned by means of a Varian quadrupole gas analyzer connected to the cell through a Granville-Phillips variable leak valve.

To determine the photocatalytic activities of the various anatase samples for IOX, a differential dynamic fixed bed reactor was used as described previously.^{2,5} The effluents were analyzed by gas chromatography.

2. *Materials.* Isobutane from the Air Liquide Co. was vacuum distilled before use. ¹⁸O₂ from the Weizmann Institute (Israel) contained 94.6 atom% ¹⁸O.

Nonporous anatase samples were prepared from TiCl₄ in a flame reactor.¹³ They differ in shape, dimensions, and hence specific areas as indicated in Table I.

3. *Procedures.* For OIE experiments, the sample was pretreated as follows. After evacuation at room temperature, O₂ (100 Torr) was admitted into the cell which was heated at 450 °C for 15 h. Then the sample was evacuated at 150 °C for 2 h and finally cooled to room temperature. It has been checked, by means of the quadrupole gas analyzer, that, after this pretreatment, no CO₂ was evolved from the sample when it was UV irradiated at room temperature either under vacuum or oxygen. This shows that the carbonaceous impurities have been eliminated. 3 × 10⁻² Torr of ¹⁸O₂ were admitted into the cell in the dark. As soon as the samples were UV irradiated, OIE took place. For all the samples, the gas phase was analyzed after a 1-min irradiation; in some cases, supplementary analyses were carried out after longer irradiation times.

To determine how the OIE and IOX reactions compete, a mixture of isobutane and of an excess of ¹⁸O₂ was admitted over TiO₂ in the dark. Mass spectra of the gas phase were recorded after various times of UV irradiation.

For OIE, as well as for IOX,⁵ a critical mass of catalyst may be defined. The photocatalytic activity which varies

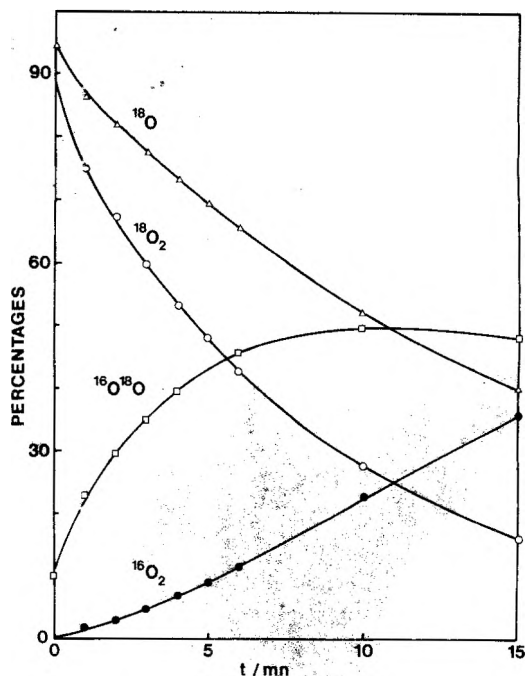


Figure 1. Changes in the isotopic composition of gas phase oxygen as a function of UV irradiation time for sample 1.

linearly as a function of the mass below this critical mass, becomes, above it, progressively independent of the mass. This critical mass, which of course changes with each anatase sample, corresponds to a completely UV irradiated layer of TiO₂. In both types of experiments (OIE and IOX), the photocatalytic activities considered are those which have been measured for a mass of catalyst slightly lower than this critical mass and related to the unit of catalyst area.

Results and Discussion

1. *Preliminary Remarks.* It has been checked that the simultaneous action of TiO₂ and UV light is required to produce the OIE reaction. As determined from pressure variations, UV irradiation of TiO₂ under O₂, previously admitted in the dark, causes simultaneous photodesorption and photoadsorption.¹⁴ After the first 5 s, photodesorption is masked by photoadsorption. For the first minute of irradiation, the decrease in pressure corresponds to a number of O₂ molecules equivalent to approximately 1% of the decrease in the number of ¹⁸O₂ molecules. Consequently, the decline in the fraction of ¹⁸O₂ molecules of the gas phase is not significantly affected by the ¹⁸O₂ molecules remaining adsorbed and this effect has been neglected in the results. On the other hand, UV irradiation of TiO₂ under isobutane previously introduced in the dark has no effect on the pressure or on the mass spectrum.

2. *Type of OIE.* Figure 1 demonstrates that UV irradiation of TiO₂ causes an immediate OIE. As a function of UV irradiation time, the percentage (*C*₃₆) of ¹⁸O₂ molecules constantly diminishes, that of ¹⁶O₂ molecules (*C*₃₂) increases and that of ¹⁶O¹⁸O molecules (*C*₃₄) passes through a maximum.

Depending on the number of surface oxygen atoms taking part in the mechanism, three types of isotopic exchange can occur.⁶⁻⁸ Using the notation of ref 8 these types will be designated as follows: R, exchange without participation of the surface oxygen atoms; R', exchange involving one such atom; R'', exchange engaging two such atoms simultaneously.

If exchange proceeds according to mechanism R, no variation in the ¹⁸O isotopic content of the gas phase should

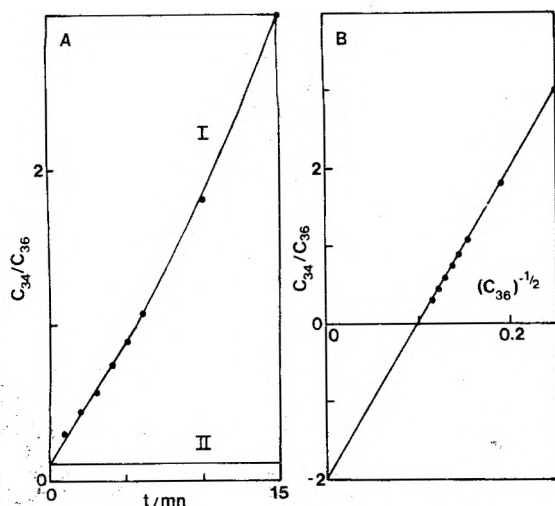


Figure 2. (A) Variations of the ratio of the concentrations of $^{16}\text{O}^{18}\text{O}$ molecules (C_{34}) to $^{18}\text{O}_2$ molecules (C_{36}) as a function of UV irradiation time for sample 1. Calculated according to mechanism R', i.e., exchange with one surface oxygen (curve I), and mechanism R'', i.e., exchange with two surface oxygen at a time (curve II); ●, experimental values. (B) C_{34}/C_{36} ratio vs. $(C_{36})^{-1/2}$ according to mechanism R'; ●, experimental values.

be observed. Figure 1 demonstrates that it is not the case and, consequently, it may be concluded that surface oxygen atoms intervene in the exchange. If mechanism R'' prevails, the fraction of $^{16}\text{O}^{18}\text{O}$ molecules in the gas phase (C_{34}) should decrease with increasing exchange time.⁶⁻⁸ On the contrary, predominance of mechanism R' should result in an increase of C_{34} at the beginning of the exchange.⁶⁻⁸ From Figure 1 it may be immediately inferred that mechanism R' predominates, since C_{34} is markedly increased during the first minutes of irradiation of the catalyst. Consideration of the isotopic ratio β between the three fractions of oxygen molecules ($\beta = C_{34}^2/C_{32}C_{36}$) gives support to this conclusion. If exchange is accomplished through an R or R' mechanism, β does not vary, provided that the initial isotopic mixture was in equilibrium.⁶⁻⁸ By contrast, the R'' mechanism is characterized by a deep minimum of β .⁶⁻⁸ In the present case, β remains close to its equilibrium value: $\beta = 4.0 \pm 0.4$. The accuracy is the worst at the beginning of the exchange when the value of C_{32} is weak and therefore introduces a relatively large error on β ; after a few minutes of exchange, the accuracy improves: $\beta = 4.0 \pm 0.15$ until C_{36} becomes too weak. In fact, it is more convenient to consider the ratio C_{34}/C_{36} which, at the beginning of the exchange, avoids the use of C_{32} . In the case of mechanism R'', the ratio C_{34}/C_{36} remains constant (Figure 2A, curve II) whereas in the case of mechanism R' it varies according to the equation:⁷

$$\frac{C_{34}}{C_{36}} = \left(\frac{C_{34}^0}{C_{36}^0} + 2 \right) \frac{C_{36}^0^{-1/2}}{C_{36}^{-1/2}} - 2$$

C_{34}^0 and C_{36}^0 being the initial values of C_{34} and C_{36} , i.e., before UV irradiation. Curve I of Figure 2A represents the values of C_{34}/C_{36} calculated by this equation using various values of C_{36} . It may be seen that the experimental points derived from Figure 1 fall perfectly on this curve which corresponds to mechanism R'. It may also be checked that they are exactly aligned on the line which represents the above equation in the diagram of the C_{34}/C_{36} ratio vs. $(C_{36})^{-1/2}$ (Figure 2B).

In conclusion, OIE over UV-irradiated anatase proceeds via mechanism R' where only one oxygen atom from the surface participates at a time, which may be written

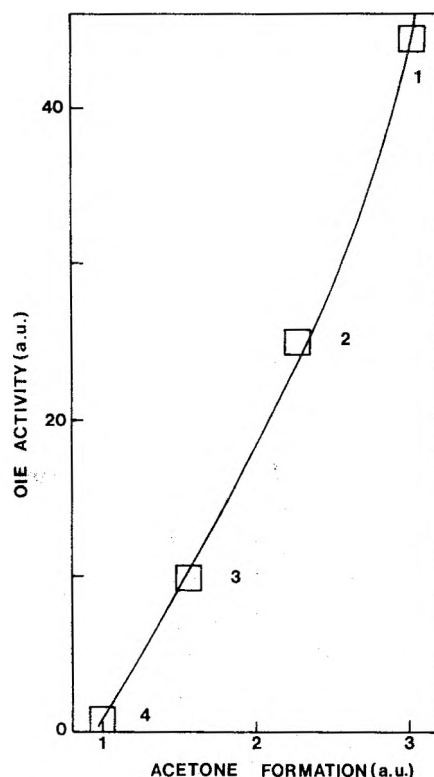
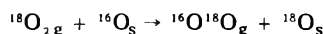


Figure 3. Comparison of the photocatalytic activities per unit of catalyst area of various anatase samples for OIE and acetone formation from isobutane. Samples labeled as in Table I.

without any assumption on the elementary steps:



It is interesting to note that OIE over TiO_2 heated above 500°C also occurs according to this mechanism.^{8,15} The mode of activation (temperature or photons) does not change the OIE mechanism. However, it must be pointed out that mechanism R'' has been less often observed.

Pure mechanism R' is seldom found for thermally activated OIE on metal oxides. Generally a mixture of the three possible mechanisms is used to account for the experimental data.^{7,8} According to the present example, it seems that the activation by photons is more selective than thermal activation.

3. Comparison of the Photocatalytic Activities for OIE and IOX. The experiments discussed in the preceding paragraph have been carried out for the various anatase samples of Table I, under the same experimental conditions: sample pretreatment, initial pressure of $^{18}\text{O}_2$, UV intensity. The photocatalytic activities for OIE are expressed in the fraction of O_2 molecules which have been exchanged per unit of catalyst area for the first minute of UV irradiation.

On the other hand, the measurements for IOX have been performed for the same anatase samples using a dynamic reactor. Identical experimental conditions have been maintained for each sample: gas flow and composition, UV intensity. The photocatalytic activities for IOX are given by the height of the acetone peak in the chromatogram per unit of catalyst area for the stationary state.

Figure 3 shows that the photocatalytic activities for these two reactions correlate. The more active catalysts to produce acetone are also those which isotopically exchange $^{18}\text{O}_2$ molecules more rapidly.

From Figure 3 it may be seen that OIE appears to be more sensitive to variations in the morphology of the catalysts than IOX. For acetone formation varying from approximately 1 to 3, the rates of isotopic exchange range

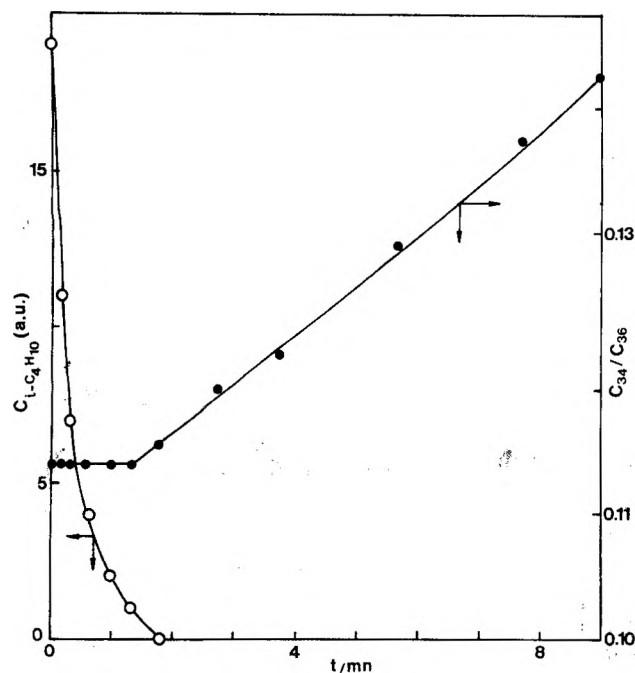


Figure 4. Changes in the C_{34}/C_{36} ratio and in the isobutane concentration (as determined from height of parent mass peak at m/e 43) as a function of irradiation time.

from about 1 to 40. It might be objected that these latter rates refer to the first minute of irradiation by the UV beam, whereas the values of acetone formation correspond to the stationary state. However, results relative to the fraction of O_2 molecules which have been exchanged after a 1-h irradiation show that the differences between various anatase samples are still larger. Accordingly, the greater sensitivity of OIE to change in morphology of the catalyst is corroborated. This may mean that all the oxygen atoms from the surface oxide which are active for OIE are not active for IOX and may be interpreted in terms of steric factors and orientation of the isobutane molecules toward the surface.

On the other hand, these results confirm that reactions photocatalyzed by metal oxides, as well as thermally catalyzed reactions,¹⁶ are sensitive to the texture, since, in addition to the IOX and OIE reactions studied here, it is also the case for the oxidation of CO ¹⁷ and NH_3 ¹⁸ over UV-irradiated anatase.

4. *Competition between the OIE and IOX Reactions.* UV irradiation of a mixture of $^{18}O_2$ and $i-C_4H_{10}$ admitted over TiO_2 in the dark results in an immediate and important decrease in the mass peak 43, the preponderant peak of isobutane (Figure 4). Simultaneously, the mass peaks referring to $^{18}O_2$ and $^{16}O^{18}O$ molecules also decrease substantially. However the ratio C_{34}/C_{36} of the concentrations of these molecules remains constant (Figure 4). These data show that the IOX reaction takes place, as expected. $^{18}O_2$ and $^{16}O^{18}O$ participate equally to the oxidation reaction, so that their ratio is not changed.

However, the compounds formed remain adsorbed since neither growth in the peaks, nor new peaks in the mass spectrum are detected during the disappearance of isobutane. This is not surprising as all the expected products (acetone, isobutanol, *tert*-butyl alcohol, carbon dioxide, and water) can readily be chemisorbed on anatase at room temperature. For the doses of isobutane admitted, the surface coverage is of the order of 10^{-2} molecules per 100 \AA^2 .

After disappearance of isobutane molecules in the gas phase and in presence of an excess of oxygen molecules, the reaction of oxygen isotopic exchange can occur, which

is demonstrated by the increase of the C_{34}/C_{36} ratio (Figure 4). As before, the variations of this ratio as a function of the UV irradiation time show that OIE proceeds via mechanism R'.

From the absence of isotopic exchange as long as the system contains isobutane molecules and from its occurrence after consumption of this hydrocarbon, it is inferred that isobutane and oxygen molecules compete for the same oxygen species and that $i-C_4H_{10}$ reacts more easily with this species. A competitive adsorption of $i-C_4H_{10}$ and O_2 molecules is ruled out, since $i-C_4H_{10}$ does not interact with the electron-hole pairs created by UV light, in contrast with O_2 . On the other hand, the easier dissociation of the C-H bond concerning the tertiary carbon atom in $i-C_4H_{10}$ ($\sim 92 \text{ kcal mol}^{-1}$) as compared with the O-O bond in oxygen ($\sim 118.6 \text{ kcal mol}^{-1}$) probably accounts for the greater reactivity of isobutane toward the surface oxygen atoms.

Similarly, it has been found¹⁹ that OIE is retarded by CO oxidation over illuminated ZnO.

Conclusion

In general terms, this work confirms that the interaction between O_2 and the electron-hole pairs created by UV light on anatase is the key phenomenon to be considered for the photooxidation of alkanes by this catalyst.

More precisely, similar variations of the photocatalytic activities for OIE and IOX over various anatase samples and the inhibition of the former reaction by the second one tend to show that both reactions proceed via the same mechanism. Since for OIE one surface oxygen atom comes into play at a time, it is inferred that a dissociated surface oxygen species equally participates in IOX.

As a O^- species has been found by means of photoconductivity measurements,⁴ it may be assumed that this species is responsible for the reactions studied here, in agreement with Tanaka⁹ who suggested the formation of an O_3^- intermediate from O^- and O_2 in the OIE over illuminated rutile at room temperature. In the case of partially reduced anatase¹⁹ and of previously UV irradiated TiO_2 deposited on SiO_2 ,²⁰ Kazanskii et al. also found a qualitative relationship between the catalytic activity for homomolecular OIE at 137 K and the EPR signals of thermally unstable O_3^- ion radicals.

It is also worth remarking that the photocatalytic activity for partial oxidation of isobutane into acetone correlates with the bonding energy of surface oxygen as inferred from OIE, whereas for thermally activated catalytic reactions the correlation refers to total oxidation and does not hold in the case of selective oxidation.^{7,8} However, in the present work, the photocatalytic activities for partial and total oxidation increase or decrease simultaneously in going from one anatase sample to another.

Acknowledgment. The authors are indebted to Dr. P. Vergnon for the gift of the anatase samples.

References and Notes

- (1) N. Djeghri, M. Formenti, F. Juillet, and S. J. Teichner, *Faraday Discuss.*, **58**, 185 (1974).
- (2) M. Formenti, F. Juillet, and S. J. Teichner, *Bull. Soc. Chim. Fr.*, 1031, 1315 (1976).
- (3) (a) S. Bourasseau, J. R. Martin, F. Juillet, and S. J. Teichner, *J. Chim. Phys.*, **71**, 1025 (1974); (b) *ibid.*, **71**, 1017 (1974).
- (4) J. Disdier, J. M. Herrmann, and P. Pichat, Vth Ibero-American Symposium on Catalysis, Lisbon, Portugal, July 1976.
- (5) M. Formenti, F. Juillet, P. Meriaudeau, and S. J. Teichner, *Chem. Technol.*, **1**, 680 (1971).
- (6) E. R. S. Winter, *Adv. Catal.*, **10**, 196 (1958).
- (7) G. K. Boreškov, *Adv. Catal.*, **15**, 285 (1964).
- (8) J. Novakova, *Catal. Rev.*, **4**, 77 (1970).
- (9) K. Tanaka, *J. Phys. Chem.*, **78**, 555 (1974).
- (10) K. Tanaka and K. Miyahara, *J. Phys. Chem.*, **7**, 2303 (1974).

- (11) J. L. Macqueron and A. Nouailhat, *Actes Colloque International CNRS, Marseille, France, 1965*, ed. CNRS, 1967, p 31.
- (12) K. Watanabe, T. Hanasaka, and T. Yamashina, *J. Catal.*, **26**, 484 (1972).
- (13) K. Watanabe, T. Hanasaka, and T. Yamashina, *J. Catal.*, **26**, 484 (1972).
- (14) R. Caillat, J. P. Cuer, J. Elston, F. Juillet, R. Pointud, M. Prettre, and S. J. Teichner, *Bull. Soc. Chim. Fr.*, 152 (1959); J. Long and S. J. Teichner, *Rev. Int. Hautes Temp. Refract.*, **2**, 47 (1965); M. Formenti, F. Juillet, P. Meriaudeau, S. J. Teichner, and P. Vergnon, *J. Colloid Interface Sci.*, **39**, 79 (1972).
- (15) H. Courbon, J. M. Herrmann, J. R. Martin, and P. Pichat, unpublished results.
- (16) E. S. R. Winter, *J. Chem. Soc. A*, 2889 (1968).
- (17) J. M. Herrmann, P. Vergnon, and S. J. Teichner, *J. Catal.*, **37**, 57 (1975).
- (18) A. Thevenet, These 3e cycle, Lyon, France, no. 230, 1973.
- (19) H. Mozzanega, These C.N.A.M., Lyon, France, 1975.
- (20) A. P. Griva, V. V. Nikisha, B. N. Shelimov, and V. B. Kazanskii, *Kinet. Catal.*, **15**, 86 (1974).
- (21) V. V. Nikisha, B. N. Shelimov, and V. B. Kazanskii, *Kinet. Catal.*, **15**, 599 (1974).

Analysis of Torsional Spectra of Molecules with Two Internal C_{3v} Rotors. 3.¹ Far-Infrared and Gas Phase Raman Spectra of Dimethylamine- d_0 , $-d_3$, and $-d_6$

J. R. Durig,* M. G. Griffin,² and P. Groner³

Department of Chemistry, University of South Carolina, Columbia, South Carolina 29208 (Received October 12, 1976)

Publication costs assisted by the University of South Carolina

The Raman spectra of gaseous dimethylamine- d_0 , $-d_3$, and $-d_6$ have been recorded between 0 and 4000 cm^{-1} . The far-infrared spectra have been recorded between 300 and 100 cm^{-1} . Considerable torsional data are reported and used to characterize the torsional potential function based on a semi-rigid model. The average effective V_3 for the dimethylamines was found to be $1052 \pm 12 \text{ cm}^{-1}$. The cos-cos coupling term was approximately 15% of the effective V_3 , whereas the sine-sine coupling term was of an order of magnitude smaller for $(\text{CH}_3)_2\text{NH}$ and $(\text{CD}_3)_2\text{NH}$. However, for the mixed isotope the sine-sine term was found to be negligible and the cos-cos about one-half the value obtained for the other two isotopes.

Introduction

The vibrational spectrum of dimethylamine has been extensively reported.⁴⁻¹² The first reported⁹ barrier to internal rotation for dimethylamine was based on the observation of one band in the far-infrared spectrum of the vapor. That barrier⁹ was the result of a necessarily simplified treatment because a proper characterization of the potential function for two interacting threefold rotors requires considerable experimental data.^{13,14} The development of reliable, high-power, continuous wave lasers as sources for the Raman experiment has opened a fertile new area for observation of torsional data, i.e., the Raman study of the gas phase molecule.^{15,16} Further, the increasing availability of computer controlled Fourier transform far-infrared spectrometers where repeated interferograms may be averaged rapidly to improve the signal-to-noise ratio and where spectral interferences may be readily subtracted has made quality far-infrared data routinely available.

Extensive torsional data for dimethylamine- d_0 , $-d_3$, and $-d_6$ are reported here and have been used to characterize the torsional potential functions of these molecules.

Experimental Section

Dimethylamine- d_0 (CP grade) was fractionated before use. Dimethylamine- $-d_3$ and $-d_6$ were purchased from Merck Sharpe and Dohme, Canada, Ltd. (98 atom % D minimum) and were used without further purification. All the dimethylamines were condensed onto activated 4-Å molecular sieves prior to the recording of the far-infrared spectra.

Far-infrared spectra were recorded using a Digilab FTS-15B Fourier transform spectrophotometer. The samples were held at their room temperature vapor

pressure in a 10-cm glass cell with polyethylene windows. Interferograms obtained after 3000 scans of sample and reference beams were transformed using a triangular apodization function and then ratioed. The theoretical resolution for the ratioed spectrum is 0.5 cm^{-1} . Interfering water vapor bands were subtracted from the final spectra.

Raman spectra were recorded utilizing a Cary Model 82 spectrophotometer equipped with a Spectra Physics Model 171 argon ion laser operating on the 5145-Å line. Power at the samples was typically 2 W. The samples were contained at their room temperature vapor pressure in a quartz cell. The laser light was multipassed through the sample using the standard Cary accessory. Frequencies reported for sharp lines are expected to be accurate to $\pm 2 \text{ cm}^{-1}$.

Results

The Raman spectrum of the vapor of dimethylamine- d_0 has been previously reported.¹² It was recorded using mercury arc excitation. The spectra of the $-d_3$ and the $-d_6$ isotopes has not been previously recorded. The Raman survey spectra of gaseous dimethylamine- $-d_0$, $-d_3$, and $-d_6$ are presented in Figure 1A, B, and C, respectively. The frequencies are listed in Table I. The assignment given in Table I is based on, and suggests only minor changes in, a previous assignment.¹² The A' CH_3 deformations have been assigned at 1483, 1467, and 1445 cm^{-1} . These modes should all produce a polarized Q-branch in the Raman spectrum of the gas. Polarized Q-branches are observed at 1554 and 1482 cm^{-1} indicating that the A' CH_3 deformations may have higher frequency than had been previously calculated.¹⁷ Polarization measurements were made for all isotopic species but were not tabulated. All observed sharp lines were clearly polarized while those

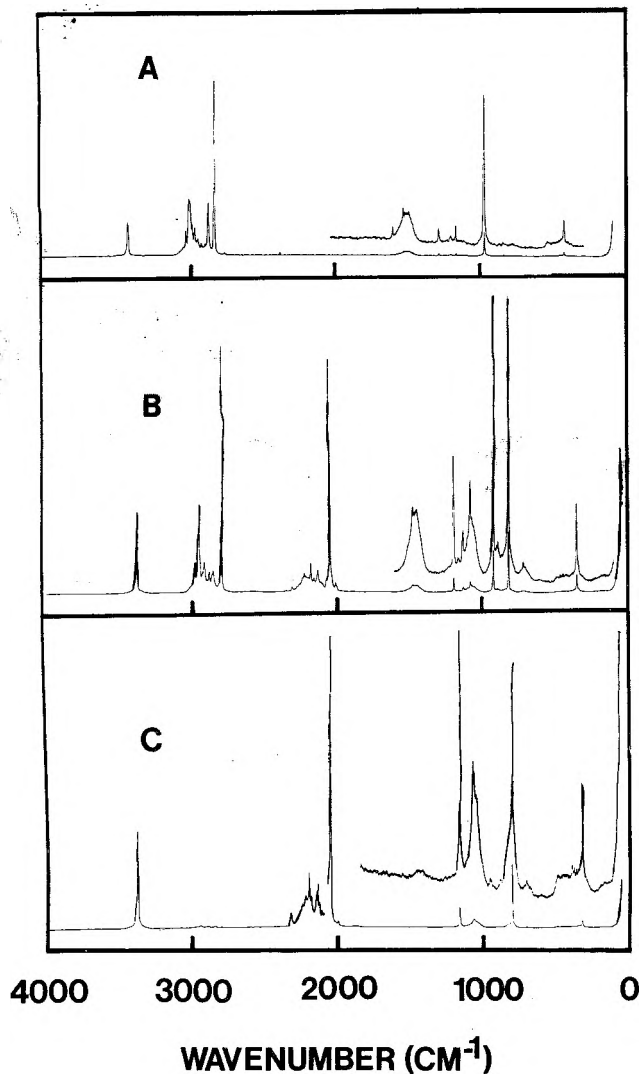


Figure 1. The Raman spectra of the vapor phase of (A) dimethylamine- d_0 , (B) dimethylamine- d_3 , and (C) dimethylamine- d_6 . Spectral slitwidth was 3.0 cm^{-1} .

regions that are listed in Table I as unresolved (e.g., 1520 to 1380 cm^{-1} and 1100 to 1030 cm^{-1}) were of undeterminable polarization.

An expanded presentation of the Raman spectra of the vapor of dimethylamine- d_0 , - d_3 , and - d_6 between 550 and 200 cm^{-1} is shown in Figure 2A, B, C, respectively. The far-infrared spectra of the vapor of dimethylamine- d_0 , - d_3 , and - d_6 between 300 and 100 cm^{-1} are presented in Figure 3A, B, and C, respectively. The far-infrared spectrum of dimethylamine- d_6 , Figure 3C, was computed from an interferogram recorded using a $12.5 \mu\text{m}$ beam splitter and, therefore, only covers the region between 220 and 100 cm^{-1} . The torsional data for dimethylamine- d_0 (Figures 2A, 3A) are listed in Table II, that for dimethylamine- d_3 (Figures 2B, 3B) in Table III, and for dimethylamine- d_6 (Figures 2C, 3C) in Table IV.

Torsional Potential Function

The Hamiltonian for $(\text{CD}_3)(\text{CH}_3)\text{NH}$ may be set up according to a $C_{3v}\text{T}-C_1\text{F}-C_{3v}\text{T}$ semirigid model (T = top, F = frame), the bar indicating that the tops are not equivalent. $(\text{CH}_3)_2\text{NH}$ and $(\text{CD}_3)_2\text{NH}$ both have a symmetry plane in the molecular frame; therefore, they may be treated as semirigid $C_{3v}\text{T}-C_s\text{F}-C_{3v}\text{T}$ models. An extensive investigation of several semirigid two-top models has recently been made by Groner and Durig^{1,18} on the basis of the internal isometric group introduced by Gunthard and co-workers.¹⁹ They obtained the internal

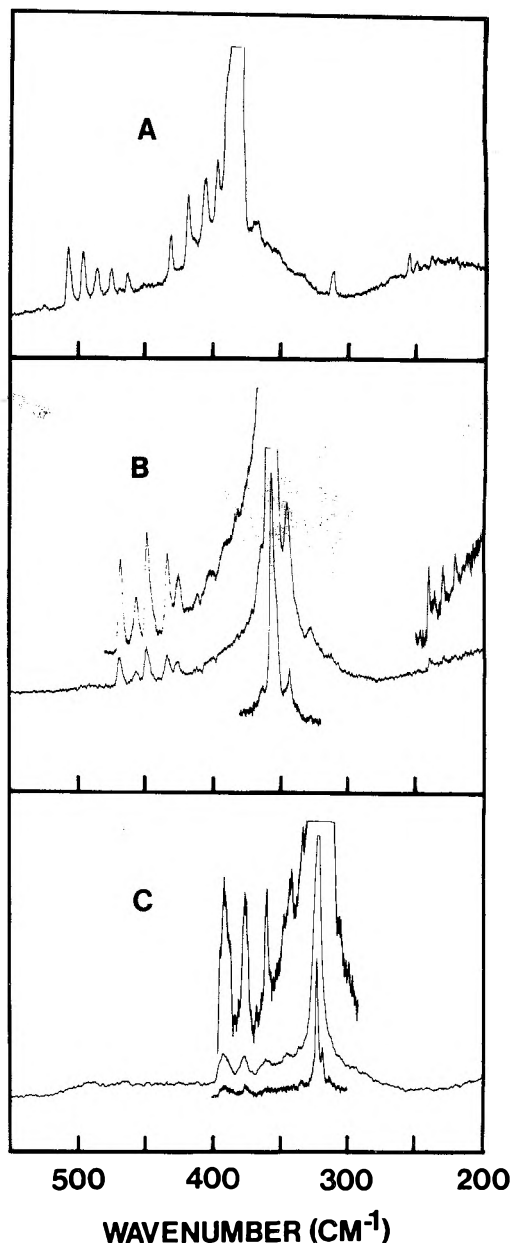


Figure 2. The Raman spectra of the vapor phase of (A) dimethylamine- d_0 , (B) dimethylamine- d_3 , and (C) dimethylamine- d_6 . Spectral slitwidth varied between 1.5 and 4.0 cm^{-1} .

Hamiltonian for the $C_{3v}\text{T}-C_1\text{F}-C_{3v}\text{T}$ model as

$$H_T = \frac{1}{2} [g^{44} p_0^2 + 2g^{45} p_0 p_1 + g^{55} p_1^2] + V(\tau_0, \tau_1) \quad (1)$$

with $V(\tau_0, \tau_1)$ in standard form as

$$V(\tau_0, \tau_1) = \frac{1}{2} [V_{30}(1 - \cos 3\tau_0) + V_{60}(1 - \cos 6\tau_0) + V_{60}' \sin 6\tau_0 + V_{03}(1 - \cos 3\tau_1) + V_{06}(1 - \cos 6\tau_1) + V_{06}' \sin 6\tau_1 + V_{33}(\cos 3\tau_0 \cos 3\tau_1 - 1) + V_{33}'(\sin 3\tau_0 \sin 3\tau_1) + V_{33}'' \sin 3\tau_0 \times \cos 3\tau_1 + V_{33}''' \cos 3\tau_0 \sin 3\tau_1] \quad (2)$$

The symmetry group of this Hamiltonian is of order 9 and isomorphic to $C_3 \otimes C_3$ with C_3 as the cyclic group of order 3. Its character table is given in ref 18. In the high barrier case, the energy levels may be labeled by the symmetry species Γ^{mn} and by the limiting vibrational quantum numbers ν and $\bar{\nu}$ of the torsional modes. According to our calculations, each torsional state $(\nu\bar{\nu})$ splits into 5 sublevels according to

$$\Gamma^{00} \oplus \Gamma^{10} \oplus \Gamma^{01} \oplus \Gamma^{11} \oplus \Gamma^{12}$$

TABLE I: The Observed Raman Spectra^a and Assignment^b of Dimethylamine-*d*₀, Dimethylamine-*d*₃, and Dimethylamine-*d*₆

(CH ₃) ₂ NH		(CH ₃)(CD ₃)NH		(CD ₃) ₂ NH		Assignment
Δ, cm ⁻¹	Rel int ^c	Δ, cm ⁻¹	Rel int ^c	Δ, cm ⁻¹	Rel int ^c	
3377	m	3370	m	3370	m	ν ₁ (A') NH stretch
2980	mw	2980	mw	2985	vvw	ν ₂ (A') CH ₃ asym stretch
2961	m			~2960	vvw, b	
2954	m	2954	m			ν ₃ (A') CH ₃ asym stretch
2947	sh					
2938	sh					
2921	w	2923	m	2926	vw	
		2912	m			
2903	w, b			2900		
				to		
2878	w	2877	w	2880		
2850	w	2855	w			
		2847	w			
				2836	vw	
2829	m					
2787	vs	2789	vs	2789	vvw	ν ₄ (A') CH ₃ sym stretch
2718	w					
2328	w	~2310	vw, b	2322	w	
		2237	w	2241	w, sh	
		2227	w	2220	w	
				2196	mw	
		2183	mw	2182	w	
		2162	w			
		2135	mw	2147	mw	
				2136	mw	
				2121	w	
				2105	w	
		2078	w	2061	ms	
		2055	vs	2046	s	ν ₄ (A') CD ₃ sym stretch
		2012	w			
		2005	w	1994	vw	
1554	vw					
1520		1520				
to		to				
1380	vw, b	1400	w, b			CH ₃ deformations
1482	vw	1478	w			
1240	w	1196	mw			ν ₈ (A') CH ₃ rock?
1159	vw, b	~1165	vw	1162	ms	ν ₈ (A') CD ₃ rock?
1123	w	1130	w			
		1100		1100		
		to		to		
		1020	w	1020	vvw	CD ₃ deformation
		1082	w	1075	vw	ν ₇ (A') CD ₃ sym deformation
				1068	vw	
				~1050	vw, b	
				948	vvw	
937	w					
929	vs	924	m			ν ₁₀ (A') H ₃ C-N stretch
		~902	vw			
		~890	vw			
		820	m	802	m	ν ₁₀ (A') D ₃ C-N stretch
798	vw, b	~720				
		to				
		700	vw			
				706	vvvw	
384	w	355	w	324	w	ν ₁₂ (A') CNC bend

^a The observed torsional data are not listed here even though they are apparent in the survey spectra of Figure 1. ^b Based on the assignment in ref 12. ^c vs = very strong, s = strong, m = medium, w = weak, b = broad, sh = shoulder.

where Γ^{00} is the totally symmetric one-dimensional representation. Each other symbol Γ^{mn} represents a complex conjugate pair of one-dimensional representations whose energy matrices are the complex conjugates of each other and contain the same eigenvalues (pseudo-degenerate representations). The torsional selection rules of this model are collected in Table V.

The internal Hamiltonian of the $C_{3v}T-C_3F-C_{3v}T$ model can be obtained according to Groner and Durig¹ from the formula above by introducing the restrictions

$$g^{44} = g^{55}, V_{30} = V_{03}, V_{60} = V_{06}, V_{60}' = V_{06}', \\ V_{33}'' = -V_{33}'''$$

Its symmetry group of order 18, $C_3 \otimes \theta_3$, is isomorphous to the direct product of the cyclic group, C_3 , of order 3 and with the dihedral group, θ_3 , of order 6. Its character table is given in Table VI. The energy levels of each torsional state ($\nu\bar{\nu}$) split in the high barrier case into the sublevels

$$\Gamma^{00\sigma} \oplus \Gamma^{10} \oplus \Gamma^{01} \oplus \Gamma^{11} \oplus \Gamma^{12\sigma}$$

σ is + or - for $\bar{\nu}$ even or odd, respectively, with $\bar{\nu}$ as the limiting vibrational quantum numbers of the torsional mode which is antisymmetric with respect to the symmetry plane of the molecular frame. $\Gamma^{00\sigma}$ are one-dimensional representations and Γ^{11} is two dimensional. $\Gamma^{12\sigma}$ ($\sigma = +$ or -) are the symbols for two complex conjugate pairs of

TABLE II: The Observed Torsional Data and Assignment for the Vapor of Dimethylamine- d_0

Raman		Far-infrared		Assignment $V_1' V_2' \leftarrow V_1 V_2$	Obsd - Calcd
Δ , cm^{-1}	Rel int ^a	cm^{-1}	Rel int ^a		
507	vs			0,2 \leftarrow 0,0	0.98
496	vs			0,3 \leftarrow 0,1	-1.91
486	m			0,4 \leftarrow 0,2	0.77
476	m				
464	w				
452	vw			1,1 \leftarrow 0,0	-1.43
432	ms			2,0 \leftarrow 0,0	-0.33
419	vs			3,0 \leftarrow 1,0	1.85
407	s				
398	s				
383	*			δ CNC	
~370	w				
~362	vw				
312	w				
256	w	256.3	vs	0,1 \leftarrow 0,0	1.83
251	w	250.8	s	0,2 \leftarrow 0,1	-0.75
~245	vvw	245.3	ms	0,3 \leftarrow 0,2	-1.06
240	vw	239.8	s	0,4 \leftarrow 0,3	0.94
		235.0	mw	1,1 \leftarrow 1,0	0.61
		227.6	mw	(0,1 \leftarrow 0,0)'	hot band of δ CNC
		222.0	mw	(0,2 \leftarrow 0,1)'	hot band of δ CNC
		219.4	m	1,0 \leftarrow 0,0	0.36
		213.0	w	2,0 \leftarrow 1,0	-0.29
		211.1	w	2,1 \leftarrow 2,0	-0.37
		202.7	w	3,0 \leftarrow 2,0	-1.17

^a vs = very strong, s = strong, m = medium, w = weak, sh = shoulder, b = broad. The intensities listed are relative to the other torsional data not to the rest of the vibrational data.

TABLE III: The Observed Torsional Data and Assignment for the Vapor of Dimethylamine- d_3

Raman		Far-infrared		Assignment $V_1' V_2' \leftarrow V_1 V_2$	Obsd - Calcd
Δ , cm^{-1}	Rel int ^a	cm^{-1}	Rel int ^a		
469	s			0,2 \leftarrow 0,0	-1.10
457	m			1,2 \leftarrow 1,0	1.88
448	vs			0,3 \leftarrow 0,1	-0.32
433	s				
425	m			0,4 \leftarrow 0,2	2.65
412	vw			1,1 \leftarrow 0,0	0.60
403	w			2,1 \leftarrow 1,0	-0.66
389	w			1,2 \leftarrow 0,1	-0.66
363	sh				
354	*			δ CNC	
344	vs			2,0 \leftarrow 0,0	-0.48
330	w			3,0 \leftarrow 1,0	0.19
312	vvw			4,0 \leftarrow 2,0	-0.04
240	mw	239.5	vs	0,1 \leftarrow 0,0	-1.37
235	w	236.5	m	1,1 \leftarrow 1,0	0.50
229	mw	229.0	ms	0,2 \leftarrow 0,1	-0.23
220	w	220.0	m	1,2 \leftarrow 1,1,	0.88,
				0,3 \leftarrow 0,2	0.91
213	vw	214.0	w		
		177.0	ms	1,0 \leftarrow 0,0	1.59
		166.3	mw	2,0 \leftarrow 1,0,	-2.78,
				2,1 \leftarrow 1,1	-0.27
		161.1	mw	3,0 \leftarrow 2,0	-0.02
		150.8	w	4,0 \leftarrow 3,0	-0.13
		138.0	w	5,0 \leftarrow 4,0	-1.90

^a vs = very strong, s = strong, m = medium, w = weak, sh = shoulder, b = broad. The intensities listed are relative to the other torsional data not to the rest of the vibrational data.

one-dimensional representations, whereas Γ^{10} represents a complex conjugate pair of two-dimensional representations thus leading to fourfold degenerate energy levels.

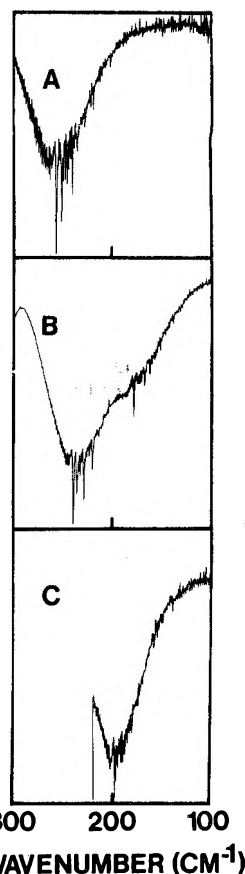


Figure 3. The far-infrared spectra (effective resolution is 0.5 cm^{-1}) of the vapor phase of (A) dimethylamine- d_0 , (B) dimethylamine- d_3 , and (C) dimethylamine- d_6 . (A) and (B) were computed from interferograms recorded with a $6.25 \mu\text{m}$ Mylar beam splitter and (C) was computed from interferograms recorded with a $12.5 \mu\text{m}$ beam splitter.

TABLE IV: The Observed Torsional Data and Assignment for the Vapor of Dimethylamine- d_6

Raman		Far-infrared		Assignment $V_1' V_2' \leftarrow V_1 V_2$	Obsd - Calcd
Δ , cm^{-1}	Rel int ^a	cm^{-1}	Rel int		
393	s, vb			0,2 \leftarrow 0,0,	-1.21,
				0,3 \leftarrow 0,1,	-0.26,
				0,4 \leftarrow 0,2	2.53
376	s, b			1,2 \leftarrow 1,0,	1.52,
				1,3 \leftarrow 1,1	2.0
360	s				
348	sh				
344	m			1,1 \leftarrow 0,0	-1.54
334	mw			2,1 \leftarrow 1,0,	2.19,
				1,2 \leftarrow 0,1	-1.62
324				δ CNC	
318	vs			2,0 \leftarrow 0,0	1.28
314	ms			3,0 \leftarrow 1,0,	1.58,
				3,1 \leftarrow 2,0	-1.20
305	m			4,0 \leftarrow 2,0	-0.40
		198.0	s	0,1 \leftarrow 0,0	0.91
		196.6	m	0,2 \leftarrow 0,1	-0.52
		195.5	w	0,3 \leftarrow 0,2	-0.64
		189.5	ms	1,2 \leftarrow 1,1	2.34
		188.5	m	1,1 \leftarrow 1,0	2.20
		181.0	mw		
		158.5	m	1,0 \leftarrow 0,0	-0.73
		157.9	m	2,0 \leftarrow 1,0	0.41
		154.8	w	3,0 \leftarrow 2,0	-0.13

^a vs = very strong, s = strong, m = medium, w = weak, sh = shoulder, b = broad. The intensities listed are relative to the other torsional data not to the rest of the vibrational data.

The selection rules were derived as described by Groner and Durig¹ and are summarized in Table V.

TABLE V: Symmetry Selection Rules for Torsional Transitions of Dimethylamine Isotopes

(CD ₃)(CH ₃)NH		(CH ₃) ₂ NH and (CD ₃) ₂ NH	
R IR ^a	pol abc hybrid	pol bc hybrid	depol a type
	$\Gamma^{00} \leftrightarrow \Gamma^{00}$	$\Gamma^{00+} \leftrightarrow \Gamma^{00+}$ $\Gamma^{00-} \leftrightarrow \Gamma^{00-}$	$\Gamma^{00+} \leftrightarrow \Gamma^{00-}$
	$\Gamma^{10} \leftrightarrow \Gamma^{10}$	$\Gamma^{10} \leftrightarrow \Gamma^{10}$	$\Gamma^{10} \leftrightarrow \Gamma^{10}$
	$\Gamma^{01} \leftrightarrow \Gamma^{01}$		
	$\Gamma^{11} \leftrightarrow \Gamma^{11}$	$\Gamma^{11} \leftrightarrow \Gamma^{11}$	$\Gamma^{11} \leftrightarrow \Gamma^{11}$
	$\Gamma^{12} \leftrightarrow \Gamma^{12}$	$\Gamma^{12+} \leftrightarrow \Gamma^{12+}$ $\Gamma^{12-} \leftrightarrow \Gamma^{12-}$	$\Gamma^{12+} \leftrightarrow \Gamma^{12-}$

^a A principal axis for (CH₃)NH and (CD₃)NH perpendicular to the symmetry plane of molecular frame and parallel to the \hat{e}_z axis in the coordinate system defined in ref 1.

Assignment

The torsional data for the dimethylamines provides another example of the complementary nature of the two prime sources of vibrational data, Raman and infrared. For example, the Raman data for dimethylamine-*d*₀ (Figure 2A) is observed to be in two apparently distinct groups (507 to 464 cm⁻¹ and 432 to the CNC bend at 383 cm⁻¹). One might reasonably assign 507 cm⁻¹ as one of the torsional 2 ← 0 transitions and 432 cm⁻¹ as the other 2 ← 0 torsional transition. The confidence in that assignment, however, increases considerably when, on inspection of the far infrared data, Figure 3A, one notes two series of Q branches for which the sum of the first two members of each series is, in fact, the appropriate transition noted in the Raman spectrum of the gas (256.3 + 250.8 = 507.1; 219.4 + 213.0 = 432.4).

The far-infrared spectrum of dimethylamine-*d*₃ (Figure 3B) is reasonably interpretable on its own. The Raman spectrum (Figure 2B) provides the confirmation for the assignment. The appropriate sums are 239.5 + 229.0 = 468.5 cm⁻¹ and 177.0 + 166.3 = 343.3 cm⁻¹. For this isotopic species, the second highest frequency in the far-infrared (236.5 cm⁻¹) is not part of the single jump series of Q branches of the high energy torsion but is the 1 ← 0 of that torsion in the first excited state of the lower energy torsion.

The least readily interpretable spectra are those of dimethylamine-*d*₆ (Figures 2C and 3C). The Q branches in the far-infrared are considerably less pronounced than those of the other isotopes. The Raman spectrum is similar to that for the *d*₃ isotope (Figure 2B). Closer attention to the Raman spectrum allows observation of a

subtle difference between it and the Raman spectra of the other isotopic species (Figure 2). The highest energy transition at 393 cm⁻¹ is the broadest of all the intense torsional transitions observed for the dimethylamines. It is, however, still possible to identify the approximate sums that allow computation of the potential function (198.0 + 196.6 = 394.6 cm⁻¹; 158.5 + 157.9 = 316.4 cm⁻¹).

Initial calculations for all these isotopic species were based on the sums noted above. Subsequent calculations were based on expanded assignments indicated by the initial calculation, etc. The reason for the anomalous appearance of the 393-cm⁻¹ transition in the Raman spectrum of dimethylamine-*d*₆ became quickly apparent. At least two, and perhaps three, of the two-quantum transitions had "piled up" there. Efforts to resolve the 393-cm⁻¹ band proved fruitless. The details of the final assignments along with the differences between the observed and calculated transitions are listed for dimethylamine-*d*₀ in Table II, for dimethylamine-*d*₃ in Table III, and for dimethylamine-*d*₆ in Table IV.

The kinetic coefficients g^{mn} for the various isotopic species were calculated from the structural parameters listed in Table VII. These parameters were obtained from a previous microwave investigation.²⁰ The values of the potential constants for all three dimethylamines are listed with their dispersions in Table VIII. Also tabulated there are the kinetic coefficients used in the calculations and the standard deviation of the frequency fit.

Discussion

The initial fitting of the torsional potential function for the dimethylamines was conducted using three potential constants, $V_{30} = V_{03}$, V_{33} , and V_{33}' (eq 2). Attempts to expand the potential function and improve the fit were futile. V_{60} , V_{06} , V_{60}' , V_{06}' , V_{33}'' , and V_{33}''' were therefore set to zero for the final computations. V_{60} and V_{06} were found to have the usual effect of shaping the potential function but were found to have such a small value for the dimethylamines that they were excluded. V_{60}' , V_{06}' , V_{33}'' , and V_{33}''' were found to have little effect on the calculated values of the transitions and were, therefore, very ill-determined so they were also excluded. These coefficients deserve further comment although we were not able to determine them from our experimental data. Coefficients of this type have been considered in the potential function of a semirigid C_{3v}T-C₁F-C_{3v}T model by Grant et al.²¹ However, to our knowledge, they have not been mentioned in the literature for the dimethylamines. Groner and Durig¹ introduced terms with these coefficients into the

TABLE VI: Character Table of the Group C₃ ⊗ C₃^{a,b}

C ₃ ⊗ C ₃		E	V ₂ ⁻¹ V ₁	V ₁ ⁻¹ V ₂	V ₁ ⁻¹ V ₂ ⁻¹ V ₁ V ₂	V ₁ ⁻¹ V ₂	V ₁ V ₂ ⁻¹	V ₁ ⁻¹ V ₂ ⁻¹ / V ₃ V ₄	V ₂ ⁻¹ / V ₃ V ₄	V ₁ V ₂ V ₃ V ₄	V ₁ ⁻¹ V ₃ V ₄	V ₂ V ₃ V ₄	V ₁ ⁻¹ V ₃ V ₄	V ₁ V ₂ V ₃ V ₄
AA ₁	Γ ⁰⁰⁺	1	1	1	1	1	1	1	1	1	1	1	1	1
AA ₂	Γ ⁰⁰⁻	1	1	1	1	1	1	-1	-1	-1	-1	-1	-1	-1
AE	Γ ¹¹	2	-1	-1	-1	2	2	0	0	0	0	0	0	0
E _a A ₁	Γ ¹²⁺	1	ε*	ε	1	ε*	ε	1	ε*	ε	ε*	ε	ε*	ε
E _b A ₁		1	ε	ε*	1	ε	ε*	1	ε	ε*	ε	ε*	ε	ε*
E _a A ₂	Γ ¹²⁻	1	ε*	ε	1	ε*	ε	-1	-ε	-ε	-ε	-ε	-ε*	-ε
E _b A ₂		1	ε	ε*	1	ε	ε*	-1	-ε	-ε	-ε	-ε	-ε*	-ε
E _a E	Γ ¹⁰	2	-ε*	-ε	-1	2ε*	2ε	0	0	0	0	0	0	0
E _b E		2	-ε	-ε*	-1	2ε	2ε	0	0	0	0	0	0	0

$$\epsilon = \exp(2\pi i/3)$$

$$\epsilon^* = \epsilon^2$$

^a The symmetry operations V_i are defined in ref 1 and 22. Note that in this group only V_3V_4 is a symmetry operation, but neither V_3 nor V_4 . ^b The first column refers to Dreizler's²² notation of the irreducible representations. The second column has been adopted correspondingly to Günthard's²³ notation (see Table V in ref 21). In the notations, $\Gamma^{00\sigma}$ and $\Gamma^{12\sigma}$, σ is the sign of the character of the corresponding irreducible representation with respect to the operation V_3V_4 .

TABLE VII: Structural Parameters for Dimethylamine^a

Bond lengths	Å	Bond angles,	deg
C-N	1.462	C-N-C	112.2
N-H	1.019	λ^b	54.6
C-H	1.084	H-N-C	108.9
C-H'	1.098	N-C-H	109.7
C-H''	1.098	N-C-H'	108.2
		N-C-C''	113.8
		H-C-H'	109.0
		H-C-H''	109.0
		H'-C-H''	107.2

^a Reference 2. ^b λ is the angle between the CNC plane and the N-H bond.

potential function of certain types of semirigid two-top models. Using the fact that the potential function is invariant with respect to operations of the internal isometric symmetry group,¹⁹ they proved that these coefficients may be nonzero by symmetry arguments. Without introducing these terms, the potential function would have the same symmetry for $(CH_3)_2NH$ as for $(CH_3)_2O$ although this seems unreasonable from a chemist's viewpoint. Model calculations with the computer program showed that the eigenvalues are very insensitive to these coefficients as long as they are small; the derivatives of the eigenvalues with respect to any of these coefficients vanish if all these coefficients are zero. As a consequence, they may be determinable only if they were of the order of magnitude of one tenth of the effective barrier height.

For dimethylamine- d_3 , it was found that V_{33}' , the coefficient of the sine-sine coupling term, was calculated to have so small a value as to be meaningless and it was also set to zero for the final computation.

As shown by Groner and Durig,¹ the parameter set commonly used for the potential function is not the best one in terms of determinability because some of the coefficients are strongly correlated. They introduced the linear combinations

$$\begin{bmatrix} V_{3s} \\ V_{3d} \\ V_{\text{eff}} \end{bmatrix} = \begin{bmatrix} 1/2 & 1/2 & 0 \\ 1/2 & -1/2 & 0 \\ 1/2 & 1/2 & -1 \end{bmatrix} \begin{bmatrix} V_{30} \\ V_{03} \\ V_{33} \end{bmatrix}$$

as determinable and less correlated parameters in place of V_{30} , V_{03} , and V_{33} . These new parameters have generally lower dispersions than the original ones. In the case of a potential function for equivalent tops, $V_{3s} = V_{03} = V_{30}$ and $V_{3d} = 0$ holds, of course. The value of the effective barrier is also given in Table VIII. The effective barrier is directly given by V_{eff} . The average effective barrier for all three isotopic species of $1052 \pm 12 \text{ cm}^{-1}$ is obtained from these

values. This value is about 75 cm^{-1} lower than the V_3 calculated from the average of the microwave splittings measured in the first excited state for each torsion.²⁴ The microwave analysis was complicated by the inversion splitting which was also averaged. In view of the compromises made in the calculations based on the microwave data, it is reasonable that the V_3 thus computed (1125 cm^{-1}) is not very different from the average "effective" V_3 (1052 cm^{-1}) reported here.

No fewer than 15 observed transitions were fit using the potential constants in Table VIII for each isotopic species. The computer program used here¹ was not dimensioned large enough to calculate the 05 level for dimethylamine- d_0 . The transition in the Raman spectrum (Figure 2A) at 476 cm^{-1} is believed to be the $05 \leftarrow 03$ transition. Since the $04 \leftarrow 03$ is assigned at 239.8 cm^{-1} (Table II), the $05 \leftarrow 04$ should then be observed at approximately 236.2 cm^{-1} . The Q branch at 235.0 cm^{-1} in the far-infrared is unexpectedly strong which suggests that both the $11 \leftarrow 10$ and $05 \leftarrow 04$ transitions might occur here. The anomalous intensity of the 235.0-cm^{-1} Q branch supports the belief that the $05 \leftarrow 03$ transition is observed at 476 cm^{-1} in the Raman spectrum.

Two Q branches in the far-infrared spectrum of dimethylamine- d_0 at 227.6 and 222.0 cm^{-1} (Figure 3A) have the same spacing as the $01 \leftarrow 00$ and the $02 \leftarrow 01$ transitions (Table II) and have intensities appropriate for them to be transitions that originate in the first excited state of the CNC bend. They are, therefore, thus assigned.

Several spectral features remain unassigned at first glance. Transitions in the Raman spectra (Figure 2) at 464 cm^{-1} for the d_0 isotope, 433 cm^{-1} for the d_3 isotope, and 360 cm^{-1} for the d_6 species are apparently members of each high frequency series of double jumps. They, however, remain steadfastly uninterpretable in terms of the potential functions reported here. The other features that remain unexplained may be located in the appropriate tables (Tables II, III, and IV) and figures (Figures 2 and 3).

The values of the potential constants in Table VIII show a reasonable agreement among the isotopes studied. Such differences as do occur probably result from the following causes. The model used for the calculations is semirigid, that is, it does not take account of nonrigidity of either frame or internal rotors and, therefore, neglects any coupling between the torsional motions and other vibrational modes. The CNC bend, if it were a pure normal mode, would be expected to shift between the d_0 and the d_3 compounds, at most, $1.05 [(33/30)^{1/2}]$ and between the d_0 and d_6 compounds about $1.1 [(36/30)^{1/2}]$. The observed shift factors for this motion are 1.08 and 1.19, respectively.

TABLE VIII: Torsional Potential Constants (cm^{-1}) and Kinetic Coefficients (cm^{-1}) for Dimethylamine- d_0 , - d_3 , and - d_6 .

Symmetry case	$(CH_3)(CD_3)NH$							
	$(CH_3)_2NH \ C_s(e)^a$		$C_s(e)$		$C_1(n)$		$(CD_3)_2NH \ C_s(e)$	
	Value	Dis- persion	Value	Dis- persion	Value	Dis- persion	Value	Dis- persion
V_{30}	1281.7	8.8	1196.5	25.1	1196.9	25.6	1351.7	12.9
V_{03}	1281.7	8.8	1196.5	25.1	1193.1	26.2	1351.7	12.9
V_{33}	227.9	11.4	134.0	29.8	132.6	30.6	312.7	15.8
V_{33}'	30.2	3.8	0		0		56.8	3.8
$[(V_{30} + V_{03})/2] - V_{33}$	1053.8	3.4	1062.5	5.2	1062.4	5.8	1039.0	3.7
$\hbar g^{44} = 2F_1$	13.243		12.900		12.900		7.4620	
$\hbar g^{45} = 2F_1'$	-2.2304		-2.0432		-2.0432		-1.8580	
$\hbar g^{55} = 2F_2$	13.243		7.8038		7.8038		7.4620	
Standard deviation of the frequency fit	1.25		1.38		1.40		1.24	

^a $C_s(e)$: C_s frame, equivalent tops, $V_{03} = V_{30}$. $C_1(n)$: C_1 frame, nonequivalent tops, $V_{03} \neq V_{30}$.

Similarly, the torsional motions, were they pure, would be expected to shift by a factor of 1.4 $[(6/3)^{1/2}]$. The $02 \leftarrow 00$ transition is observed to shift 1.29 between the d_0 and d_6 compounds.

It is therefore reasonable to suggest that there is some coupling between the torsions and the bending mode which is symmetric with respect to the symmetry plane of the molecular frame. In the high barrier case it can, therefore, interact with all torsional energy levels ($v\bar{v}$) with even \bar{v} . Since the energy levels (02) and (20) are in the vicinity of the first excited state of the bending mode, Fermi-type interactions are likely, although we have the impression that they are small in the case of the dimethylamines since the frequency fit is reasonably good for all isotopes. They might be responsible for the slightly different potential coefficients in the different isotopes.

It should be pointed out that the set of transitions used for any particular isotope is not identical with the set used for any other isotope. This may provide a difference in emphasis in the calculations that would account for some of the differences in the values of any particular potential constant among the isotopes. Lastly, whatever errors may be associated with the structures (Table VII) would also be reflected in the kinetic coefficients (Table VIII) used in the calculations here, and they may also account for some of the variation of the potential constants.

Acknowledgment. The authors gratefully acknowledge the financial support given this work by the National

Aeronautics and Space Administration through Grant NGL-41-002-003.

References and Notes

- (1) For Part 2, see *J. Chem. Phys.*, in press.
- (2) Taken in part from the thesis of M. G. Griffin to be submitted to the Department of Chemistry in partial fulfillment of the Ph.D. Degree.
- (3) Present address: Laboratorium fur Phys. Chemi, Universitatstr. 22, CH-8006, Zurich, Switzerland.
- (4) R. A. Russell and H. W. Thompson, *J. Chem. Soc.*, 483 (1955).
- (5) D. A. Barr and R. N. Haszeldine, *J. Chem. Soc.*, 4169 (1955).
- (6) J. Bellanato, T. Sardina, and J. R. Barcelo, *An. R. Soc. Esp. Fis. Quim., Ser. B*, 51, 271 (1955).
- (7) J. R. Barcelo and J. Bellanato, *Spectrochim. Acta*, 8, 34 (1956).
- (8) J. E. Stewart, *J. Chem. Phys.*, 30, 1259 (1959).
- (9) W. G. Fateley and F. A. Miller, *Spectrochim. Acta*, 18, 977 (1962).
- (10) J. P. Peachard, M.-T. Forel, and M.-L. Josien, *J. Chim. Phys.*, 61, 652 (1964).
- (11) M. J. Butler and D. C. McKean, *Spectrochim. Acta*, 21, 485 (1965).
- (12) G. Garner and H. Wolff, *Spectrochim. Acta, Part A*, 29, 129 (1973).
- (13) J. D. Swalen and C. C. Costain, *J. Chem. Phys.*, 31, 1562 (1959).
- (14) K. D. Moller and H. G. Andresen, *J. Chem. Phys.*, 37, 1800 (1962).
- (15) J. R. Durig, W. E. Bucy, L. A. Carriera, and C. J. Wurrey, *J. Chem. Phys.*, 60, 1754 (1974).
- (16) J. R. Durig, W. E. Bucy, and C. J. Wurrey, *J. Chem. Phys.*, 60, 8293 (1974).
- (17) G. Dellepiane and G. Zerbi, *J. Chem. Phys.*, 48, 3573 (1968).
- (18) J. R. Durig, Y. S. Li and P. Groner, *J. Mol. Spectrosc.*, 62, 159 (1976).
- (19) A. Bauder, R. Meyer, and Hs. H. Gunthard, *Mol. Phys.*, 28, 1305 (1974); 31, 647 (1976).
- (20) J. E. Wollrab and V. W. Laurie, *J. Chem. Phys.*, 48, 5058 (1968).
- (21) D. M. Grant, R. J. Pugmire, R. C. Livingston, K. A. Strong, H. L. McMurry, and R. M. Brugger, *J. Chem. Phys.*, 52, 4424 (1976).
- (22) H. Dreizler, *Z. Naturforsch. A*, 16, 1354 (1961).
- (23) J. Meier, A. Bauder, and Hs. H. Gunthard, *J. Chem. Phys.*, 57, 1219 (1972).
- (24) J. E. Wollrab and V. W. Laurie, *J. Chem. Phys.*, 54, 532 (1971).

Selective Carbon-Hydrogen Bond Fission in Partially Deuterated 3-Methylpentane Glasses Irradiated at 77 K as Studied by Electron Spin Resonance

Takahisa Ichikawa* and Nobuaki Ohta¹

Department of Applied Chemistry, Hiroshima University, Senda-machi, Hiroshima 730, Japan (Received September 13, 1976)

Publication costs assisted by Hiroshima University

There exist four possible radicals produced by rupture of the C-H bonds of 3-methylpentane- h_{14} , i.e., $\dot{C}H_2CH_2CH(CH_3)CH_2CH_3$, $CH_3\dot{C}HCH(CH_3)CH_2CH_3$, $CH_3CH_2\dot{C}(CH_3)CH_2CH_3$, and $CH_3CH_2CH(CH_2)CH_2CH_3$. Results obtained from radiolysis of 3-methyl- d_3 -pentane and 3-methylpentane-3- d_1 eliminate the possible formation of the two primary radicals and a tertiary radical and lead to the formation of only the secondary radical. On the other hand, radiolysis of 3-methylpentane-2,2,4,4- d_4 gives a radical produced by rupture of the tertiary C-H bond, indicating the isotope effect in the bond fission reaction. Photolysis of HI or 3-iodo-3-methylpentane- h_{13} in the four 3-methylpentanes mentioned above shows the same results as the radiolysis of the four 3-methylpentanes. Consideration is given to specific bond rupture in the 3MP systems.

Introduction

Radiolysis of 3-methylpentane- h_{14} (3MP- h_{14}) glass at 77 K produces trapped free radicals. The ESR spectrum consists of six lines with an average spacing of 23 G and a binominal intensity ratio of 1:5:10:10:5:1. Henderson and Willard² attributed the spectrum to the radical $CH_3\dot{C}HCH(CH_3)CH_2CH_3$ (R_{II} - h_{14}). The identification was made by comparing the ESR spectrum with those of four possible radicals, i.e., $CH_3CH_2\dot{C}(CH_3)CH_2CH_3$ (R_I - h_{14}), R_{III} - h_{14} , $CH_3CH_2\dot{C}(CH_3)CH_2CH_3$ (R_{III} - h_{14}), and $CH_3CH_2CH(CH_2)CH_2CH_3$ (R_{IV} - h_{14}). These four radicals were produced by radiolysis of the corresponding iodides and chlorides. 1-Iodo-3-methylpentane and 3-iodo-3-methylpentane gave ESR spectra with intensity ratios of 1:3:4:4:3:1 and 1:3:3:1, respectively. 3-Iodo-3-methyl-

pentane gave a poorly resolved even-line spectrum. Only the secondary halides of 3MP- h_{14} yielded ESR spectra similar to that obtained from 3MP- h_{14} .

These results, however, do not exclude the possibility of formation of R_I - h_{14} and R_{IV} - h_{14} because the binominal intensity distribution of 1:5:10:10:5:1 can be constructed by superimposing lines with the intensity distribution of 1:3:4:4:3:1 and 2:6:6:2. In our preliminary study, a six-line spectrum with intensity ratios being approximately binominal was obtained by 77 K radiolysis of a mixture of 1-bromo-3-methylpentane (50 mol %) and 3-bromo-3-methylpentane (50 mol %).

This paper attempts to answer the question whether or not only R_{II} - h_{14} is responsible for the six-line spectrum observed in γ -irradiated glassy 3MP- h_{14} . For this purpose,

we synthesized three kinds of selectively deuterated 3MP ($\text{CH}_3\text{CH}_2\text{CH}(\text{CD}_3)\text{CH}_2\text{CH}_3$, $\text{CH}_3\text{CH}_2\text{CD}(\text{CH}_3)\text{CH}_2\text{CH}_3$, and $\text{CH}_3\text{CD}_2\text{CH}(\text{CH}_3)\text{CD}_2\text{CH}_3$) and their ESR spectra are compared with the 3MP- h_{14} spectrum. ESR spectra of photolyzed 3MP glasses containing hydrogen iodide or 3-iodo-3-methylpentane are also compared with those of γ -irradiated 3MP glasses.

Experimental Section

Materials. 3-Methylpentane- h_{14} (3MP- h_{14}), which was obtained from Chemical Sample Co. with 99% purity, was further purified by stirring with H_2SO_4 ,³ washing with water and aqueous solutions of K_2CO_3 , followed by drying over CaCl_2 and passage through a 30-cm column containing a fine grade of silica gel. The effluent was fractionally distilled using a packed distillation column with 20 theoretical plates and was stored over 13X molecular sieve under vacuum.

3-Methyl- d_3 -pentane (3MP- d_3) was synthesized using acetic- d_4 acid (Stohler Isotope Chemical Co. with 99.5 atom % D) as the starting material. The synthetic procedures include acetylation of acetic- d_4 acid; addition of acetyl- d_3 chloride to a Grignard reagent from ethyl bromide, followed by hydrolysis; chlorination of 3-methyl- d_3 -3-pentanol; hydrolysis of a Grignard reagent from 3-chloro-3-methyl- d_3 -pentane.

The synthetic procedures of 3-methylpentane-2,2,4,4- d_4 (3MP- d_4) include base-catalyzed exchange of 3-pentanone with D_2O (Merck Sharp and Dohm, Canada with 99.7% D); addition of 3-pentanone-2,2,4,4- d_4 to a Grignard reagent from methyl bromide, followed by hydrolysis; chlorination of 3-methyl-3-pentanol-2,2,4,4- d_4 ; hydrolysis of a Grignard reagent from 3-chloro-3-methylpentane-2,2,4,4- d_4 .

3-Methylpentane-3- d_1 (3MP- d_1) was prepared by adding D_2O to a Grignard reagent from 3-chloro-3-methylpentane.

Each of these crude deuterated 3MPs, which were obtained as ether solutions, was fractionally distilled, purified by the same method as described in the purification of 3MP- h_{14} , and stored over 13X molecular sieve under vacuum. Gas chromatographic analysis of each deuterated 3MP showed that the presence of ether is not detected and that the impurity at the retention time of 2-methylpentane is <3 vol %. Isotopic purity in the labeled positions was >96 atom % D from nuclear magnetic resonance and mass spectrometric analysis.

Anhydrous HI for photolysis work was prepared by addition of 60% aqueous solutions of HI to excess P_2O_5 on the vacuum line and stored at 77 K. 3-Iodo-3-methylpentane was prepared by passing gaseous HI into 3-methyl-3-pentanol kept cold. The product was decolorized by shaking with sodium thiosulfate solution, washed with water, and then dried over CaCl_2 , followed by fractional distillation at reduced pressure.

Preparation of Samples. Purified 3MP was further dried over sodium mirrors before use, degassed by several freeze-pump-thaw cycles on the vacuum line, and sealed in calibrated quartz ESR tubes (3-mm i.d., Suprasil). Samples for photolysis were prepared by adding metered amounts of iodide (0.3 mol %) to 3MP on the vacuum line.

Irradiations and ESR Measurements. Radiolysis was made at 77 K under liquid nitrogen for 45 min at a dose rate of 6.2×10^{17} eV g^{-1} min^{-1} with a ^{60}Co source. Photolysis was performed using a Toshiba 400-W medium-pressure mercury arc. Samples were immersed in liquid nitrogen in a partially unsilvered quartz dewar at a distance of 10 cm from the lamp and were illuminated for 30 min. Radiation from the lamp was passed through a Toshiba UV-D25 glass filter (235 nm < λ < 415 nm). To

bleach the color centers produced in the quartz sample tubes, samples after radiolysis were illuminated at 77 K for 5 min by filtered light from the lamp attached a Toshiba UV-310 glass filter (280 nm < λ). Photobleaching by this light did not change the intensities of 3-methylpentyl radicals produced by radiolysis and changes in line shapes of the 3-methylpentyl radicals were small under our experimental conditions. Willard et al.^{4,5} observed that exposure of 3-methylpentyl radicals produced by radiolysis of 3MP- h_{14} glass to light in the 250-nm region induces marked enhancement of the resolution of the ESR spectrum.

ESR measurements were carried out with a Model PE-1X Japan Electron Optics spectrometer operated at 9.15 GHz with 100-kHz modulation frequency and a modulation amplitude of 3.2 G. First derivative absorption spectra were recorded at 77 K under liquid nitrogen with a microwave power of 0.1 mW.⁶ ESR spectra of γ -irradiated samples were recorded within an hour after irradiation and then the samples were immediately subjected to photobleaching. ESR measurements of photobleached samples and photolyzed iodide-3MP samples were made within 3 min after illumination.

Relative intensities of ESR signals were determined by comparing the areas under the absorption curves which were obtained from the first derivative spectra with an electronic integrator⁷ and the areas were measured with a planimeter.

Simulated ESR spectra were calculated with a TOS-BAC-3400 Model-40 computer. Observed ESR line shapes were more nearly Gaussian rather than Lorentzian. After a number of trials, spectra which fitted observed ones were found to be produced on the assumption that splittings of hyperfine structure and line widths as measured between points of maximum slope are 22.2 and 16.2 G, respectively.⁸

Results

3-Methylpentane- h_{14} (3MP- h_{14}). Figure 1A shows the six-line ESR spectrum of 3MP- h_{14} glass γ irradiated at 77 K. Unsymmetrical components which are discernible in the neighborhood of the center of the spectrum disappeared during 5-min photobleaching (Figure 1B). The signals which disappeared are attributable to the color centers of the γ -irradiated sample tube. The photobleaching enhanced to some degree the resolution of spectrum A. When the samples were held at 77 K in the dark for 7 days following photobleaching, the intensity decreased to about one-fifth and changes in the ESR lines were not observable except that the resolution of the individual lines became somewhat poor⁹ (Figure 1C). A weak signal near the center of spectrum C is due to the remaining color centers. Neiss and Willard⁴ have found that in γ -irradiated 3MP- h_{14} glass the ratio of the first derivative ESR peak height of 3-methylpentyl radicals to the area under the absorption curve increases as decay proceeds during storage at 77 K. The fact, however, does not necessarily mean the presence of more than two paramagnetic species. Nakano et al.⁷ demonstrated a nonlinear relationship between the heights of the first derivative ESR spectra and the areas under the absorption curves at high radical concentrations.

Figure 1D shows the ESR spectrum of 3MP- h_{14} glass containing 0.3 mol % HI photolyzed at 77 K. The spectrum is almost of the same shape as in Figure 1B. These six-line spectra agree closely with the computed $R_{\text{T}}\text{-}h_{14}$ spectrum (Figure 1E) having component lines with intensity ratios of 1:5:10:10:5:1, a separation of 22.2 G, and a Gaussian shape. Nevertheless, the observed spectra are

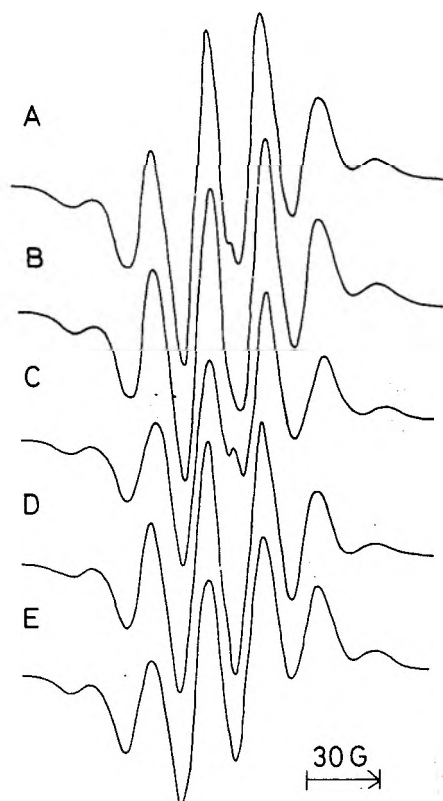


Figure 1. ESR spectra of 3MP- h_{14} measured at 77 K: (A) after radiolysis; (B) after photobleaching of A; (C) after annealing of B at 77 K for 7 days. (D) ESR spectrum of photolyzed HI-3MP- h_{14} at 77 K. (E) Computed ESR spectrum with line intensity ratios of 1:5:10:10:5:1.

not exclusively assigned to the $R_{II}h_{14}$ radical for the reason mentioned in the Introduction.

3-Methyl- d_3 -pentane (3MP- d_3). Figure 2 shows a series of 3MP- d_3 spectra to be compared with the 3MP- h_{14} spectra. Six-line spectra almost same as the corresponding 3MP- h_{14} spectra were obtained, except that peaks 1 and 6 from the low-field side showed slightly asymmetrical line shapes (dotted lines in spectrum A were recorded at a high instrument gain and a slow field sweep). As discussed later, the asymmetrical line shapes are attributable to an anisotropic proton interaction with an unpaired electron. These results indicate no noticeable interaction between the unpaired electron and the substituted deuterons. This leads to the formation of the $R_{II}d_3$ radical ($CH_3CHCH(CD_3)CH_2CH_3$) whose spectrum is expected to be almost same as that of $R_{II}h_{14}$. Neiss and Willard⁴ have found that the ESR spectra of 3-methylpentyl radicals produced in γ -irradiated 3MP- d_3 systems are similar to those obtained in 3MP- h_{14} systems.

The above results, however, does not completely eliminate the possibility that the $R_I d_3$ radical ($CH_2CH_2CH(CD_3)CH_2CH_3$) is still trapped together with $R_{II}d_3$. This comes from the fact that the shape of the computed $R_{II}d_3$ ($R_{II}h_{14}$) spectrum is not effectively changed by superposition of the computed $R_I d_3$ ($R_I h_{14}$) spectrum with line intensity ratios of 1:3:4:4:3:1 and a line separation of 22.2 G. Even if the $R_I d_3$ lines are superimposed on the $R_{II}d_3$ lines at equal radical concentrations, the resultant spectrum (Figure 2E) does not differ much in the shape from the original $R_{II}d_3$ spectrum (Figure 2B).

3-Methylpentane-3- d_1 (3MP- d_1). Radiolysis of 3MP- d_1 glass gave five-line ESR spectra (Figures 3A and 3B) with additional narrow lines as indicated by arrows. Photolysis of HI in 3MP- d_1 glass yielded a similar spectrum (Figure 3D), but the intensities of the narrow lines and the center line are relatively weak. On annealing at 77 K the narrow

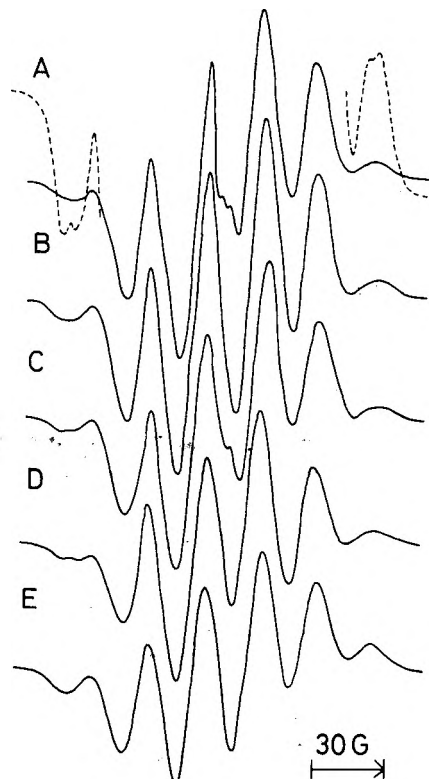


Figure 2. ESR spectra of 3MP- d_3 measured at 77 K: (A) after radiolysis; (B) after photobleaching of A; (C) after annealing of B at 77 K for 7 days. (D) ESR spectrum of photolyzed HI-3MP- d_3 at 77 K. (E) Computed ESR spectrum with line intensity ratios of 1.5:5.5:9:9:5.5:1.5.

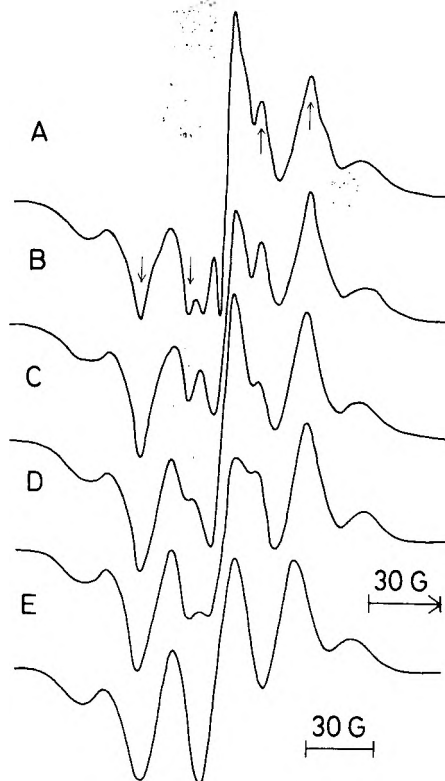


Figure 3. ESR spectra of 3MP- d_1 measured at 77 K: (A) after radiolysis; (B) after photobleaching of A; (C) after annealing of B at 77 K for 7 days. (D) ESR spectrum of photolyzed HI-3MP- d_1 at 77 K. (E) Computed ESR spectrum with line intensity ratios of 1:4:6:4:1.

lines decayed faster than the five main lines (Figure 3C). In the purification procedures, repeated treatments of 3MP- d_1 with fresh 13X molecular sieve were effective to weaken the intensities of the narrow lines, which implies

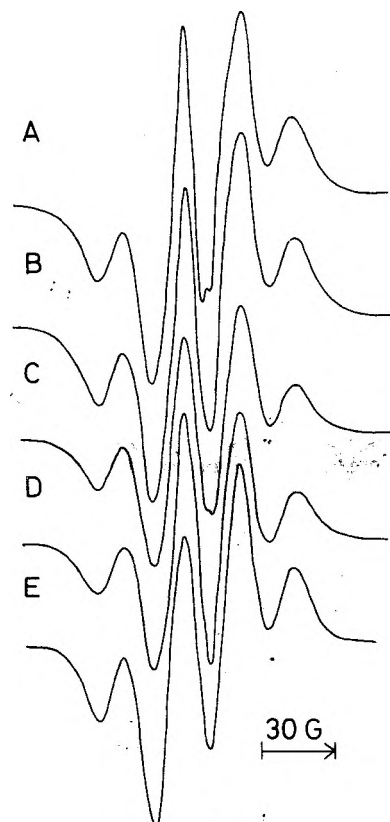


Figure 4. ESR spectra of 3MP- d_4 measured at 77 K: (A) after radiolysis; (B) after photobleaching of A; (C) after annealing of B at 77 K for 7 days. (D) ESR spectrum of photolyzed HI-3MP- d_4 at 77 K. (E) Computed ESR spectrum with line intensity ratios of 1:3:3:1.

that the signals are due to contaminants included in 3MP- d_1 . The sharp center line of Figure 3C in comparison with that of Figure 3D is accounted for by superposition of a peak due to surviving color centers.

The intensity distribution of the five lines is compatible with the binominal distribution of 1:4:6:4:1 with a separation of 22.2 G as determined by comparison with the computed spectrum (Figure 3E). The five-line spectra are attributed to the R_{II-d_1} radical ($\text{CH}_3\text{CHCD}(\text{CH}_3)\text{CH}_2\text{CH}_3$) where the one α and three β protons couple equally with the unpaired electron. Small splittings due to the β deuterium ($a^D = 0.153a^H$) are smeared out because of the broad line width (16.2 G) of the component lines.

3-Methylpentane-2,2,4,4- d_4 (3MP- d_4). Radiolysis of 3MP- d_4 glass (Figures 4A, 4B, and 4C) and photolysis of HI in glassy 3MP- d_4 (Figure 4D) all gave four-line spectra which match the computed spectrum (Figure 4E) with binominal intensity ratios of 1:3:3:1 and a separation of 22.2 G. The result indicates the formation of a radical having three equally coupled protons. The R_{IV-d_4} radical ($\text{CH}_3\text{CD}_2\text{CH}(\text{CH}_2)\text{CD}_2\text{CH}_3$) and also the R_{III-d_4} radical ($\text{CH}_3\text{CD}_2\text{C}(\text{CH}_3)\text{CD}_2\text{CH}_3$) produce four-line spectra with binominal intensity ratios. The former possesses two α and one β proton interacting with the unpaired electron. The unpaired electron in the latter couples with the three β protons and the four β deuterons, but the deuteron couplings are expected to be unresolved by reason of the broad line width (16.2 G). The observed line separation of 22.2 G, however, is close to the reported splitting constant values for protons in methyl groups attached to a tertiary carbon, i.e., 22.7 G for $(\text{CH}_3)_3\text{C}$ and 22.8 G for $(\text{CH}_3)_2\text{CCH}_2\text{CH}_3$.¹⁰ On the other hand, the average line separation of the primary polypropylene radical ($-\text{CH}_2\text{CH}(\text{CH}_2)\text{CH}_2-$) has been reported to be 25.5 G.¹¹ Radiolysis of 3-chloromethylpentane- h_{13} at 77 K is ex-

pected to produce the $R_{IV-h_{14}}$ radical by rupture of the C-Cl bond. The spectrum observed had four lines with the overall splitting being 1.14 times as large as that of the spectrum in Figure 4B. This leads to an average separation of the $R_{IV-h_{14}}$ lines of 25.4 G.¹² All of these results suggest that the 3MP- d_4 spectra with a line separation of 22.2 G should be ascribed to R_{III-d_4} rather than R_{IV-d_4} . γ irradiation of 3-chloro-3-methylpentane-2,2,4,4- d_4 at 77 K which is expected to yield R_{III-d_4} exhibited a four-line spectrum identical with Figure 4B. The result confirms the above identification.

Photolysis of 3-Iodo-3-methylpentane- h_{13} (3-I-3MP- h_{13}) in 3MP Glasses. Henderson and Willard² have found that every one of the four 3-methylpentyl radicals (R_I-h_{14} , $R_{II-h_{14}}$, $R_{III-h_{14}}$, and $R_{IV-h_{14}}$) which are produced by photolysis of the corresponding iodides in 3MP- h_{14} glasses at 77 K abstracts a secondary hydrogen from the matrix molecules. It is interesting to test this kind of experiment in deuterated 3MP glasses. Photolysis of 3-I-3MP- h_{13} in the four 3MP glasses gave the same results as the photolysis of HI in the four 3MP glasses, i.e., tertiary 3MP radical formation in case of 3MP- d_4 and secondary radical formation in cases of 3MP- h_{14} , 3MP- d_3 , and 3MP- d_1 . It should be noted that the marked difference in radical yields was not found in the photolysis of HI or 3-I-3MP- h_{13} in the four 3MP glasses.¹³ In case of radiolysis, radical yields of the four 3MP glasses were found coincide with each other within the limit of error (25%).

Discussion

As mentioned in the preceding section, the six-line spectra of 3MP- h_{14} (Figure 1) can be ascribed not only to the secondary radical ($R_{II-h_{14}}$) but also to a mixture of two primary radicals (R_I-h_{14} and $R_{IV-h_{14}}$). The possibility of $R_{IV-h_{14}}$ formation, however, is denied from the result that the shapes of the six lines were not affected noticeably by deuterium substitution of the branched methyl H as shown in Figure 2. When the tertiary H was substituted by D, the six-line spectra changed into a five-line spectra (Figure 3). This indicates clearly that the radical site is restricted to carbon C_{II} (carbon atoms in the 3MP skeleton are designated as $C_I-C_{II}-C_{III}(C_{IV})-C_{II}-C_I$). Since the effects of deuterium substitution at carbon C_{III} or C_{IV} are considered to be very small for the H-rupture reaction at carbon C_{II} , the above results lead to the conclusion that the observed six-line spectra of 3MP- h_{14} are due to only the secondary radical.

The six-line spectra of 3MP- h_{14} agree closely with the spectrum (Figure 1E) calculated on the assumption that the shapes of the component lines are symmetrical. Provided that the four β and one α proton of the $R_{II-h_{14}}$ radical are equally coupled with the unpaired electron, the observed six-line spectra can be explained. However, theory¹⁴ predicts asymmetrical line shapes caused by an anisotropic interaction between the unpaired electron and the α proton. The fact that the observed spectra can be described by symmetrical component lines is considered to derive from a certain amount of motional freedom in the glassy matrix which would partially average out the anisotropic interaction.¹⁵ Close examination of the second derivative ESR spectra of 3MP- h_{14} showed indications of asymmetrical line shapes. It is discernible that the shapes of peaks 1 and 6 from the low-field side of the 3MP- d_3 spectra (Figure 2) are asymmetrical. In case of 3MP- d_3 , deuterium substitution at the C_{IV} carbon would somewhat reduce the interaction between the unpaired electron and nuclear spins,¹⁶ which would reveal more clearly the asymmetrical shapes.

The deuterium substitution of the secondary H resulted

in loss of the tertiary H rather than loss of the secondary D, which indicates the deuterium isotope effect in the bond fission reaction. This result also shows that H-atom loss from the tertiary bond predominates over H-atom loss from the primary bond; nevertheless the number of tertiary bonds is one-ninth the number of primary bonds. H-atom loss from the tertiary bond rather than from the primary bonds in 3MP-*d*₄ glass might be explained from the data of bond strengths in gaseous alkanes.¹⁷ However, preferential secondary H-atom loss in fully protonated 3MP glass is not a simple problem. Willard and Henderson² discussed this problem in detail. To our knowledge the observed selectivity does not seem to have been explained satisfactorily.

It was suggested that radicals produced by radiolysis of alkanes (C₆-C₉) with branching in the 3 or 4 position originate mainly from loss of a hydrogen atom from the secondary carbon atom nearest the end of the longest carbon chain.² Lund¹⁸ found that single crystals of *n*-paraffins (C₆-C₁₆) γ irradiated at 77 K give rise to ESR spectra from two kinds of secondary radicals, CH₃CHCH₂R and R'CH₂ĊCH₂R'', and that the formation of the former is preponderant over that of the latter. Iwasaki et al.¹⁹ who observed ESR spectra of single crystals of *n*-decane X-irradiated at 1.5 and 4.2 K suggested that almost all alkyl radicals are inherently formed in pairs and that random scission of C-H bonds at any carbon takes place at 4.2 K. Lin and Willard²⁰ found formation of radical pairs in 3MP glass γ irradiated at 77 K. The ESR spectra of 3MP-*h*₁₄ glass γ irradiated at 4.2 K were observed by Smith and Pierony,²¹ however, analysis of the ESR spectra was not completely done. It was demonstrated that the primary radical (-CH₂CH(CH₂)CH₂-) and the tertiary radical (-CH₂C(CH₃)CH₂-) both are trapped in polypropylene after radiolysis at 77 K.¹¹ Kanic et al.²² found that a room-temperature ESR spectrum of γ -irradiated adamantane containing 3MP-*h*₁₄ can be assigned to the tertiary radical of 3MP-*h*₁₄.

There exists no evidence that radicals observed after radiolysis of 3MP at 77 K are paramagnetic species primarily formed by decomposition through excitation of 3MP molecules (RH \rightsquigarrow RH* \rightarrow R + H and RH \rightsquigarrow RH* + e⁻ \rightarrow RH* \rightarrow R + H).²³ The present results can be explained if we assume that the trapped radicals consist mainly of radicals secondarily formed by attack by primary decomposition products such as H atoms and 3MP radicals. Such species will be born with excess energy capable of abstracting H atoms from neighboring 3MP molecules. Preferential attack to the specific bonds of 3MP molecules may be expected from the observed abstraction reactions of photolytically produced H atoms and 3MP radicals in fully protonated and partially deuterated 3MP glasses. The same selective abstraction reactions have been observed in the photolysis of methyl, ethyl, *n*-propyl, *n*-butyl, isobutyl, and *tert*-butyl iodides in 3MP glasses.²⁴ In correlation with our results preferential rupture at C-H bonds relative to C-D bonds has been reported by Willard et al.²⁵ in HI (DI)- or CH₃I (CD₃I)-3MP-*h*₁₄ (3MP-*d*₁₄) systems irradiated at 77 K. They drew conclusions that hot H or CH₃ can abstract D from C-D bonds of 3MP-*d*₁₄ and that thermal H or CH₃ can abstract H from C-H bonds which are contained as an impurity (1%) of 3MP-*d*₁₄, while D abstraction from the C-D bonds does

not occur. In the present work, photolysis of HI in 3MP-*d*₄ glass gave chiefly the tertiary radical.²⁶ Within the limit of error (25%), its yield was the same as that of the secondary radical produced in photolyzed HI-3MP-*h*₁₄ glass. The results seem to indicate that the hot H atoms produced discriminate the "weak" bonds in 3MP molecules. In contrast with the above deduction, Rebert and Ausloos²⁷ concluded that the hot CH₃ radical produced by photolysis of CH₃I in partially deuterated hydrocarbon matrices abstracts an H atom or D atom with equal probability. The conclusion was obtained from product analysis after warming the samples to room temperature, a process which may be the cause of the discrepancy, or our results obtained in the 3MP systems may be a special case.

Acknowledgment. We thank the Research Institute for Nuclear Medicine and Biology of our university for use of their facilities for radiolysis.

References and Notes

- (1) Present address: Department of Chemistry, Osaka University, Machikaneyama, Toyonaka 560, Japan.
- (2) D. J. Henderson and J. E. Willard, *J. Am. Chem. Soc.*, **91**, 3014 (1969).
- (3) Formation of 2-methylpentane caused by this treatment was found to be within 3%. Any effect on the line shapes of the 3MP spectra was not discernible.
- (4) M. A. Neiss and J. E. Willard, *J. Phys. Chem.*, **79**, 783 (1975).
- (5) E. D. Sprague and J. E. Willard, *J. Chem. Phys.*, **63**, 2603 (1975).
- (6) During the ESR measurements care was not taken to prevent exposure of samples to illumination from room lighting. The trapped electrons formed during radiolysis, accordingly, were almost bleached by the light.
- (7) K. Nakano, H. Tadano, and M. Oshima, *J. Chem. Soc. Jpn.*, **93**, 2453 (1972).
- (8) In this calculations, anisotropic proton couplings are entirely neglected. The value of 22.2 G does not represent the true isotropic proton coupling constants and is considered to be values averaged on various complex factors affecting line separations.
- (9) Similar changes in spectral resolution have been reported in ref. 4.
- (10) R. W. Fessenden and R. H. Schuler, *J. Chem. Phys.*, **39**, 2147 (1963).
- (11) M. Iwasaki, T. Ichikawa, and K. Toriyama, *Polym. Lett.*, **5**, 423 (1967).
- (12) The value of 23 G which has been reported in ref. 2 for the R_{1V}-*h*₁₄ radical should be corrected.
- (13) The reproducibility of data for the radical yields was not good by comparison with data obtained in γ radiolysis because of the instability of the iodides in the preparation of the samples.
- (14) E. L. Cochran, F. J. Adrian, and V. A. Bowers, *J. Chem. Phys.*, **34**, 1161 (1961); R. Lefebvre and J. Muruani, *ibid.*, **42**, 1480 (1965).
- (15) Typical instances that trapped radicals having α coupling protons show symmetrical ESR lines are seen in the paper by P. B. Ayscough and C. Thomson, *Trans. Faraday Soc.*, **58**, 1477 (1962).
- (16) Isotropic parts of γ -proton hyperfine coupling constants were reported to be 0.4-1.1 G (ref. 10). K. Toriyama, K. Nunome, and M. Iwasaki (*J. Chem. Phys.*, **64**, 2020 (1976)) found that the superhyperfine coupling tensor of proton in the nearest neighboring molecules is (3.07, 0.24, 0.26).
- (17) J. A. Kerr, *Chem. Rev.*, **66**, 465 (1966).
- (18) A. Lund, *J. Phys. Chem.*, **76**, 1411 (1972).
- (19) M. Iwasaki, K. Toriyama, H. Muto, and K. Nunome, *J. Chem. Phys.*, **65**, 596 (1976).
- (20) D. P. Lin and J. E. Willard, *J. Phys. Chem.*, **78**, 2233 (1974).
- (21) D. R. Smith and J. J. Pierony, *Can. J. Chem.*, **45**, 2723 (1967).
- (22) S. W. Kanic, R. E. Linder, and A. C. Ling, *J. Chem. Soc. A*, 2971 (1971).
- (23) Ion-molecule reactions (RH⁺ + RH \rightarrow R + RH₂⁺) are one of many possible reactions to produce 3MP radicals. At present, the contribution to 3MP radical formation in the glassy state is not clear.
- (24) T. Ichikawa, unpublished. Allyl iodide did not produce 3MP radicals by photolysis ($\lambda > 235$ nm).
- (25) (a) L. Perkey and J. E. Willard, *J. Chem. Phys.*, **60**, 2732 (1974); (b) M. A. Neiss, E. D. Sprague, and J. E. Willard, *ibid.*, **63**, 1118 (1975); (c) D. D. Wilkey and J. E. Willard, *ibid.*, **64**, 3976 (1976).
- (26) Formation of secondary and/or primary radicals, less than 20% of the tertiary radical yield, is possible because of poor spectral resolutions.
- (27) R. E. Rebert and P. Ausloos, *J. Chem. Phys.*, **48**, 306 (1968).

Utility of Pulse Nuclear Magnetic Resonance in Studying Protons in Coals[†]

B. C. Gerstein,* C. Chow, R. G. Pembleton, and R. C. Wilson

Ames Laboratory-ERDA and the Energy and Minerals Resources Research Institute, Iowa State University, Ames, Iowa 50011
(Received August 16, 1976; Revised Manuscript Received December 28, 1976)

Publication costs assisted by Ames Laboratory

ESR, pulse NMR, and multiple pulse NMR were used to study free radical concentrations, and the extent to which protons in coals may be characterized by damping constants under specific radio-frequency pulse sequences in two Virginia vitrains, three Iowa vitrains, and selected model compounds. ESR measurements confirmed previously found correlations between free radical content and carbon content. Electron g factors varying from 2.0025 to 2.0028 are not inconsistent with assignment of free radicals to aromatic ring systems. NMR pulse techniques were used to determine damping constants associated with proton spin-spin and spin-lattice relaxation. Multiple pulse line narrowing experiments were capable of narrowing the proton line width from roughly 30 kHz in all coals to roughly 700 Hz. Comparison of results on coals with pulse and multiple pulse measurements on the model compounds naphthalene, 2-methylnaphthalene, 4,4'-bismethylbenzophenone, *m*-tolylacetic acid, polystyrene, polyethylene, and polybutadiene indicated the following: (a) roughly 400 Hz of the residual proton line width in the coals under multiple pulse line narrowing experiments is due to free radical electron spin-nuclear spin dipolar coupling, (b) there is not a simple relation between spin-spin damping constants in coals, and aliphatic/aromatic proton ratios, and (c) resolution into aromatic and aliphatic protons will require removal of interproton dipolar interactions, proton chemical shift anisotropies, and electron-proton interactions by a combination of multiple pulse line narrowing experiments and magic angle rotation. The second moments of the proton absorption spectrum decrease with increasing proton concentration. This result is shown not to be an effect of free radical concentration, but is thought to be associated with increasing rigidity of coal structures with age.

Introduction

The response of nuclear magnetic moments to transient resonant radio-frequency signals is characterized by one or more damping constants. For example, if the nuclei are in molecules tumbling in a gas or a liquid and, in addition, are all in the same chemical environment, e.g., protons in C_6H_6 ,¹ the damping constant is the spin-lattice relaxation time, T_1 , which is equal to the spin-spin relaxation time, T_2 , in the absence of dc field inhomogeneities. In the presence of appreciable chemical shift anisotropy, even for a molecule in a nonviscous liquid in the extreme narrowing limit, relaxation of a given nucleus is characterized by damping constants T_1 and $T_2 \neq T_1$. For nuclei in a solid, there exist a number of different relaxation mechanisms, e.g., dipole-dipole interaction, electric quadrupole interaction, chemical shift anisotropy interaction, and scalar coupling interaction. Each of these interactions provides a relaxation path to equilibrium dependent upon the magnitude of the interaction, and therefore characterized by a different damping constant for each interaction. If different nuclei of a given chemical identity in a molecule, e.g., protons in aliphatic and aromatic compounds containing carbon, nitrogen, oxygen, sulfur, and aromatic rings which are capable of stabilizing free radicals, are sufficiently localized in their interactions with given groups of molecular fragments, it may be possible to use the damping constants characterizing these groups of protons to identify their local environment, and therefore to identify molecular fragments responsible for the chemistry of the compounds in question. For example, in an aliphatic compound such as polyethylene, the nearest neighbor proton-proton distance is 1.763 Å. In an aromatic compound such as naphthalene, this distance is 2.407 Å. In solids such as

these, homonuclear dipolar interactions are the dominant mechanism for spin-spin relaxation. Since this interaction is proportional to the inverse cube of the sum of interproton distances, one might expect that aliphatic and aromatic protons could be characterized by quite different spin-spin damping constants in the absence of molecular motion. A rough calculation of the spin-spin damping constant, as inferred from the structure of the rigid lattice, may be made by calculating the line width at half-height, $2\Delta f$, from the square root of the second moment. The rigid lattice second moment, for a randomly oriented ensemble of spin 1/2 systems is given by¹

$$4\langle\Delta f\rangle^2 = \frac{9\gamma^4\hbar^2}{20\pi^2} \sum_j r_{ij}^{-6} \text{ Hz}^2$$

For a Lorentzian line, in the absence of spin-lattice relaxation, the full width at half-height is related to the spin-spin damping constant by $2\Delta f = (\pi T_2)^{-1}$ Hz. While the second moment for a Lorentzian line is infinite, in practice a second moment may be calculated with suitable termination. For a Gaussian line, which could result from inhomogeneous broadening, the second moment is defined, but a spin-spin damping constant in terms of the second moment is not. Nevertheless, one may define an effective damping constant for a Gaussian line as

$$T_2^* = -(2S)^{1/2}$$

where S is the slope of the natural log of the amplitude of the decay plotted as a function of t^2 . One may similarly estimate a magnitude for this damping constant from the second moment, as described above. For naphthalene, the structure of which has been determined by Cruikshank,² the second moment in the rigid lattice limit calculated by taking into account all protons within 6 Å of a single proton on a given naphthalene molecule leads to a damping constant, inferred from the second moment, of 12.3 μ s. For

[†] Work performed for the U.S. Energy Research and Development Administration under Contract No. W-7405-eng-82, and The Iowa Coal Project of the Iowa State University Energy and Minerals Resources Research Institute.

polyethylene, this damping constant, similarly inferred, is roughly 7 μ s. In the rigid lattice limit therefore, one might expect that a mixture of naphthalene and polyethylene would yield two damping constants under a FID response to a single pulse NMR experiment that would characterize the ratio of aromatic to aliphatic protons in the mixture. Similarly, one would expect vastly different spin-lattice damping constants for protons bound to carbon, a species with a low abundance, low gyromagnetic ratio spin 1/2 nucleus, then for protons bound to nitrogen, a species with a high abundance spin 1 nucleus, because quadrupolar interactions are much more efficient in providing spin-lattice relaxation than are dipolar interactions.

With the advent of recent advances in pulsed and multiple pulse NMR, it is possible to further separate damping constants associated with differing relaxation mechanisms, since one may selectively design pulse sequences which remove specific interactions leading to spectral broadening. For example, under appropriate conditions, the CPMG sequence,³ used to determine spin-spin relaxation times, selectively eliminates internal interactions associated with dc field inhomogeneities, and with spin-other spin coupling. The multiple pulse phase altering experiments recently introduced by Dybowski and Vaughan⁴ are capable of removing chemical shifts (and shift anisotropies). The multiple pulse sequences described by Waugh and co-workers,⁵ by Mansfield,⁶ and by Rhim, Ellman, and Vaughan⁷ are capable of selectively removing homonuclear dipolar relaxation while scaling chemical shifts, providing the cycle time is short compared to the magnitude of the dipolar interaction. The present work is devoted to investigating the utility of a combination of these techniques to determine chemical environments of protons in coals.

In the past, the utility of NMR to the study of protons in coals has been limited to broad line work, utilizing second moments to infer chemical information,⁸ and to high resolution work on solvent extracts of coals.⁹⁻¹³ There are two difficulties with these approaches. First, the interpretation of broadline NMR failed to take into account the effect of variable concentrations of free radicals upon line broadening. Second is the problem of justification in assuming that soluble extracts, representing less than 30% of the total in most cases, bear a close relation to the parent structures. With respect to the latter, there is also the possibility of a change in structure in the solution process.

In the present work, we determine free radical content by electron spin resonance, and investigate the feasibility of utilizing recently developed NMR pulse techniques to distinguish chemical environments of protons in samples of two Virginia vitrains, three Iowa vitrains, and selected model compounds. Free induction decays are used to measure the effective spin-spin damping constant, T_2^* . The Rhim-Ellman-Vaughan eight-pulse sequence is used to remove the effect of homonuclear dipolar coupling, in the region where the magnitude of such coupling is not large compared to a 21- μ s eight-pulse cycle time. Finally, a standard [π , τ , $\pi/2$] sequence is used to measure damping constants associated with spin-lattice relaxation.

Experimental Section

ESR Spectra. ESR spectra were recorded at room temperature with both a Varian V-4500 spectrometer and a Strand Labs 602 spectrometer operating at a nominal frequency of 9.5 GHz. g factors were determined by sample interchange with a standard DPPH sample. Line widths were calibrated utilizing the hyperfine splitting of

DPPH in benzene and a proton gaussmeter. Spin concentrations were estimated by comparing the area of the absorption curve, or the second moment of the derivative spectrum, with a standard DPPH sample freshly prepared, and calibrated against a standard Mn^{2+} sample. Sample sizes were adjusted to keep the absolute number of spins similar in all samples, with the result that a minimum adjustment of the spectrometer was necessary when changing samples. No noticeable changes in cavity attenuation were observed as a function of sample. The major uncertainty in the estimation of spin concentration lay in the calculation of the absolute spin concentration present in the standard DPPH. The precision of the measurements was found to be 15%.

NMR Spectra. All spectra were taken on an instrument similar to those of Waugh¹⁴ and of Vaughan,¹⁵ recently designed and constructed in this laboratory, operating at a frequency of 56.5 MHz for protons. The block diagram is shown in Figure 1. A deuterium lock designed and constructed in this laboratory stabilized the spectrometer to within 10 Hz. The resolution of a spherical nonspinning sample of undoped water was 5 Hz. Combined receiver-dc amplifier dead time after a 500-W pulse at 56.5 MHz was 1.5 μ s, of which all but 10 ns was associated with probe ring-down. The receiver was constructed of three stages, the first two being Spectrum Microwave Model SML-D10 limiting amplifiers, and the third being an AvanteK Model UTO-502 amplifier. The transmitter was an IFI Model 404 distributed amplifier system, capable of delivering 500 W in pulsed operation. The spectrometer was completely broad banded except where tuned with quarter wavelength cables as indicated in Figure 1, and where series-tuned LC-resonant circuits were inserted between the first and second, and second and third stages of the receiver. The Q of the probe was 28. The pulse programmer allowed for the utilization of any sequence of up to 24 pulses in four channels, differing by an adjustable phase angle. All data were accumulated by alternating the preparation pulse by 180° and subtracting alternate responses to remove instrumental artifacts such as baseline shift and pulse transients independent of the phase of the exciting pulse.¹⁶

Coal Samples. Measurements were made on two Virginia vitrains; Powellton and Pocahontas No. 4, supplied by H. L. Retcofsky of the Pittsburgh Energy Research Center, ERDA, and on vitrain samples obtained from the Mich, Star, and Lovilia mines in southeastern Iowa. All samples were measured before and after drying for 8 h at 100 °C and a pressure of 10^{-7} Torr. Analysis for major constituents of all samples are given in Table I. Carbon and hydrogen were determined by combustion analyses ASTM D-3178. Nitrogen was determined by ASTM D-3179. Sulfur was determined by ASTM D-3177. The mineral matter content was determined by the method of Bishop and Ward.¹⁷ Oxygen was determined by neutron activation analysis.

Model Compounds. Naphthalene, (α -methyl-naphthalene, m -tolylacetic acid, 4,4'-bismethylbenzophenone, polystyrene), isopolybutadiene, and polyethylene were used as models of prototype aromatic, (mixed aromatic-aliphatic), and aliphatic compounds, respectively. The first four samples in the above list were checked for purity via standard IR and high-resolution NMR, and found to be at least 98% pure. Polyethylene, of density 0.945, was obtained in rod form from Cadillac Chemical Co., Davenport, Iowa. The measured density corresponded to a crystalline fraction of 0.64.

Relaxation Measurements. All relaxation measurements were made on about 50 mg of sample in standard

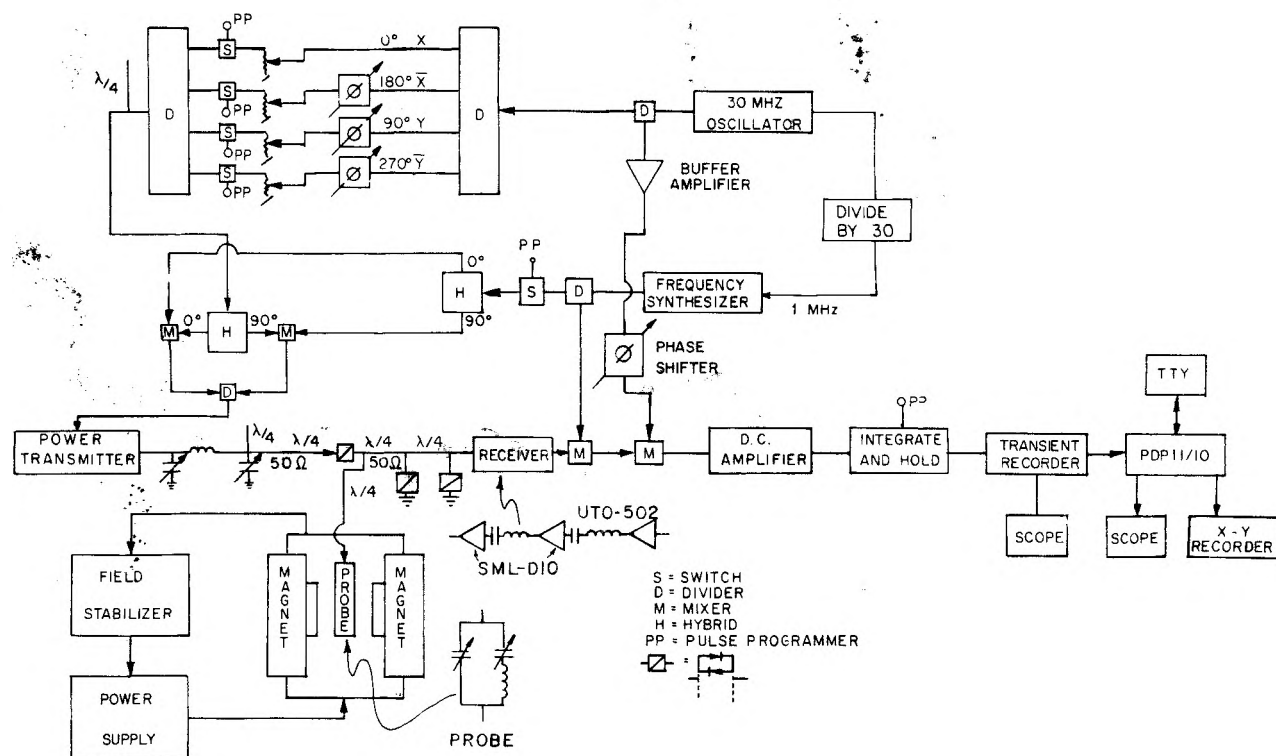


Figure 1. Block diagram of pulse NMR spectrometer used in studying protons in coals and in model compounds.

TABLE I: Major Constituent Analyses of Coals, wt %^d

Sample	C	H	N	S	O ^c
Pocahontas No. 4	90.3(2) ^a	4.43(4)	1.28 ^b	0.85 ^b	4.96(20)
Powellton	85.1(3)	5.36(5)	1.54 ^b	0.79(3)	9.11(38)
Upper Mich	81.0(3)	6.14(6)	0.98(11)	5.53 ^b	15.7(63)
Lower Mich	81.55(18)	6.58(16)	1.37	4.16 ^b	
Star	77.0(1)	6.04(4)	1.17(14)	5.02 ^b	7.11(29)
Lovilia	75.0(1)	5.80(4)	1.36(9)	2.64	13.6(54)

^a Numbers in parentheses are root mean square deviations. ^b Only one determination made. ^c Oxygen analyses performed utilizing neutron activation so oxygen in mineral portion is included. The Upper Mich contained the largest fraction of mineral matter (13.45%) of all coals studied. ^d Moisture, ash free.

5-mm o.d. NMR tubes. Spin-lattice relaxation times, T_1 , were determined utilizing a $(\pi, \tau, \pi/2)$ sequence. Two seconds between pulse sequences was greater than four T_1 for all coal samples. Damping constants under a single pulse excitation were determined utilizing a total scan of 400 μ s. The magnitude of T_2^* for all coals was such that, for the transmitter power available, the CPMG sequence was of no utility for determining damping constants from which to infer magnitudes of spin-other spin interactions.

Multiple-Pulse NMR. The Rhim-Ellman-Vaughan eight (REV-8) pulse cycle⁷ was used to remove homonuclear proton-proton dipolar interactions. The phase altered⁴ REV-8 sequence was used to remove homonuclear dipolar interactions, chemical shifts, and chemical shift anisotropy broadening. Phase transients¹⁵ were minimized and symmetrized utilizing a π circuit at the output of the transmitter (see Figure 1) to match the transmitter to the probe at the field determined by the deuterium lock. The probe was tuned utilizing a Hewlett-Packard Model 4815 A vector impedance meter (VIM). Fine tuning of the probe utilized a VIM frequency obtained by beating the frequency of the VIM against the frequency of the single sideband output, with the spectrometer tuned for protons at resonance, at the field determined by the deuterium lock. This VIM frequency, set to obtain zero beats in the above experiment, was then used in tuning the probe. With probes tuned in this manner, phase transient impurities of less than 100 Hz were routinely obtained.

Typical chemical shift scaling factors were determined to be in the range 1.8–1.9, compared to the theoretical value⁷ of $3/\sqrt{2}$. The ability of the instrument to remove homonuclear dipolar interactions was determined utilizing the REV-8 cycle on ¹⁹F with the external field along the (111) direction of a cylindrical single crystal CaF₂. A line width of 34 Hz was obtained in such measurements. Tuning for REV-8 pulse measurements on protons in coals was accomplished using a spherical water sample. Damping of switching transients utilizing narrow banding elements, as previously described, led to cycle times as short as 21 μ s. Typical $\pi/2$ pulse widths were 1.25 μ s.

Results and Discussion

ESR Measurements. g values, line widths, and free radical concentrations of all coal samples are listed in Table II. All samples exhibited Lorentzian line shapes with the exception of Star and Pocahontas. The heated Pocahontas sample exhibited a narrow line superimposed upon the same line observed in the other coals. One explanation for this effect is the presence of a small amount of fusain contained within the predominantly vitrain sample. Heating and pumping would remove the broadening effect of the oxygen in the sample, and allow for observation of the characteristically sharper line in the fusain. The g values of the Virginia vitrains agree to within experimental error with those found by Retcofsky et al.¹⁸ The free radical concentrations are higher by a factor of 3 for the

TABLE II: Results of ESR Measurements on Coals

Sample	<i>g</i> value ^a	Line width, G	Free-radical concn, spins g ⁻¹ × 10 ⁻¹⁹
Pocahontas No. 4	u		4.0
	h	2.0025	6.8(2)
Powellton	u		9.5
	h	2.0025	3.0
Upper Mich	u		3.4
	h	2.0025(2)	1.8
Star	u		1.8
	h	2.0025(2)	1.6
Lovilia	u		2.4
	h	2.0025(2)	1.0
	h		8.4(2)
	h		1.3

^a u = unheated, h = heated at 100 °C and pumped at 10⁻⁷ Torr for 8 h.

heated Powellton, and a factor of 2 for the heated Pocahontas No. 4.

Relaxation Measurements. The results of proton NMR relaxation measurements on the coal samples are given in Table III, as are the second moments of the absorption spectra obtained from the Fourier transformed free induction decays. Where more than one damping constant characteristic of a particular pulse sequence was observed, the fraction of the species characterized by that damping constant is given. These values were obtained from an appropriate extrapolation of the decays to zero time, taken to be the center of the preparation pulse.¹⁹ Values in parentheses are root mean square deviations obtained from a least-squares fit of the log of the amplitude of the envelope of the signal vs. time.

Spin-Lattice Damping Constants. The spin-lattice relaxation times surprisingly decreased with decreasing free radical concentration. One Virginia vitrain, Powellton, and one Iowa vitrain, Upper Mich, exhibited two spin-lattice damping constants when unheated. When heated at 100 °C and pumped at 10⁻⁷ Torr for 8 h, all spin-lattice damping constants increased, and the multiple damping constants disappeared for the Powellton and the Upper Mich samples. Increase of spin-lattice damping times upon pumping and heating is an expected effect of the removal of paramagnetic oxygen from the samples. It could also be associated with removal of volatile free radical containing molecules. Free radical content as inferred from

ESR indicates that the heated samples contain more free radicals than do the unheated, however. The damping constants of 42 ms for the Upper Mich, 32 ms for the Lovilia, and 19 ms for the Star samples are particularly interesting. If an important mechanism for spin-lattice relaxation is interaction with the magnetism of the antiferromagnetic pyrites in the samples, then spin-lattice damping constants of the Iowa coals compared to the Virginia coals is in accord with the higher sulfur content of the Iowa coals. However, for the Iowa coals, the shorter *T*₁'s are associated with lower sulfur contents. Since there is at present no way of distinguishing between pyrite sulfur and organic sulfur in coals, and since, in fact, standard methods of analysis may well be missing portions of the pyrite sulfur in the form of 10-μm diameter polyhedra,²⁰ the sulfur contents reported in Table I may not accurately reflect pyritic magnetic centers available for spin-lattice relaxation. The results may indicate the possibility of utilizing spin-lattice relaxation to fingerprint inorganic sulfur in coals.

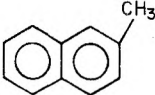
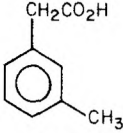
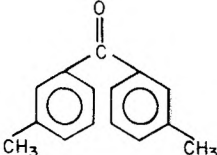
Spin-Spin Damping Constants. Free Precession Following a Single Pulse Excitation. Under the FID response to a single pulse experiment, all of the coals exhibit an effective spin-spin damping constant of the order of 10 μs with the species exhibiting this value of *T*₂* being the major contributor in all samples. In addition, all unheated Iowa vitrains exhibit a second *T*₂* of roughly 100 μs, the fraction contributing to relaxation being roughly 5%. Upon heating, only the Upper Mich sample maintains two damping constants, again of order 10 and 100 μs. As noted in the Introduction, the rigid lattice value for a spin-spin damping constant for an aromatic molecule such as naphthalene is roughly 10 μs. The rigid lattice value for a long chain hydrocarbon might be expected to be shorter by roughly a factor of 2. On the other hand, in an amorphous material such as coal, one might expect appreciable motional narrowing, and the existence of two damping constants as observed above gives rise to the possibility that these values might be a fingerprint of aromatic and aliphatic protons in coals. Results of *T*₂* measurements on selected model aromatic, aliphatic, and mixed compounds (vide infra) indicate that this is not the case, that the shorter damping constant characterizes both aliphatic and aromatic protons in rather rigidly held structures, and that the longer damping constants may be associated with relatively small, mobile molecules which

TABLE III: Results of Proton NMR Relaxation Measurements on Vitrain Coals^a

Coal		<i>T</i> ₁ , ms	<i>T</i> ₂ under FID, μs	10 ⁻⁹ <i>M</i> ₂ , Hz ²	% C ^b	2 δ <i>f</i> , REV-8	2δ <i>f</i> , φ Pull
Pocahontas No. 4	u	116(5), 100%	9.5(1), 100%				
	h	425(10), 100%	10.6(3), 100%				
Powellton	u	214(20), 91(2)% 237(20), 8.7(3)%	10(1), 100%	4.34	90.3	1058	540
	h	412(13), 100%	17(1), 100%		85.1	730(20)	
Upper Mich	u	42(4), 23(1)% 119(4), 77(1)%	9.2(8), 92(15)% 120(10), 7.8(1)%	3.33	81.0	753(30)	480
	h	139(3), 100%	10(1), 96(11)% 61(4), 4.0(2)%			542	310
Star	u	19.2(4), 100%	92(21), 5(2)% 8(1), 95(33)%		78	675(50)	
	h	99(3), 100%	6.0(5), 100%				
Lovilia	u	32(1), 100%	102(1), 7.0(5)% 6.6(4), 93(17)%	2.92	75	700(50)	360
	h	115(7), 100%	7.7(1), 100%			650(30)	
				2.63		753(30)	500

^a u = unheated, h = heated. ^b Moisture, ash free.

TABLE IV: Results of NMR Measurements on Model Compounds

Model compd					$[-\text{CH}-\text{CH}_2-]_n$ C_6H_5	$[-\text{CH}_2-]_n$	Isopolybutadiene
T_2^* FID, μs	13	~13	17	20	19	12	300
$(2\Delta f \approx 1/\pi T_2)$	(24 kHz)		241			48	(1400 Hz)
T_2^* CPMG, μs	94		360			44.1	
T_2^* , μs	13.9		2593			433	
rigid lattice limit						3	3
$2\Delta f$, Hz	262		338		276	129	30
REV-8							
$t_c = 25 \mu\text{s}$							
$2\Delta f$, Hz	271		250		261	~100	5
phase pull							

are removed, at least for the Lovilia and Star samples, upon pumping at 100 °C. The second moments obtained from the FID response to a single pulse excitation would be expected to decrease with increasing carbon content if the only contribution to broadening is interproton dipolar interaction. This is just a reflection of the idea that the average interproton distance increases with increasing carbon content. The observed second moments, however, increase with carbon content, as shown in Table III, and in Figure 2. One possible explanation for the increase in second moment with decreasing proton content is the fact that the free radical concentration increases with decreasing proton content, and that the increase in second moment is associated with free radical-proton dipolar broadening. Normalization of second moment to unit free radical content leads to the "expected" trend, shown as the lower curve in Figure 2. Results of multiple pulse decoupling experiments on both coals and model compounds (*vide infra*), however, prove that the maximum line width contributed to the proton NMR spectra by the free radicals is about 700 Hz. Second moments associated with this broadening are only of order of 10^7 Hz^2 , compared to the observed total value of 10^9 Hz^2 . Free radical-proton interactions therefore cannot account for the observed trend in proton NMR second moments under a single pulse excitation experiment. The observed increase in second moments with decreasing proton content appears to be real, and not an artifact associated with impurities. One possible explanation for this observed trend is that upon aging, i.e., increase in carbon content, protons move from relatively mobile aliphatic structures to more rigid aromatic structures, with line widths characteristic of the proton line width in naphthalene, and that this enhanced rigidity more than compensates for increase in average interproton distance.

Multiple Pulse NMR Measurements. Two sequences were used in this study. The first was the REV-8, which removes homonuclear dipolar broadening to second order.⁷ The second was the phase altered version of this sequence,⁴ in which a preparation pulse is lacking, offset is due only to the zeroth order Hamiltonian $\mathcal{H}_p^{(0)} = (2/t_c)(\phi_x - \phi_x) I_y$ associated with phase errors ϕ_x and ϕ_x in the x and \bar{x} pulses and both chemical shift anisotropy and homonuclear dipolar broadening are removed to first order. In addition, the operator I_z is scaled by a factor of $\sqrt{2}/3$, i.e., chemical shifts and spin-other spin interactions are scaled by roughly a factor of 1/2. The results of these two sequences on the coals are given in the last two columns of Table III,

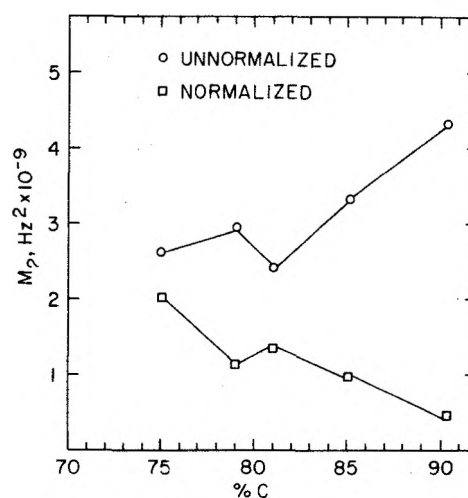


Figure 2. Second moments obtained from FID response to single pulse experiment. Results normalized to unit free radical concentration show "expected" decrease with increasing carbon content, but the "expected" results is incorrect (see text).

and a typical spectrum of a coal under REV-8 is shown in Figure 3. The two Virginia vitrains, with higher carbon and free radical content, are narrowed from 30 kHz to about 1 kHz under the REV-8. The lower carbon content, lower free radical content Iowa vitrains are narrowed from 30 kHz to about 700 Hz. All heated vitrains are further narrowed by 300 to 500 Hz upon application of the phase altered sequence. From these results, and the results on the model compounds (*vide infra*), we infer that an upper limit to the free radical-proton broadening is about 400 Hz for the samples studied and that residual line widths under the phase altered sequence are associated with quadrupole broadening of protons by, e.g., ^{33}S , and by ^{14}N , and with instrumental broadening associated with failure to remove second-order dipolar terms. The line shape under REV-8 is Lorentzian with no structure indicative of separation between aliphatic and aromatic protons.

Model Compounds. To aid in an interpretation of the results of pulse and multiple pulse experiments on the coals, similar measurements were made on model aliphatic, aromatic, and mixed aromatic-aliphatic compounds. These results are presented in Table IV. We note that typical aromatics exhibit one spin-spin damping constant, of order $10 \mu\text{s}$ under a single pulse excitation. This is as expected for these compounds in the rigid lattice limit. In addition, mixed aliphatic-aromatics such as 4,4'-bis-

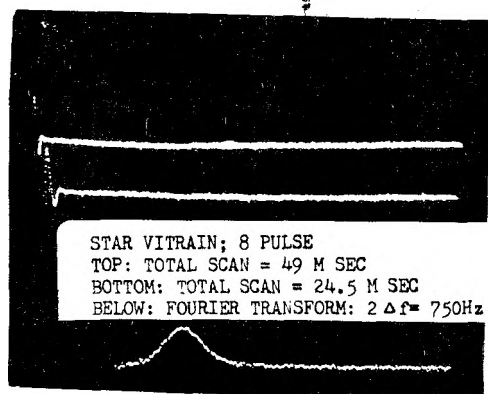


Figure 3. Typical response of coal under REV-8 sequence: top, decay; bottom, spectrum obtained from Fourier transform of decay.

methylbenzophenone, α -methyl-naphthalene, and polystyrene also exhibit only one spin-spin damping constant, of about the same value. Rotation of the methyl groups and rocking of methylene bridges are not sufficient for narrowing beyond 30 kHz. Polyethylene exhibits two distinct damping constants of 12 and 48 μ s associated with the rigid, crystalline fraction of the sample, and the relatively loose, amorphous portion, respectively, indicating that aliphatics alone in polymeric type form can give rise to at least two spin-spin damping constants. *m*-Tolylacetic acid does exhibit two damping constants, of magnitude 17 and 241 μ s, with relative fractions contributing to each in the ratio of 6/4. It is tempting to associate the longer damping constant with the aliphatic protons, but the results on the other mixed compounds do not support this association. Line widths of all model compounds with the exception of polyethylene, under REV-8, are roughly 300 Hz. Polyethylene narrows to 129 Hz under REV-8, indicative of a smaller chemical shift anisotropy for the protons in this compound. The limit of narrowing under REV-8 is determined by application of the phase altered sequence, and is typically 200 Hz. Residual line width is due to pulse imperfections and to second-order dipolar effects. The results of multiple pulse measurements on

the model compounds indicate a chemical shift anisotropy of 250 Hz, or 8 ppm including the chemical shift scaling factor, for the aromatic and mixed aliphatic-aromatic compounds. This value supports the contention that the free radical-proton broadening is about 400 Hz for the coals.

Acknowledgment. The magnet and power supply used in this work were donated by Dow Chemical Co. Isopolybutadiene was obtained from Dr. R. W. Vaughan of the Chemical Engineering Department at the California Institute of Technology. Thanks are due to Douglas Adduci for assistance in spectrometer design and construction, and in computer programming. Dr. Jesse Cude assisted in the measurements. Discussions with Drs. C. R. Dybowski and R. W. Vaughan were enormously helpful in interpretation of results.

References and Notes

- (1) A. Abragam, "Nuclear Magnetism", Oxford, 1961, p 112.
- (2) D. W. J. Cruikshank, *Acta Crystallogr.*, **10**, 504 (1957).
- (3) S. Meiboom and D. Gill, *Rev. Sci. Instrum.*, **29**, 688 (1958).
- (4) C. R. Dybowski and R. W. Vaughan, *Macromolecules*, **8**, 50 (1975).
- (5) J. S. Waugh, L. M. Huber, and U. Haeberlen, *Phys. Rev. Lett.*, **20**, 180 (1968).
- (6) P. Mansfield, *J. Phys. Chem., Solid State Phys.*, **4**, 1444 (1971).
- (7) W.-K. Rhim, D. P. Elleman, and R. W. Vaughan, *J. Chem. Phys.*, **58**, 1772 (1973).
- (8) W. R. Ladner and A. E. Stacy, *Fuel*, **40**, 295 (1961).
- (9) J. F. M. Oth and H. Tshamler, *Fuel*, **42**, 467 (1963).
- (10) J. K. Brown, W. R. Ladner, and N. Sheppard, *Fuel*, **39**, 79 (1960).
- (11) R. A. Durie, Y. Shewchuk, and S. Sternhell, *Fuel*, **45**, 99 (1966).
- (12) H. L. Retcofsky and R. A. Friedel, "Spectrometry of Fuels", Plenum Press, New York, N.Y., 1970, p 70.
- (13) H. L. Retcofsky and R. A. Friedel, *Adv. Chem. Ser.*, **No. 55**, 503 (1966).
- (14) J. D. Ellett, Jr., M. G. Gibby, U. Haeberlen, L. M. Huber, M. Mehring, A. Pines, and J. S. Waugh, *Adv. Magn. Reson.*, **5**, 117 (1971).
- (15) R. W. Vaughan, D. D. Elleman, L. M. Stacey, W.-K. Rhim, and J. W. Lee, *Rev. Sci. Instrum.*, **43**, 1356 (1972).
- (16) E. O. Stejskal and J. Schaefer, *J. Magn. Reson.*, **18**, 560 (1975).
- (17) M. Bishop and D. L. Ward, *Fuel (London)*, **37**, 191 (1958).
- (18) H. L. Retcofsky, J. M. Start, and R. A. Friedel, *Anal. Chem.*, **40**, 1699 (1968).
- (19) D. Bernal and I. J. Lowe, *Phys. Rev. Lett.*, **11**, 258 (1963).
- (20) R. Greer, Working Paper No. 4, Iowa Coal Project, available from Document Library, Ames Laboratory-ERDA, Iowa State University, Ames, Iowa 50011.

Electron Spin Resonance Spectra of *tert*-Butyl Substituted Naphthalene Anion Radicals

Ira B. Goldberg*

Science Center, Rockwell International, Thousand Oaks, California 91360

and Barrie M. Peake

Chemistry Department, University of Otago, Dunedin, New Zealand (Received December 2, 1976)

Publication costs assisted by Rockwell International

The hyperfine splittings (hfs) of the ring protons and the g factors of seven *tert*-butylnaphthalene anions were measured. The hfs data were utilized in a multiple linear least-squares analysis in order to determine parameters for use in an additivity model. This gives satisfactory prediction of the ring proton hfs. g factors were also treated by least squares in an additivity model. The hfs additivity parameters were correlated against those determined for methyl substituents and were found to be only in moderate agreement, probably because of different structural changes induced by the substituent groups. The additivity parameters were also correlated against Hückel molecular orbital theory from which the best inductive parameter to represent the effect of the *tert*-butyl group was -0.07 . The g factors were also fit to the Hückel calculation, assuming that the substituent group only changed the energy of the π electron system. This gave a value of $\delta_c = -0.30$. The discrepancy between both values of δ_c probably arises from lower energy excited states which contribute to shifts of the g factor from the free electron value.

Introduction

Alkyl substituted aromatic hydrocarbon radical ions are of considerable interest because they provide chemically simple series of radicals in which the effect of substituent groups can be correlated to molecular orbital calculations. Electron spin resonance (ESR) is readily used to probe the orbital containing the unpaired electron, and provide an accurate map of the spin density distribution which reveals small changes in the electronic structure of the radical.

The additivity model¹ has been used to correlate spin density distributions in radical anions with the effect of substituent groups. This model has been applied to studies of a variety of substituent groups in *p*-benzosemiquinone radicals,¹⁻³ nitrogen heteroatoms and methyl groups in diazine and naphthyridine anions,⁴ vibronic interactions in deuterionaphthalene anions,⁵ and methyl substituted naphthalene anions.⁶ This model has also been applied to a few *tert*-butylacenaphthalene anions.⁷ This additivity model represents a perturbation on one atom of a molecule as having a small effect on every other atom of the rest of the molecule. An example would be the effect of substituting an alkyl group for a proton in an aromatic radical ion. If several substituent groups are then placed around the molecule, then the change of the spin density at any position would be represented by the sum of the perturbations due to each substituent on that position.

The success of this model on deuterionaphthalenes⁵ and on methylnaphthalenes⁶ has led us to investigate the effect of the *tert*-butyl group on naphthalene anions. Although the *tert*-butyl group has a smaller effect than the methyl group toward separating the degenerate orbitals of the benzene anion,⁸ conflicting results have been obtained for benzosemiquinone anions.¹⁻³ For the additivity model to provide a reasonable representation of the effect of substituent groups, several conditions are required: primarily, the perturbation must be sufficiently small so that it can be represented by first-order perturbation theory; i.e., second-order effects can be neglected. It is also required that the effects of the substituents be of similar physical nature such that added strain, geometric changes, solvation changes, or ion association changes do not occur as a result of several substituents placed in different positions. These

conditions are achieved in alkylnaphthalene anions reduced with Na in a good solvating agent. *tert*-Butyl groups, however, cannot be placed on adjacent carbon atoms or in *peri* positions (1,8-disubstituted). Crystal structures of 1,2-di-*tert*-butylbenzenes indicate changes in the bond angles occur to accommodate both groups⁹ while ESR studies of 1,8-di-*tert*-butylnaphthalene anions¹⁰ demonstrate that the 1,8 positions are displaced onto opposite sides of the median plane of the naphthalene nucleus. We have measured the ring proton hyperfine splittings and g factors of seven mono-, di-, and tri-*tert*-butylnaphthalene anions which provides 32 uniquely determined hfs. Four of these naphthalenes are substituted in the identical positions as some of the methylnaphthalenes which have been previously reported.⁶ To our knowledge, this is the only extensive investigation of the effect of *tert*-butyl substituents on aromatic hydrocarbons.

Experimental Section

Materials. 2-*tert*-Butylnaphthalene (2-BN) and 2,7-di-*tert*-butylnaphthalene (2,7-DBN) were obtained from the American Petroleum Institute (Carnegie-Mellon University, Pittsburgh, Pa.). Other naphthalenes were synthesized as described in the literature: 1,4-DBN, ref 11; 2,6-DBN, ref 11; 1,3-DBN, ref 12; 1,3,5-TBN, ref 12; and 1,3,6-TBN, ref 12.

Dimethoxyethane (DME) was obtained from Matheson Coleman and Bell, and was purified first by fractional distillation, retaining the central boiling 50%, then by refluxing over potassium followed by LiAlH_4 , and distillation into LiAlH_4 . The DME was then degassed and distilled under vacuum into a cylinder containing tetracene (Aldrich Chemical Co.) and a sodium mirror. The tetracene was dissolved and allowed to react to the dinegative ion for storage. Naphthalenide samples were prepared by reduction on a sodium mirror in DME. These samples were stable at room temperature for 3-6 months. Following this time the anion could be regenerated by again exposing the solution to the metallic sodium.

ESR Spectra. ESR spectra were recorded on a computer-controlled spectrometer which has been previously

TABLE I: Proton Hyperfine Splittings for *tert*-Butylnaphthalene Anions^a and Comparison with Values for Methyl Substituted Naphthalene Anion^b

Substituted position	Ring proton	Hyperfine splittings			$\Delta a_H/a_H^c$	
		Methyl subst	<i>tert</i> -Butyl subst	<i>tert</i> -Butyl ^d calcd	Methyl subst	<i>tert</i> -Butyl subst
2	1	-4.584	-4.632	-4.692	-0.072	-0.062
	4	-5.054	-5.013	-4.923	0.023	0.015
	5	-5.054	-5.212	-5.121	0.023	0.055
	8	-4.759	-4.731	-4.842	-0.037	-0.042
	3	-2.313	-2.035	-2.200	0.267	0.115
	6	-1.322	-1.631	-1.590	-0.271	-0.106
	7	-2.256	-2.035	-1.909	0.236	0.115
1,4	5,8	-5.393	-5.124	-5.146	0.092	0.037
	2,3	-1.671	-1.769	-1.624	-0.084	-0.031
	6,7	-1.832	-1.769	-1.840	0.004	-0.031
2,6	1,5	-4.65	-4.846	-4.891	-0.059	-0.019
	4,8	-4.82	-4.846	-4.843	-0.020	-0.019
	3,7	-2.77	-2.200	-2.237	0.518	0.205
2,7	1,8	-4.36	-4.677	-4.611	-0.117	-0.053
	4,5	-5.21	-5.050	-5.122	0.054	0.022
	3,6	-1.83	-1.817	-1.918	0.002	-0.004
1,3	5		-5.18	-5.185		0.048
	8		-5.06	-5.002		0.024
	4		-4.463	-4.465		-0.097
	2		-1.957	-2.022		0.072
	6		-1.957	-1.823		0.072
1,3,5	7		-1.637	-1.645		-0.103
	2		-2.100	-1.940		0.151
	4		-4.432	-4.347		-0.121
	6		-1.426	-1.650		-0.219
	7		-1.426	-1.571		-0.219
1,3,6	8		-4.764	-4.776		-0.036
	2		-1.734	-1.745		-0.039
	4		-4.406	-4.386		-0.112
	5		-4.984	-4.956		0.003
	7		-2.196	-1.973		0.084
	8		-4.984	-5.004		0.013

^a Reduced with sodium or potassium. Temperature at which spectrum is taken is -60°C . ^b Hyperfine splittings for methyl substituted naphthalenes taken from ref 6. ^c $\Delta a_H/a_H = -[a_H(\text{substituted naphthalene}) - a_H(\text{naphthalene})]/a_H(\text{naphthalene})$ values of naphthalene splittings taken as 4.940 for the 1, 4, 5, and 8 positions and 1.825 for the 2, 3, 6, and 7 positions from ref 6. ^d Calculated from additivity parameters.

described.¹³ The spectrometer was modified from a V-4502 system and utilizes a 15-in. magnet. Hyperfine splittings (hfs) were determined using a perylene anion reference.¹⁴ *g* factors were also measured against the perylene anion¹⁵⁻¹⁸ (apparent *g* factor, 2.002657). Analysis of the hfs was done using the line centers in a multivariable linear least-squares analysis. Standard deviations of the hfs were 0.0025 G or smaller. At least eight separate experiments were done to determine the *g* factor. A region of between +2 and -2 G of the center of the spectra of the substituted naphthalene and perylene anions was scanned, and signals from both the sample and reference channels were recorded. The center of the naphthalene and perylene spectra were then determined by weighting resolved lines which fell within this region. Initial experiments were done utilizing a dual-channel recorder. More recently the on-line computer was used for these measurements. No difference in standard deviations was observed, however, the measurements are more easily carried out utilizing the computer facility. *g* factors were corrected for second-order shifts.

Results and Discussion

Experimental Data. Proton hfs observed for the substituted naphthalene anions are given in Table I. Assignments for 2-BN⁻, 1,4-DBN⁻, 2,6-DBN⁻, and 2,7-DBN⁻ were based on the assignments of the corresponding methylnaphthalenes,⁶ which also agreed with assignments

based on Hückel molecular orbital (HMO) theory. Assignments for 1,3-DBN⁻, 1,3,5-TBN⁻, and 1,3,6-TBN⁻ were based on HMO calculations with one exception. In 1,3-DBN, the two largest hfs of 4.92 and 5.07 G are predicted for the 5 and 8 positions, respectively. The experimental values of 5.06 and 5.18 G were initially assigned to these positions. Better correlation was obtained when the 5.18- and 5.06-G splittings were assigned to the 5 and 8 positions, respectively, rather than in the other order. Because these hfs are very close in magnitude, the calculations are only nominally affected by this change.

No 1,8- or 2,3-disubstituted compounds were included in this study since there is a possibility that strain would influence the proton hfs. Because the γ proton hfs of the *tert*-butyl group are sufficiently small that they are not completely resolved, it is simple to interpret spectra of asymmetric naphthalene derivatives, as noted for substituted acenaphthalenes.⁷

In most cases, the perturbation by the *tert*-butyl group is smaller than the perturbation by a methyl group substituted in the same positions. This is reflected in the values of $\Delta a_H/a_H$ in Table I. Exceptions to this occur at the 5 and 8 positions of 2-BN⁻ and the 1 and 4 positions of 1,4-DBN⁻.

g factors of the naphthalene compounds are given in Table II. The value obtained in this laboratory for the naphthalene anion is in good agreement with other reported values of the naphthalene anion under the same

TABLE II: g Factors of *tert*-Butyl Substituted Naphthalene Anions at -60°C Reduced with Sodium in Dimethoxyethane

Compound	Value ^{a,b}	$(g - g_e) \times 10^3$	Error $\times 10^3$
Unsubstituted	2.002 736	0.416	0.003
2	2.002 739	0.420	0.008
1,3	2.002 761	0.442	0.006
1,4	2.002 756	0.440	0.004
2,6	2.002 756	0.442	0.006
2,7	2.002 749	0.437	0.004
1,3,5	2.002 764	0.445	0.004
1,3,6	2.002 757	0.438	0.005

^a g factors are corrected for second-order shifts.¹⁵

^b Values relative to g factor of perylene^{•-} (ref 15) with correction (ref 16).

conditions.^{15-17,19,20} No g factors of *tert*-butyl or other alkyl substituted naphthalenes have been reported in the literature to our knowledge.

Ring Proton Splittings. The α -ring proton splittings of substituted naphthalene anions were assumed to be determined by the additivity of perturbations caused by substituents on the molecule. For example, a *tert*-butyl group at the 1 position causes perturbations to the ring proton hfs at positions 2 through 8, represented by $\Delta_{1,2}, \Delta_{1,3}, \dots, \Delta_{1,8}$. Similarly, a substituent at the 2 position causes perturbations to the ring proton hfs at positions 1 and 3 through 8 represented by $\Delta_{2,1}, \Delta_{2,3}, \dots, \Delta_{2,8}$. This notation is different than that used by Moss et al.,⁶ and is compared in Table III for convenience. The hfs of the unsubstituted anion would then be given by $a_s^H(0)$.

In order to compute the hfs of position s in the substituted anion from the parameters $\Delta_{r,s}$, the molecule is rotated or reflected through a plane in one of the symmetry axes of the naphthalene nucleus, such that each substituent group is ultimately in the 1 or 2 position (denoted r'). The perturbations acting on position s' , which is the transformed position of s , are summed. Thus the hfs of position s in the substituted anion is given by

$$a_s^H = a_s^H(0) + \sum_{r \neq s} \Delta_{r',s'} n_{s'} \quad (1)$$

where $n_{s'}$ can be either 0 or 1 depending upon whether the substituent group is absent or present. For example, in 1,3-DBN^{•-}, the β -ring proton splitting of position 2 is given by

$$a_2^H = a_2^H(0) + \Delta_{1,2} + \Delta_{2,3}$$

For the 1,3,5-TBN^{•-}, the α -ring proton splitting at the 4 position is given by

$$a_4^H = a_1^H(0) + \Delta_{1,4} + \Delta_{2,1} + \Delta_{1,8}$$

where the $\Delta_{r,s}$ terms arise from the perturbations by *tert*-butyl groups at the 1, 3, and 5 positions, respectively. In this way, the data in Table I can be separated into 17 splittings attributed to the α -ring protons (1, 4, 5, and 8 positions) and 15 splittings attributed to the β -ring protons (2, 3, 6, and 7 positions). The α -ring proton hfs were then assigned to a linear series of equations such as eq 1, in which the parameters $\Delta_{1,4}, \Delta_{1,5}, \Delta_{1,8}, \Delta_{2,1}, \Delta_{2,4}, \Delta_{2,5},$ and $\Delta_{2,8}$ can be determined while the β -ring proton hfs were similarly assigned such that $\Delta_{1,2}, \Delta_{1,3}, \Delta_{1,6}, \Delta_{1,7}, \Delta_{2,3}, \Delta_{2,6},$ and $\Delta_{2,7}$ can be determined. These equations were then utilized in a multiple linear least-squares analysis²¹ where the intercepts $a_1^H(0)$ and $a_2^H(0)$ were also treated as unknown parameters. Table III shows the result of this analysis as well as a comparison with results obtained from similar analysis of methyl group perturbations.⁶ In general, the parameters are smaller for the *tert*-butyl substituted compounds than for the methyl substituted compounds. The α - and β -proton hfs extrapolated to an unsubstituted compound are -4.921 ± 0.074 and -1.87 ± 0.11 G, respectively, in good agreement with the experimental values of -4.940 and -1.825 G.⁶

We consider the small standard deviations observed for values of $\Delta_{r,s}$ determined from α -ring proton hfs to be fortuitous, and are probably dependent upon the sample population. More realistic uncertainties are obtained for those values obtained from the β -ring proton hfs.

Correlation with HMO Theory. The proton hfs in an aromatic system are directly proportional to the spin density ρ_s^* on the adjacent trigonal carbon atom, according to the McConnell equation

$$a_s^H = Q_{\text{CH}}^H \rho_s^* \pi \quad (2)$$

where Q_{CH}^H is the proportionality constant and is typically in the order of -24 to -27 G. Using simple HMO theory it is assumed that the spin density, or more correctly the unpaired electron density, is given by the square of the coefficient of atom s in the molecular orbital ν containing the unpaired electron so that

$$a_s^H = Q_{\text{CH}}^H c_{s\nu}^2 \quad (3)$$

The agreement between values of $c_{s\nu}^2$ (0.1809 and 0.0691 for the α and β positions) and the hfs of the naphthalene

TABLE III: Additivity Assignments and Mutual Polarizabilities for Methyl- and *tert*-Butyl Substituted Naphthalene Anions

Parameter ^a	Atoms r,s	π_{rs}^ν	$\Delta_{r,s}(\text{Me})^{2b}$	$\Delta_{r,s}(t\text{-Bu})$
α-Ring Proton Hyperfine Splittings				
$\Delta_{1,4}$ d	1-4	-0.2012	0.522 ± 0.06	0.225 ± 0.003
$\Delta_{1,5}$ e	1-5	0.1342	-0.298 ± 0.06	-0.344 ± 0.004
$\Delta_{1,8}$ h	1-8	0.2033	-0.013 ± 0.06	0.119 ± 0.003
$\Delta_{2,1}$ a'	2-1	-0.2033	0.395 ± 0.05	0.229 ± 0.003
$\Delta_{2,4}$ d'	2-4	0.0467	-0.075 ± 0.05	-0.002 ± 0.003
$\Delta_{2,5}$ e'	2-5	0.0894	-0.115 ± 0.05	-0.002 ± 0.003
$\Delta_{2,8}$ h'	2-8	-0.0224	0.201 ± 0.05	0.080 ± 0.003
$a_1^H(0)$			-4.971 ± 0.05	-4.921 ± 0.074
β-Ring Proton Hyperfine Splittings				
$\Delta_{1,2}$ b	1-2	-0.2033	0.491 ± 0.04	0.173 ± 0.020
$\Delta_{1,3}$ c	1-3	0.0467	-0.136 ± 0.04	0.074 ± 0.030
$\Delta_{1,6}$ f	1-6	0.0894	0.398 ± 0.04	0.086 ± 0.025
$\Delta_{1,7}$ g	1-7	-0.0224	-0.299 ± 0.04	-0.055 ± 0.025
$\Delta_{2,3}$ c'	2-3	0.2033	-0.386 ± 0.05	-0.328 ± 0.018
$\Delta_{2,6}$ f'	2-6	-0.0894	0.569 ± 0.05	0.281 ± 0.020
$\Delta_{2,7}$ g'	2-7	0.0915	-0.361 ± 0.05	-0.038 ± 0.024
$a_2^H(0)$			-1.934 ± 0.05	-1.87 ± 0.11

^a Notation $\Delta_{r,s}$ used here, alphabetic used in ref 6. ^b Data from ref 6.

TABLE IV: Values of the Inductive Parameter, δ_c , Determined from Additivity Parameters

	Methyl	<i>tert</i> -Butyl
14 additivity points	-0.14 ± 0.04^a	-0.073 ± 0.021
13 additivity points ($\Delta_{1,8}$ eliminated)		-0.092 ± 0.019
<i>g</i> factor	-0.50^b	-0.30 ± 0.08
Alkyl group splittings	-0.31 ± 0.01^a	Not obsd

^a Based on data in ref 6. ^b Based only on *g* factors for 1,5- and 2,6-dimethylnaphthalene anion.

anion is fortuitous. If $Q_{CH}^H = -27.06$ G, the calculated values of the α - and β -ring proton hfs are -4.895 and -1.870 G, respectively. This agrees with the respective experimental values of -4.940 and -1.825 G.⁶

The effect of a substituent group may often be represented by adding an inductive parameter to the Coulomb integral, eq 4,²² in the HMO secular determinant. Here,

$$\alpha_r = \alpha^0 + \delta_c \beta_{cc}^0 \quad (4)$$

α_r represents the Coulomb integral of the trigonal carbon atom *r* adjacent to the substituent group, α^0 is the Coulomb integral of the unsubstituted atom, taken as a reference point, and δ_c is the inductive parameter in units of the resonance integral for an aromatic C-C π bond, β_{cc}^0 (about 2.5 eV). The change in the value of c_{sv}^2 due to an inductive effect at atom *r* can be computed by first-order perturbation theory and has been treated in a number of papers.^{5,6,23} The result is

$$c_{sv}^2 = c_{sv}^0{}^2 + \frac{1}{2} \delta_c \sum_{r, \mu \neq v} \frac{4c_{rv}c_{r\mu}c_{s\mu}c_{sv}}{\epsilon_\mu - \epsilon_v} \quad (5)$$

where the summation is over all molecular orbitals, μ , except the one containing the unpaired electron, ν . The energies ϵ are given in units of β_{cc}^0 . For convenience, the inner summation is defined as the atom-atom polarizability of atomic orbital ν , $\pi_{r,s}^\nu$, so that

$$c_{sv}^2 = c_{sv}^0{}^2 + \frac{1}{2} \delta_c \sum_r \pi_{r,s}^\nu \quad (6)$$

Substitution of eq 6 into eq 2 gives the result

$$a_s^H = a_s^H(0) + \frac{1}{2} Q_{CH}^H \delta_c \sum_r \pi_{r,s}^\nu \quad (7)$$

This equation has the same form as the additivity equation, eq 1, where

$$\Delta_{r,s} \equiv \frac{1}{2} Q_{CH}^H \delta_c \pi_{r,s}^\nu \quad (8)$$

A plot of $\Delta_{r,s}$ determined from the experimental data against $\pi_{r,s}^\nu$ calculated from the Huckel molecular orbital is shown in Figure 1. The data of Moss et al.⁶ are used in the values for methyl substitution. The lines drawn were determined from least-squares analysis in which all data are uniformly weighted. The slope of the line determined for the methyl group is approximately two times that of the line determined for the *tert*-butyl group. If the intercept is ignored, the slope of the lines may be utilized to determine the best value of δ_c to be used in the inductive model for either group. The "y intercepts" in both cases were reasonably small, and the results are not significantly altered if the least-squares line is constrained to pass through the origin. Results of δ_c determined for both groups are given in Table IV. The value of δ_c for the methyl group was -0.14 as determined by Moss⁶ using a regression of each of the hfs as a function of $\sum \pi_{r,s}^\nu$. The value for the *tert*-butyl group determined here is -0.07 .

The broken line in Figure 1 is the least-squares fit determined without the parameter $\Delta_{1,8}$. This value may

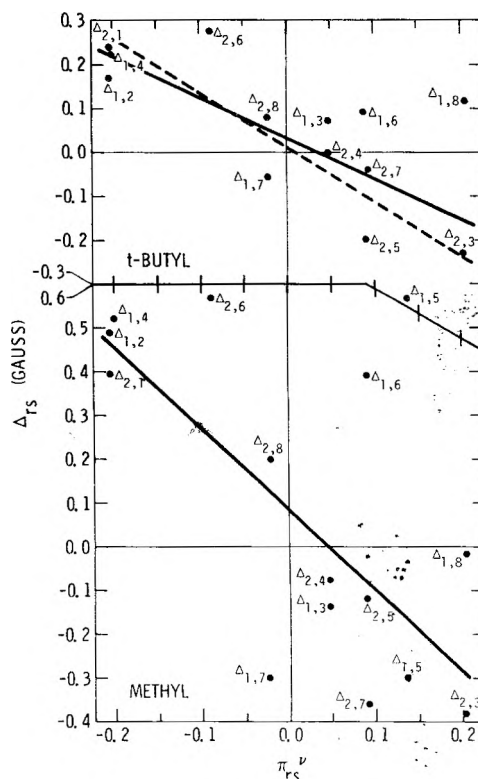


Figure 1. Values of $\Delta_{r,s}$ parameters of the additivity model in the methyl and butyl substituted naphthalene anions plotted against the mutual atom polarizability $\pi_{r,s}^\nu$ calculated from Huckel molecular orbital theory. The broken line is the line determined without $\Delta_{1,8}$. Data for the methyl substituted anions are taken from ref 6.

be considered suspect since steric interactions may cause nonplanarity in the $(C_2)C-H$ fragment, as discussed in the next section. The value of δ_c determined in this manner is -0.09 , within the uncertainty of δ_c determined using all the $\Delta_{r,s}$ parameters.

As shown in Figure 1, the correlation between $\Delta_{r,s}$ and $\pi_{r,s}^\nu$ is not particularly good. This is no reflection on the validity of the additivity model. Rather, it suggests that the HMO model does not accurately predict changes in the spin distribution of the radical due to alkyl group substitution, although a well-defined trend is observed. This may be due in part to the initial assignment of ring proton splittings. More likely, the inductive-HMO model is inadequate because it does not permit additional conjugation to be considered, nor does it take into account changes due to structure or vibronic interactions. One observation on these anions is that there is a tendency toward degeneracy of the hfs beyond that required by symmetry. This is observed in all of the anions except 2,7-DBN \cdot and 1,3,6-TBN \cdot for at least one pair of ring proton hfs. We question whether this reflects a structural change which achieves a lower energy configuration, or is merely coincidental.

Correlation of Methyl and *tert*-Butyl Additivity Parameters. The data given in Table IV as well as Figures 1 and 2 show that the values of $\Delta_{r,s}$ for the methyl group are typically larger than those of the *tert*-butyl group, and are somewhat correlated. Figure 2 shows a plot of $\Delta_{r,s}$ for the methyl group plotted against $\Delta_{r,s}$ for the *tert*-butyl group. The line drawn represents the least-squares line in which the values on the ordinate and abscissa are assigned equal uncertainty. The slope of this line is 0.56. There are no outstanding deviations from this line. Thus one can infer that there is no abnormally large perturbation on the planarity of the proton at the 8 position due to the *tert*-butyl group at the 1 position, as reflected in the value

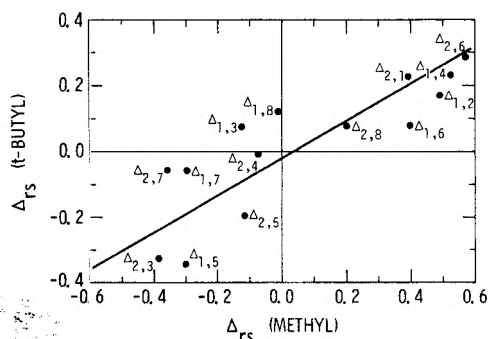


Figure 2. Values of Δ_{rs} for the *tert*-butyl substituted naphthalene anions plotted against values of Δ_{rs} for the methyl substituted anions. Data for methyl substituted anions are taken from ref 6.

of $\Delta_{1,8}$. If one arbitrarily assumes that this deviation from the best line is due to a small nonplanarity, then the angle of deviation of the proton from the naphthalene plane, θ , can be calculated from²⁴

$$a_s^H = \left[Q_{CH^H} + A \cos^2 \left(\frac{\pi}{2} - \phi \right) \right] \rho_s \pi \quad (9)$$

where A has the value of about 100 G.²⁵ Using the value of 0.181 for $\rho_s \pi = c_{8,6}^2$, θ is about $5 \pm 3^\circ$. It is doubtful, however, that this is significant.

Many points in Figure 2 deviate from the line by an amount slightly greater than the experimental error. These discrepancies cannot easily be assigned to specific steric interactions arising from the *tert*-butyl group. It is therefore difficult to say whether they arise from various distortions of the aromatic system due to alterations in bond lengths or bond angles or by vibronic interactions caused by the insertion of a substituent group. Since neither group correlates particularly well with HMO theory, this cannot be utilized as a reference point for any assignment as to which group exerts a greater distortion. These data do suggest that the perturbations exhibited by either substituent group are not entirely proportional to each other.

g Factors. Provided that the alkyl group contributes very little to the coupling of the unpaired electron with excited states which give rise to deviations of the *g* factor from the free electron value, g_e , then according to the theory of Stone,²⁶ the *g* factor deviation, $g - g_e$ is

$$g - g_e = A + B\epsilon_v \quad (10)$$

where A and B are empirical parameters. Several determinations of A and B have been reported.^{15-17,27} A quadratic form for $g - g_e$ has also been reported.²⁸ Utilizing the linear form, the weighted average of the value of B is 18.9×10^{-5} .

The change in the value of ϵ_v due to substituents can also be calculated from first-order perturbation theory based on Hückel molecular orbitals, and is

$$\epsilon_v = \epsilon_v^0 + \delta_c \sum_r c_{rv}^2 \quad (11)$$

where the summation is over all substituted positions, and c_{rv} is the molecular orbital coefficient of the unsubstituted anion. The change of *g* between a substituted naphthalene and the unsubstituted anion, Δg , is then

$$\Delta g = B \delta_c \sum_r c_{rv}^2 \quad (12)$$

The contributions due to Δg were separated into contributions due to substituted α and β positions, and a multiple linear least-squares analysis was carried out. The

ratio of the contributions of the α to β substituents was 1.7 as compared to with the ratio of squares of the coefficients which is 2.6. These are in moderate agreement considering the small values of Δg . A simple linear least-squares treating $B\delta_c$ as an unknown coefficient in eq 12 yields a value of $\delta_c = -0.30$, larger than the value assigned to account for the ring proton hfs.

Since no *g* factors of methyl substituted naphthalene anions have been reported, preliminary values of the *g* factors of 1,5-dimethyl- and 2,6-dimethylnaphthalene anions were determined in order to compare with δ_c for the ring proton hfs. The *g* factors were 2.002749 and 2.002746, respectively. These yield a value of δ_c of -0.50 , also larger than the value of -0.14 determined from ring proton hfs.

Apparently, the alkyl substituent provides low energy excited states for delocalization of the unpaired electron in addition to changing the energy of the orbital containing the unpaired electron. This is not surprising since the alkyl groups provide orbitals from which bonding and antibonding orbitals can be constructed. This will create additional terms in the summation of group contributions to the *g* factor, beyond those provided by the CH fragment. This will be treated elsewhere.

Conclusions

Measurements of the ring proton hfs and *g* factors of seven *tert*-butyl substituted naphthalene anions were reported. These values were used in determination of the additivity parameters which describe substituent effects on ring proton hfs and *g* factors. The value of the inductive parameter determined from Hückel molecular orbital calculations was found to be -0.07 for the *tert*-butyl group as compared to -0.14 for the methyl group.⁶ The agreement between the hfs observed for the anions and the calculated values is very good as shown in Table I. The values obtained for δ_c are probably reasonable to be used in many aromatic radical anions. However, these determinations are based on HMO models, which typically underestimate large spin densities and overestimate small spin densities. Thus the value for Q_{CH^H} used in HMO calculations is larger than typically employed in other calculations such as the McLachlan-HMO model,²⁹ which provides better agreement with observed hfs than does the HMO model, when values of Q_{CH^H} of about -24 to -25 G are used. Thus δ_c in those calculations would need to be increased by about 10%. Unfortunately, the McLachlan-HMO model gives poor agreement with the experimental values of the naphthalene anion, and it was therefore not considered fruitful to utilize this model in this study.

An analysis of the effect of the *tert*-butyl group on the hfs of the tropanyl radical has been reported.³⁰ Using HMO theory they calculate the hfs from weighted contributions due to two wave functions which, degenerate in the unsubstituted radical, are slightly split by the substituents. The best value of δ_c was found to be -0.020 ± 0.005 , much smaller than we obtain here; however, it is in more reasonable agreement than values typically utilized (-0.2 to -0.5) to account for alkyl substituents. The additivity model does not appear valid for the tropanyl system probably because of the nonlinear contributions to the hfs.

In an extensive series of HMO calculations, the value of δ_c for *tert*-butylnaphthalene anions was found to be of the order of -0.05 ,³¹ using preliminary data collected for this work.

Values of *g* factors of the alkylnaphthalenes were also utilized to calculate δ_c for the methyl and *tert*-butyl groups.

Because of the relatively small changes of the g factors, there is a large uncertainty in those values; however, they are -0.5 and -0.30 , respectively, considerably larger than that calculated from ring proton hfs. This is probably due to additional excited states made available to the unpaired electron and also to a small change in the energy of the molecular orbital containing the unpaired electron.

In addition to the inductive model, other models have also been utilized to account for alkyl substituents.^{2,24} We observe no particular advantage to this approach and, in fact, it makes a direct correlation of the data with the theoretical model considerably more difficult due to the larger number of parameters which must be taken into account. Heteroatom and hyperconjugative models break the substituent into a C-X-Y fragment. Usually the resonance integral between C and X is small and of negative energy while the Coulomb integral of X is very large and negative. It can thus be shown that the results of the calculation are typically parallel to the inductive model.

In conclusion, we find that ring proton hfs are accurately represented by an additivity model for the *tert*-butyl substituents. These additivity parameters are correlated with values determined by using the inductive HMO model. Finally, the effects of methyl and *tert*-butyl substitutions are also correlated.

Acknowledgment. This work was supported in part by the Office of Naval Research. The authors thank Dr. Richard W. Franck (Fordham University) for generous samples of 1,3-di-*tert*-butylnaphthalene, 1,3,5-tri-*tert*-butylnaphthalene, and 1,3,6-tri-*tert*-butylnaphthalene. We also appreciate discussions with Dr. Robert Cloney (Fordham University) and Dr. Beatrice Darragh (Marionopolis College).

References and Notes

- (1) B. Venkatraman, B. G. Segal, and G. K. Fraenkel, *J. Chem. Phys.*, **30**, 1006 (1959).
- (2) C. Trapp, C. A. Tyson, and G. Giacometti, *J. Am. Chem. Soc.*, **90**, 1394 (1968); J. A. Pederson, *Mol. Phys.*, **28**, 1031 (1974).
- (3) P. Ashworth, *Mol. Phys.*, **30**, 313 (1975).
- (4) P. Cavallieri d'Oro, R. Danielli, G. Maccaganani, G. F. Pedulli, and P. Palmieri, *Mol. Phys.*, **20**, 365 (1971).
- (5) R. G. Lawler, J. R. Bolton, M. Karplus, and G. K. Fraenkel, *J. Chem. Phys.*, **47**, 2149 (1967).
- (6) R. E. Moss, N. A. Ashford, R. G. Lawler, and G. K. Fraenkel, *J. Chem. Phys.*, **51**, 1765 (1969).
- (7) A. S. Huffadine, B. M. Peake, and L. W. Deady, *J. Chem. Soc., Perkin Trans. 2*, 1263 (1975).
- (8) J. R. Bolton, A. Carrington, A. Forman, and L. E. Orgel, *Mol. Phys.*, **5**, 43 (1962).
- (9) H. C. Stam, *Acta Crystallogr., Sect. B*, **28**, 2715 (1972).
- (10) I. B. Goldberg, H. R. Crowe, and R. W. Franck, *J. Phys. Chem.*, **79**, 1740 (1975).
- (11) H. van Bekkum, Th. J. Nieuwstad, J. van Barneveld, P. Klapwijk, and B. M. Wepster, *Recl. Trav. Chim. Pays-Bas*, **88**, 1028 (1969).
- (12) R. W. Franck and E. G. Leser, *J. Org. Chem.*, **35**, 3932 (1970); *J. Am. Chem. Soc.*, **91**, 1577 (1969).
- (13) I. B. Goldberg, H. R. Crowe, and R. S. Carpenter, II, *J. Magn. Reson.*, **18**, 84 (1975).
- (14) J. R. Bolton, *J. Phys. Chem.*, **71**, 3702 (1967). The perylene anion at room temperature exhibits hfs of 0.4503 ± 0.0012 , 3.0437 ± 0.0013 , and 3.4934 ± 0.0012 G.
- (15) B. G. Segal, M. Kaplan, and G. K. Fraenkel, *J. Chem. Phys.*, **43**, 4191 (1965).
- (16) R. D. Allendoerfer, *J. Chem. Phys.*, **55**, 3615 (1971).
- (17) K. Mobius, *Z. Naturforsch. A*, **20**, 1102 (1965).
- (18) The apparent g factors of perylene according to ref 15 and 16 is 2.002657, while that of ref 17 is 2.002689. The measured apparent g factors of pyrene were 2.002710 and 2.002717, respectively. We have compared the values of pyrene⁻ with perylene⁻, and the difference that we obtained (5.5×10^{-3}) agrees with ref 15 and 16. We have, therefore, used their value for our standard.
- (19) W. G. Williams, R. J. Pritchett, and G. K. Fraenkel, *J. Chem. Phys.*, **52**, 5584 (1970).
- (20) C. L. Dodson and A. H. Reddoch, *J. Chem. Phys.*, **48**, 3226 (1968).
- (21) See, for example, P. R. Bevington, "Data Reduction and Error Analysis for the Physical Sciences", McGraw-Hill, New York, N.Y., 1969, Chapter 9.
- (22) A. Streitwieser, Jr., "Molecular Orbital Theory", Wiley, New York, N.Y., 1962, Chapters 2 and 4.
- (23) C. A. Coulson and H. C. Longuet-Higgins, *Proc. R. Soc. London, Ser. A*, **191**, 39 (1947).
- (24) A. Berndt, *Tetrahedron*, **25**, 37 (1969).
- (25) F. Gerson, K. Mullen, and E. Vogel, *Helv. Chim. Acta*, **54**, 2731 (1971).
- (26) A. J. Stone, *Mol. Phys.*, **6**, 509 (1963); **7**, 311 (1964); *Proc. R. Soc. London, Ser. A*, **271**, 424 (1963).
- (27) M. S. Blois, Jr., H. W. Brown, and J. E. Maling, *Arch. Sci. (Geneva)*, **13**, 243 (1960).
- (28) R. A. Rouse and M. T. Jones, *J. Magn. Reson.*, **19**, 294 (1975).
- (29) A. D. McLachlan, *Mol. Phys.*, **3**, 233 (1960).
- (30) G. Vincow, M. L. Morrell, F. R. Hunter, and H. J. Dauben, Jr., *J. Chem. Phys.*, **48**, 2876 (1968).
- (31) B. Darragh, Thesis, Fordham University, 1972.

Calculation of the Electronic Spectra of Chlorophyll a- and Bacteriochlorophyll a-Water Adducts¹

Lester L. Shipman* and Joseph J. Katz

Chemistry Division, Argonne National Laboratory, Argonne, Illinois 60439 (Received October 4, 1976)

Publication costs assisted by Argonne National Laboratory

Exciton calculations have been carried out for the lower-energy manifold of electronic transitions of (chlorophyll a-H₂O)_n and (bacteriochlorophyll a-H₂O)_n stacks. Most of the oscillator strength of a stack is concentrated in the lowest energy transition. The position of the lowest energy transition ranges from 693 to 721 nm for chlorophyll a hydrate stacks and from 848 to 908 nm for bacteriochlorophyll a hydrate stacks as *n* is varied from 2 to infinity. A comparison of the calculated spectra for chlorophyll a hydrate stacks and bacteriochlorophyll a hydrate stacks with the absorption spectra of in vivo antenna chlorophyll a and bacteriochlorophyll a, respectively, reveals that chlorophyll a hydrate stacks are probably not major components of antenna chlorophyll a in green plants and algae but that bacteriochlorophyll a hydrate stacks may be identified with the more red-shifted components of antenna bacteriochlorophyll a in purple photosynthetic bacteria.

I. Introduction

Chlorophyll a (Chl a; Figure 1) is the primary photo-receptor in green plants and algae and is present in all photosynthetic organisms that evolve molecular oxygen. Because of its importance to photosynthesis, the spectral properties of Chl a have been extensively studied in vitro and in vivo. Most of the in vivo antenna Chl a absorbs in the red in the 662–683-nm range.² Monomer Chl a-L or Chl a-L₂ in vitro has its principal absorption maximum in the red in the 659–671-nm range, the magnitude of the red shift depending upon the number and type of ligands coordinated to the central Mg atom and upon the nature (i.e., polarizability, dipole moment) of the solvent.^{3–5} Oligomers of Chl a, (Chl a)_n, formed by coordination interactions of the ring V keto carbonyl of one Chl a to the central Mg atom of another have their principal absorption maxima in the red near 678 nm in aliphatic hydrocarbon solvents.^{4,5} The close similarity between the principal absorption maximum (~678 nm) of in vivo antenna Chl a and the principal absorption maximum of the Chl a species ((Chl a)_n) formed in aliphatic hydrocarbon solvents has led to the proposal that these species are plausible models for in vivo antenna Chl a in green plants and algae.^{4,6–8} A Chl a-water adduct can be prepared in aliphatic hydrocarbon solvents and this adduct has a principal absorption maximum at 743 nm in the red.^{9,10} This 743-nm Chl a-water adduct is photoactive and exhibits a reversible photo-ESR signal.¹¹ "Crystalline" monolayers of methyl chlorophyllide a (Figure 1), a molecule closely related to Chl a, spread on water have a principal absorption maximum at 735 nm.¹²

Recently, the X-ray crystallographic structure of ethyl chlorophyllide a-2H₂O has been determined by Strouse et al.^{13,14} and the structure has been confirmed by Kratky and Dunitz.¹⁵ This X-ray structure has been very useful because it has provided a structural basis for the rationalization of the spectroscopic properties of hydrated chlorophyll species. The three-dimensional crystal of ethyl chlorophyllide a-2H₂O is formed by the stacking of hexagonal sheets along the *c* axis of the crystal. Adjacent sheets are rotated about the *c* axis by 120° with respect to each other (threefold screw axis). Within a hexagonal sheet all chlorophyllide molecules are related by translational symmetry only, i.e., the sheet can be thought of as a two-dimensional crystal with one molecule per unit cell. The chlorophyllide molecules within the sheet are

bound together through interactions with two types of water molecules. The type I water is strongly bound, and is simultaneously coordinated to the Mg atom of one chlorophyllide molecule, hydrogen bonded to the ring V keto carbonyl of a second chlorophyllide molecule, and hydrogen bonded to a type II water molecule. Type I water molecules bind the chlorophyllide molecules into one-dimensional stacks (Figure 2) parallel to one of the axes of the hexagonal sheet. The results of exciton calculations on these stacks is a primary concern of this paper. Type II water molecules are much less strongly bound than type I water molecules as judged by the nature of the interactions they have (three hydrogen bonds bind type II water molecules and this is to be compared to one coordination bond and two hydrogen bonds for the type I water molecules) and by the thermal parameters deduced for it from the X-ray crystallographic study. Type II water is simultaneously hydrogen bonded to a type I water molecule, hydrogen bonded to the ring V carbomethoxy carbonyl of the same chlorophyllide molecule, and hydrogen bonded to the ethyl ester carbonyl of a second chlorophyllide molecule. Type II water molecules cross link the linear stacks to form sheets in the *ab* crystal plane. As there are no hydrogen bonding or coordination interactions between sheets, it is reasonable to place the forces holding the crystal together in the following hierarchy of decreasing strength: intrastack forces > interstack forces within sheets > intersheet forces.

Fischer et al.¹⁶ have proposed a Chl a hydrate model for antenna Chl a. (Chl a-H₂O)_n stacks have been proposed by Strouse^{13,14,17} as models for in vivo antenna Chl a in green plants. In this paper we have explored the applicability of the Chl a hydrate stack model by first carrying out exciton calculations of the low-energy electronic transitions of (Chl a-H₂O)_n stacks and then making a comparison of the computed spectra with the spectra observed for in vivo antenna Chl a.

Less is known about bacteriochlorophyll a-(Bchl a; Figure 3) water adducts than about Chl a-water adducts. No crystal structures for Bchl a or bacteriochlorophyllide hydrates have been published. Three Bchl a-water adducts with absorption maxima at 800, 825, and 850 nm have been prepared in an aliphatic hydrocarbon solvent at room temperature and these Bchl a-water adducts have been shown to be photoactive by the ESR criterion.¹⁸ Upon dilution of a Bchl a solution in methanol or acetone

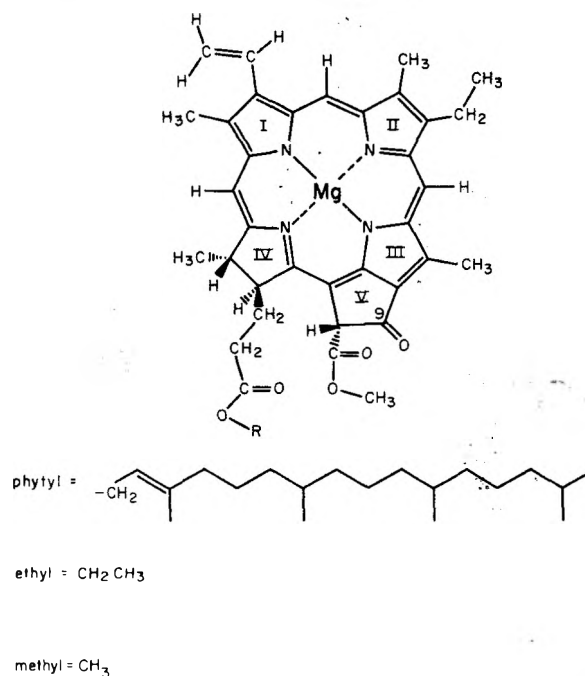


Figure 1. Molecular structures for chlorophyll a (Chl a), ethyl chlorophyllide a, and methyl chlorophyllide a: R = phytol for chlorophyll a, R = ethyl for ethyl chlorophyllide a, and R = methyl for methyl chlorophyllide a.

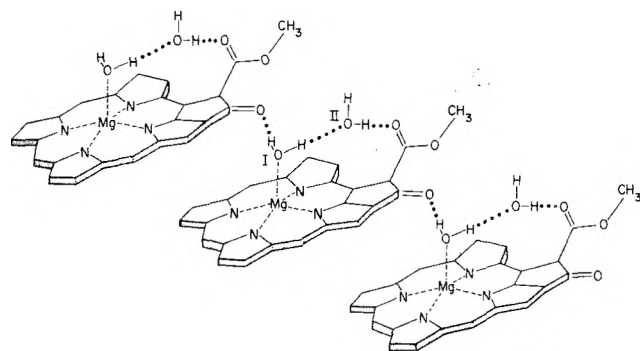


Figure 2. Structure of a chlorophyll hydrate stack showing the strongly held (type I) and weakly held (type II) water molecules. For clarity, the groups attached to the macrocycle (except the carbomethoxy group) are not shown.

with water a colloid forms with absorption maxima at 785 and 848 nm.¹⁹ If an amount of water is added to a solution of Bchl a in acetone so that the acetone:water ratio is 10:90, the principal absorption maxima are in 850 and 920 nm.²⁰ Red-shifted Bchl a species have been observed in monolayers of Bchl a spread on a water surface.²¹ The absorption spectrum of these monolayers and the variations of the absorption spectrum with increasing compression of the film may be interpreted in terms of Bchl a species absorbing at 805, 870, 908, and 950 nm, with the more red-shifted species favored at higher compression. Microcrystalline suspensions of Bchl a hydrate in isooctane at 4 °C have a principal absorption maximum at 940 nm.²² Microcrystalline suspensions of bacteriochlorophyllide a hydrate have a principal absorption maximum at 840 nm.²³ In vivo antenna Bchl a in purple photosynthetic bacteria have principal absorption maxima at 800–805, 850–860, and 880–890 nm.^{18,20,24} The close similarity between the principal absorptions in laboratory-prepared Bchl a-water adducts and in vivo antenna Bchl a has led to the proposal that Bchl a-water adducts are plausible models for in vivo antenna Bchl a.¹⁸ In the present study we have carried out exciton calculations on (Bchl a-H₂O)_n stacks of the type

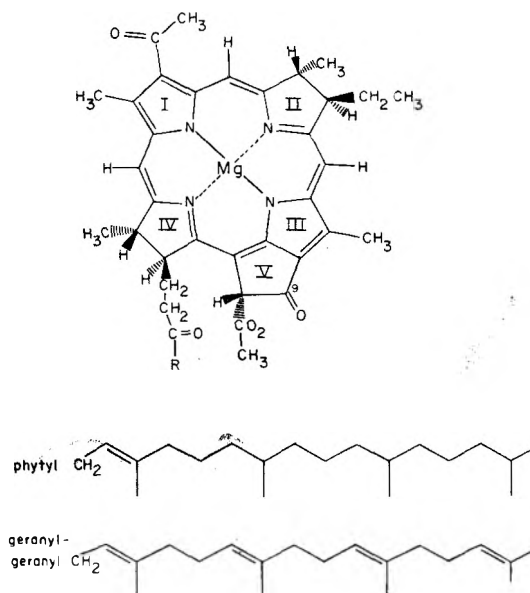


Figure 3. Molecular structure of bacteriochlorophyll a (Bchl a). Usually R = phytol, but R = geranyl-geranyl is found for *Rhodospirillum rubrum*.

found for ethyl chlorophyllide a hydrate and we have then compared the calculated spectra with the spectra observed for in vivo antenna Bchl a.

II. Exciton Calculations.

A recently derived exciton formalism²⁵ for Chl aggregates was used for the exciton calculations on (Chl a-H₂O)_n and (Bchl a-H₂O)_n stacks. Unlike other exciton formulations that have been applied to the calculation of the electronic transitions in Chl aggregates, this newly derived formalism²⁵ simultaneously treats both transition density shifts and environmental shifts of transition energies. For the discussion to follow we shall use the notation of ref 25. We have considered only the mixing of the S₀ → S₁ electronic transitions in the present calculations; we feel that the S₀ → S_n n > 2 transitions are either sufficiently well-separated in energy from S₀ → S₁ or sufficiently weak (i.e., low oscillator strength) so that they would not substantially perturb the calculated results for the S₀ → S₁ manifold of transitions. The exciton calculations were carried out at the geometry of the ethyl chlorophyllide a-H₂O stacks (see section I and Figure 2) found in the Strouse X-ray crystallographic structure of ethyl chlorophyllide a-2H₂O.^{13,14} We take the direction of the S₀ → S₁ transition moment to be along the N(I)-N(III) axis. The exciton calculations have been performed by (i) constructing the H'' matrix,²⁵ (ii) diagonalizing H'' to find the eigenvalues which are the exciton transition energies, and the eigenvectors which describe the exciton states. We have then (iii) used the eigenvalues to calculate the transition wavelengths and the eigenvectors to calculate the normalized dipole strengths and the distribution of excitation energy along the linear stack for each exciton transition. The diagonal elements, H''_{ii}, of H'' are the S₀ → S₁ transition energies for each of the chlorophyll molecules in the stack environment in the absence of transition density interactions. An off-diagonal element, H''_{ij}, of H'' is the transition density-transition density interaction energy between molecule i and molecule j. We have approximated the transition density-transition density interaction energy as the interaction energy between point transition dipoles of length 5.15 D for Chl a²⁶ (6.05 D for Bchl a) at the centers of molecules i and j. The first molecule in the stack, i = 1, must have a distinctly different environment from the rest, i ≥ 2, in that it is not

strongly hydrogen bonded at its ring V keto carbonyl. For Chl a we estimate the transition energy, H_{11}'' , for the first molecule to be 15038 cm^{-1} (665 nm) midway in the observed³⁻⁵ range of values (659–671 nm) reported for monomeric Chl a. For Bchl a we estimate the transition energy, H_{11}'' , to be 12788 cm^{-1} (682 nm), the position of the principal absorption maximum of Bchl a-pyridine in CCl_4 .

We have estimated the transition energies, H_{ii} , for the $i \geq 2$ molecules in the Chl a hydrate stack by noting that they have environments in the stack that are quite similar to the environments of molecules in the *ab* crystalline sheets in the crystal structure of ethyl chlorophyllide $a \cdot 2\text{H}_2\text{O}$. It is reasonable to expect that the crystalline monolayers of methyl chlorophyllide a (λ_{max} 735 nm¹²) spread on water have the same structure as the *ab* crystalline sheets in the crystal structure of ethyl chlorophyllide $a \cdot 2\text{H}_2\text{O}$. These sheets have one molecule per unit cell, and for the special case of one molecule per unit cell the environmental shifts and transition density shifts of transition energies are additive. Thus, the transition energy $H_{ii}'', i \geq 2$ may be computed by taking the difference between the observed transition energy (13605 cm^{-1} , 735 nm) for the monolayer and the sum of the transition density-transition density interaction energies between any molecule in the sheet and all other molecules in the sheet (-975 cm^{-1}). The result is $H_{ii}'' = 13605 + 975 = 14580 \text{ cm}^{-1}$ (686 nm) for $i \geq 2$.

Unlike the case of Chl a, the crystal structure of a Bchl a-water adduct has not been published. Therefore it has not been possible to calculate directly the environmental shift of the $S_0 \rightarrow S_1$ transition energy in a Bchl a hydrate stack. We have obtained an estimate of the transition energy of a Bchl a molecule with stacklike interactions by an indirect procedure. Recently Vermeiglio and Clayton²⁷ have proposed from linear dichroism measurements that the P865 chromophore (special pair) of bacterial reaction centers has a principal absorption maximum at 865 nm (11561 cm^{-1}) and a minor absorption maximum at 810 nm (12346 cm^{-1}) and that these two absorptions are assignable to two exciton transitions of the special pair. The P865 chromophore is thought to be composed of two Bchl a molecules with nearly identical environments and held together by π - π stacking and strong hydrogen bonding to the ring V keto carbonyls quite similar to the interactions in a Bchl a hydrate stack.²⁶ The 810- and 865-nm exciton transitions imply that the transition energies in the absence of transition density interactions are both at $1/2(11561 + 12346) = 11954 \text{ cm}^{-1}$ (837 nm). For our calculations in the present study we have used this estimate of 837 nm for the transition energies, $H_{ii}'', i \geq 2$ in a Bchl a hydrate stack. Support for the 837-nm value also comes from the observation of a principal absorption maximum at 940 nm for a microcrystalline suspension of Bchl a hydrate in isoctane at 4 °C.²² This absorption maximum is in an identical position with the absorption maximum at 942 nm that we calculate for a Bchl a hydrate sheet based upon the 837-nm value. The splitting (785 cm^{-1}) between the 810- and 865-nm exciton transitions implies a Bchl a transition dipole length 6.05 D for the special-pair structure proposed in ref 27. This transition dipole length is in good agreement with the value (6.13 D) determined by Sauer et al.²⁸ for the Bchl a monomer.

The results of exciton calculations for $n = 2 \rightarrow 10$ are given in Table I for $(\text{Chl } a \cdot \text{H}_2\text{O})_n$ stacks and in Table II for $(\text{Bchl } a \cdot \text{H}_2\text{O})_n$ stacks. Exciton calculations were also carried out for stacks of infinite length as models for the exciton transitions in very long stacks. All the oscillator

TABLE I: Calculated Spectra for Linear $(\text{Chlorophyll } a \cdot \text{H}_2\text{O})_n$ Stacks

	λ^a	F^b	Percentage of the total excitation residing on each molecule																	
			1	2	3	4	5	6	7	8	9	10								
Dimer	659	0.11	81	19																
	693	0.89	19	81																
Trimer	658	0.10	73	24	3															
	676	0.01	19	23	58															
	703	0.89	8	53	38															
Tetramer	658	0.06	70	24	5	1														
	670	0.05	14	5	49	32														
	688	0.00	12	38	3	47														
	709	0.89	4	33	42	21														
Pentamer	658	0.05	69	24	6	1	0													
	667	0.00	10	1	28	43	18													
	679	0.06	11	17	29	7	36													
	695	0.00	7	37	4	19	33													
Hexamer	712	0.89	3	21	34	30	12													
	658	0.04	68	24	6	2	0	0												
	665	0.01	7	0	15	34	32	11												
	674	0.00	10	7	34	3	20	26												
Heptamer	686	0.07	8	24	5	31	0	32												
	700	0.00	5	30	14	1	26	23												
	714	0.88	2	14	26	29	21	8												
	658	0.03	68	24	6	2	0	0	0											
	664	0.00	5	0	9	25	32	23	7											
	671	0.02	8	3	28	15	1	26	19											
Octamer	680	0.00	8	14	18	8	23	3	26											
	692	0.07	6	25	0	24	12	7	26											
	704	0.00	4	24	20	1	8	26	17											
	715	0.88	1	10	20	25	23	15	6											
	658	0.03	68	24	6	2	0	0	0	0										
	664	0.00	4	0	6	17	27	26	16	4										
	669	0.00	7	1	21	22	2	8	26	13										
	676	0.02	7	8	23	0	23	8	10	21										
Nanomer	685	0.00	6	17	5	22	2	24	0	24										
	696	0.07	5	23	3	10	24	2	13	20										
	707	0.00	3	19	21	7	1	14	23	12										
	716	0.87	1	7	15	21	22	19	11	4										
	658	0.03	68	24	6	2	0	0	0	0	0									
	663	0.00	3	0	4	12	21	24	21	12	3									
	667	0.01	6	1	15	23	9	0	14	23	10									
	673	0.00	6	4	23	4	10	21	1	15	17									
Decamer	681	0.02	6	11	12	8	16	4	19	2	21									
	690	0.00	5	18	0	22	4	14	14	3	21									
	699	0.07	4	21	8	2	20	13	0	16	16									
	709	0.00	2	15	20	11	1	4	16	20	10									
	717	0.87	1	5	12	17	20	19	15	9	3									
	658	0.02	68	24	6	2	0	0	0	0	0									
	663	0.00	2	0	3	9	17	21	21	16	9	2								
	666	0.00	5	0	11	21	14	1	4	17	20	7								
Nanomer	671	0.01	6	2	20	10	1	19	2	0	18	13								
	677	0.00	6	7	17	1	20	2	15	10	6	18								
	685	0.02	5	14	5	17	2	18	1	20	0	19								
	693	0.00	4	18	1	14	13	1	19	5	7	18								
	702	0.07	3	18	11	0	12	19	5	2	17	13								
	710	0.00	2	12	19	14	4	0	8	17	17	8								
	718	0.87	0	4	9	14	17	18	16	12	7	2								

^a Wavelength in nanometers. ^b Fraction of the total dipole strength of the stack.

strength in an infinite stack is concentrated in the lowest energy transition at 721 nm for the Chl a hydrate stack and at 908 nm for the Bchl a hydrate stack.

III. Discussion of Results

We have calculated (Table I) that the primary absorptions for $(\text{Chl } a \cdot \text{H}_2\text{O})_n$ are at 693, 703, 709, 712, 714, 715, 716, 717, and 718 nm for $n = 2, 3, 4, 5, 6, 7, 8, 9$, and

TABLE II: Calculated Spectra for Linear (Bacteriochlorophyll a-H₂O)_n Stacks

	λ^a	F^b	Percentage of the total excitation residing on each molecule										
			Molecule no.										
			1	2	3	4	5	6	7	8	9	10	
Dimer	773	0.16	86	14									
	848	0.84	14	86									
Trimer	772	0.13	83	16	1								
	816	0.00	11	30	58								
	871	0.87	6	54	40								
Tetramer	772	0.09	82	16	2	0							
	804	0.04	7	10	53	30							
	838	0.00	8	42	2	48							
	883	0.87	3	32	44	22							
Pentamer	772	0.07	82	16	2	0	0						
	799	0.00	5	4	32	42	17						
	822	0.06	7	22	26	9	36						
	854	0.00	5	38	6	18	34						
	889	0.87	2	20	34	31	13						
Hexamer	772	0.06	82	16	2	0	0	0					
	796	0.01	3	2	20	36	30	10					
	812	0.00	5	12	33	2	22	26					
	836	0.06	5	27	3	32	0	32					
	865	0.00	4	30	16	1	26	24					
	894	0.87	1	13	26	30	22	8					
Heptamer	772	0.05	82	16	2	0	0	0	0				
	794	0.00	2	1	13	27	31	21	6				
	806	0.01	4	6	30	12	2	27	18				
	824	0.00	5	17	15	10	22	4	27				
	847	0.07	4	26	0	24	14	6	26				
	873	0.00	2	24	21	2	8	26	17				
	897	0.87	1	9	19	25	24	16	6				
Octamer	772	0.04	82	16	2	0	0	0	0	0			
	793	0.00	1	1	8	20	27	24	15	4			
	802	0.00	3	4	24	20	1	10	26	13			
	816	0.02	4	11	22	3	24	7	11	21			
	834	0.00	4	20	3	23	1	25	0	24			
	856	0.07	3	24	5	9	24	2	12	21			
	879	0.00	2	18	22	7	0	13	24	13			
	899	0.86	1	7	15	21	22	19	12	4			
Nanomer	772	0.04	82	16	2	0	0	0	0	0	0		
	792	0.00	1	0	6	14	22	24	19	11	3		
	799	0.00	3	2	18	22	6	1	15	23	9		
	810	0.00	4	7	22	2	12	20	0	16	16		
	825	0.02	4	14	10	10	15	6	19	2	21		
	843	0.00	3	20	0	21	4	13	15	3	21		
	863	0.07	2	20	9	2	20	14	0	16	17		
	883	0.00	1	15	21	12	1	4	16	20	10		
	900	0.86	0	5	11	17	20	19	15	9	3		
	Decamer	772	0.04	82	16	2	0	0	0	0	0	0	
792		0.00	1	0	4	11	18	21	20	15	8	2	
798		0.00	2	2	14	21	12	1	5	18	20	7	
806		0.01	3	5	21	7	3	20	10	1	18	13	
819		0.00	3	10	15	2	20	1	16	9	6	18	
834		0.02	3	15	3	18	1	19	0	20	0	19	
851		0.00	3	19	1	13	14	1	19	6	7	18	
869		0.07	2	18	12	0	11	19	5	2	17	13	
887		0.00	1	12	19	14	4	0	8	17	17	8	
901		0.86	0	4	9	14	17	18	16	12	7	2	

^{a, b} See footnotes to Table I.

10, respectively. For (Bchl a-H₂O)_n we calculate (Table II) that the primary absorptions are at 848, 871, 883, 889, 894, 897, 899, 900, and 901 nm for $n = 2, 3, 4, 5, 6, 7, 8, 9,$ and $10,$ respectively. The calculated values for the Chl a hydrate stacks may be directly compared with the values of 674, 679, 682, 684, 686, 687, and 687 nm for $n = 2, 3, 4, 5, 6, 7,$ and $8,$ respectively, calculated by Chow et al.¹⁴ Our values for the Bchl a hydrate stacks may be directly compared with the values of 796, 809, 817, 822, 825, and

827 nm for $n = 2, 3, 4, 5, 6,$ and $7,$ respectively, calculated by Strouse.¹⁷ There is obviously poor agreement between our calculated results and those of Chow et al.¹⁴ for Chl a and Strouse¹⁷ for Bchl a. The primary reason for the discrepancy is the values assumed for the transition energies, H_{ii}'' . Chow et al.¹⁴ have used a monomeric Chl a value of 662 nm and Strouse¹⁷ has used a monomeric Bchl a value of 770 nm for all H_{ii}'' while we have assigned an environmental shift to 686 nm for Chl a in the stack environment and an environmental shift to 837 nm for Bchl a in the stack environment. We feel that the assumption of monomeric transition energies (662 and 770 nm for Chl a and Bchl a, respectively) is in error because such an assumption leads to the prediction that a Chl a hydrate sheet will have a principal absorption maximum at 708 nm, when the observed value is 735 nm.¹² Thus there are substantial environmental shifts to the red associated with the environment (π - π stacking, strong hydrogen bonding at the ring V keto carbonyl, etc.) of a chlorophyll molecule in a stack; our calculations have accounted for this environmental shift while the calculations of Chow et al.¹⁴ and Strouse¹⁷ have not.

Most of the dipole strength of a Chl a hydrate stack or a Bchl a hydrate stack is concentrated in the lowest energy transition, and the remaining dipole strength is scattered through the remaining transitions. One consequence of assigning a transition energy, H_{11}'' , to molecule $i = 1$ that is higher than the rest is to limit the broadening of the exciton transition band to higher energy as n is increased. From 68 to 89% of the excitation in the highest energy transition is localized in the molecule $i = 1$. For $n \geq 3$ the distribution of excitation energy in the lowest energy transition (the principal absorption) has a maximum in the middle of the stack and tails to both ends of the stack.

IV. Conclusions

Our exciton calculations do not support the proposal^{13,14,17} that in vivo antenna Chl a consists of Chl a hydrate stacks. We find that while in vivo antenna Chl a has a principal absorption maximum near 678 nm^{2,4} Chl a hydrate stacks have principal absorption maxima in the 693–721-nm range. This does not imply that hydrated Chl a species are unimportant in green plant photosynthesis. To the contrary, there is good evidence that special pairs of Chl a bound together with water (or with appropriate amino acid side chains) are a reasonable model for in vivo photoreactive Chl in reaction centers.²⁷

On the basis of a comparison between the principal absorption maxima of Bchl a hydrate stacks (848–908-nm range) and the observed principal absorption maxima for in vivo antenna Bchl a (800–805, 850–860, and 880–890 nm) of purple photosynthetic bacteria, we find that short Bchl a hydrate stacks are a reasonable model for the two more red-shifted components (i.e., the 850–860- and 880–890-nm components) of in vivo antenna Bchl a. The 800–805-nm component of in vivo antenna Bchl a is not accounted for by a Bchl a hydrate stack of the type considered here. Despite the many assumptions that must be made in the Bchl a calculations, agreement between the absorption values calculated for Bchl a hydrate stacks of various lengths and the position of the principal absorption maxima of the various components of in vivo antenna Bchl a is surprisingly good.

As it has been shown that Bchl a hydrates are photoactive,¹⁸ the question then arises what is the difference between antenna and photoreaction center Bchl a? We feel that the near proximity of a suitable electron acceptor forms a reaction center, and the resulting possibility for photomediated electron transfer is the important factor

in distinguishing photoreaction center Bchl a from antenna Bchl a in vivo.

Note Added in Proof: Wasielewski et al. (M. R. Wasielewski, U. H. Smith, B. T. Cope, and J. J. Katz, *J. Am. Chem. Soc.*, submitted for publication) have recently synthesized a linked-dimer derivative of Bchl a in which two Bchl a macrocycles are covalently linked via ring IV propionic ester functions. The proton magnetic resonance spectrum of the hydrated linked dimer strongly supports a folded structure similar to, if not identical with, the special pair structure proposed by Shipman et al.²⁶ However, the red peak in the visible absorption spectrum of the hydrated linked dimer has its maximum at 803 nm, not at ~ 865 nm as required by an environmental shift to 837 nm. It now appears possible that a strong environmental shift to ~ 837 nm may require π - π stacking and strong perturbation (via strong hydrogen bonding or coordination bonding) at both the ring V keto $\text{C}=\text{O}$ and the ring I acetyl $\text{C}=\text{O}$ functions of the Bchl a special pair.

References and Notes

- (1) This work was performed under the auspices of the Division of Physical Research, U.S. Energy Research and Development Administration.
- (2) C. S. French, J. S. Brown, and M. C. Lawrence, *Plant Physiol.*, **49**, 421 (1972).
- (3) G. R. Seely and R. G. Jensen, *Spectrochim. Acta*, **21**, 1835 (1965).
- (4) T. M. Cotton, A. D. Trifunac, K. Ballschmitter, and J. J. Katz, *Biochim. Biophys. Acta*, **368**, 181 (1974).
- (5) L. L. Shipman, T. M. Cotton, J. R. Norris, and J. J. Katz, *J. Am. Chem. Soc.*, **98**, 8222 (1976).
- (6) A. A. Krasnovskii in "Progress in Photosynthesis Research", H. Metzner, Ed., 1969, pp 709-732.
- (7) R. Livingston, *Q. Rev. Chem. Soc.*, **14**, 174 (1960).
- (8) S. S. Brody and M. Brody, *Nature (London)*, **189**, 547 (1961).
- (9) J. J. Katz and K. Ballschmitter, *Angew. Chem.*, **7**, 286 (1968).
- (10) K. Ballschmitter, T. M. Cotton, H. H. Strain, and J. J. Katz, *Biochim. Biophys. Acta*, **180**, 346 (1969).
- (11) J. R. Norris, R. A. Uphaus, H. L. Crespi, and J. J. Katz, *Proc. Natl. Acad. Sci. U.S.A.*, **68**, 625 (1971).
- (12) G. L. Gaines, W. D. Bellamy, and A. G. Tweet, *J. Chem. Phys.*, **41**, 2572 (1964).
- (13) C. E. Strouse, *Proc. Natl. Acad. Sci. U.S.A.*, **71**, 325 (1973).
- (14) H.-S. Chow, R. Serlin, and C. E. Strouse, *J. Am. Chem. Soc.*, **97**, 7230 (1975).
- (15) C. Kratky and J. D. Dunitz, *Acta Crystallogr., Sect. B*, **31**, 1586 (1975).
- (16) M. S. Fischer, D. H. Templeton, A. Zalkin, and M. Calvin, *J. Am. Chem. Soc.*, **94**, 3613 (1972).
- (17) C. E. Strouse, *Prog. Inorg. Chem.*, **21**, 159 (1976).
- (18) J. J. Katz, W. Oettmeier, and J. R. Norris, *Phil. Trans. R. Soc. London, Ser. B*, **273**, 227 (1976).
- (19) A. A. Krasnovskiy, K. K. Voinovskaya, and L. M. Kosobutskaya, *Dokl. Akad. Nauk SSSR*, **85**, 389 (1952).
- (20) J. G. Komen, *Biochim. Biophys. Acta*, **22**, 9 (1956).
- (21) P. Reinach, B. B. Aubrey, and S. S. Brody, *Biochim. Biophys. Acta*, **314**, 360 (1973).
- (22) K. Sauer in "Bioenergetics of Photosynthesis", Govindjee, Ed., Academic Press, New York, N.Y., 1975, pp 115-181.
- (23) E. E. Jacobs, A. S. Holt, R. Kromhout, and E. Rabinowich, *Arch. Biochem. Biophys.*, **72**, 495 (1957).
- (24) J. M. Olson and E. K. Stanton in "The Chlorophylls", L. P. Vernon and G. R. Seely, Ed., Academic Press, New York, N.Y., 1966, pp 381-398.
- (25) L. L. Shipman, J. R. Norris, and J. J. Katz, *J. Phys. Chem.*, **80**, 877 (1976).
- (26) L. L. Shipman, T. M. Cotton, J. R. Norris, and J. J. Katz, *Proc. Natl. Acad. Sci. U.S.A.*, **73**, 1791 (1976).
- (27) A. Vermeiglio and R. K. Clayton, Presented at the Brookhaven Symposium in Biology, Brookhaven National Laboratory, June 7-9, 1976; *Biochim. Biophys. Acta*, **449**, 500 (1976).
- (28) K. Sauer, J. R. Lindsay Smith, and A. J. Schultz, *J. Am. Chem. Soc.*, **88**, 2681 (1966).

The Compressibility and Electrical Conductivity of Concentrated Aqueous Calcium Nitrate Solutions to 6 kbar and 150 °C

L. Pickston, S. I. Smedley,* and G. Woodall[†]

Chemistry Department, Victoria University of Wellington, Wellington, New Zealand (Received August 20, 1976)

From conductivity and volume measurements of $\text{Ca}(\text{NO}_3)_2 \cdot 3.63\text{H}_2\text{O}$, $\text{Ca}(\text{NO}_3)_2 \cdot 4.85\text{H}_2\text{O}$, $\text{Ca}(\text{NO}_3)_2 \cdot 5.98\text{H}_2\text{O}$, and $\text{Ca}(\text{NO}_3)_2 \cdot 7.02\text{H}_2\text{O}$ over the temperature range 25-150 °C and from 1 bar to 6 kbar we have calculated the molar conductivities, densities, compressibilities, expansivities, and internal pressures. Molar conductivities have been fitted to the empirical VTF equation to obtain the parameters A , B , and T_0 . The constant pressure and constant volume "activation energies" increase with decreasing temperature as predicted by the VTF equation, the "activation volume" ΔV_A increases with decreasing temperature, and increases with increasing pressure, which has not been previously demonstrated for molten salts or concentrated aqueous solutions.

Introduction

The isobaric composition dependence of the fluidity, $1/\eta$, and the molar conductivity, Λ , of the $\text{Ca}(\text{NO}_3)_2/\text{H}_2\text{O}$ system have been shown to obey the empirical VTF equation

$$\Lambda, 1/\eta = A_{(\Lambda, 1/\eta)} T^{-1/2} \exp \left(\frac{-B_{(\Lambda, 1/\eta)}}{T - T_0} \right) \quad (1)$$

over the composition range 8-26 mol % $\text{Ca}(\text{NO}_3)_2$ and $T = 1.3T_0$ to $1.9T_0$.¹ Λ and $1/\eta$ are the transport properties of interest, and for a given composition and pressure A , B , and T_0 are constants. T_0 is the temperature at which

ionic mobility in the liquid falls to zero, and is referred to as the "ideal glass transition temperature". For this system T_0 and B increase linearly with composition, and B may be written as DT_0 , where D is a constant. Angell et al.² have also shown that T_0 is linearly dependent on pressure, and that for a given composition eq 1 can be modified to describe the pressure dependence of the conductivity κ

$$\kappa = AT^{-1/2} \exp \left[- \frac{B}{T - (T_0^1 + bP)} \right] \quad (2)$$

where T_0^1 is the value of T_0 at 1 bar, and $b = dT_0/dP$. This study was restricted to the composition range 9-20 mol % $\text{Ca}(\text{NO}_3)_2$, the temperature range $1.5T_0$ to $1.9T_0$, and to 3 kbar. Equation 2 has also been successfully applied over a limited temperature range to the pressure dependence

[†] Present address: Department of Chemical Engineering and Applied Chemistry, University of Toronto, Toronto, Canada, M5S1A4.

of the conductivity of $\text{Ca}(\text{NO}_3)_2/\text{KNO}_3$ mixtures.

For the $\text{Ca}(\text{NO}_3)_2/\text{H}_2\text{O}$ system Angell and Tucker³ have measured the heat capacities of the crystalline, liquid, and vitreous states, and by extrapolation have been able to calculate the temperature, T_0 , at which the entropy of the internally equilibrated supercooled liquid will equal that of the crystalline glass. The value of T_0 obtained by this method and that obtained by best fitting values to eq 2 for $\text{Ca}(\text{NO}_3)_2 \cdot 4\text{H}_2\text{O}$ are 200 ± 4 and 201 K, respectively. This result substantiates the view that T_0 may represent the temperature at which the configurational part of the liquid entropy becomes zero, thus establishing the thermodynamic significance of T_0 as a base temperature for the equilibrium and time-dependent properties of the liquid. This hypothesis is the basis of the configurational entropy theory of transport in liquids.⁴ According to this theory, mass transport occurs through cooperative rearrangements of independent subsystems in the fluid. If the free energy barrier per particle, opposing rearrangement in the subsystem, is $\Delta\mu$, the minimum configurational entropy of the subgroup is S_c^* , and the total configurational entropy of the liquid is S_c , then the probability of rearrangement can be given as

$$W(T) = A \exp\left(-\left[\frac{\Delta\mu S_c^*}{kTS_c}\right]\right) \quad (3)$$

and $W(T) \rightarrow 0$ as $S_c \rightarrow 0$. Now S_c can be expressed as

$$S_c = \int_{T_0}^T \frac{\Delta C_p}{T} dT \quad (4)$$

where ΔC_p is the difference in heat capacity between the extrapolated heat capacity of the glass and that of the liquid at temperature T . If

$$\Delta C_p = \text{constant}/T = D/T \quad (5)$$

as assumed by Angell and Bressel then

$$S_c = D(T - T_0)/TT_0 \quad (6)$$

therefore

$$W(T) = A \exp\left[-\frac{\Delta\mu S_c^* T_0}{kD(T - T_0)}\right] \quad (7)$$

It is found experimentally that A has a $T^{-1/2}$ temperature dependence, if this is inserted into eq 7, and if $W(T)$ is assumed to be proportional to Λ , κ , and $1/\eta$, then (7) becomes eq 1, with

$$B = \Delta\mu S_c^* T_0 / kD \quad (8)$$

Equation 1 predicts that the "activation volume" ΔV , defined as

$$\Delta V = -RT \left(\frac{\partial \ln \Lambda}{\partial P}\right)_T = \frac{RTbB}{(T - T_0)^2} \quad (9)$$

and the "activation energies" at constant pressure and volume

$$(E_p)_\Lambda = -\left(R \frac{\partial \ln \Lambda}{\partial (1/T)}\right)_p = -\frac{RT}{2} + \frac{RBT^2}{(T - T_0)^2} \quad (10)$$

$$(E_v)_\Lambda = -\left(\frac{R \partial \ln \Lambda}{\partial (1/T)}\right)_v = -\frac{RT}{2} + \frac{RB \left[T^2 + \left(\frac{\partial T_0}{\partial (1/T)}\right)_v \right]}{(T - T_0)^2} \quad (11)$$

will tend to infinity as $T \rightarrow T_0$. These predictions have been partially confirmed for both $\text{Ca}(\text{NO}_3)_2/\text{KNO}_3$ and $\text{Ca}(\text{NO}_3)_2/\text{H}_2\text{O}$ mixtures.⁵ Angell, Pollard, and Strauss were able to show that both ΔV_κ and $(E_p)_\kappa$ tend to large values as T approaches T_0 . However, it has been demonstrated that for both of these systems $(E_p)_\kappa$ becomes constant at very low temperatures in the vicinity of T_0 , and that eq 1 does not fit the experimental data.^{6,7}

Angell and co-workers^{2,5} were not able to determine the density of their systems and thus were unable to calculate E_v and test its dependence on temperature, nor were they able to observe the effect of pressure on ΔV_Λ which, according to eq 1, should be pressure dependent.

This work is an extension of the study of the $\text{Ca}(\text{NO}_3)_2/\text{H}_2\text{O}$ system by Angell, Pollard, and Strauss. We have increased the pressure range to 6 kbar, and simultaneously measured conductivity and volume. We can therefore test the predictions based on eq 9-11 more reliably than before.

Experimental Section

The solutions were held in a Pyrex glass conductivity cell containing two platinum and one mercury electrode. This design enabled the simultaneous measurement of conductivity and sample volume, and has been described in detail by Barton and Speedy.⁸ The principal feature of this cell is the mercury electrode. The mercury acts as an electrode for volume measurement and also isolates the solution from the hydraulic oil in the pressure vessel. The pressure vessel was constructed from Nimonic 105 alloy and contained a working space $2.5 \text{ cm} \times 2.5 \text{ cm}$.

Pressures of up to 6 kbar were generated by pumping Shell Tellus 23 oil from a hydraulic handpump into a pressure intensifier and then into the pressure vessel. A Heise bourden gauge calibrated in 10-bar divisions and accurate to ± 5 bar was used to measure pressure.

The pressure vessel was maintained at constant temperature by immersing it in a stirred oil bath controlled to ± 0.05 °C by a Bayley Instrument Co. temperature controller. Temperatures were measured by calibrated mercury thermometers graduated in 0.1 °C divisions. These thermometers were placed in the oil bath adjacent to the pressure vessel. When the conductance of a sample inside the pressure vessel remained constant after a change in pressure or a temperature adjustment, the cell was assumed to be in thermal equilibrium with the oil bath.

Conductance was measured with a Wayne Kerr bridge, Model B224; the bridge was connected to the pressure vessel by shielded coaxial cable so as to avoid effects due to stray capacitance.

The conductivity cells were standardized with 0.1 *m* KCl, for which the conductivity⁹ and density¹⁰ are known precisely. It was important to know the density of the calibrating solution in order to calculate the volume of the cells.

$\text{Ca}(\text{NO}_3)_2$ solutions were prepared from Analar BDH $\text{Ca}(\text{NO}_3)_2 \cdot 4\text{H}_2\text{O}$ which was diluted when necessary with doubly distilled water. All samples were degassed by freezing the solutions at liquid air temperatures, and then melting them under vacuum. This technique was carried out four times with each sample. The solutions were introduced into the conductance cells while under vacuum. The cell was weighed before and after filling so that the mass of the sample could be calculated. A sample of each solution was analyzed for Ca^{2+} content by titrating a known mass of sample with EDTA as described by Vogel.¹¹

Results

All measurements were obtained by maintaining the

TABLE I: Compressibilities and Expansivities of Some Selected Ca(NO₃)₂ Solutions as a Function of Pressure

Compressibilities			
	<i>T</i> , °C	$-(\partial \ln V / \partial P)_T / \text{bar}^{-1}$	Exptl variance
Ca(NO ₃) ₂ ·3.63H ₂ O	25	0.5652E(-9) <i>P</i> - 0.1528E(-4)	2.9E(-5)
	122.4	0.1105E(-8) <i>P</i> - 0.2108E(-4)	4.5E(-5)
Ca(NO ₃) ₂ ·4.85H ₂ O	24.9	0.8134E(-9) <i>P</i> - 0.1675E(-4)	3.3E(-6)
	123.5	0.7825E(-9) <i>P</i> - 0.1850E(-4)	3.5E(-6)
Ca(NO ₃) ₂ ·5.98H ₂ O	55.3	0.9488E(-9) <i>P</i> - 0.2042E(-4)	5.0E(-5)
	149.7	0.1040E(-9) <i>P</i> - 0.2232E(-4)	1.1E(-4)
Ca(NO ₃) ₂ ·7.02H ₂ O	80.9	0.9888E(-9) <i>P</i> - 0.2213E(-4)	1.8E(-5)
	147.2	0.1031E(-8) <i>P</i> - 0.2318E(-4)	6.8E(-7)
Expansivities			
	<i>P</i> , kbar	Temp range, °C	$(\partial \ln V / \partial T) 10^4 / \text{K}^{-1}$
Ca(NO ₃) ₂ ·3.63H ₂ O	0.001	25-125	5.1 ± 0.4
	6.0	25-125	3.8 ± 0.3
Ca(NO ₃) ₂ ·4.85H ₂ O	0.001	25-125	4.9 ± 0.4
	6.0	25-125	3.8 ± 0.3
Ca(NO ₃) ₂ ·5.98H ₂ O	0.001	50-150	4.6 ± 0.4
	6.0	50-150	3.8 ± 0.3
Ca(NO ₃) ₂ ·7.02H ₂ O	0.001	50-150	4.4 ± 0.4
	6.0	50-150	3.8 ± 0.3

TABLE II: Compressibilities of Concentrated Ca(NO₃)₂ Compared with Pure Water and Some Molten Nitrates

	<i>T</i> , °C	10 ⁶ β/bar ⁻¹ at 1 bar	10 ⁶ β/bar ⁻¹ at 6 kbar
NaNO ₃ ^a	319.8	19.0	
	472.4	23.5	
KNO ₃ ^a	331.4	19.5	
	467.9	27.6	
H ₂ O ^b	25	45.24	15.8
	150	55.0	18.1
Ca(NO ₃) ₂ ·3.63H ₂ O	25	16.0 ± 1.3	11.0 ± 0.9
	150	22.3 ± 1.8	16.8 ± 1.3
Ca(NO ₃) ₂ ·4.85H ₂ O	25	16.5 ± 1.3	12.0 ± 1.0
	150	22.2 ± 1.8	16.1 ± 1.3
Ca(NO ₃) ₂ ·5.98H ₂ O	25	19.5 ± 1.6	13.5 ± 1.0
	150	18.8 ± 1.5	11.0 ± 0.9
Ca(NO ₃) ₂ ·7.02H ₂ O	25	20.5 ± 1.7	14.8 ± 1.2
	150	20.8 ± 1.7	15.6 ± 1.2

^a Reference 19. ^b Reference 18.

apparatus at constant temperature while the pressure was increased in 500-bar increments. After a pressure increase the conductance stabilized in 10–15 min, and the cell was assumed to be in thermal equilibrium with the oil bath.

The conductance of the Ca(NO₃)₂·*R*H₂O (*R* = 3.63, 4.85, 5.98, or 7.02) solutions in the upper and lower chambers of the conductance cell were measured over a range of 20–150 °C and 1 to 5500 bar. Each solution was tested for frequency dependence which was found to be negligible between 1 and 10 kHz. By using the technique of Barton and Speedy⁸ the data obtained from the bottom chamber of the cell were converted to volumes, and because the mass of the solution was known it was possible to calculate the density. All the data were processed by a computer program which printed out conductivity, molar conductivity, density, and volume at a given temperature and pressure. Due to experimental error and the error arising from the curve-fitting technique the resultant errors in β and α are quite large and these data serve mainly to illustrate the magnitude and trends of these quantities. The full range of results obtained for the Ca(NO₃)₂·3.63H₂O is

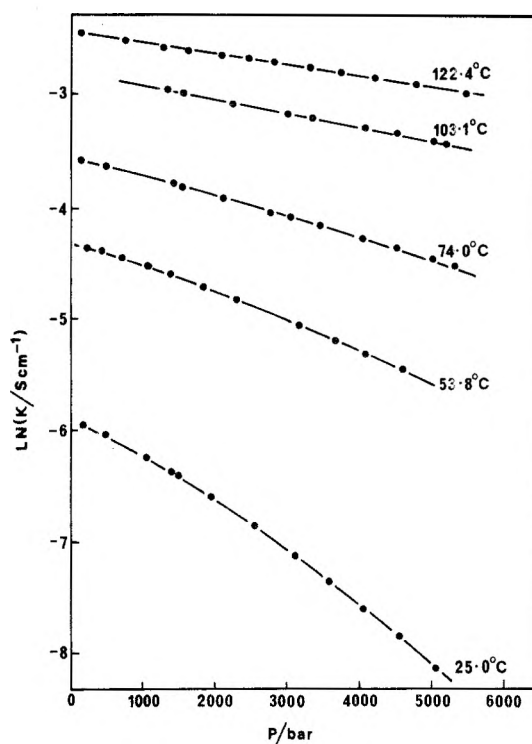


Figure 1. Experimental results for Ca(NO₃)₂·3.63H₂O, κ is the conductivity in S cm⁻¹ (Ω⁻¹ cm⁻¹).

displayed in Figure 1, while a selection of results for the other three samples is shown in Figure 2.

The compressibility β and the expansivity α, defined as

$$\beta = -\frac{1}{V} \left(\frac{\partial V}{\partial P} \right)_T = - \left(\frac{\partial \ln V}{\partial P} \right)_T \quad (12)$$

$$\alpha = \frac{1}{V} \left(\frac{\partial V}{\partial T} \right)_P = \left(\frac{\partial \ln V}{\partial T} \right)_P \quad (13)$$

were calculated by curve fitting the data to equations for ln *V* vs. *P* and ln *V* vs. *T*, Table I. For the sake of

TABLE III: Parameters Derived from Equation 1

P , kbar	T_0 , K	T_0 , K ^a	dT_0/dP / K(kbar) ⁻¹	dT_0/dP / K(kbar) ^{-1 a}	A	B
$\text{Ca}(\text{NO}_3)_2 \cdot 3.63\text{H}_2\text{O}$						
0.001	199 ± 3	208	4.5 ± 0.8	4.3 ± 0.4	2.19 ± 0.09	721 ± 32
2	206 ± 2				2.26 ± 0.12	747 ± 24
4	216 ± 3				2.24 ± 0.16	744 ± 40
6	226 ± 2				2.21 ± 0.13	733 ± 29
$\text{Ca}(\text{NO}_3)_2 \cdot 4.85\text{H}_2\text{O}$						
0.001	169 ± 2	192	4.5 ± 1	4.2	2.43 ± 0.07	707 ± 17
2	181 ± 2				2.34 ± 0.06	684 ± 18
4	191 ± 4				2.35 ± 0.13	685 ± 39
6	198 ± 7				2.49 ± 0.28	719 ± 74

^a Data from ref 2.

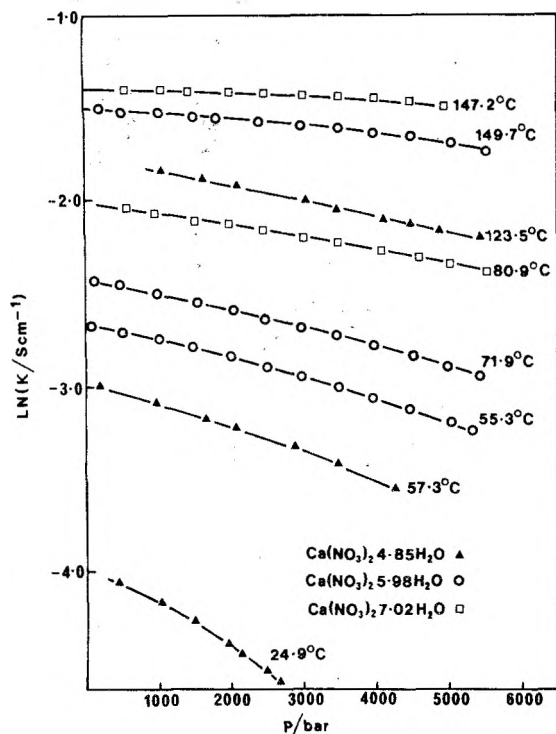


Figure 2. Some selected experimental results for $\text{Ca}(\text{NO}_3)_2 \cdot \text{H}_2\text{O}$ mixtures. κ is the conductivity in S cm^{-1} ($\Omega^{-1} \text{cm}^{-1}$).

comparison some selected compressibilities are compared with those of pure water, NaNO_3 , and KNO_3 in Table II. The compressibilities for $\text{Ca}(\text{NO}_3)_2/\text{H}_2\text{O}$ solutions increases with temperature and increasing $\text{Ca}(\text{NO}_3)_2$ content at constant pressure. However, the compressibility of all solutions decreases with increasing pressure.

Ideal glass transition temperatures and the constants A and B were obtained by a best fit procedure to the VTF equation, see Table III. Since the molar conductivities of $\text{Ca}(\text{NO}_3)_2 \cdot 5.98\text{H}_2\text{O}$ and $\text{Ca}(\text{NO}_3)_2 \cdot 7.02\text{H}_2\text{O}$ are in the Arrhenius region of transport dependence under the experimental conditions of temperature and pressure pertaining in these experiments, it was not possible to use the above technique to obtain T_0 values. The low value of T_0 , compared to those of Angell et al.,² is due largely to the fact that, in order to fit the data to eq 1, we have to transpose our molar conductivity isotherms to molar conductivity isobars. This technique gives only a few experimental points and hence makes the curve-fitting procedure less reliable. Furthermore, our fit to the VTF equation was made over a higher temperature range than used in earlier measurements, e.g., 298–428 K as compared with 253–323 K in ref 1.

The quoted error in T_0 , A , and B represents the amount these parameters must change for the best fit experimental

variance to change by half. The errors in the quantities of interest are as follows: conductivity has an error of $\pm 0.5\%$, volume 1%, molar conductivity 2%, ΔV_k 1%, ΔV_Λ 4%, compressibility and expansivity 4.3%.

Discussion

The empirical VTF equation adequately represents the isobaric temperature dependence of the molar conductivity of $\text{Ca}(\text{NO}_3)_2 \cdot 3.63\text{H}_2\text{O}$ and $\text{Ca}(\text{NO}_3)_2 \cdot 4.85\text{H}_2\text{O}$ up to 6 kbar. This conclusion is substantiated by the quoted reliability of the derived parameters $\ln A$, B , and T_0 and substantiates the work of Angell, Pollard, and Strauss.² In further agreement with the work of Angell et al., T_0 is found to be linearly dependent on pressure and that one can relate T_0 to T_0^1 , the value of T_0 at 1 bar, by the equation

$$T_0 = T_0^1 + bP$$

where b is the pressure coefficient of T_0 and P is the pressure. Thus for molar conductivity at constant composition the VTF equation may be written as

$$\Lambda = AT^{-1/2} \exp\left(\frac{-B}{T - (T_0^1 + bP)}\right) \quad (14)$$

The "activation volume" $\Delta V_\Lambda = -RT(\partial \ln \Lambda / \partial P)_T$ is therefore given by

$$\Delta V_\Lambda = \frac{RTbB}{(T - (T_0^1 + bP))^2} \quad (15)$$

This equation predicts that for a fixed composition at constant pressure, ΔV_Λ will tend to very large values as $T \rightarrow (T_0^1 + bP)$, and that at constant temperature ΔV_Λ will increase and tend to very large values as pressure is increased.

Figure 3 illustrates how ΔV_Λ depends on temperature and that for the most concentrated solution ΔV_Λ is tending to very large values at low temperatures. T_0 is also a function of composition at constant pressure, as indicated by our work, and shown more explicitly by Angell and Bressel.¹ Their experiments show that T_0 is linearly proportional to the mole percent composition of $\text{Ca}(\text{NO}_3)_2$ from 8 to 24 mol %. Consequently, at the temperatures and pressures involved in our study, the $\text{Ca}(\text{NO}_3)_2 \cdot 3.63\text{H}_2\text{O}$ solution is always closest to its T_0 value, and on the basis of eq 15 one would expect this solution to be most sensitive to temperature and pressure within the range of conditions used in our experiments. The trends exhibited in Figure 3 have been observed to a lesser extent by Angell, Pollard, and Strauss for both $\text{Ca}(\text{NO}_3)_2/\text{H}_2\text{O}$ and $\text{Ca}(\text{NO}_3)_2/\text{KNO}_3$ mixtures.^{2,5}

Figure 3 illustrates that ΔV_Λ is also a function of pressure as predicted by eq 15 and, as expected, the $\text{Ca}(\text{NO}_3)_2 \cdot 3.63\text{H}_2\text{O}$ solution is the most sensitive to pressure. The pressure dependence is greatest at lower

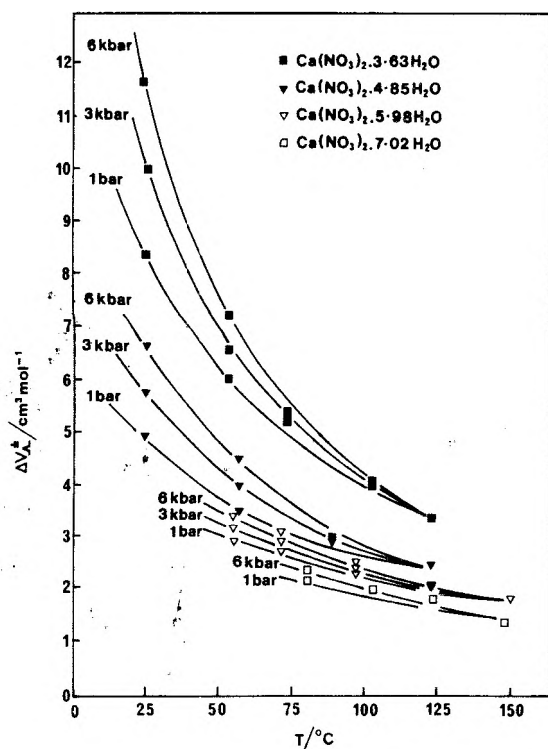


Figure 3. Activation volume for molar conductivity vs. temperature at various pressures.

temperatures and diminishes rapidly with increasing temperature. For the more dilute solutions $\text{Ca}(\text{NO}_3)_2 \cdot 5.98, 7.02\text{H}_2\text{O}$ the pressure dependence is barely distinguishable at the highest temperature, 150 °C. These trends are in complete agreement with those predicted by eq 15. For the aforementioned reasons we are not able to fit the data from our two most dilute solutions to eq 1. However, Angell and co-workers have shown that conductivity data for solutions up to $\text{Ca}(\text{NO}_3)_2 \cdot 10\text{H}_2\text{O}$ fit eq 2. Accordingly, we feel justified in testing the data for these solutions against the predictions based on eq 1. The composition dependence of ΔV_A may be accounted for by substituting $T_0 = T_0^0 + bP + cx$ into eq 9 where c is the composition coefficient of T_0 . The result is as follows:

$$\Delta V_A = \frac{RTb_x B_x}{(T - (T_0^0 + bP + cx))} \quad (16)$$

where b_x and B_x refer to the value of parameters b and B at the composition x . Both b and B have been shown to be composition dependent by Angell and Bressel¹ and, to a lesser extent, by this work.

In the Introduction to this paper we referred to the very low temperature work of Ambrus, Moynihan, and Macedo.⁷ They have demonstrated that $(E_p)_x$ for the $\text{Ca}(\text{NO}_3)_2 \cdot \text{H}_2\text{O}$ system tends to constant values at very low temperatures in the vicinity of T_0 , i.e., $T = 1.13T_0$. Similar behavior has also been observed for $0.4\text{Ca}(\text{NO}_3)_2/0.6\text{KNO}_3$, molten B_2O_3 , and some organic fluids.¹² The environmental relaxation model has been developed to explain the three regions of transport now observed: the high temperature Arrhenius region, the middle temperature range non-Arrhenius region where the VTF equation is applicable, and the low temperature Arrhenius region.¹² This theory relates the distributions of ultrasonic relaxation times, and activation energies, to an order parameter, λ , controlling the microstructure of the local environment in the fluid. The change in the width of the above distributions is proportional to the change in the distribution of local environments of the flow species in the fluid. The en-

vironment which affects the relaxation or activation of a molecule is designated a range r_0 . Relaxation mechanisms of the flowing species or molecules are then determined by the nature of the environment within the radius r_0 . Thus in the low temperature Arrhenius region the microstructure has large fluctuations (large λ), and the relaxation volumes $V_0 = 4/3\pi r_0^3$ are well imbedded within the fluctuations, $\lambda \gg r_0$, so that further increases in λ have little effect on the environment of relaxing molecules. The distribution of activation energies is therefore saturated, so that the mean activation energy remains constant. On the basis of this theory one would expect ΔV_A to tend to a constant value at low temperatures or very high pressures. Such a trend is not observed at the temperatures and pressures involved in this work.

Angell, Poillard, and Strauss² have argued that since B is independent of pressure and T_0 increases with pressure, then $\Delta\mu$, given by eq 8, must decrease with pressure. $\Delta\mu$ is the free energy barrier to rearrangement per particle and would be expected to have a pressure dependence similar to T_0 . In a $\text{Ca}(\text{NO}_3)_2 \cdot 4.04\text{H}_2\text{O}$ mixture T_0 increases by 2% per kilobar and, therefore, to maintain B constant $\Delta\mu$ must decrease accordingly. However, if $\Delta\mu$ is pressure dependent, then it is reasonable to suppose that it must also be temperature dependent, which would introduce a temperature dependence into B . The error limits quoted by Angell et al. for B suggest that B is certainly not temperature dependent, i.e., that the VTF equation is the correct parametric form. It would appear that none of the terms in eq 8 are temperature dependent; in addition we believe that they are also independent of pressure. It seems likely that the fault lies in assuming the constant D to be independent of pressure. If D is pressure dependent then, to accommodate for the increase in T_0 while maintaining B constant, D must increase with pressure. D is defined as being related to ΔC_p and T by the equation

$$\Delta C_p = D/T \quad (17)$$

ΔC_p is the difference between the extrapolated glass heat capacity at T , and the heat capacity of the supercooled liquid at T . If D increases with increasing pressure, then ΔC_p must also increase. That is, at some constant temperature, the difference between the glass and liquid capacities will increase with pressure. The heat capacity of many nitrate glasses, including $\text{Ca}(\text{NO}_3)_2 \cdot 4\text{H}_2\text{O}$, is more temperature dependent than the corresponding supercooled liquid formed from those glasses.³ It might reasonably be supposed that the C_p of the glass is also more pressure dependent than that of the liquid and therefore will decrease more rapidly with increasing pressure than C_p of the supercooled liquid. If ΔC_p has a pressure dependence such that $\Delta C_p = (D + CP)/T$ where C is a constant, then by following through eq 4 and 7

$$B = \frac{k\Delta\mu S_c^* T_0}{D + CP} \quad (18)$$

A more exact expression for C_p must await a detailed knowledge of the heat capacities of the liquid and glass over a range of temperatures and pressures. However, in this form B will be independent of temperature and pressure.

The molar conductivity at any temperature and pressure is, among other things, proportional to the concentration of charge carriers. An equilibrium of the form



has been clearly established for the $\text{Ca}(\text{NO}_3)_2 \cdot 4\text{H}_2\text{O}$ system. Hester and Plane¹³ have shown that this equilibrium is

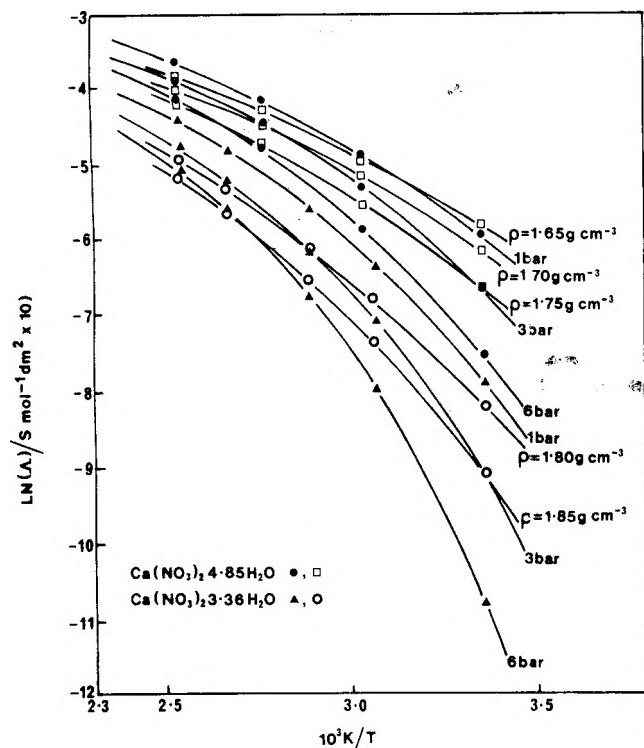


Figure 4. $\ln \Lambda$ (molar conductivity) vs. $1/T$ for some $\text{Ca}(\text{NO}_3)_2 \cdot \text{H}_2\text{O}$ mixtures at constant pressure and at constant density (volume).

temperature dependent and that it moves to the right with decreasing temperature; an increase in pressure appears to have a similar effect.¹⁴ The changes in magnitude of the equilibrium quotient $K = [\text{CaNO}_3^+]/[\text{Ca}^{2+}][\text{NO}_3^-]$ would appear to be significantly large enough to alter the conductivity by a detectable amount. This could be accounted for by a further modification of the parameter A or B . It would appear that in the light of the above arguments the insensitivity of B to temperature and pressure is a consequence of the very narrow range of conditions that this and other studies have covered.

The expression for the constant pressure and constant volume, "activation energies", $(E_p)_\Lambda$ and $(E_v)_\Lambda$, respectively, are given in terms of the VTF expression by eq 10 and 11. They predict that as $T \rightarrow T_0$ both E_p and E_v should tend to large values. Figure 4 displays $\ln \Lambda$ vs. $1/T$ at constant pressure and at constant volume for $\text{Ca}(\text{NO}_3)_2 \cdot 3.63\text{H}_2\text{O}$ and $\text{Ca}(\text{NO}_3)_2 \cdot 4.85\text{H}_2\text{O}$. The slope of these curves at any point is proportional to E_p or E_v . It is evident that E_p increases rapidly as $T \rightarrow T_0$, particularly for the $\text{Ca}(\text{NO}_3)_2 \cdot 3.63\text{H}_2\text{O}$ solution at 6 kbar which at a given temperature is closest to T_0 . The $(\ln \Lambda)_v$ vs. $1/T$ curves are not so steep, indicating that E_v is less temperature dependent over the same temperature range. This aspect emphasizes the distinction between the separate effects of temperature and density on the mobility of ions.

The internal pressures of $\text{Ca}(\text{NO}_3)_2 \cdot 3.63$ and $\cdot 7.02\text{H}_2\text{O}$ mixtures defined as $\pi = \alpha T/\beta$ are displayed in Figure 5 along with those of pure water and other pure molten salts.¹⁵ They are intermediate between water and pure salts, and have a very steep gradient typical of liquids comprised of small hard sphere molecules such as Hg, NaNO_3 , and LiNO_3 .

According to Rice¹⁶ small activation volumes are to be expected when the intermolecular repulsive potential is

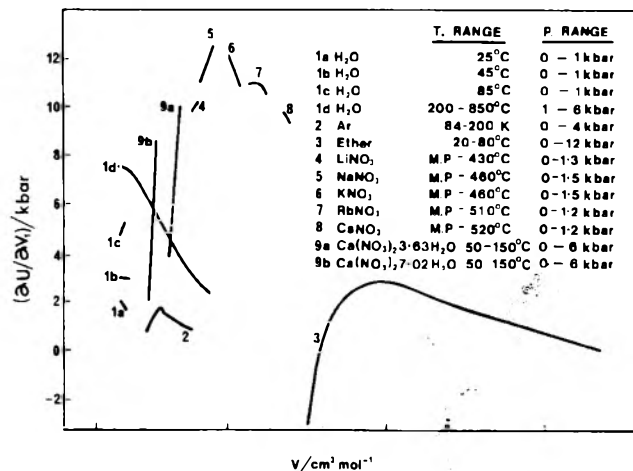


Figure 5. Comparison of internal pressure vs. volume of $\text{Ca}(\text{NO}_3)_2 \cdot 3.63\text{H}_2\text{O}$ and $\text{Ca}(\text{NO}_3)_2 \cdot 7.02\text{H}_2\text{O}$ with other polar and ionic fluids.

very steep on a molecular scale, for example, in liquid argon $\Delta V_{\text{diff}} = 32 \text{ cm}^3 \text{ mol}^{-1}$,¹⁶ compared with $\Delta V_\Lambda = 3.8 \text{ cm}^3 \text{ mol}^{-1}$ for NaNO_3 .¹⁷ The π vs. volume curve for NaNO_3 is quite steep compared to that of argon. Similarly, ΔV_Λ 's for $\text{Ca}(\text{NO}_3)_2/\text{H}_2\text{O}$ mixtures at high temperatures, i.e., at least $T = 2T_0$, are small and in the limit of high temperatures tend to a value of $\Delta V_\Lambda \approx 1 \text{ cm}^3 \text{ mol}^{-1}$ at 1 bar. Clearly, at low temperatures where $T \rightarrow T_0$ and cooperative particle movements become dominant the above criterion relating ΔV_Λ to the steepness of the intermolecular potential is not valid.

Conclusion

The molar conductivity of $\text{Ca}(\text{NO}_3)_2 \cdot 3.63, 4.85\text{H}_2\text{O}$ solution obeys the VTF equation up to 122 °C and 6 kbar. ΔV_Λ for $\text{Ca}(\text{NO}_3)_2 \cdot 3.63, 4.85, 5.98, 7.02\text{H}_2\text{O}$ mixtures is a function of temperature and pressure as predicted by the VTF equation. The B parameter in the VTF equation is a complex term which is unlikely to be independent of temperature and pressure over a wide range of conditions.

References and Notes

- (1) C. A. Angell and R. D. Bressel, *J. Phys. Chem.*, **76**, 3244 (1972).
- (2) C. A. Angell, L. J. Pollard, and W. Strauss, *J. Solution Chem.*, **6**, 517 (1972).
- (3) C. A. Angell and J. C. Tucker, *J. Phys. Chem.*, **78**, 278 (1974).
- (4) G. Adam and J. H. Gibbs, *J. Chem. Phys.*, **43**, 139 (1965).
- (5) C. A. Angell, L. J. Pollard, and W. Strauss, *J. Chem. Phys.*, **50**, 2694 (1968).
- (6) F. S. Howell, R. A. Bose, P. B. Macedo, and C. T. Moynihan, *J. Phys. Chem.*, **78**, 639 (1974).
- (7) J. H. Ambrus, C. T. Moynihan, and P. B. Macedo, *J. Electrochem. Soc.*, **119**, 192 (1972).
- (8) A. F. M. Barton and R. J. Speedy, *J. Chem. Soc., Faraday Trans.*, **70**, 506 (1974).
- (9) Y. C. Chiu and R. M. Fuoss, *J. Phys. Chem.*, **72**, 4123 (1968).
- (10) A. J. Ellis, *J. Chem. Soc. A*, 1579 (1966).
- (11) A. I. Vogel, "Quantitative Inorganic Analysis", 3rd ed, Chaucer Press, Great Britain, 1966.
- (12) H. Tuerer, J. H. Simmons, and P. B. Macedo, *J. Chem. Phys.*, **54**, 1952 (1970).
- (13) R. F. Hester and R. A. Plane, *J. Chem. Phys.*, **40**, 411 (1964).
- (14) B. Balshaw and S. I. Smedley, *J. Phys. Chem.*, **79**, 1323 (1975).
- (15) A. F. M. Barton, *J. Chem. Educ.*, **48**, 156 (1971).
- (16) J. Naghizadeh and S. A. Rice, *J. Chem. Phys.*, **36**, 2710 (1962).
- (17) A. F. M. Barton, B. Cleaver, and G. J. Hills, *Trans. Faraday Soc.*, **64**, 208 (1968).
- (18) W. C. Burnham, J. R. Holloway, and N. F. Davis, "Thermodynamic Properties of Water to 1000 °C and 10 000 bar", American Geological Society, 1969.
- (19) A. F. M. Barton, G. J. Hills, D. J. Fray, and J. W. Tomlinson, *High Temp. High Pressure*, **2**, 437 (1970).

Hydrogen-1 and Carbon-13 Nuclear Magnetic Resonance Investigation of Nicotinic Acid, Its Anion, and Cation in Water and Water-Dimethyl Sulfoxide Mixtures. Influence of Dimethyl Sulfoxide on Relative Acidities

Tauqir Khan, Jean-Claude Halle, Marie-Paule Simonnin, and Robert Schaal*

Laboratoire de Physicochimie des Solutions, LA 146, and Laboratoire de Spectrographie RMN, ERA 390, E.N.S.C.P., 11 rue Pierre et Marie Curie, 75231 Paris Cedex 05, France (Received October 4, 1976)

Publication costs assisted by the University Pierre et Marie Curie

¹H and ¹³C NMR spectra of nicotinic acid, its anion, and cation have been studied in water and in the 20:80 (v/v) H₂O/Me₂SO mixture (concentration 0.148 M). Characteristic protonation shifts for N protonation and COO⁻ protonation allow an unambiguous determination of the protonation site and reveal an inversion of relative acidities on going from water to H₂O/Me₂SO mixture. Experimental results indicate that the tautomeric equilibrium between neutral forms of nicotinic acid is displaced toward the zwitterionic form in water, but toward the molecular form in Me₂SO. pK_a values calculated from ¹³C titration curves obtained at 20 °C are in excellent agreement with those obtained by a potentiometric study.

Introduction

Nuclear magnetic resonance spectroscopy has proved to be a powerful method to study structural problems such as tautomeric equilibrium¹ and protonation and deprotonation of heterocyclic compounds.²⁻⁵ Various pK_a values and thermodynamic functions of substituted pyridines have been obtained by ¹H NMR.^{6,7} Recent ¹³C NMR study of compounds of biological interest, whose spectra are pH dependent,⁸ has led to different investigations concerning various nitrogen heterocyclic compounds,^{2,5} acids,^{9,10} and amino acids.^{11,12} The results clearly indicate that ¹³C NMR allows a safe determination of the site of protonation.

The results of Goldstein¹³ and Feeney¹⁴ on N protonation of nicotinamide suggest that ¹³C chemical shift information may be useful to study a similar but more complex system such as that of nicotinic acid, for which four species in equilibrium may be present (Scheme I), depending on solvent composition and pH.

According to previous spectrometric and/or potentiometric studies, the zwitterionic Z form would be largely favored (≈95%) in pure water¹⁵⁻¹⁷ whereas the molecular M form would be the only one present in water-dimethyl sulfoxide mixtures containing more than 60% Me₂SO.¹⁷ Therefore the successive protonations of the anion B⁻ would essentially occur through path 1 in water and through path 2 in mixtures containing more than 60% Me₂SO.

In this paper, we report the results of ¹H and ¹³C NMR investigations of nicotinic acid in water and in the 20:80 (v/v) H₂O/Me₂SO mixture, over a wide range of pH values. Since ¹H and ¹³C chemical shifts are expected to be affected differently by the protonation of the nitrogen or the COO⁻ group, this study provides unambiguous proof of a different protonation sequence in dimethyl sulfoxide than in water.

Results and Discussion

I. *Proton Chemical Shift Data.* Proton spectra were run at 100 MHz in water and in the 20:80 (v/v) H₂O/Me₂SO mixture in the pH range 1-10. Proton assignments were made by comparing the measured H-H coupling constants with reported values for 3-substituted pyridines.¹⁸ Table I summarizes the results of ¹H chemical shifts for the four possible forms of nicotinic acid in water

Scheme I

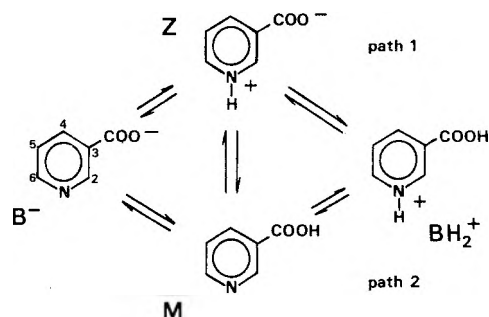


TABLE I: ¹H Chemical Shifts^a of Nicotinic Acid and Its Charged Species (C = 0.148 M)

Proton	H ₂ O solvent		20:80 (v/v) H ₂ O/Me ₂ SO solvent			
	Anion pH	Zwitterion pH	Cation pH	Anion pH	Mole- cule pH	Cation pH
	10.45	3.43	0.06	>15	3.80	0.4
2	8.9 ₃	9.1 ₄	9.3 ₈	8.9 ₉	9.1 ₀	9.3 ₁
4	8.2 ₄	8.9 ₁	9.1 ₄	8.2 ₂	8.3 ₅	9.0 ₈
5	7.5 ₀	8.0 ₉	8.2 ₆	7.4 ₃	7.6 ₂	8.3 ₂
6	8.6 ₀	8.8 ₆	9.0 ₄	8.5 ₅	8.8 ₁	9.1 ₈

^a δ values in ppm from DSS as internal reference.

and in the 20:80 (v/v) H₂O/Me₂SO mixture.

Figure 1 shows the influence of the two successive protonations on the ¹H chemical shifts on going from the anionic B⁻ form to the cationic BH₂⁺ form. In agreement with previous observations, each protonation results in a decreased shielding of the protons.² For anionic and cationic forms, δ values exhibit only a weak dependence on the solvent composition. On the contrary, for the neutral form, large chemical shift differences are observed for H₄ and H₅, confirming the existence of two different tautomeric forms M and Z, depending on the solvent composition.

Pugmire and Grant² reported that β and γ protons are more affected than the α protons by N protonation of pyridine. Here, the largest downfield shifts of about 0.7-0.8 ppm are observed for H₄ and H₅ during the first protonation in water and the second protonation in the

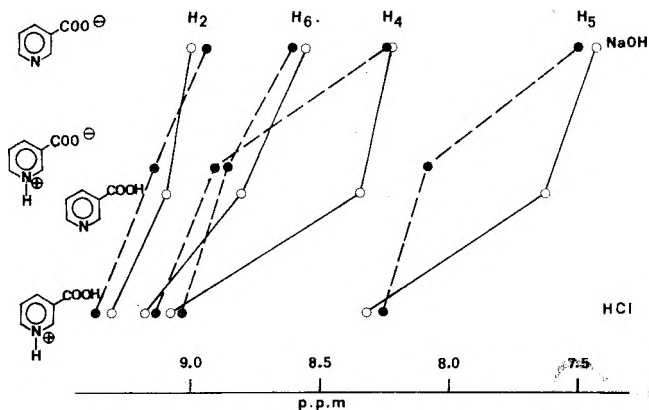


Figure 1. Influence of solvent composition on ^1H chemical shifts of nicotinic acid and its charged species: anion, zwitterion, and cation in water (●—●); anion, molecule, and cation in $\text{H}_2\text{O}/\text{Me}_2\text{SO}$ (20:80 v/v) mixture (○—○) (δ in ppm from DSS).

$\text{H}_2\text{O}/\text{Me}_2\text{SO}$ mixture. This clearly shows that protonation of the carboxylate group follows the N protonation in water, while this COO^- protonation occurs first in the 20:80 (v/v) $\text{H}_2\text{O}/\text{Me}_2\text{SO}$ mixture. The observation that all the protons move slightly downfield during the protonation of the COO^- group further confirms these protonation sequences.

II. Carbon-13 Chemical Shift Data. ^{13}C spectra were run with proton noise decoupling. Assignments of individual carbons were made by selective proton irradiation experiments. Tables II and III summarize the results in water and in the 20:80 (v/v) $\text{H}_2\text{O}/\text{Me}_2\text{SO}$ mixture, respectively.

Solvent Effects on $\delta_{13\text{C}}$ of Anionic and Cationic Forms. Comparison of Tables II and III indicates that ^{13}C chemical shifts of the anionic B^- and cationic BH_2^+ forms of nicotinic acid are solvent dependent. In general, ^{13}C are more shielded in the $\text{H}_2\text{O}/\text{Me}_2\text{SO}$ mixture than in water, except for C_3 in the anion which is deshielded by 0.7 ppm. These solvent shifts are related to changes in solvation of both polar groups in B^- and BH_2^+ forms of nicotinic acid.

TABLE II: ^{13}C Chemical Shifts^a of Nicotinic Acid and Its Charged Species (Solvent H_2O ; $C = 0.148\text{ M}$)

Carbon	Anion pH 10.45	$\Delta\delta^b$ N proton- ation	Zwit- terion pH 3.43	$\Delta\delta^c$ COO^- proton- ation	Cation pH 0.06
2	151.6 _s	-6.3 _s	145.3 _o	+0.2 _o	145.5 _o
3	134.8 _o	+3.1 _s	137.9 _s	-4.8 _o	133.1 _s
4	140.3 _s	+8.0 _s	148.4 _o	+1.4 _s	149.8 _s
5	126.6 _o	+2.9 _s	129.5 _s	+0.7 _s	130.3 _o
6	153.0 _s	-7.2 _o	145.8 _s	+1.1 _s	147.0 _o
CO	175.9 _o	-4.9 _s	170.9 _s	-3.6 _o	167.3 _s

^a δ values in ppm from DSS as internal reference at $t \approx 20 \pm 2^\circ\text{C}$. ^b N protonation shifts: $\Delta\delta = \delta_{\text{zwitterion}} - \delta_{\text{anion}}$. ^c COO^- protonation shifts: $\Delta\delta = \delta_{\text{cation}} - \delta_{\text{zwitterion}}$. Negative values indicate upfield shifts.

TABLE III: ^{13}C Chemical Shifts^a of Nicotinic Acid and Its Charged Species (Solvent 20:80 (v/v) $\text{H}_2\text{O}/\text{Me}_2\text{SO}$; $C = 0.148\text{ M}$)

Carbon	Anion pH > 15	$\Delta\delta^b$ COO^- proton- ation	Mole- cule pH 3.80	$\Delta\delta^c$ N proton- ation	Cation pH 0.25
2	151.5	-0.1	151.4	-7.5	143.9
3	135.5	-7.1	128.4	+3.4	131.8
4	138.6	+0.6	139.2	+8.9	148.1
5	124.9	+1.0	125.9	+3.5	129.4
6	151.4	+3.2	154.6	-8.7	145.9
CO	170.5	-2.4	168.1	-3.3	164.8

^a δ values in ppm from DSS as internal reference at $t \approx 20 \pm 2^\circ\text{C}$. ^b COO^- protonation shifts: $\Delta\delta = \delta_{\text{molecule}} - \delta_{\text{anion}}$. ^c N protonation shifts: $\Delta\delta = \delta_{\text{cation}} - \delta_{\text{molecule}}$. Negative values indicate upfield shifts.

Moreover, ring carbons are less affected (<1.8 ppm) than the carboxyl carbon for which solvent shifts of 2.6 and 5.4 ppm are observed for the BH_2^+ and B^- forms, respectively. The noticeable solvent effect exhibited by the COO^- group indicates that the negative charge density is smaller in water than in the $\text{H}_2\text{O}/\text{Me}_2\text{SO}$ mixture, thus suggesting a much stronger solvation of the carboxylate group by

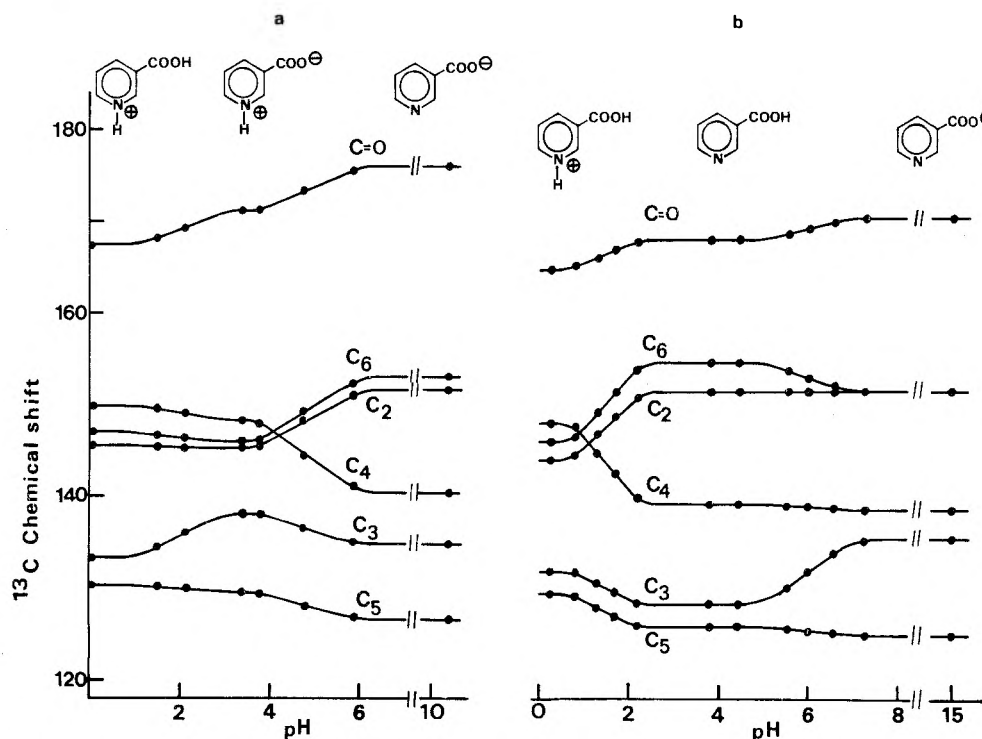


Figure 2. ^{13}C chemical shifts (ppm from DSS) as a function of pH of nicotinic acid in water (a) and in $\text{H}_2\text{O}/\text{Me}_2\text{SO}$ (20:80 v/v) mixture (b).

water than by Me₂SO. This is in agreement with the well-known ability of Me₂SO to badly solvate small anions with localized charge.¹⁹

N Protonation. ¹³C chemical shifts of nicotinic acid are plotted against pH values in water (Figure 2a) and in the 20:80 (v/v) H₂O/Me₂SO mixture (Figure 2b). These graphs reveal the strong influence of Me₂SO on the protonation sequence.

It has been shown² that nitrogen protonation of pyridine results in an upfield shift of the α carbons (-7.78 ppm) and a downfield shift of both β and γ carbons (β +5.04 ppm; γ +12.42 ppm). Similarly, when the nicotinamide becomes protonated in D₂O,¹⁴ the α carbons and the carbonyl carbon move upfield (C₂ -6.43 ppm; C₆ -8.06 ppm; CO -4.08 ppm) while the β and γ carbons move downfield (C₃ +3.85 ppm; C₅ +3.65 ppm, C₄ +9.41 ppm).

In the case of nicotinic acid, a very similar trend is observed for the first protonation in water whereas this behavior is observed for the second protonation in the H₂O/Me₂SO mixture. Therefore, ¹H NMR as well as ¹³C data prove unambiguously that the successive protonations of the anionic form of nicotinic acid follow primarily path 2 in the 20:80 (v/v) H₂O/Me₂SO mixture instead of path 1 in water.

On the other hand, N protonation shifts are smaller in water than in the H₂O/Me₂SO mixture. This behavior cannot be attributed only to the existence of the tautomeric equilibrium between the Z and M forms of nicotinic acid in water, since the small amount of M (≈ 5%)¹⁵⁻¹⁷ is not sufficient to explain the observed differences. These differences may be a consequence of solvation of nitrogen lone pair by water. Indeed, EHT calculations²⁰ indicate that hydrogen bonding between pyridine and water (or methanol) increases the electronic density at C_α; N protonation results in a similar but more important variation.

COO⁻ Protonation. Previous studies of ¹³C chemical shifts in aliphatic carboxylic acids¹⁰ and α-amino acids^{11,12} indicate that, contrary to chemical intuition based on the inductive model only, protonation of the carboxylate group causes an upfield shift of all the carbons and the importance of these effects decreases in the order CO > C_α > C_β.

During protonation of the COO⁻ group of nicotinic acid, which occurs at pH < 3 in water and for 4.0 < pH < 10.0 in the 20:80 (v/v) H₂O/Me₂SO mixture, the shielding of C₄, C₅, and C₆ decreases, whereas that of C₂ remains approximately constant; at the same time, shielding of both the carbonyl carbon and C₃ increases and, unexpectedly, C₃ is more affected than the carbonyl cation. This behavior might be related to the aromatic character of the pyridine ring.

Influence of Me₂SO Content on the M ⇌ Z Tautomeric Equilibrium. In order to confirm the influence of solvent composition on the tautomeric equilibrium,¹⁷ we studied ¹³C chemical shifts of nicotinic acid in different H₂O/Me₂SO mixtures.

In spite of the low nicotinic acid concentration (C = 0.148 M) used throughout this work, the drastic solubility decrease observed in the H₂O/Me₂SO mixtures containing less than 70% Me₂SO precludes experiments over a wide range of solvent composition. Results obtained in water and in mixtures containing 75-100% Me₂SO (0.41-1 mole fraction) are summarized in Table IV.

A decrease in the Me₂SO mole fraction from 1 to 0.41 results in variations which do not exceed 0.7 ppm. These variations, which are similar in magnitude and direction (except for the substituted 3 carbon) to those reported for

TABLE IV: ¹³C Chemical Shifts^a of the Neutral Forms of Nicotinic Acid in Various H₂O/Me₂SO Mixtures (C = 0.148 M).

Me ₂ -SO, vol %	Me ₂ -SO, mole fraction	C ₂	C ₃	C ₄	C ₅	C ₆	CO
100	1	151.8	128.1	138.6	125.5	154.9	167.9
90	0.697	151.6	128.2	138.8	125.6	154.8	167.9
80	0.487	151.4	128.4	139.2	125.9	154.6	168.1
75	0.41	151.3	128.4	139.3	125.9	154.5	168.2
0	0	145.3	138.0	148.4	129.6	145.9	170.9

^a δ values in ppm from DSS as internal reference at t ≈ 20 ± 2 °C.

nicotinamide on going from pure Me₂SO to water,¹³ reflect the solvent effect on the molecular form M of nicotinic acid. On the other hand, important variations are observed when the Me₂SO mole fraction decreases from 0.41 to 0.0; greatest effects are observed for C₃ (downfield shift +9.6 ppm) and C₆ (upfield shift -8.6 ppm) in accordance with the trend expected for simultaneous N protonation and COOH deprotonation involved in the M → Z transformation.

III. pK_a Values Determination. Plots of ¹³C chemical shifts againsts pH values (Figure 2a,b) allow an easy and precise determination of the acidity constants in water and in the 20:80 (v/v) H₂O/Me₂SO mixture.

The experimental chemical shifts of the *i*th carbon, δ₁^{*i*} and δ₂^{*i*}, during the first and the second titration, are given by

$$\delta_1^i = P_{\text{BH}_2^+} \delta_{\text{BH}_2^+}^i + P_{\text{BH}} \delta_{\text{BH}}^i \quad (1)$$

$$\delta_2^i = P_{\text{BH}} \delta_{\text{BH}}^i + P_{\text{B}^-} \delta_{\text{B}^-}^i$$

where δ_{BH₂⁺ and δ_{B⁻ represent the chemical shift of the *i*th carbon in the cationic and anionic forms and δ_{BH}^{*i*} represents the chemical shift of the *i*th carbon in the neutral species (Z in water and M in the 20:80 (v/v) H₂O/Me₂SO mixture). The values of δ_{BH₂⁺, δ_{BH}^{*i*}, and δ_{B⁻ are obtained from the plateaus of Figures 2a,b. Indeed the existence of these plateaus suggests that ¹³C chemical shifts of these species are not affected by ionic strength. P_{BH₂⁺}, P_{BH}, and P_{B⁻} represent the fractional populations of the corresponding species and are related by}}}}

$$P_{\text{BH}_2^+} + P_{\text{BH}} = 1 \quad (2)$$

$$P_{\text{BH}} + P_{\text{B}^-} = 1$$

From (1) and (2) the ratios P_{BH}/P_{BH₂⁺} or P_{B⁻}/P_{BH}, identical with the respective concentration ratios C_{BH}/C_{BH₂⁺} or C_{B⁻}/C_{BH}, can be calculated for each pH value.

The low concentration used in this work allows an estimation of activity coefficients *y*, so that not only apparent pK_a values at the ionic strength of the measurement, but the thermodynamic pK_a values may be determined by

$$\text{p}K_a^1 = \text{pH} - \log \frac{C_{\text{BH}}}{C_{\text{BH}_2^+}} + \log y_{\text{BH}_2^+} \quad (3)$$

$$\text{p}K_a^2 = \text{pH} - \log \frac{C_{\text{B}^-}}{C_{\text{BH}}} - \log y_{\text{B}^-}$$

As usual, activity coefficients of the neutral species BH (Z or M) are taken equal to one.²¹ Those of charged species are given by

$$\log y_{\pm} \approx -A\sqrt{I}/(1 + \sqrt{I}) \quad (4)$$

which is suitable for ionic strength *I* up to 0.1.²² At 20 °C,

the constant A of expression 4 is 0.507 in water²² and 0.50 in the 20:80 (v/v) H₂O/Me₂SO mixture.²³

From the midpoint of the titration curves, where the errors are minimum, the average pK_a values calculated from most affected carbons are as follows: 1.37 ± 0.04 , 6.14 ± 0.04 for the two successive ionizations in the H₂O/Me₂SO mixture and 4.93 ± 0.04 for the second ionization in water (at $t = 20$ °C). These results are in full agreement with the thermodynamic pK_a values directly measured by potentiometric titrations which are 1.39, 6.12, and 4.90, respectively.¹⁷ However it should be noted that the accuracy is less for the first ionization of nicotinic acid in water, since the pK_a value obtained from NMR is 1.87 which is about 0.15 units lower than the thermodynamic value measured by the potentiometric or spectroscopic method.^{16,17,24} This discrepancy arises from the fact that ¹³C chemical shifts are only slightly affected by the protonation of the carboxylate group in water, therefore only C₃ and the carbonyl carbon may be considered in the pK_a calculation.

Conclusion

Previous studies have emphasized the difficulty in relating ¹³C protonation shifts with charge densities alone and indicated that the electric field effect¹⁰ as well as variations in bond order² and in excitation energy^{4,12} have to be taken into account. As pointed out by Quirt et al.,¹² the lack of agreement between experimental and calculated ¹³C NMR shifts is due to the various approximations involved in the calculations; moreover the calculated charge densities are appropriate to the gas phase and neglect changes in solvation which may be important in the course of the experimental titrations.

The results obtained in this study indicate that experimental protonation shifts of nicotinic acid are, indeed, solvent dependent, thus confirming the importance of solvation effect. Despite the difficulty in rationalizing ¹³C protonation shifts, their values allow us to distinguish between N protonation and COO⁻ protonation, so that the strong influence of Me₂SO on the protonation sequence of nicotinic acid is clearly demonstrated. Whereas the carboxylic group of nicotinic acid is more acidic than the NH⁺ center in water, addition of Me₂SO progressively decreases the difference between the respective pK_a values, which results in an inverse protonation sequence in the 20:80 (v/v) H₂O/Me₂SO mixture.

Similar inversions have been reported in other related systems.^{25,26} The results clearly emphasize the importance of solvation effects, which was recently noticed by the observation of inversions in the relative acidities of a number of substrates when comparing results in the gas phase and various solvents.²⁷

Experimental Section

Nicotinic acid (Schuchardt) was used without further purification. Dimethyl-*h*₆ sulfoxide (Société Nationale des Pétroles d'Aquitaine) was dried overnight over CaH₂ and distilled under vacuum. The 20:80 (v/v) H₂O/Me₂SO mixture corresponds to a mole fraction of 0.487 in Me₂SO.

The total concentration of nicotinic acid ($C = 0.148$ M) was kept constant and the different solutions were prepared by adding either hydrochloric acid or sodium hydroxide. Obviously the ionic strength, I , was not constant along the titration curves but, for each midpoint, $I = 0.074$.

The pH measurements were performed at 20 °C with an electronic pH meter (Taccussel ISIS 20 000) equipped with a Radiometer G 202 B glass electrode and a Ra-

diometer K 100 calomel electrode. The glass electrode was standardized in water with usual mineral buffers. Since it has been shown that the normal potential of the glass electrode is notably affected by Me₂SO,²⁸ the glass electrode was standardized in the 20:80 (v/v) H₂O/Me₂SO mixture by using the organic buffers previously standardized in the same mixture with a hydrogen electrode.²⁹

NMR spectra were recorded on a Varian XL-100-12 W. G. spectrometer. ¹H and ¹³C chemical shifts were measured with sodium 4,4-dimethyl-4-silapentanesulfonate (DSS) as internal reference. The ¹³C chemical shift of DSS relative to TMS in the 20:80 (v/v) H₂O/Me₂SO mixture is $\delta_{DSS} = -1.7 \pm 0.03$ ppm. ¹H spectra (100 MHz, 5-mm tubes) were studied using the CW mode. ¹H resonance of the solvent was used to provide the field frequency lock. ¹³C spectra (25.17 MHz, 10-mm tubes) were collected using the Fourier transform technique. The instrument was equipped with a 620L-100-16K on-line computer. The temperature of the sample was maintained at 20 ± 2 °C. A capillary, filled with D₂O, served as an internal lock. About 20 000 to 46 000 free induction decays were accumulated in order to achieve a good signal-to-noise ratio. In the case of H₂O/Me₂SO mixtures, data were accumulated in the block averaging mode. Typical parameters for the pulse experiments were as follows: spectral width 5000 Hz, pulse width 10 μ s, pulse delay 0.4 s, acquisition time 0.8 s (0.4 s). ¹H-¹³C double resonance experiments were carried out using the gyrocode of the XL-100. The δ values are within 0.02 ppm for ¹H data and within 0.05 and 0.1 ppm for ¹³C data in water and H₂O/Me₂SO mixtures, respectively.

References and Notes

- (1) U. Vogeli and W. Von Philipsborn, *Org. Magn. Reson.*, **5**, 551 (1973).
- (2) R. J. Pugmire and D. M. Grant, *J. Am. Chem. Soc.*, **90**, 697 (1968).
- (3) R. J. Pugmire and D. M. Grant, *J. Am. Chem. Soc.*, **90**, 4232 (1968).
- (4) A. J. Jones, D. M. Grant, J. G. Russell, and G. Fraenkel, *J. Phys. Chem.*, **73**, 1624 (1969).
- (5) G. Müller and W. Von Philipsborn, *Helv. Chim. Acta*, **56**, 2680 (1973).
- (6) M. W. Mosher, C. B. Sharma, and M. R. Chakrabarty, *J. Magn. Reson.*, **7**, 247 (1972).
- (7) M. R. Chakrabarty, C. S. Handloser, and M. W. Mosher, *J. Chem. Soc., Perkin Trans. 2*, 938 (1973).
- (8) D. E. Dorman and J. D. Roberts, *Proc. Natl. Acad. Sci. U.S.A.*, **65**, 19 (1970).
- (9) A. Patterson and R. Ettinger, *Z. Elektrochem.*, **64**, 98 (1960).
- (10) R. Hagen and J. D. Roberts, *J. Am. Chem. Soc.*, **91**, 4504 (1969).
- (11) W. J. Horsley and H. S. Sternlicht, *J. Am. Chem. Soc.*, **90**, 3738 (1968).
- (12) A. R. Quirt, J. R. Lyster, I. R. Peat, J. S. Cohen, W. F. Reynolds, and M. H. Freedman, *J. Am. Chem. Soc.*, **96**, 570 (1974).
- (13) K. R. Long, R. C. Long, and J. H. Goldstein, *J. Magn. Reson.*, **8**, 207 (1972).
- (14) B. Birdsall, J. Feeney, and P. Partington, *J. Chem. Soc., Perkin Trans. 2*, 2145 (1973).
- (15) H. H. Jaffe, *J. Am. Chem. Soc.*, **77**, 4445 (1955).
- (16) R. W. Green and H. K. Tong, *J. Am. Chem. Soc.*, **78**, 4896 (1956).
- (17) T. Khan, J.-C. Halle, and R. Schaal, manuscript in preparation.
- (18) V. J. Kowalewski and D. G. de Kowalewski, *J. Chem. Phys.*, **36**, 266 (1962).
- (19) A. J. Parker, *Chem. Rev.*, **69**, 1 (1969).
- (20) W. Adam, A. Grimison, and R. Hoffmann, *J. Am. Chem. Soc.*, **90**, 1509 (1968).
- (21) A. Albert and E. P. Serjeant, "Ionization Constants of Acids and Bases", Methuen, London, 1962, p. 119.
- (22) R. A. Robinson and R. H. Stokes, "Electrolyte Solutions", 2nd ed, Butterworths, London, 1959.
- (23) J.-C. Halle, R. Gaboriaud, and R. Schaal, *Bull. Soc. Chim. Fr.*, 1851 (1969).
- (24) P. O. Lumme, *Suomen Kemi*, **30B**, 168 (1957).
- (25) J.-C. Halle and R. Schaal, *Anal. Chem. Acta*, **60**, 197 (1972).
- (26) J.-C. Halle, F. Terrier, and R. Gaboriaud, *Bull. Soc. Chim. Fr.*, 1231 (1973).
- (27) C. Agami, *Bull. Soc. Chim. Fr.*, 869 (1974), and references therein.
- (28) J.-C. Halle, R. Harivel, and R. Gaboriaud, *Can. J. Chem.*, **52**, 1774 (1974).
- (29) J.-C. Halle, R. Gaboriaud, and R. Schaal, *Bull. Soc. Chim. Fr.*, 2047 (1970).

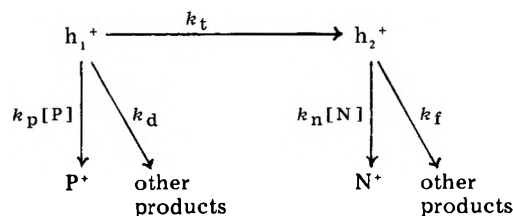
COMMUNICATIONS TO THE EDITOR

Selective Capture of Migrating Holes by Pyrene and Naphthalene in γ -Irradiated Butyl Chloride Glasses at 77 K

Publication costs assisted by The Institute of Physical and Chemical Research

Sir: γ -Irradiation of solutions in alkyl halide glasses produces cation radicals of solute molecules,¹ which will be referred to as cations. The cation formation is explained in terms of capture of migrating holes by solute molecules.^{2,3} Spectra which may be associated with stabilized holes have been measured and the kinetics of hole scavenging has also been studied;¹⁻⁴ however, the nature of the migrating hole has not been clarified yet. Recently it has been suggested that vibrational excited states of solute-molecule cations may be the migrating hole.⁴ In this communication we present the results for hole scavenging by pyrene and naphthalene in a *sec*-butyl chloride glass at 77 K. The interesting finding is that each of these solutes captures a different state of the hole.

Glasses of *sec*-butyl chloride containing both naphthalene and pyrene were γ irradiated to a dose of 2×10^{22} eV kg⁻¹ at 77 K. The yield of the pyrene cation was measured as D_p , the optical density for the 791-nm band of the pyrene cation.⁵ The yield of the naphthalene cation was measured as D_n , the optical density for its 703-nm band;⁵ D_n was corrected for the superposing pyrene-cation absorption. The dependence of both D_p and D_n on solute concentration is shown by the Stern-Volmer plots in Figures 1 and 2. The naphthalene-cation yield depends on the naphthalene concentration as shown in Figure 1A and on the pyrene concentration as shown in Figure 1B. The pyrene-cation yield is dependent on pyrene concentration but independent of naphthalene concentration as shown in Figure 2. The scheme that both solutes competitively trap the single state of the hole can never satisfy the four plots simultaneously. Instead, the following scheme can account for the results:



Pyrene first reacts with h_1^+ , the hole in a certain state, and forms the pyrene cation P^+ . The h_1^+ is assumed to be unreactive with naphthalene. A portion of the holes that survive the capture by pyrene changes to h_2^+ , another state of the hole, which selectively reacts with naphthalene to form the naphthalene cation. Using the notation of rate constants given in the above diagram, we can write the equations

$$\frac{Y_h}{Y_p} = 1 + \frac{k_d + k_t}{k_p [P]} \quad (1)$$

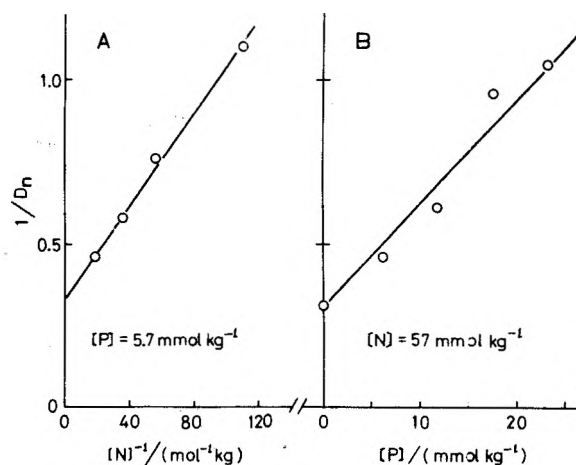


Figure 1. The dependence of the naphthalene-cation yield on naphthalene concentration (A) and on pyrene concentration (B).

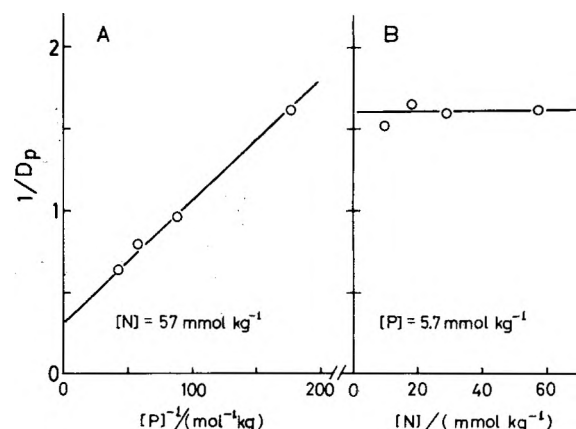


Figure 2. The dependence of the pyrene-cation yield on pyrene concentration (A) and on naphthalene concentration (B).

$$\frac{Y_h}{Y_n} = \left(1 + \frac{k_d + k_p[P]}{k_t}\right) \left(1 + \frac{k_f}{k_n [N]}\right) \quad (2)$$

where Y_h represents the h_1^+ yield; Y_p , the pyrene-cation yield; and Y_n , the naphthalene-cation yield. The ratio Y_h/Y_p in eq 1 can be replaced by D_p^0/D_p , where D_p^0 is the D_p value extrapolated on the ordinate. Consequently, the plot in Figure 2A fits eq 1, and $(k_d + k_t)/k_p$ is evaluated as 2.4×10^{-2} mol kg⁻¹. The fact that the pyrene-cation yield is independent of naphthalene concentration (Figure 2B) is explained in terms of eq 1. Equation 2 can reproduce the lines of Figure 1, when it is written using the optical density ratio D_n^0/D_n . The plot in Figure 1A gives a value of 2.1×10^{-2} mol kg⁻¹ for k_f/k_n .

Hamill and co-workers have studied capture of the hole in glassy solutions of 3-methylpentane containing two solutes.^{2,3} Most of their results are not enough to judge whether the holes captured by the two solutes are of the same state or not, since the effects of two solutes on each of the two cations were not examined. Furthermore, the processes involved in the systems they dealt with may be complicated. According to current knowledge, 2-methylpentene-1 and toluene may form dimer cations in

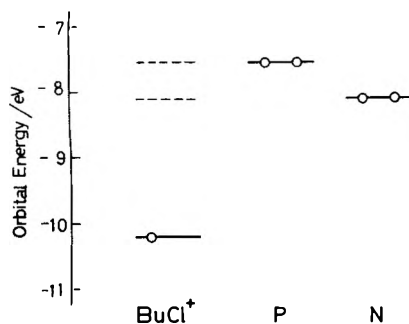


Figure 3. Energy diagram of the highest occupied orbitals of butyl chloride cations, pyrene, and naphthalene.

a 3-methylpentane matrix without thermal annealing.^{6,7} Their results for the solute pair of toluene and carbon tetrachloride³ suggest that each of these solutes reacts selectively with a different precursor. However, these different precursors do not immediately mean the different states of the hole, since the resultant transient originating in carbon tetrachloride is not identified definitely with CCl_4^+ . Therefore, we will not attempt to interpret their results and ours together but will discuss only ours.

Figure 3 shows an energy diagram based on gas-phase ionization potentials. The above proposed scheme is incompatible with the model that the migrating hole is the ground state of the solvent cation which is depicted in Figure 3. The selective capture of the hole by the two

solutes suggests that an electron transfers resonantly from a solute molecule to the hole. Therefore, a simple model compatible with the scheme is as follows. Excited states of either solvent cations or solvent aggregate cations hop in a glass, losing the excitation energy. These are migrating holes. The resonant charge transfer occurs when the energy of the migrating excited state becomes as high as the energy levels of the highest occupied orbitals of the solute molecules, as indicated by dotted lines in Figure 3. This model indicates that pyrene whose ionization potential is lower than that of naphthalene captures the hole before naphthalene does. Experiments on various solute pairs are in progress.

References and Notes

- (1) W. H. Hamill, "Radical Ions", E. T. Kaiser and L. Kevan, Ed., Interscience, New York, N.Y., 1968.
- (2) J. B. Gollivan and W. H. Hamill, *J. Chem. Phys.*, **44**, 2378 (1966).
- (3) D. W. Skelly and W. H. Hamill, *J. Phys. Chem.*, **70**, 1630 (1966).
- (4) S. Arai, A. Kira, and M. Imamura, *J. Phys. Chem.*, **80**, 1968 (1976).
- (5) T. Shida and S. Iwata, *J. Am. Chem. Soc.*, **95**, 3473 (1973).
- (6) B. Badger and B. Brocklehurst, *Trans. Faraday Soc.*, **65**, 2576, 2582 (1969).
- (7) R. E. Buhler and W. Funk, *J. Phys. Chem.*, **79**, 2098 (1975).

The Institute of Physical and
Chemical Research
Wako, Saitama 351, Japan

Akira Kira*
Takashi Nakamura
Masashi Imamura

Received October 28, 1976

PHYSICAL PHENOMENA

spectroscopy,
thermodynamics,
reaction kinetics,
and other areas
of experimental
and theoretical
physical chemistry
are covered
completely in

THE JOURNAL OF PHYSICAL CHEMISTRY

The biweekly JOURNAL OF PHYSICAL CHEMISTRY includes over 25 papers an issue of original research by many of the world's leading physical chemists. Articles, communications, and symposia cover new concepts, techniques, and interpretations. A "must" for those working in the field or interested in it, the JOURNAL OF PHYSICAL CHEMISTRY is essential for keeping current on this fast moving discipline. Complete and mail the coupon now to start your subscription to this important publication.

AVAILABLE IN HARD COPY
OR MICROFICHE.

**The Journal of Physical Chemistry
American Chemical Society**

1155 Sixteenth Street, N.W.
Washington, D.C. 20036

1977

Yes, I would like to receive the JOURNAL OF PHYSICAL CHEMISTRY at the one-year rate checked below:

	U.S.	Foreign and Canada	Latin America
ACS Member*	<input type="checkbox"/> \$24.00	<input type="checkbox"/> \$34.00	<input type="checkbox"/> \$33.00
Nonmember	<input type="checkbox"/> \$96.00	<input type="checkbox"/> \$106.00	<input type="checkbox"/> \$105.00
Bill me <input type="checkbox"/>	Bill company <input type="checkbox"/>	Payment enclosed <input type="checkbox"/>	

Air freight rates available on request.

Name _____

Street _____

Home
Business

City _____

State _____

Zip _____

Journal subscriptions start in January '77.

Allow 60 days for your first copy to be mailed.

*NOTE: Subscriptions at ACS member rates are for personal use only.

New... for the Physical Chemist

LIQUID STATE CHEMICAL PHYSICS

R.O. Watts & I.J. McGee

A comprehensive account of the theory of liquids and the relation between this theory and the determination of intermolecular forces. Written at an introductory level, it describes several different types of liquids, including simple atomic fluids, aqueous systems, liquid metals, and molten salts. The book is specifically designed for those who do not have a strong mathematical background.

334 pp. (0 471 91240-9) 1976 \$24.95

ADVANCES IN CHEMICAL PHYSICS, Vol. 36

I. Prigogine & Stuart A. Rice

Contents: Semiclassical Theory of Bound States (I. Percival) • The Correspondence Principle in Heavy-Energy Surfaces and Elastic and Inelastic Scattering (D. Truhlar and R. Wyatt) • Theoretical Aspects of Ionization Potentials and Photoelectron Spectroscopy: A Green's Function Approach (L. Cederbaum and W. Domcke) • Application of Diagrammatic Quasidegenerate RSPT in Quantum Molecular Physics (V. Kvasnicka) • Interactions of Slow Electrons with Benzene and Benzene Derivatives (L. Christophorou, M. Grant, and D. McCorkle). *Advances in Chemical Physics Series* approx. 608 pp. (0 471 02274-8) 1977 \$31.95

SELF-ORGANIZATION IN NONEQUILIBRIUM SYSTEMS

From Dissipative Structures to Order through Fluctuations
G. Nicolis & I. Prigogine

Because evolutionary processes lead to vast diversification and increasing complexity, the behavior of a macroscopic system with many interacting subunits can substantially differ from the random superposition of the independent subunits' evolution. This monograph explores the self-organization phenomena arising in such systems while giving a unified treatment of self-organization based on the techniques of irreversible thermodynamics, nonlinear mathematics, and kinetic theory.

approx. 544 pp. (0 471 02401-5) 1977 \$27.50

STATISTICAL MECHANICS, 2nd Ed.

Joseph Edward Mayer & the late Maria Goeppert Mayer

An up-to-date new edition of a classic work first published in 1940. Emphasizes the logic and fundamental structure of statistical mechanics. Chapters and sections are self-contained, giving definitions of symbols, explanations of notation and statements of the basic starting equations, and references to previous sections and equations. Includes an historical perspective discussing the use of probabilities and probability densities; the logic and formalism of the Gibbs ensemble method with master equations and their interrelations; and explanations of various paradoxes.

491 pp. (0 471 57985-8) 1977 \$23.50

FORTRAN IV IN CHEMISTRY

An Introduction to Computer Assisted Methods
G. Beech

The most advanced features of FORTRAN IV are used here with programs ranging from simple calculation of molar masses to powerful curve fitting techniques. They're small enough to be used on most small to medium sized computers and provide a nucleus for any course involving the applications of computers in chemistry. The programs are listed complete with test input and output data.

Problems at the end of each chapter test the student's comprehension of the material, with answers (or hints) given for each question. 303 pp. (0 471 06165-4) 1975 \$23.50

PRINCIPLES OF ULTRAVIOLET PHOTOELECTRON SPECTROSCOPY

J. Wayne Rabalais

A detailed presentation of the principles of UV photoelectron spectroscopy in terms of modern chemical physics, i.e., the phenomenon of photoionization and its resulting consequences by means of modern quantum chemical methods. Includes a table of molecules with references to PE spectra as well as numerous illustrations, examples, and mathematical derivations.

454 pp. (0 471 70285-4) 1977 \$29.95

CLASSICAL KINETIC THEORY OF FLUIDS

P. Résibois & M. De Leener

This self-contained introduction to the methods of nonequilibrium statistical mechanics starts from first principles and advances to the point where comparison with experiment is possible. Brownian motion and the Boltzmann equation are presented in a unique language framework that makes the corresponding modern approaches of correlation function method and generalized kinetic equations appear as a natural generalization.

approx. 688 pp. (0 471 71694-4) 1977 \$29.50

ADVANCES IN PHOTOCHEMISTRY, Vol. 10

J.N. Pitts, Jr., George S. Hammond, & Klaus Gollnick

Contents: Vapor Phase Photochemistry of the Neutral Oxides and Sulfides of Carbon • Photolysis of Saturated Alcohols, Ethers, and Amines • Excitation and Deexcitation of Benzene • Primary Photochemical Processes of Organo-Transition Metal Compounds • Intramolecular Proton Transfer in Electronically Excited Molecules • Excited State Behavior of Some Bichromophoric Systems.

Advances in Photochemistry Series

approx. 480 pp. (0 471 02145-8) 1977 \$29.50

STRUCTURE AND SPECTRA OF ATOMS

W. G. Richards & P.R. Scott

Utilizing a qualitative pictorial argument when possible, and avoiding mathematical problems found in many advanced texts, Richards/Scott provides readers with an introduction emphasizing the relevance of atomic spectra to chemistry and includes references to topics that are distinct branches of spectroscopy.

98 pp. (0 471 01654-3) cloth 1976 \$10.50

98 pp. (0 471 01759-0) paper 1976 \$ 4.50

VIBRATIONAL STATES

S. Califano

This general theoretical introduction to vibrational spectroscopy at the graduate level also includes topics of a more advanced character for the benefit of research workers. The book considers the vibrations of isolated molecules at a theoretical level while it examines coordinate transformations, extensively employs quantum field and group theory methods, emphasizes the role of off-diagonal operators in the construction of symmetry coordinates, and gives a detailed treatment of redundancies.

335 pp. (0 471 12996-8) 1976 \$39.95

THE HARTREE-FOCK METHOD FOR ATOMS

A Numerical Approach

Charlotte Froese Fischer

An up-to-date, integrated treatment of the HF approximation for bound states of atoms, its definition, the derivation of the HF equations, and the properties of the approximation. Z-dependent perturbation theory is used to show how the approximation can be improved by means of a multi-configuration (MCHF) approximation. Features graphs of radial functions to show their general form, some exact results for the hydrogenic case, and a list of readily available programs for atomic structure calculations.

approx. 320 pp. (0 471 25990-X) 1977 \$22.95

Available at your bookstore or write to Nat Bodian, Dept. A 2393-51.

Prices subject to change without notice.



WILEY-INTERSCIENCE

a division of John Wiley & Sons, Inc.

605 Third Avenue New York, N.Y. 10016

In Canada: 22 Worcester Road, Rexdale, Ontario

092 A2393-51

26 W.A. 2520